Mathematical Modelling of Electrokinetic Phenomona in Soft Nanopores

by

Mpumelelo Matse

M.Sc., Simon Fraser University
PGDip., African Institute for Mathematical Sciences (AIMS)
B.Sc., University of Swaziland

Thesis Submitted in Partial Fulfillment of the
Requirements for the Degree of
Doctor of Philosophy

in the
Department of Physics
Faculty of Science

SIMON FRASER UNIVERSITY
Spring 2020

Approval

Name:	**Mpumelelo Matse**
Degree:	**Doctor of Philosophy (Physics)**
Title:	**Mathematical Modelling of Electrokinetic Phenomona in Soft Nanopores**
Examining Committee:	**Chair:** Dr. John Bechhoefer Professor

Dr. Malcolm Kennett
Senior Supervisor
Associate Professor

Dr. Michael Eikerling
Supervisor
Professor
IEK-13, Forschungszentrum Jülich GmbH, Germany

Dr. Peter Berg
Supervisor
Professor of Mathematics and Physics
Department of Science, University of Alberta

Dr. Karen Kavanagh
Supervisor
Professor

Dr. David Sivak
Internal Examiner
Assistant Professor

Dr. Zuzanna S. Siwy
External Examiner
Professor
Department of Physics and Astronomy
University of California Irvine

Date Defended: **April 15, 2020**

Abstract

In and around porous systems with at least one characteristic dimension below 100 nm, solid/liquid interfaces play a key role in surface-charge-governed transport, separation processes and energy storage devices. Nanopores with well-defined geometry and chemical characteristics have emerged as valuable tools to unravel interactions between external and induced electric fields and the underlying transport, in the presence of embedded charges. In this thesis, theoretical and numerical investigations of electrokinetic effects in soft cylindrical nanochannels with uniformly distributed surface charges are carried out within continuum mean-field approximations. The aim is to provide a theoretical framework through which one can access a comprehensive understanding of the coupling between electrokinetic transport, double-layer charging and wall deformations in nanochannels embedded in soft polymeric membranes.

In the first part of the thesis, numerical calculations using the coupled continuum mean-field equations are conducted to quantify ion and fluid transport in a finite, cylindrical and rigid nanochannel connected to cylindrical electrolytic reservoirs. Results of these calculations, verified by experiments, serve as a guide for theoretical investigations in later components of the thesis. Subsequently, the transport of protons and water in a long, negatively charged channel is studied from a theoretical point of view. A theoretical model is developed that describes nonlinear coupling between wall deformation and water and proton flows in a charged, deformable nanochannel whose viscoelasticity is governed by the linear Kelvin-Voigt model. In addition to focusing on transport phenomena in an open nanochannel, we direct attention to the equilibrium structure of the electric double layers. This was achieved by considering a physical situation where the charged channel is finite and sealed at both ends by metal electrodes under external voltage bias. Size-modified mean-field equations were used to account for finite ion sizes, subject to a self-consistent electroneutrality condition which demands that the net amount of charge on both electrode surfaces balances. Equilibrium ion distributions and differential capacitance curves are presented and analysed. Motivated by electroactuators, the last part of the thesis added deformations of the channel walls to the closed-channel system modelling.

Keywords: Electrokinetic phenomena; Poisson-Boltzmann; Nernst-Planck; Electroosmosis; Streaming potential; Counterions; Electric double layer; Electroactuator

Dedication

To my mother

Acknowledgements

This thesis, the result of a period of labour and patience, would not be what it is today without the involvement of all of those who, in a way or another, contributed their valuable assistance to lead it to the end. First and foremost, I offer many thanks to my supervisors Dr. Michael Eikerling and Dr. Peter Berg who, despite multiple duties, dedicated their time providing guidance, support and enthusiasm during my research. I have been blessed with a friendly and cheerful group of fellow students from Dr. Eikerling's group and SFU physics. I thank them for the challenging discussions and their helpful advice. I am grateful to the Department of Physics at the University of Alberta for welcoming me and offering me a relaxed work environment during my visits to Edmonton for discussions with Dr. Berg. Finally, I acknowledge SFU, NSERC and the University of Alberta for financial support.

Table of Contents

Approval ii

Abstract iii

Dedication iv

Acknowledgements v

Table of Contents vi

List of Tables ix

List of Figures x

Nomenclature xiii

1 Introduction 1

1.1 Background and motivation 1

1.2 Structure of the thesis 5

2 Electrokinetic Phenomena and Continuum Modelling 7

2.1 Electrokinetic effects 8

2.1.1 Electric double layer 8

2.1.2 Electroosmosis 8

2.1.3 Streaming potential 9

2.1.4 Diffusiophoresis and diffusioosmosis 10

2.2 Nanochannel phenomena and applications 10

2.2.1 Polymer electrolyte membranes 11

2.2.2 Nanofluidic channels 11

2.2.3 Biological nanochannels 13

2.3 Continuum modelling of electrokinetic phenomena 14

2.3.1 Poisson-Boltzmann equation 15

2.3.2 Nernst-Planck equation 17

2.3.3 Hydrodynamics equations 18

2.4 Nanochannel model system . . . 19
2.4.1 Electrokinetic length and time scales . . . 19
2.4.2 EDL overlap and perm-selectivity . . . 21
2.4.3 Electroneutrality . . . 22

3 Numerical Simulations for a Cylindrical Nanochannel 24
3.1 Model description . . . 25
3.1.1 Schematics and assumptions . . . 25
3.1.2 Governing equations . . . 26
3.1.3 Boundary conditions . . . 26
3.2 Numerical implementation . . . 27
3.2.1 Problem identification and geometry definition . . . 27
3.2.2 Multiphysics modelling . . . 28
3.2.3 Discretization scheme . . . 28
3.2.4 Post-processing and visualization . . . 29
3.3 Results and discussion . . . 29
3.3.1 Hydrodynamic equilibrium . . . 29
3.3.2 Ionic fluxes . . . 33
3.3.3 Ionic selectivity . . . 39
3.3.4 Experimental validation . . . 40
3.4 Summary . . . 40

4 Theory of Proton Transport Through a Soft Nanochannel 42
4.1 Analytical solutions for a long and rigid nanochannel . . . 43
4.1.1 Assumptions . . . 43
4.1.2 Analytical solutions . . . 44
4.2 Breakdown of electroneutrality . . . 48
4.2.1 Non-insulating channel walls . . . 48
4.2.2 Impact on water and proton transport . . . 51
4.3 Model of deformable nanochannels . . . 52
4.4 Effective 1-D viscoelastic model . . . 53
4.4.1 Water continuity equation in 1-D . . . 54
4.4.2 Stokes equation in 1-D . . . 55
4.4.3 Nernst-Planck equation in 1-D . . . 57
4.4.4 Poisson equation in 1-D . . . 61
4.4.5 Wall pressure balance . . . 63
4.4.6 Dimensionless viscoelastic model formulation . . . 63
4.4.7 Non-viscous and elastic nanochannel . . . 65
4.4.8 Advection-diffusion model . . . 65
4.5 Summary . . . 66

5 Impact of Channel Elasticity on Proton and Water Transport **67**
5.1 Linear perturbative solution . . . 67
5.2 Wall deformation dynamics . . . 69
5.3 Deformation-flux coupling . . . 73
5.4 Onsager transport coefficients . . . 77
5.5 Electrokinetic energy conversion . . . 80
5.5.1 Maximizing power output . . . 80
5.5.2 Maximizing efficiency . . . 81
5.6 Summary . . . 85

6 Cylindrical and Finite Nanochannel Under Closed Confinement **87**
6.1 Methodology . . . 88
6.1.1 Schematics and assumptions . . . 88
6.1.2 Governing equations . . . 90
6.1.3 Boundary conditions and electroneutrality . . . 91
6.1.4 Constitutive relations and numerical methods . . . 93
6.2 Results and discussion . . . 93
6.2.1 Time evolution of double layers . . . 93
6.2.2 Differential capacitance . . . 97
6.2.3 Effect of asymmetry in ion properties . . . 103
6.2.4 Effect of surface charge density modulation . . . 105
6.3 Summary . . . 107

7 Closed and Deformable Nanochannel: Model for an Ionic Polymer Actuator **108**
7.1 Model system . . . 109
7.2 Model in 1-D . . . 110
7.2.1 Theory for the electric potential in 1-D . . . 110
7.2.2 Swelling model . . . 113
7.3 Numerical methods . . . 115
7.4 Results and discussion . . . 117
7.5 Summary . . . 121

8 Conclusions and Outlook **123**
8.1 Conclusions . . . 123
8.2 Outlook . . . 125

Bibliography **127**

List of Tables

Table 3.1 Typical parameters for a rigid cylindrical nanochannel connected to reservoirs. 27

Table 5.1 Parameters of the deformable channel system, based on common properties of PEMs. 69

Table 5.2 Axial-dependent variables of the system. 69

Table 6.1 Parameters of the system. 93

List of Figures

Figure 2.1 Schematic illustration of the EDL in a narrow channel. 9
Figure 2.2 Schematic depiction of the physical situation leading to the generation of streaming potential. 10
Figure 2.3 Schematic illustration of electrokinetic power generation in a nanofluidic channel. 13
Figure 2.4 Schematic of the nanochannel system connected to two reservoirs . 20

Figure 3.1 Schematic of the numerical system consisting of a cylindrical nanochannel system connected to two cylindrical reservoirs 25
Figure 3.2 2D axisymmetric model mesh, with an increased density of elements close to the channel wall. 29
Figure 3.3 Typical surface plot of the computed fluid axial velocity u_z on the system's r–z plane 30
Figure 3.4 Fluid axial velocity profile in r direction at the center of the channel 31
Figure 3.5 Fluid pressure profile in z direction along the channel's centerline . 32
Figure 3.6 Surface plot of the computed electric potential on the system's r–z plane 34
Figure 3.7 Contributions of advection (first column), diffusion (second column) and migration (third column) to the total ionic current 35
Figure 3.8 Sectionally averaged current plotted as a function of σ_p 36
Figure 3.9 Sectionally averaged fluid-induced ionic current coefficient η_{coef} plotted as a function of σ_p 37
Figure 3.10 The concentration of cations and anions along the center of the channel 38
Figure 3.11 Ionic selectivity of the channel 39
Figure 3.12 Comparison of numerical results with experimental data for the dependence of the electric conductance on the bulk KCl concentration 41

Figure 4.1 Numerical results illustrating the effect of the channel's aspect ratio. 45
Figure 4.2 Comparison of numerical results with analytical results for the electric potential across the centre of the channel. 47
Figure 4.3 Effect of $\varepsilon_{\text{ratio}}$. 52

Figure 4.4 Schematic illustration of the deformed channel configuration. 54
Figure 4.5 Comparison of $\bar{u}_z$ from 2-D numerical model to the one for 1-D model. 57
Figure 4.6 Dependence of ξ_u and ξ_E on Λ. 60
Figure 4.7 Comparison of $\bar{J}_z$ from 2-D numerical model to the one for 1-D model 61

Figure 5.1 The deformation profile for a nanochannel after application of a pressure step for a small deformation 70
Figure 5.2 example 71
Figure 5.3 Variation of the relaxation time of the walls with the position along the channel. 72
Figure 5.4 Profiles of total proton flux along the nanochannel at different times 73
Figure 5.5 Variation of the average proton flux at steady state with surface charge 74
Figure 5.6 Variation of the average convective, diffusive and migration proton fluxes 75
Figure 5.7 Variation of the average proton flux at steady state with surface charge 75
Figure 5.8 Variation of the average water flux at steady state with surface charge for different elasticity constants. 76
Figure 5.9 Transport coefficients against the channel's cross-sectional area $\tilde{a}$. . 79
Figure 5.10 Dependence of electrokinetic conversion efficiency on the cross-correlation coefficient at maximum output power and maximum efficiency. . . . 81
Figure 5.11 Electrokinetic energy conversion efficiency at maximum efficiency against surface charge density 82
Figure 5.12 Electrokinetic energy conversion efficiency at maximum efficiency against surface charge density 84
Figure 5.13 Comparison of the 1-D model with experimental results for electrokinetic energy efficiency 85

Figure 6.1 Schematic illustration of the closed cylindrical channel configuration 89
Figure 6.2 Two-dimensional view of the time evolution and relaxation of the EDL. 94
Figure 6.3 Variation of the total ion concentration, $c_t = c_+ + c_-$, along the center of the channel. 95
Figure 6.4 Variation of C_{diff} with ΔV and Cross-sectionally averaged total ion concentration with distance from the left electrode 98
Figure 6.5 Variation of the total net charge on the right electrode against the electrode potential bias ΔV 99
Figure 6.6 The influence of surface charge density on the point of zero charge on the right electrode 100
Figure 6.7 The influence of Q_{T} on (a) the total charge on the right electrode and (b) the differential capacitance as a function of the voltage bias. 101

Figure 6.8 Variation of the differential capacitance with the electrode potential bias at different values of a. 102
Figure 6.9 Differential capacitance against the electrode potential bias at various values of (a) z_+/z_- and (b) a_+/a_-. 103
Figure 6.10 Cross-sectional concentration of cations and anions along the length of the channel at different anion valencies. 104
Figure 6.11 Effect of σ_0 on charge distribution within the channel for the case $n_\sigma = 2$. 106
Figure 6.12 Net ion concentration along the center of the channel for different values of σ_0. 107

Figure 7.1 Schematic illustration of the electroactuating system 109
Figure 7.2 Stress analysis in a cross-section of the cylindrical channel. 113
Figure 7.3 The elastic response of the channel vs. the radius. 116
Figure 7.4 Typical axial profiles of the functions $\tilde{\psi}_0$, $\tilde{\psi}_0$, $\tilde{\psi}_0$ and $\tilde{\psi}_0$. 118
Figure 7.5 Typical radial profiles of the electric potential $\tilde{\psi}(\tilde{r})$ 119
Figure 7.6 Radial deformation of the channel as a function of $\tilde{z}$ 120
Figure 7.7 The influence of (a) $\tilde{\sigma}$, (b) $\Delta\tilde{V}$, (c) $\tilde{c}_0$ and (d) ℓ on the opening of the cathode end and shrinkage of the anode side of the channel. . . 121

Nomenclature

Parameter/Variable	Description	Units
k_B	Boltzmann constant	J/K
T	Temperature	K
ε	permittivity	1
ε_0	vacuum permittivity	F/m
q	elementary charge	C
η	channel wall viscosity	Pa s
μ	ion mobility	$m^2/J\,s$
ν	fluid kinematic viscosity	Pa s
D	ion diffusivity	m^2/s
h_0	channel wall thickness	m
Y	wall elasticity constant	Pa
R_p	channel radius	m
L_p	channel length	m
σ_p	surface charge density	C/m^2
α	surface charge scaling parameter	1
c	ion concentration	$1/m^3$
ψ	electric potential	V
p	fluid pressure	Pa
$\boldsymbol{u}$	fluid velocity	m/s
$\boldsymbol{J}$	ion flux density	$1/m^2\,s$

Chapter 1

Introduction

This thesis presents the development of a physical-mathematical treatment and its numerical simulations for electrokinetic transport phenomena of water molecules and ions in a charged, cylindrical nanochannel with soft walls. The modelling approach is based on continuum mean-field theories for mass and momentum conservation. This chapter presents context and motivation for this work, together with a brief outline of the structure of the remainder of the thesis.

1.1 Background and motivation

Pioneering exploration of electrical phenomena in the late eighteenth century, particularly the work of Alessandro Volta in 1798, set the stage for active research on the influence of an electrical current on transport phenomena in various media. Among the electrical experiments were those performed in 1808 in Moscow by the German scientist Ferdinand Friedrich Reuss [1,2], who investigated the influence of direct electrical current on electrolyte solutions. Reuss's discovery marked the birth of a very important branch of surface and colloid science, later called 'electrokinetic phenomena': the electric field–induced transport of fluids and ions relative to a charged solid surface. Reuss established linearity between the mobility and the applied electric field. Although a number of quantitative experiments with various porous media were carried out following Reuss's work, the basic electrokinetic mechanism remained enigmatic for a long time.

It was not until 1879 that a quantitative theory for electrokinetic phenomena was proposed by von Helmholtz [3], which was developed further by Smoluchowski [4]. Helmholtz–Smoluchowski's classical theory still remains the basis of continuum models used to study electrokinetic systems today, and it rests on the fundamental concept of a diffuse 'electric double layer' (EDL): when a solid surface is in contact with an electrolyte solution, the static charges on the solid surface will attract counter-ions and repel co-ions in the electrolyte. This leads to the enrichment of counter-ions in a layer of fluid adjacent to the charged surface. The region with a net charge near the surface interacts with applied electric fields. In

the most simplistic conceptual model proposed by Helmholtz [3], the EDL structure is analogous to that of a conventional dielectric capacitor with planar electrodes. Subsequently, and continuing until today, theories of the EDL have gone through many refinements and paradigm changes. These ideas led to the discovery of some classical electrokinetic phenomena such as electroosmotic flow and streaming potential [5]. The former refers to the generation of bulk fluid flow when an externally applied electric field interacts with the ions in the EDL, while the later phenomenon describes the generation of a potential difference from a pressure-induced flow of a fluid in contact with a charged substrate in the absence of any external electric field.

A more comprehensive theoretical consideration of the EDL model was pioneered by classical works of Gouy [6] in 1910 and Chapman [7] in 1913. In the 'Gouy–Chapman' picture, the ions (regarded as point-like particles/charges) are mobile in a solvent that is described as a continuum dielectric, and are driven by the coupled influences of diffusion and electrostatic forces within the framework of the Poisson–Nernst–Planck (PNP) equations. The equilibrium concentration of ionic species is given by the Boltzmann distribution, and the local electric potential in the EDL is determined by the Poisson–Boltzmann (PB) equation assuming constant electrolyte permittivity. This results in the so-called 'diffuse layer' of mobile ions near the charged substrate.

The neglect of ion sizes, ion-ion interactions and the structure of the solvent, associated with the application of the PB equation, however, is invalid for large surface charges and electric potentials. Specifically, high ionic concentrations introduce steric repulsion and additional correlations among ions due to over-crowding [25]. Therefore, there has been a continuous endeavour toward modification of the PB and PNP models to aptly account for the effect of finite ion size in the electrolyte solution. Stern, in his acclaimed work [9], incorporated the ion size effect in the EDL theory by taking into account a distance of closest approach whereby mobile ions are excluded from the first molecular layer close to the surface. He described the EDL as two layers, namely, (i) the Stern layer (or Helmholtz layer), referring to the compact layer of immobile ions interacting with the electrode surface, and (ii) the diffuse layer where the ions are highly mobile and the Gouy–Chapman model applies. The total EDL capacitance consists of Stern layer and diffuse layer capacitances in series.

Later studies on the inclusion of steric effects were based, predominantly, on statistical mechanical considerations within mean-field approximations [10, 11]. Typically, the two dimensional (2-D) lattice-gas formalism [11, 12] was adopted to model the statistical distribution function of ions and derive the free energy in the mean field approximation, from which size-modified PB and PNP equations were obtained. The first complete size-modified PB model was developed by Bikerman [13], who considered anions and cations of equal size by including an additional entropy term in the free energy. Over the next several years, many researchers have worked on the reformulation of Bikerman's modified PB (mPB)

model to handle ion size effects. Notable work has been reported by Freise [14], Wickie and Eigen [15–17], Strating and Wiegel [18, 19], Borukhov *et al.* [10, 11], Bohinc *et al.* [20, 21], Kornyshev [22], Kilic *et al.* [23, 24] and Bazant *et al.* [25].

A practical need for a clear, fundamental understanding of the structural properties of the EDL arises from the necessity to control and manipulate the flow rates of fluids and ions for a wide array of engineering systems. Electrokinetic transport in nanometer-sized channels at characteristic dimensions below 100 nm enables the occurrence of rich phenomena not seen at bigger length scales. At such scales (below 100 nm), surface charges at the channel walls largely dictate the functionality [5, 26]. Ion selectivity is most prominent if the diffuse charge screening length is comparable to the smallest dimension of the nanochannel cross section [26], leading to a predominantly counterion-containing nanometer-sized aperture. One significant benefit of such nanoscale flows is that they present the possibility of learning new science using custom-made regular nanostructures. The capability to steer the flow of ions and fluids in nanopores and nanochannels with high precision and selectivity carries major implications for nanofluidic devices [27–29], water desalination [30], energy harvesting and conversion [31, 32], biochemical systems [33, 34], bionanosensing [35] and polymer electrolyte membranes (PEMs) in fuel cells and electrolysers [36, 37].

In the realm of PEM fuel cells, polymeric membranes serve as charge-selective electrolytes that facilitate proton conduction through water-filled nanopores. The polymeric pore walls are comprised of dissociated anionic moieties exposed to an aqueous phase. The most commonly used material is Nafion, which consists of a tetrafluoroethylene backbone and perfluoroalkyl ether side chains terminated in negatively charged sulfonic acid groups [37, 38]. Only hydrated proton-complexes (cations) and water are transported in the channels. Thermodynamic forces due to pressure and/or electrostatic potential gradients result in a displacement of water and protons along the channels from the anode side of the fuel cell to the cathode. A plethora of studies has been undertaken toward a better understanding of hydration dynamics and transport phenomena in PEMs, motivated by the desire to optimize fuel cell design and operation [39–45].

Over the past few years, theoretical pore-level models for PEMs were proposed in the literature. These include equilibrium pore sorption and swelling models [46, 47] and other aspects of continuum modelling [48–50], and molecular dynamics simulations [51]. Within the domain of continuum modelling, three-dimensional Poisson–Nernst–Planck (PNP) equations are employed to describe ion transport phenomena. The validity of the PNP equations at the nanoscale, however, requires that the channel radius be at least 2 nm for valid continuum approximations to hold and the EDLs from opposite sides of the walls do not have a strong overlap [52, 53]. Hence, continuum models can predict experimental results provided the nanochannels have strongly charged walls where double layers do not overlap. Generally, strongly charged walls increase the concentration of counterions inside the channel, and this leads to the reduction of the double layer thickness. One significant step towards finding full

analytical solutions for the PNP–Stokes equations is in the modelling framework recently taken by Ladipo *et al.* [50], whereby the membranes were modelled as cylindrical channels with negative, uniform surface charge density.

A major limitation of existing electrokinetic flow models in most of the theoretical literature is that they do not account for viscoelastic deformations of the nanochannel walls, and they assume negligible axial electrolyte concentration and electric field variations. In pressure-steered flows, soft matter nanochannels with high aspect ratio tend to deform elastically [54]. Consequently, the understanding of flow characteristics in these media is compromised if deformations are not taken into account. Nafion, for instance, shows viscous and elastic properties at fuel-cell operating conditions [55]. Elastic deformations have been cleverly exploited to synthesize valves [56–58] and to model peristaltic vascular dynamics [59, 60]. Understanding the interplay between the walls' viscoelasticity and their surface charge density, and its impact on the transport dynamics is essential for accurate modelling of such systems.

One area where the coupling of ion flux, solvent flux and wall deformation is crucial is in electroactuator systems. Usually, in this field a phenomenological coupling coefficient is used in the modelling of the electroactuator response [61] and – to the best of our knowledge – a fundamental theory for the coupling between pore expansion and fluxes of ions and solvent has not been developed. Among bio-inspired actuation materials, ionic polymer metal composite (IPMC) actuators have been intensively studied [62–64]. These find applications in various engineering fields such as bio-mimetic robots [66–68], MEMS devices [69], adaptive optics and medical devices [70–72], energy harvesting [73], and biosensing [74].

Motivated by the necessity to rigorously and accurately model transport mechanism in ionic nanoporous media, this thesis presents a continuum-based theoretical and numerical treatment of electrokinetic flow in a fluid-filled cylindrical nanochannel with charged walls. More importantly, this work goes a step further by introducing deformations of the channel walls. The starting points are the three-dimensional PNP and Stokes equations for the ion-fluid system under the influence of an electric driving field and pressure gradients, along with a model for deformations that couples the internal fluid pressure and elastic response on the soft channel walls. A comprehensive theoretical and numerical study of a finite channel connected to reservoirs is explored first, with emphasis on the dynamical and thermodynamic equilibrium properties near and far away from reservoirs. For a long channel away from reservoirs, an effective 1-D model is constructed that couples counter-ion and fluid flow with viscoelastic wall deformations. Finally, double layer charging in a closed, finite channel is investigated numerically both for the case of a rigid cylindrical channel and a deformable channel characteristic of cylindrical capacitors and electroactuators.

1.2 Structure of the thesis

This thesis is divided into eight chapters, the contents of which are as follows:

Chapter 1: Introduction. This chapter provides context and motivation for the presented research.

Chapter 2: Electrokinetic Phenomena and Continuum Modelling. This chapter presents a detailed discussion of EDL-induced electrokinetic phenomena with continuum modelling methods available in the literature, with emphasis on cylindrical nanochannels.

Chapter 3: Numerical Simulations for a Cylindrical Nanochannel. As a benchmark for theoretical considerations and assumptions in later chapters, this chapter develops numerical tools for simulating transport in ionic solution for a finite and rigid cylindrical nanochannel connected to electrolyte reservoirs.

Chapter 4: Theory of Proton Transport Through a Soft Nanochannel. Here, a 1-D theoretical model is developed that describes nonlinear coupling between wall deformations and the flow of water molecules and protons in a charged, deformable nanochannel with the viscoelasticity of the walls governed by the Kelvin-Voigt model.

Chapter 5: Impact of Channel Elasticity on Proton and Water Transport. Results from the 1-D model developed in Chapter 4 are presented. We investigate the driving mechanism behind deformation and relaxation dynamics of the channel walls in response to the water-proton flow in it. Within the framework of nonequilibrium thermodynamics, compact formulae are derived for the electrokinetic transport parameters in terms of Onsager phenomenological coefficients and, subsequently, for the energy conversion efficiency.

Chapter 6: Cylindrical and Finite Nanochannel Under Closed Confinement. This chapter presents numerical simulations of electric double layer charging in a closed, finite and cylindrical nanochannel with charged walls and sealed at both ends by metal electrodes under external voltage bias.

Chapter 7: Closed and Deformable Nanochannel: Model for an Ionic Polymer Actuator. This chapter extends the results of Chapter 6. A theoretical and numerical investigation of the closed nanochannel is explored further, while allowing the channel walls to exhibit elastic deformations in response to an internal voltage-triggered fluid and osmotic pressure from within. This carries implications for accurately simulating ionic

polymer electroactuators.

Chapter 8: Conclusions and Outlook. A summary of the findings of the work is presented together with suggestions of possible directions for future study.

Chapter 2

Electrokinetic Phenomena and Continuum Modelling

The discussion begins with an introduction to the relevant physics governing electrokinetic transport processes through nanochannels. The channels of interest can be smooth cylindrical nanotubes [75], slit-like nanopores [76], or nanopores of complex geometries as observed in biological systems [77,78]. In the present study, we are interested in channels of cylindrical geometry, which are ideal for exploring fundamental transport phenomena due to simplifications in the mathematical formalism (yielded by radial symmetry) while enabling control and characterization of all channel dimensions with ease. Also, studies reveal that highly swollen polymeric membranes tend to self-organize into cylindrical pore structures [79–81].

Electrokinetic flows can be maneuvered using several kinds of volume (long-range) forces from pressure gradients and electric fields to magnetic fields. These fields are either applied externally, e.g., at channel inlets and outlets, or generated locally within the channel. As dimensions decrease, the relative importance of surface to volume forces increases. The basic physics underpinning the behaviour of the flow can be modelled down to the quantum level. Such level of detail, however, is mostly unnecessary for practical purposes since the de Broglie wavelength of the ions and fluid molecules is usually smaller than the average inter-ionic/molecular distance and all entities can thus be treated in a classical manner. The most detailed results which can be obtained from modelling come from molecular dynamics (MD), Monte Carlo (MC), Brownian dynamics (BD) and mean-field approximation methods.

In classical MD simulations, ions and solvent molecules are treated as discrete particles and described in atomic detail, and then Newton's equations of motion are solved for each particle to calculate their new positions and momenta. The MC method uses random sampling to generate different microscopic configurations of a system which share the same macroscopic state. In BD simulations, the motions of particles follow a stochastic governing equation describing some effective potential effects. Further simplifications are based on mean-field approximations, whereby ion species are represented by macroscopic ion concentrations instead of microscopic distributions of discrete particles. As previously

mentioned, one of the most celebrated mean field theories for electrokinetic transport is the Poisson-Nernst-Planck (PNP) theory. In the PNP theory, the Poisson equation describes the electric field in terms of the electrostatic potential, whose gradient serves as the electric driving force of ion motion. The Nernst-Planck (NP) equation describes the electrodiffusion of ions in terms of ion concentrations.

2.1 Electrokinetic effects

For this work, the drivers of electrokinetic phenomena are the externally applied electric field and mechanical actuation by application of a pressure gradient between the channel openings. Here, we provide a brief literature overview of some electrokinetic effects and focus on how they impact transport through nanochannel structures.

2.1.1 Electric double layer

When considering an aquous ionic solution in chemical equilibrium with the channel walls, the origin of electrokinetic effects lies in the presence of fixed surface charges on the walls that arise from the dissociation of surface groups, specific adsorption of ions from solution [82–84], or through isomorphic substitution where ions with certain valency are replaced by ions with a different valency [85].

Owing to the fixed surface charges at the wall interface, ions in the vicinity of the wall experience electrostatic interaction wherein counter-ions are attracted and co-ions are repelled from the charged surface. Consequently, a layer of fluid enriched in counter-ions and excluding co-ions is formed adjacent to the charged walls. This layer is known as an 'electrical double layer' (EDL) and is shown in Figure 2.1. The shielding of the walls by counter-ions is such that the bulk, far away from the walls towards the center of the channel, is electroneutral. In narrow channels, double layers on opposite surfaces can interact and even overlap, which can create perm-selective openings that repel co-ions.

Several phenomenological models have been developed to understand the structure of the EDL. The Gouy-Chapman-Stern (GCS) model finds widespread use within the interfacial science community. As mentioned, within this model, the EDL is described by two layers, namely, (i) the 'Stern layer', referring to the compact layer of counter-ions strongly interacting with the surface, and (ii) the 'diffuse layer' composed of a mixture of co-ions and counter-ions that move under tangential stress since they are not immobilized in the Stern layer. Because of its resemblance to macroscopic capacitive devices, the EDL's structure is most conveniently probed by studying its capacitance.

2.1.2 Electroosmosis

The development of the EDL near the channel walls, discussed above, exerts a considerable impact on processes which involve fluid flow. If an external electric field is applied along

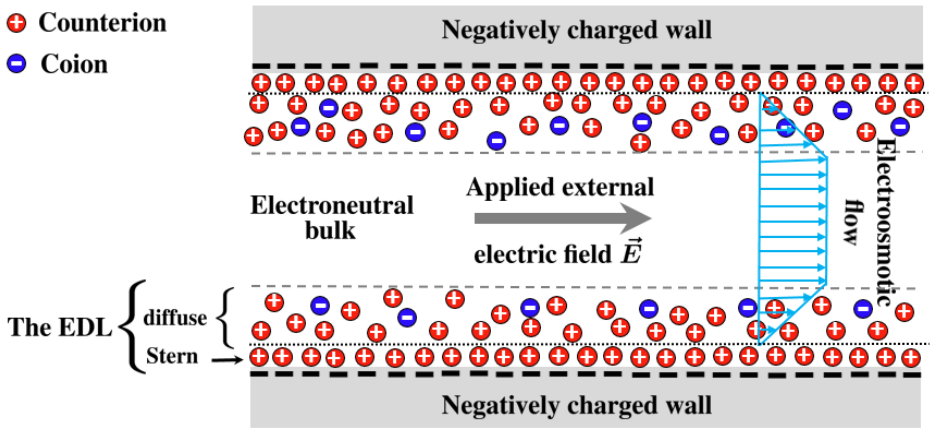

Figure 2.1: Schematic illustration of the EDL in a narrow channel. Arrows represent the typical fluid flow velocity $\boldsymbol{u}$.

the channel, the net counterions in the diffuse EDL experience a net electrostatic force. This eventually manifests itself as a net body force on the fluid. In the absence of any opposing forces, the fluid would thus start flowing toward the cathode (negative terminal of the voltage supplier). This phenomenon is called 'electroosmotic flow' (EOF) and the resulting velocity profile of EOF in nanochannels is plug-like (see Figure 2.1), where the velocity increases as the ionic strength increases. There is no net effect of the action of the electric field far from the walls since the total charge is zero and the fluid is only driven by the fluid pressure gradients and viscous forces along the channel.

2.1.3 Streaming potential

Now, consider the situation when a mechanical flow is actuated in the channel, for instance with an applied pressure gradient, instead of an electric field. In this scenario, pressure-driven fluid flow through the channel triggers downstream movement of ions in the diffuse part of the EDL. This generates an electric current, which is termed the 'streaming current', flowing in the same direction as the liquid and it leads to an effective accumulation of ions downstream under certain boundary conditions. The downstream ion accumulation gives rise to an electric field, which causes a current to flow in the opposite direction to that of the liquid conduction current (see Figure 2.2). This induced electric field is called 'the streaming electric field' and the resultant electrostatic potential difference between the two ends of the channel is referred to as the 'streaming potential'. When the conduction current is equal to the streaming current, a steady state is achieved.

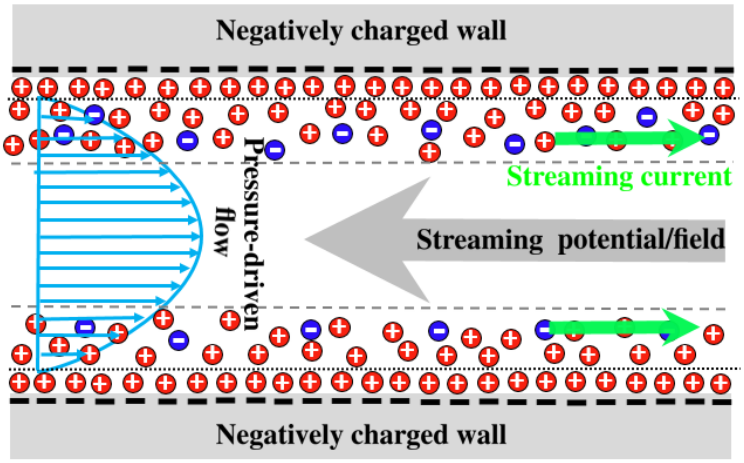

Figure 2.2: Schematic depiction of the physical situation leading to the generation of the streaming potential.

2.1.4 Diffusiophoresis and diffusioosmosis

When an ionic concentration gradient exists along the channel (parallel to the walls), a dielectric colloidal particle can spontaneously migrate along the channel from low to high ion concentration regions via a phenomenon called 'diffusiophoresis'. This mechanism arises from interaction of the particle with the EDL by means of the van der Waals and/or dipole attractive forces. It finds application in particle manipulation and DNA sequencing [86,87]. If the particle is charged, migration is caused by electrostatic interactions between the particle and ions in the solution. In addition, electrostatic forces will strengthen the magnitude of the concentration gradient at the channel walls. This results in a significant gradient in osmotic pressure along the walls, and a resulting fluid velocity field along the channel from high to low ion concentration. This so-called 'diffusioosmosis' process is opposite to the usual direction of the fluid flow in an osmotic process, which is from low to high ion concentration.

2.2 Nanochannel phenomena and applications

Since the beginning of the 19th century, control of the flows of ions and fluids in nanochannels has found applications in technology, most importantly in ion-selective devices, and energy conversion and storage devices. In parallel with technological developments, nanochannel research has produced new physical insights into various functional mechanisms of naturally-occuring ion channels. This section provides an overview of some electrokinetic channels found in engineering and science.

2.2.1 Polymer electrolyte membranes

Fuel cells are one of the most attractive, sustainable means for power generation with the advantages of high efficiency and minimal environmental impact [88]. Among various types of fuel cells, the most attractive for applications in the automotive and portable electronics industry is the polymer electrolyte fuel cell (PEFC). At the anode of the PEFC, solvated protons are generated by oxidation of hydrogen and transported through a water-swollen polymer electrolyte membrane (PEM) to the cathode, where they take part in the electrochemical reduction of oxygen leading to water production [37, 38].

As an electronic insulator and a transport medium of protons, the membrane is a key component of PEFCs and must exhibit specific capabilities such as chemical stability, enhanced water permeability and retention, high proton conductivity but low electronic conductivity, thermal stability, and mechanical strength [89]. Nowadays, state-of-the-art commercial membranes commonly used in PEFC are based on poly(perfluorosulfonic) acid (PFSA) ionomer, and the most popular is Nafion® [55, 90, 91] manufactured by DuPont™.

The ability of a Nafion® membrane to facilitate the transport of protons rests upon the property that its fully hydrated state differs from its dehydrated state. Nafion® consists of a polytetrafluoroethylene (PTFE) backbone and pendant short perfluoroalkyl ether side-chains terminated in negatively charged sulfonic acid groups [38]. The hydrated morphology of the PEM has a direct bearing on the transport of protons and water in the membrane. Owing to the immiscible nature of the hydrophobic PTFE backbone and hydrophilic sulfonic acid groups, fully hydrated Nafion® represents a two phase system that consists of a network of water containing clusters or pores surrounded by the PTFE medium, giving the PEM stability and immobilizing the dissociated sulfonic acid groups.

It is customary to model the PEM pores as cylindrical channels [43–45], typically of radius in the order of 1 nm and length $\sim$ 10–50 nm [48, 49, 79, 80]. A body of experimental and theoretical work [39–45] has been directed to understanding the nature and character of water in pores. In response to an electric field and pressure drop applied at the electrodes, water and protons are believed to be transported in the EDLs between sulfonic acid groups fixed on the walls of hydrophilic channels. Protons may also be transported in PEM via structural diffusion, more commonly known as the 'Grotthus mechanism' – the ostensible tunnelling of protons from one water molecule to the next via hydrogen-bonding [92].

2.2.2 Nanofluidic channels

Nanofluidics deals with the use of fabricated nanochannels to control and manipulate the transport of fluids and ions in a manner similar to the functionality of solid-state electronic devices, such as diodes and transistors. To fabricate nanofluidic devices with nanochannels, a variety of methods have been used, including high-energy beam milling [93, 94], sacrificial

layer deposition [95, 96], selective ion-track etching [97], polymer replication [99], e-beam lithography [100], and nanoimprint lithography [98].

Developments in nanofluidics are driven by the rising demand for a more refined understanding of nanoscale processes and their potential for use in chemical analysis. In contrast to microfluidics, the reduced physical dimensions (1 to 100 nm diameter) in nanofluidics shortens the analysis time due to enhanced mass transport and, in addition, the considerably higher surface-to-volume ratio leads to the emergence of rich surface-induced electrokinetic phenomena, discussed in Section 2.1, presenting opportunities for a new class of sensors, molecular separation techniques, energy conversion and storage devices.

As far as separation methods are concerned, nanofluidic desalination techniques [101] are established methods for drinking water production from seawater or brackish water and are considered a key solution to mitigating the world-wide drinking water scarcity. Water desalination of sea water is commonly performed on the basis of the energy-efficient 'reverse osmosis' method [102], which consists of forcing the passage of salty water through a membrane that rejects ions. This category of desalination techniques relies on utilizing the ion-selectivity property of the membrane channels, induced by the overlap of EDLs. By applying a voltage bias along the channel, the use of voltage-induced reverse osmosis to create osmotic diodes can be realized in asymmetric membranes. One technique was suggested by Deng *et al.* [103], which takes advantage of nonlinear structures induced by concentration polarization in order to purify water.

Another interesting application of nanofluidic concepts is in the field of sustainable energy harvesting. Under an applied hydrostatic pressure difference at the ends, a streaming potential develops along the channel as counter-ions that form the EDL are carried downstream. When the resulting streaming current is driven through an external load resistor, electrical energy is harvested from the fluidic system and this corresponds to the 'power generation mode' (see Figure 2.3). Electrokinetic energy conversion in the 'pumping mode' indicates a conversion of electrical energy into mechanical energy: when an external electric field is imposed on an ion-fluid system, electrostatic pressure develops from electrosmotic flow of the fluid and this can be used to do mechanical work, e.g., in electroactuators [104–106]. The conversion efficiency of the power generation mode is the same as for the pumping mode. A leading experimental observation of electrokinetic energy conversion, working with fluid capillaries, was conducted by Osterle [107]. Osterle predicted a low conversion efficiency of 0.39%. Later, theoretical modelling and experimental results have been reported on the effect of geometry and surface charge on the electrokinetic energy efficiency [108–111].

Nanofluidic channels can be used in technology to create ionic devices that mimic solid-state electronic circuits. Certain types of nanofluidic channels exhibit the ionic current rectification effect [112] for which changing the polarity of the applied electric field turns the ionic flow on and off. This diode-like effect results from asymmetry in channel geom-

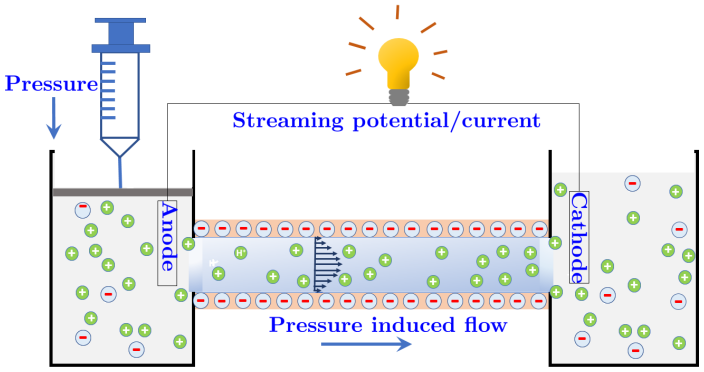

Figure 2.3: Schematic illustration of electrokinetic power generation in a nanofluidic channel.

etry, surface charge, solution concentrations, or a combination of these aspects [112–115]. Nanofluidic diodes have been proposed for use as biosensors [114]. In some practical considerations, the nanochannel is embedded together with an electrically controllable gate electrode. This so-called 'nanofluidic field effect transistor' offers a simple means of controlling the surface charge property of the channel, which in turn regulates the electrokinetic transport phenomena within [115].

2.2.3 Biological nanochannels

In parallel with synthetic nanochannels, nanopores functioning under the influence of electrokinetic effects are found naturally in living organisms. Biological systems contain highly-ordered structures in compartmentalized environments separated by membranes, which are marked by different transporters to regulate the distribution of biologically relevant species. Among the transporters are ion channels, usually localized in particular areas within cells [116]. The driving force of ionic movement in these channels is determined by membrane function, concentration gradients and electric potential differences present across the membrane, or electrostatic interactions between ions and the charged membrane surface. Ion channels are usually highly selective for particular ions, and they can open or close via a conformational change when detecting an external factor, such as a chemical molecule or a changing voltage, a property known as 'gating' [117].

Design guidelines for synthetic nanopores can be derived from a comprehensive understanding of the transport and gating characteristics of biological nanopores. Biological nanopores offer promising devices for developing sensitive biosensors, DNA sequencing, bio-inspired batteries and nanotransistors [28, 29]. Compared to their synthetic counterparts, biological nanopores can be reproducibly fabricated and modified with an atomic level of precision. One challenge in synthesizing biological channels is their limited mechanical stability owing to the fragility of the lipid bilayers that support the channel. Synthesized biological channels should have their sizes at least comparable to that of diffusing ions

($\sim$ 0.2–0.6 nm) and their walls should be subject to proper chemical residues for selective interactions with the ions.

Biological nanopore technology has been fuelled predominantly by interest in developing bio-inspired biological and chemical sensing applications. Biosensing is a single-molecule approach which converts a biological response into an electrical signal to study features of biomolecules that cannot be accessed by considering ensemble systems. The sensing principle is as follows: when a target molecule enters a charged nanopore, the charge distribution and transport around the pore is perturbed. This perturbation manifests itself as an electrical signal from the intermittent ionic blockade event and can be analysed statistically by measuring the amplitudes, duration, frequencies, and shapes of the blockade events to obtain real time properties of the target molecule at the single-molecule level. This has been used to detect various biomolecules including oligonucleotides, peptides, oligosaccharides, organic molecules, and disease-related proteins [116, 118].

One rapidly growing industry in biosensing engineering is DNA sequencing. The idea of using a nanopore for DNA sequencing was first demonstrated by Kasianowicz *et al.* [119] in the 1990s. In principle, a negatively charged DNA molecule is driven through a nanopore in a membrane from head to tail by applying an electric field. Changes in the ion current passing through the pore or transverse electronic currents across the membrane itself are measured as discrete conductance blockade levels and used to determine the nucleotide sequence [120–122].

2.3 Continuum modelling of electrokinetic phenomena

The continuum modelling approach adopted here is based on the Gouy-Chapman [6, 7] picture, where interactions of charged species with solvents hinge on the classical theory of interaction of mobile point charges within dielectric continuum media. It should be stressed that continuum models are not always valid in nanochannel systems. It has been found that continuum theories largely overestimate shielding effects when the pore radius is of the order of the size of EDLs [52, 53]. This becomes an issue when one studies capacitive properties of the EDLs – since ion sizes play a crucial role in ion arrangement in the EDL. In such cases, steric (finite ion-size) effects can be accounted for in the continuum models. However, most of the discussions that follow will not include steric effects. In Chapter 6, however, steric effects will be discussed and included in the model since we will be studying EDL charging.

Mean-field theories reduce the complexity of the many-body problem by presenting equations in terms of continuous-space density functions (i.e., distributions per unit volume) of certain quantities like fluxes and free energies. This implies that the effective electrostatic potential implicitly incorporates the influence of all the ions in the system. Through the

use of the divergence and transport equations in three-dimensional space, local equations of conservation of fluids and ions (continuity equations) are obtained, along with the relation between the electrostatic field and the ions.

2.3.1 Poisson-Boltzmann equation

We start with the ionic species treated as mobile point charges in the electrolyte domain Ω, which comprises the volumetric interior of the channel and reservoirs, if considered. Local density approximations require the free energy of each ion species at every point $\boldsymbol{r}$ in the volumetric domain to depend only on local quantities such as the the electric potential ψ [V] (here [V] denote units, Volts, of the quantity ψ) or the ionic charge density

$$\rho^{\text{ion}}(\boldsymbol{r}) = \sum_i q z_i c_i(\boldsymbol{r}) \ , \tag{2.1}$$

where c_i $[\text{m}^{-3}]$ denotes an average distribution (local concentration expressed as the number of ions per unit volume) of ions of i^{th} species with valency z_i and $q = 1.602 \cdot 10^{-19}$ C denotes the elementary charge.

The total electrostatic free-energy functional of ions in Ω can be expressed as

$$\mathcal{F}[\psi, \rho^{\text{ion}}] \ = \ \int_\Omega \left[-\frac{\varepsilon\varepsilon_0}{2} |\nabla\psi(\boldsymbol{r})|^2 \ + \ \rho^{\text{ion}}(\boldsymbol{r})\psi(\boldsymbol{r}) + \sum_i \mu_i(\boldsymbol{r}) c_i(\boldsymbol{r}) \right] d^3\boldsymbol{r} \ , \tag{2.2}$$

where $\varepsilon_0 = 8.85 \cdot 10^{-12}$ F/m is the permittivity of free space and ε is the relative permittivity (assumed to be space independent) of the electrolyte domain. The first term in Equation (2.2) is the dielectric self-energy of the electric field $\boldsymbol{E} = -\nabla\psi$, the second term gives the electrostatic energy of mobile ions, and the last term couples the system to the bulk, where μ_i [J] denotes the chemical potential of ion species i [123]. The entropic contribution due to steric effects is neglected since ions are considered as point charges and are thus assumed to not occupy any space in the aqueous solution.

Minimizing $\mathcal{F}$ with respect to ψ, i.e., $\partial\mathcal{F}/\partial\psi = 0$, gives the electrostatic Poisson equation

$$\nabla^2\psi(\boldsymbol{r}) \ = \ -\frac{\rho^{\text{ion}}(\boldsymbol{r})}{\varepsilon\varepsilon_0} \ , \tag{2.3}$$

which presents a relationship between a static electric field and the electric charges that cause it – the standard definition of the differential form of Gauss' law in the absence of a dynamic magnetic field.

The electrochemical potential $\bar{\mu}_i$ of the i^{th} ionic species, defined as the total mechanical work done in bringing 1 mole of an ion from a standard state to a specified concentration and electrical potential at constant pressure and temperature, is equivalent to the variation of $\mathcal{F}$ with respect to c_i,

$$\bar{\mu}_i(\boldsymbol{r}) \;=\; \frac{\partial \mathcal{F}}{\partial c_i} \;=\; z_i q\psi(\boldsymbol{r}) + \mu_i(\boldsymbol{r}) \;, \tag{2.4}$$

highlighting contributions from electrostatics ($z_i q\psi$) and the chemical potential μ_i. Take the bulk to be electroneutral and located far away from the channel walls so that $\rho^{\text{ion}} = 0$ and $c_i = c_{0i}$ hold, and set $\psi = 0$ there. In principle, this bulk region could be at one of the reservoirs, or at the center of the channel if the channel is wide enough that the EDL is much smaller than the channel radius. From this perspective, the chemical potential is given as [5, 37, 124]

$$\mu_i(\boldsymbol{r}) \;=\; \mu_i^0 + k_B T \ln\left[\gamma_a \frac{c_i(\boldsymbol{r})}{c_{0i}}\right] \;, \tag{2.5}$$

where γ_a is the activity coefficient, μ_i^0 the standard chemical potential of ion i, $k_B = 1.38 \cdot 10^{-23}$ J/K the Boltzmann constant, and T [K] the absolute temperature. Hence,

$$\bar{\mu}_i(\boldsymbol{r}) \;=\; z_i q\psi(\boldsymbol{r}) + \mu_i^0 + k_B T \ln\left[\gamma_a \frac{c_i(\boldsymbol{r})}{c_{0i}}\right] \;. \tag{2.6}$$

At equilibrium, the electrochemical potential of the ions must be the same everywhere, i.e.,

$$\nabla \bar{\mu}_i(\boldsymbol{r}) = 0 \quad \Longleftrightarrow \quad \nabla\left\{\ln\left[\gamma_a \frac{c_i(\boldsymbol{r})}{c_{0i}}\right]\right\} = -\frac{z_i q}{k_B T}\nabla\psi(\boldsymbol{r}) \;. \tag{2.7}$$

Integrating Equation (2.7) from a point in the bulk solution, where $\psi = 0$ and $c_i = c_{0i}$, leads to the Boltzmann equation, giving the local concentration of each type of ion in the diffuse layer,

$$c_i(\boldsymbol{r}) = c_{0i} \exp\left[-\frac{z_i q\psi(\boldsymbol{r})}{k_B T}\right] \;. \tag{2.8}$$

Note that γ_a vanishes when performing the integration. Substituting Equations (2.1) and (2.8) into Equation (2.3), we obtain the complete PB equation, which describes how the electrostatic potential due to a distribution of ions varies in Ω at equilibrium,

$$\nabla^2\psi(\boldsymbol{r}) \;=\; -\frac{q}{\varepsilon\varepsilon_0} \sum_i z_i c_{0i} \exp\left[-\frac{z_i q\psi(\boldsymbol{r})}{k_B T}\right] \;. \tag{2.9}$$

For a binary symmetric $z:z$ electrolyte (all positive ions have valency z and all negative ions have valency $-z$, where $z > 0$, and $c_{0i} = c_0 \;\forall i = 1, 2$), we have

$$\nabla^2\psi(\boldsymbol{r}) \;=\; \frac{2qc_0}{\varepsilon\varepsilon_0} \sinh\left[-\frac{zq\psi(\boldsymbol{r})}{k_B T}\right] \;. \tag{2.10}$$

2.3.2 Nernst-Planck equation

The PB equation (Equation (2.9)) presented above is only valid at equilibrium. However, one needs to understand the dynamical evolution of ψ and c from some nonequilibrium state, where the Poisson equation (Equation (2.3)) still holds. The most obvious approach is to appeal to the mass conservation law for each ionic species, defined by

$$\frac{\partial c_i(\boldsymbol{r})}{\partial t} + \nabla \cdot \boldsymbol{J}_i(\boldsymbol{r}) \;=\; G_i(\boldsymbol{r}) \; . \tag{2.11}$$

The quantity $\boldsymbol{J}_i$ $\left[\mathrm{m}^{-2}\mathrm{s}^{-1}\right]$ is the total flux density for ionic species i, and G_i $\left[\mathrm{m}^{-1}\mathrm{s}^{-1}\right]$ denotes the rate of production of i per unit volume in Ω. In this work, we set $G_i = 0$.

The total ionic flux density is a combination of different transport contributions which are classified into electrochemically-induced and fluid-induced transport, i.e.,

$$\boldsymbol{J}_i(\boldsymbol{r}) \;=\; \boldsymbol{J}_i^{\text{electrochemical}}(\boldsymbol{r}) + \boldsymbol{J}_i^{\text{fluid}}(\boldsymbol{r}) \; . \tag{2.12}$$

The electrochemical contribution is an electrodiffusion flux arising from diffusion and the interaction of ions with the electric field and is proportional to the gradient of the electrochemical potential according to the Einstein-Smoluchowski relation:

$$\boldsymbol{J}_i^{\text{electrochemical}}(\boldsymbol{r}) \;=\; -\frac{D_i}{k_B T}\, c_i(\boldsymbol{r}) \nabla \bar{\mu}_i(\boldsymbol{r}) \; , \tag{2.13}$$

where D_i $\left[\mathrm{m}^2\mathrm{s}^{-1}\right]$ is the diffusion constant for ionic species i. The fluid contribution comes from the advection of ions by the fluid velocity field $\boldsymbol{u}(\boldsymbol{r})$ $\left[\mathrm{ms}^{-1}\right]$ via

$$\boldsymbol{J}_i^{\text{fluid}}(\boldsymbol{r}) \;=\; c_i(\boldsymbol{r}) \boldsymbol{u}(\boldsymbol{r}) \; . \tag{2.14}$$

Using Equation (2.6) for the electrochemical potential appearing in Equation (2.13), the total flux density becomes

$$\boldsymbol{J}_i(\boldsymbol{r}) = -D_i \nabla c_i(\boldsymbol{r}) - \omega_i z_i c_i(\boldsymbol{r}) \nabla \psi(\boldsymbol{r}) + c_i(\boldsymbol{r}) \boldsymbol{u}(\boldsymbol{r}) \; , \tag{2.15}$$

where ω_i $\left[\mathrm{C} \cdot \mathrm{kg}^{-1}\mathrm{s}\right]$ is the mobility for ion species i which is related to the diffusivity by virtue of the Nernst-Einstein relation [125],

$$\omega_i = \frac{q D_i}{k_B T} \; . \tag{2.16}$$

Equation (2.15) is known as the Nernst-Planck (NP) equation. The first term is the diffusive component of the flux, described by Fick's first law of diffusion. The minus sign indicates that the flux is directed from higher to lower ion concentration regions. The second term indicates transport by electromigration – the transport of ions and charged small particles due to the electric field without an underlying source related to the existence of an EDL.

Positive ions electromigrate from higher to lower electric potentials and negative ions from lower to higher electric potentials. Accordingly, the ions would accelerate in the absence of any viscous forces. At a stationary state, however, there is a balance of the diffusion, advective and electromigration fluxes. A system of the NP equations (Equations (2.15) & (2.11)), describing the fluxes of individual ions, and the Poisson field equation (Equation (2.3)) constitutes a mathematical framework for a deterministic description of ionic electrodiffusion in the continuum approximation.

2.3.3 Hydrodynamics equations

To complete the system of differential equations, the hydrodynamics part of the model is considered to couple the fluid to ion transport. Under isothermal conditions, a Newtonian fluid, i.e., a fluid viscosity that is not dependent on shear stress, has its velocity perturbation fully described by the continuity and momentum conservation (Navier-Stokes) equations:

$$\frac{\partial \rho_{\mathrm{f}}}{\partial t} + \nabla \cdot [\rho_{\mathrm{f}} \boldsymbol{u}(\boldsymbol{r})] \;=\; 0 \tag{2.17}$$

$$\rho_{\mathrm{f}} \frac{\partial \boldsymbol{u}(\boldsymbol{r})}{\partial t} + \rho_{\mathrm{f}} \left[\boldsymbol{u}(\boldsymbol{r}) \cdot \nabla\right] \boldsymbol{u}(\boldsymbol{r}) \;=\; -\nabla p(\boldsymbol{r}) + \nu \nabla^2 \boldsymbol{u}(\boldsymbol{r}) + \sum \boldsymbol{f}_{\mathrm{body}}(\boldsymbol{r}) \;, \tag{2.18}$$

where ρ_{f} $\left[\mathrm{kg} \cdot \mathrm{m}^{-3}\right]$ is the mass density of the fluid, p [Pa] the hydrostatic pressure, and ν [Pa $\cdot$ s] the dynamic viscosity; $\boldsymbol{f}_{\mathrm{body}}$ $\left[\mathrm{N} \cdot \mathrm{m}^{-3}\right]$ are body forces per unit volume externally applied to the fluid. In Equation (2.18), the first term on the left hand side corresponds to inertia and the second term is a measure of advective momentum transport. The ∇p term corresponds to fluid transport by mechanical force due to the internally generated pressure gradient and the $\nu \nabla^2 \boldsymbol{u}$ term constitutes viscous momentum transport.

The body force term may contain different contributions (e.g. gravitational, electrostatic, or magnetic forces), but in our case of interest the only body force considered is one that develops because of the electric field in the EDL:

$$\sum \boldsymbol{f}_{\mathrm{body}}(\boldsymbol{r}) \;=\; -\rho^{\mathrm{ion}}(\boldsymbol{r}) \nabla \psi(\boldsymbol{r}) \;=\; -\sum_i q z_i c_i(\boldsymbol{r}) \nabla \psi(\boldsymbol{r}) \;. \tag{2.19}$$

The effect of gravity is typically neglected in such analyses as can be gleaned from a simple order-of-magnitude calculation.

To reduce the complexity of Equations (2.17) & (2.18), a number of approximations can be made. The fluid is taken to be incompressible and of uniform density, i.e., $\partial \rho_{\mathrm{f}} / \partial t \approx 0$ and $\nabla \rho_{\mathrm{f}} = 0$. At the nanoscale, the fluid flow velocity is much less than the speed of sound. Using the low Mach number expansions of the velocity fields [126], the flow can be assumed steady, essentially rendering flow inside the channel completely inertia-free ($\partial \boldsymbol{u} / \partial t \approx 0$). The ratio between advective and viscous terms is measured by the Reynolds number $\mathrm{Re} = \rho_{\mathrm{f}} U L / \nu$,

where L and U are characteristic length scale and fluid speed, respectively. For water and typical values in a nanochannel, $L \sim 10^{-6}$ m, $U \sim 10^{-4}$ ms^{-1}, $\rho_\mathrm{f} \sim 10^3$ $\mathrm{kg\,m}^{-3}$, and $\nu = 10^{-4}$ $\mathrm{kg\,m}^{-1}\mathrm{s}^{-1}$, we obtain $\mathrm{Re} \sim 10^{-3} \ll 1$, implying a limit where viscous forces are large compared to advective momentum forces. Hence, the advective term in the Navier-Stokes equation can be neglected ($\rho_\mathrm{f}\left[\boldsymbol{u}\cdot\nabla\right]\boldsymbol{u} \approx 0$). We end up with the much simplified equations,

$$\nabla \cdot \boldsymbol{u}(\boldsymbol{r}) \;=\; 0\,, \tag{2.20}$$

$$\nu\nabla^2\boldsymbol{u}(\boldsymbol{r}) - \nabla p(\boldsymbol{r}) - \sum_i q z_i c_i(\boldsymbol{r})\nabla\psi(\boldsymbol{r}) \;=\; 0\,. \tag{2.21}$$

Equation (2.21) is the Stokes equation, and is valid for fluid flows under very low Reynolds numbers (the so-called 'creeping flow' approximation). The above set of equations can be solved for any given boundary conditions. In nanofluid channels under consideration, the no-slip boundary condition is assumed at the wall-fluid interface, where $\boldsymbol{u} = 0$.

2.4 Nanochannel model system

The electrokinetic effects and the continuum model discussed in Section 2.3 are assumed to hold for all nanoporous geometries. In what follows, we study the specific nanochannel system, which forms the basis for the rest of the thesis.

Figure 2.4 shows a schematic of a conventional channel with negative surface charges on the walls. In our model system, a cylindrical nanochannel is connected to two large reservoirs. Reservoirs are filled with aqueous ionic solutions with controlled pH and liquid pressure. In addition to surface-induced transport, the flow of ions and fluid can be controlled by applying an electrical potential to reversible electrodes located in the reservoirs and/or applying a pressure drop between the reservoirs. In these conditions, anions will flow toward the positive electrode and cations toward the negative one, and the fluid will be forced against the pressure gradient. Other electrokinetic effects outlined in Section 2.1, introduced by the surface charges, will be observed.

2.4.1 Electrokinetic length and time scales

The nanochannel is characterized by a radius R_p and length L_p (the subscript p stands for 'pore'). Typical ranges are $R_p \sim$ 1–100 nm and $L_p \sim$ 10–1000 nm. Beyond these two parameters, electrokinetic phenomena in the channel entail a number of length scales closely coupled due to the long range nature of electrostatics.

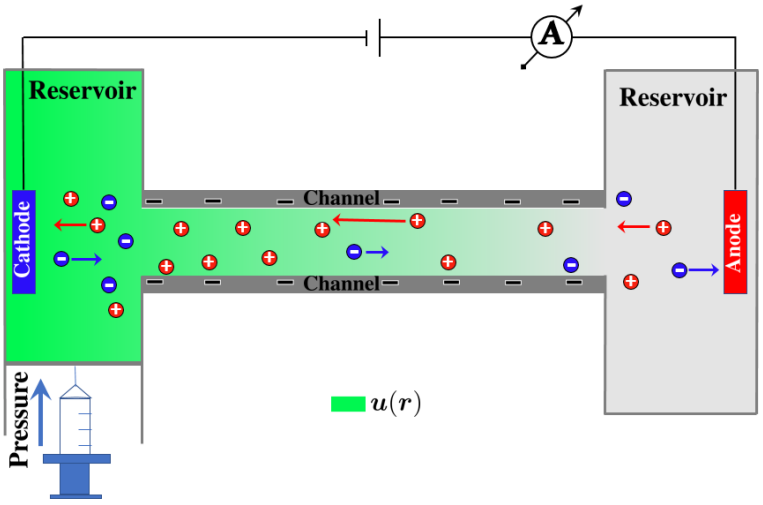

Figure 2.4: Schematic of the nanochannel system connected to two reservoirs, with ion solution driven by external electric field and/or pressure drop at the reservoirs.

Debye length. In order to gain insight into Equation (2.10), we may linearize the exponential term to obtain the linearized PB equation

$$\nabla^2\psi(\boldsymbol{r}) \;=\; \frac{1}{\boldsymbol{\lambda}_D^2}\,\psi(\boldsymbol{r})\;, \tag{2.22}$$

where

$$\boldsymbol{\lambda}_D = \sqrt{\frac{\varepsilon\varepsilon_0 k_B T}{q^2\sum_i c_{0i} z_i^2}} \tag{2.23}$$

is called the 'Debye screening length', which is a measure of the EDL thickness. It is interesting to note that $\boldsymbol{\lambda}_D$ is smaller for a larger bulk concentration, and it is independent of the channel's surface charge density. Typically, $\boldsymbol{\lambda}_D$ ranges from a few Angstroms to tens of nanometres. In nanochannels, it is instructive to report $\boldsymbol{\lambda}_D$ relative to the channel radius R_p via the dimensionless Debye screening parameter $\ell_D = \boldsymbol{\lambda}_D/R_p$.

Bjerrum length. The Bjerrum length is defined as the distance at which the electrostatic interaction energy between two charged species in a dielectric medium is equal to the thermal energy unit, k_BT. It is given by

$$\boldsymbol{\lambda}_B = \frac{z^2q^2}{4\varepsilon\varepsilon_0 k_B T}\;.$$

More intuitively, the Bjerrum length is the scale below which direct electrostatic interactions dominate over thermal effects. For bulk water, $\varepsilon \approx 81$, so at room temperature and valency $z = 1$, the Bjerrum length is about 7 Å . In this case, $\boldsymbol{\lambda}_B$ compares with molecular sizes.

Surface charge length scales. Both the Debye and Bjerrum lengths are independent of surface charges on the channel walls. From the surface electrostatic properties, however, length scales may be constructed that depend on the amount of charges on the channel.

The first is the Gouy-Chapman length,

$$\lambda_{\mathrm{GC}} = \frac{q}{2\pi\sigma_p\lambda_B} , \tag{2.24}$$

defined as the distance from the channel wall where the electrostatic interaction energy of a single ion with the wall is equal to k_BT. Here, σ_p is the surface charge density on the channel wall. The Gouy-Chapman length is large for a strongly charged channel. For a typical surface charge density, say $\sigma_p = 50$ mC/m^2, we have $\ell_{\mathrm{GC}} \approx 1$ nm.

Another surface charge dependent length scale is the Dukhin length,

$$\lambda_{\mathrm{Du}} = \frac{\sigma_p}{qc_0} \sim \frac{\lambda_D^2}{\lambda_{\mathrm{GC}}} . \tag{2.25}$$

This length scale relates the surface charges to the bulk charges and, physically, it characterizes the channel width below which surface conduction dominates over bulk conduction. Hence, it plays an important role for the study of ion conductance in nanochannels, in which surface effects prevail. Typically, for $\sigma_p = 50$ mC/m^2 and $c_0 = 1$ M, we have $\ell_{\mathrm{Du}} \approx 0.5$ nm. A measure of the relative importance of surface conductivity is given by the dimensionless Dukhin number, $Du = \sigma_p R_p/c_0$.

Transport time scales. Dimensional analysis of the Nernst-Planck equation allows us to define a few characteristic time scales for the EDL,

$$\tau_{_L} = \frac{L_p^2}{D}, \quad \tau_{\mathrm{EDL}} = \frac{\lambda_D^2}{D}, \quad \tau_{\mathrm{adv}} = \frac{L_p}{u_z} . \tag{2.26}$$

Here, $\tau_{_L}$ is the characteristic time for an ion in bulk to diffuse the axial length of the channel L_p, τ_{EDL} is the characteristic equilibration time of the EDL, and τ_{adv} is the characteristic time it takes for an ion in the EDL to be advectivelly transported from one end of the channel to the other, given a typical axial fluid speed u_z.

2.4.2 EDL overlap and perm-selectivity

For an aqueous electrolyte solution confined in a nanochannel, the EDLs from opposite walls may have strong interactions. The phenomenon is referred to as the 'EDL overlap', which results in significant changes in the composition of the electrolyte, the related electric field,

and transport properties – consequently, novel transport effects emerge, with applications for chemical analysis. Broadly speaking, EDL overlap is realized when $\ell_D = \lambda_D/R_p \gtrsim 1$.

One important physical effect associated with EDL overlap is the so-called 'Donnan equilibrium': Long-range excess charges introduced by the fixed charges on the channel walls lead to the build-up of a potential drop, termed 'Donnan potential', between the channel's interior and the external reservoirs to maintain a spatially uniform chemical potential of the ions. Plecis *et al.* [127] demonstrated that nanochannels with EDL overlap and non-vanishing Donnan potential exhibit a selective permeability for ion transport: co-ions have a lower permeability than counter-ions. The diffusive flux of counter-ions will be accordingly larger than for co-ions, leading to charge-specific effective diffusivities for co- and counter-ions. The difference in ion permeability can lead to a charge separation between the two ends of the channel. This, therefore, leads to the creation of an opposing electric field along the channel, pointing to the complex couplings associated with ion transport in nanochannels.

2.4.3 Electroneutrality

One important assumption in electrochemistry is the electroneutrality approximation, which assumes that charge separation in electrolyte solutions is impossible at appreciable length scales. Early use of the electroneutrality approximation was by Walther Nernst in 1889 [128] in his study of electromotive forces in electrolyte solutions at appreciable scales. Electroneutrality is usually applied 'globally' for a closed system and 'locally' if a continuum model is used to describe the charge distribution. For a continuum distribution of ions with concentration c_i inside a confined channel volume Ω with boundaries $\partial\Omega$ and having surface charge density σ_p, global electroneutraliy can be expressed as

$$\int_\Omega \sum_i q z_i c_i(\boldsymbol{r}) d^3\boldsymbol{r} = \int_{\partial\Omega} \sigma_p(\boldsymbol{r}) d^2\boldsymbol{r} \ , \tag{2.27}$$

and local electroneutrality as

$$\sum_i z_i c_i(\boldsymbol{r}) d^3\boldsymbol{r} = 0 \ . \tag{2.28}$$

Note that Equation (2.27) reduces to Equation (2.28) only when there are no concentration gradients and the channel is uncharged. In a nanochannel system, global electroneutrality (Equation (2.27)) is a consequence of the Poisson equation when the boundary condition

$$\nabla\psi(\boldsymbol{r}) \cdot \hat{\boldsymbol{n}}(\boldsymbol{r}) = \frac{\sigma_p(\boldsymbol{r})}{\varepsilon\varepsilon_0} \tag{2.29}$$

is utilized. Here, $\hat{\boldsymbol{n}}$ is the unit outward normal vector of the channel surface. The equivalence of Equation (2.27) with the Poisson equation (Equation (2.3)), provided Equation (2.29) is satisfied, can easily be checked by integrating the Poisson equation and using the divergence theorem.

Local electroneutrality defined by (2.28), however, cannot hold in nanochannels where ion concentration profiles depart from their bulk values due to the interaction of ions with the surface charges. In fact, dimensional analysis reveals that the local electroneutrality approximation breaks down at nanosecond and nanometre scales [129]. For a uniform radius channel, the following local electroneutrality condition that comes naturally from Equation (2.29) is defined in place of Equation (2.28):

$$\int_{\Gamma_z} \sum_i q z_i c_i \, d\Gamma_z = 2\pi R_p \sigma_p \, , \tag{2.30}$$

where local electroneutrality is interpreted as a perfect balance between the total net charges within a given cross section (denoted Γ_z) of the channel and the total charges on the part of the surface surrounding the cross section. Equation (2.30) assumes σ_p is uniform. This can be applied to all cross sections along the channel length. Implicitly, Equation (2.30) is a hidden assumption in the model and it emanates from the boundary condition (2.29). Since global electroneutrality is ensured, local electroneutrality will simply be referred to as 'electroneutrality' for the rest of the thesis, and it is the one defined by Equation (2.30).

Equation (2.29) is a consequence of Gauss's Law when the electric field outside the channel is assumed to vanish. In real systems, however, the surrounding medium can be conducting (can have nonzero permittivity) and can lead to 'dielectric leakage'. This could arise from non-insulating walls of the channels, or a different conducting medium outside the channel. In this scenario, electroneutrality is violated. Assuming that the electrolyte is embedded in a constant dielectric medium with permittivity constant ε_{out}, the electric potentials inside ψ_{in} and outside ψ_{out} the channel are governed by a set of PB and Laplace equations,

$$\nabla^2 \psi_{\text{in}}(\boldsymbol{r}) \;=\; -\frac{q}{\varepsilon_{\text{in}}\varepsilon_0} \sum_i z_i c_0 \exp\left[-\frac{z_i q \psi(\boldsymbol{r})}{k_B T}\right] , \qquad \forall \boldsymbol{r} \in \Omega \, , \tag{2.31}$$

$$\nabla^2 \psi_{\text{out}}(\boldsymbol{r}) \;=\; 0 \, , \qquad \forall \boldsymbol{r} \notin \Omega \, , \tag{2.32}$$

and the boundary condition in Equation (2.29) becomes

$$\hat{\boldsymbol{n}}(\boldsymbol{r}) \cdot [\varepsilon_{\text{out}} \nabla \psi_{\text{out}}(\boldsymbol{r}) - \varepsilon_{\text{in}} \nabla \psi_{\text{in}}(\boldsymbol{r})] = \sigma_p(\boldsymbol{r}) \, . \tag{2.33}$$

Chapter 3

Numerical Simulations for a Cylindrical Nanochannel

This chapter develops rigorous numerical tools for quantitative simulations of electrokinetic flow in a cylindrical nanochannel. A preliminary step involves solving the continuum-based model comprising the fully coupled steady-state Poisson-Nernst-Planck (PNP) and Stokes equations for a finite, rigid channel that is connected to reservoirs of cylindrical geometry. The influence of several important factors – including bulk electrolyte concentration, geometry of the channel, externally applied voltage and pressure, and density of charges grafted to the channel surface – on the electrokinetic transport of ions and fluid are investigated.

It is important to remark that although the numerical problem investigated here has been reported in the literature [130–132], this work aims to assess a number of features of the transport to identify the dominant physical phenomena that must be accounted for as a benchmark for understanding the theoretical work presented in the later chapters, where effects such as channel deformations and closed confinement are explored.

The structure of the present chapter is as follows. First, a detailed discussion of the physical-mathematical model of the system is presented in Section 3.1, comprising a brief outline of the governing equations and boundary conditions. Section 3.2 provides a description of the numerical method employed and its implementation. Section 3.3 presents numerical results. Here, we first study the hydrodynamic transport properties of the channel. This is followed by an in-depth analysis of the ionic current as a function of the channel geometry, surface charge density, bulk ion concentration, and applied voltage. Next, the ion-selective properties of the channel are explored. Numerical results for the continuum model are verified by experimental data of the nanochannel conductance available in the literature. Finally, Section 3.4 concludes this chapter with a summary of results.

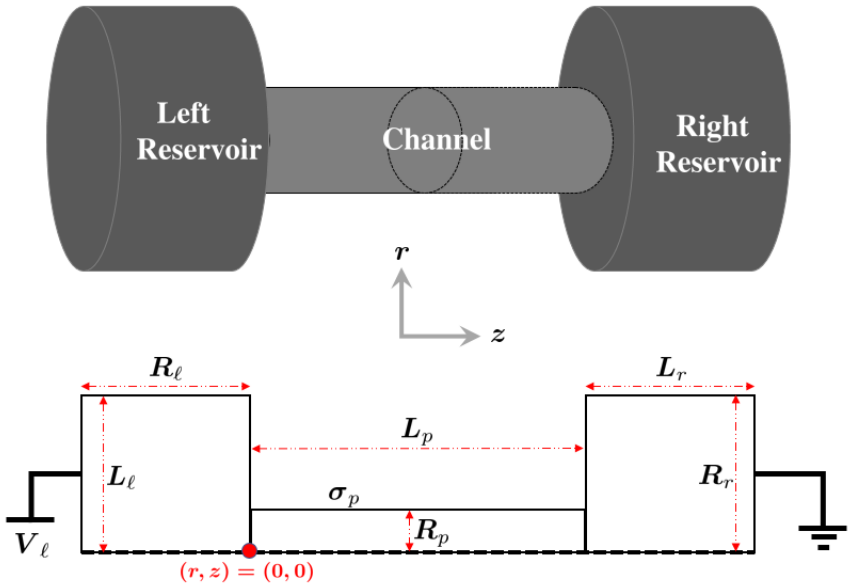

Figure 3.1: Schematic of the numerical system consisting of a cylindrical nanochannel system connected to two cylindrical reservoirs

3.1 Model description

3.1.1 Schematics and assumptions

Figure 3.1 shows the schematic of the computational domain simulated in the present study. A nanochannel of radius R_p and length L_p is connected to two large cylindrical reservoirs. The left reservoir has radius R_ℓ and length L_ℓ, and the right reservoir has radius R_r and length L_r. Herein, we consider nanochannels with R_p between 2 nm and 10 nm, while the length of the channel varies between 25 nm and 100 nm. A voltage bias V_ℓ and a pressure difference P_ℓ are applied across the reservoirs-channel system. To guarantee a constant electric potential and bulk ion concentration at the far ends, reservoirs should have dimensions which are much larger than the dimensions of the channel. Both the channel and the reservoirs are loaded with an aqueous 1:1 binary electrolyte (e.g., KCl) solution, and the walls of the nanochannel have fixed uniform charge density σ_p. Cylindrical coordinates (r, θ, z), with the origin indicated in Figure 3.1, are adopted to formally frame the problem. Because the present problem is θ-symmetric, only the 2-D axisymmetric (r, z) domain is considered.

To make the problem mathematically and numerically tractable, we rely on the following key assumptions undertaken for this study:

- isothermal conditions prevail
- electric potential and ion concentration are invariant with time (steady state)

- steric and solvation effects of ions are neglected
- anions and cations have the same and constant effective diffusivity, independent of electrolyte concentrations and position
- permittivity ε and dynamic viscosity ν of the fluid are invariant parameters

3.1.2 Governing equations

The local steady-state and equilibrium electric potential in the electrolyte solution (ψ), concentrations of positive and negative ionic species (c_+ and c_-, respectively), the fluid velocity field ($\boldsymbol{u}$) and pressure (p) are modelled by the PNP and Stokes equations:

$$-\varepsilon\varepsilon_0\nabla^2\psi \;=\; q\;(c_+ - c_-)\;, \tag{3.1a}$$

$$\nabla\cdot\boldsymbol{J}_\pm \;=\; 0\;, \quad \boldsymbol{J}_\pm \;=\; -D\nabla c_\pm \mp \frac{D}{k_BT}\,c_\pm\nabla\psi + c_\pm\boldsymbol{u}\;, \tag{3.1b}$$

$$\nu\nabla^2\boldsymbol{u} - \nabla p - q(c_+ - c_+)\nabla\psi \;=\; 0\;, \tag{3.1c}$$

$$\nabla\cdot\boldsymbol{u} \;=\; 0\;. \tag{3.1d}$$

A comprehensive discussion of Equations (3.1a)–(3.1d), along with explanations of parameters, is accessible in Chapter 2. Here, $D = D_+ = D_-$ is taken as the constant effective diffusivity of all ionic species.

3.1.3 Boundary conditions

The numerical study focuses on an aqueous binary-symmetric electrolyte solution at room temperature characterized by the set of physical parameters summarized in Table 6.1. The following boundary conditions are assumed for Equations (3.1a)–(3.1d): an external electric field is applied by setting $\psi = V_\ell$ on the furthest end of the left reservoir and grounding the furthest end of the right reservoir ($\psi = 0$). An analogous pressure drop is applied with $p = P_\ell$ at the left reservoir end and $p = 0$ at the right reservoir end.

At the far-end walls of the reservoirs, ion concentrations are maintained at their bulk value, $c_+ = c_- = c_0$. For the Stokes equation, a no-slip boundary condition ($\boldsymbol{u} = 0$) is imposed at the channel walls and the side walls of the reservoirs, with the assumption that the fluid flow is normal to boundaries at the farthest reservoir ends. The side walls of the reservoirs are taken to be ion impenetrable ($\hat{\boldsymbol{n}}\cdot\boldsymbol{J}_\pm = 0$) and uncharged ($\nabla\psi\cdot\hat{\boldsymbol{n}} = 0$). Channel walls are ion impenetrable ($\hat{\boldsymbol{n}}\cdot\boldsymbol{J}_\pm = 0$) and have inner surface charge density σ_p with an insulation boundary condition for the electric potential (i.e., $\varepsilon\varepsilon_0\nabla\psi\cdot\hat{\boldsymbol{n}} = \sigma_p$).

Parameter	Description	Value (range)
q	elementary charge	$1.602 \cdot 10^{-19}$ C
k_B	Boltzmann constant	$1.38 \cdot 10^{-23}$ J/K
ε_0	vacuum permittivity	$8.85 \cdot 10^{-12}$ F/m
ε	dielectric constant	80
ν	dynamic viscosity	$0.5 \cdot 10^{-4}$ Pa s
T	temperature	300 K
D	ion diffusivity	$2 \cdot 10^{-9}$ m^2/s
R_p	channel radius	2 – 10 nm
L_p	channel length	25 – 100 nm
$\lvert\sigma_p\rvert$	surface charge density	0 – 0.3 C/m^2
$\lvert V_\ell\rvert$	external voltage bias	0 – 100 mV
P_ℓ	external pressure drop	0 – 20 kPa

Table 3.1: Typical parameters for a rigid cylindrical nanochannel connected to reservoirs.

3.2 Numerical implementation

Equations (3.1a)–(3.1d), along with the associated boundary conditions, are numerically solved by the finite element method (FEM), implemented by using the COMSOL Multiphysics® commercial simulation package. The FEM, initially coined by Clough [133] in the early 1960s for structural analysis, is based on discretizing the computational domain into individual spatial subdomains, called finite elements, connected by 'nodes' whose potential energy functions can be approximated from the system's governing differential equations using the so-called 'trial base functions' [134–136]. The resulting potential energy expression for the assembled discrete system is a set of algebraic equations which are minimized to form an approximate set of nodal solutions for the individual finite elements. The solution for the global continuous system is found by interpolating between the nodal solution values using approximate functions called 'shape functions', usually low-order polynomials.

COMSOL Multiphysics allows for a straightforward application of the FEM outlined above, as well as permitting easy coupling of multiple physical effects on one system. Next, we present details of the implementation of the problem. In COMSOL, simulations can be performed from the Graphical User Interface (GUI) or can be set up to interface with Matlab. In this work, we only use the GUI. Implementation involves four main stages, namely; problem identification and geometry definition, multiphysics modelling, discretization, and post-processing and results visualization.

3.2.1 Problem identification and geometry definition

The first step is to identify and classify the problem based on the physical phenomena involved. The problem can be defined in 1-D, 3-D, 2-D in-plane and 2-D axisymmetric dimensions, and solved for stationary, time or frequency dependent conditions. In consideration of the cylindrically axisymmetric nature of the problem (see Figure 3.1), the 2D

axisymmetric coordinate system is chosen. We seek stationary solutions. The simulation geometry consists of three rectangular domains in the r–z plane: one for the channel and the other two for the reservoirs. User-defined parameters are fed into the model instead of using COMSOL's parametrized 'solid geometry'.

3.2.2 Multiphysics modelling

This step involves setting up the model equations and all boundary conditions using fully coupled multiphysics solvers. All global parameters are defined first. Contingent on the implementation procedure, modelling of Equations (3.1a)–(3.1d) can be classified into equation-based modelling and module-based modelling. The former entails manually inputting the equations using the 'Mathematics' interface, and we use it for the Nernst-Planck equations. The latter uses modules (predefined models from Electromagnetism, Fluid Flow, Acoustics, Chemical Engineering, etc.) already built into COMSOL to allow for more efficient and straightforward handling of the physics, and we use it for the Poisson and Stokes equations.

For the Poisson equation, the 'electrostatics' interface under the 'AC/DC module' is used. Equation (3.1a) is loaded by the 'Charge Conservation' tree, with the nonhomogeneous function set up under 'Space Charge Density'. The far end boundary conditions for the electric potential are fed in by selecting 'Electric Potential' tree and applying the appropriate boundaries. The electric flux boundary conditions, on the channel walls and reservoir side walls, are implemented by selecting 'Surface Charge Density'.

The Nernst Planck equations are implemented using the 'General Form PDE' tree of the PDE interface under the 'Mathematics' model builder. The 'General Form PDE' interface has the advantage that it allows the equation to be set up in term of fluxes, whose boundary conditions can be treated with ease. Zero ionic fluxes are automatically imposed on the boundaries. The bulk ionic concentration boundary conditions at the reservoir ends are added by selecting 'Dirichlet Boundary Condition'.

Finally, the Stokes equations are implemented using the 'Laminar Flow' interface under the 'Fluid Flow Module'. The no-slip boundary conditions are added by selecting 'no-slip' under the 'Wall' tree. Pressure boundary conditions at the reservoir ends are added by choosing 'inlet' and 'outlet'. The electroosmotic force term in the Stokes equation is treated separately by selecting 'Volume Force'. It should be noted that with the additional 'Fluid Flow Module', this force is easily implemented by selecting 'Migration' under the main tree of the model builder.

3.2.3 Discretization scheme

Once the model equations in the domains and the boundary conditions are set up, the next crucial step is to discretize the geometry. In essence, the accuracy of the solution is easily improved by increasing the number of elements in regions where high gradients of

field quantities are expected[1]. User-controlled meshing is used inside the channel. Here, a triangular finite mesh is adopted. Close to the channel boundaries, a user-controlled mesh is heavily refined with maximum element sizes of 1.2 Å. This ensures sufficient resolution of the physics in the EDL for accuracy. Outside these boundary domains, corresponding to the channel interior and the reservoirs, a predefined mesh explicitly optimized for fluid dynamics is used. A typical mesh for the full geometry is shown in Figure 3.2.

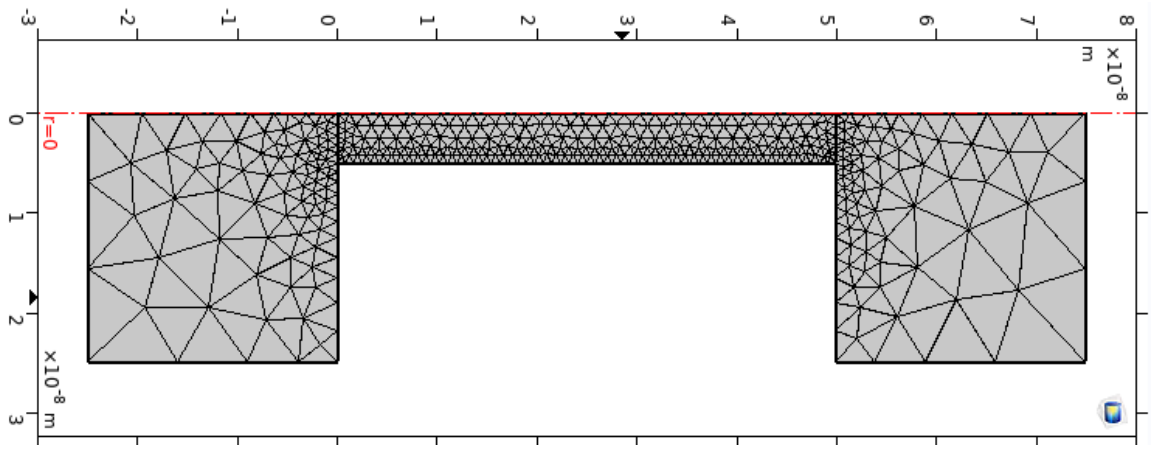

Figure 3.2: 2D axisymmetric model mesh, with an increased density of elements close to the channel wall.

3.2.4 Post-processing and visualization

Once the computation is finished, the results are analysed and evaluated in several ways. Quick inspection of results can be done on COMSOL's graphical interface. Under the model tree, local functions are defined that do data post-processing procedures like domain integration, projections, functional evaluations etc. In some cases, data is manually exported to Matlab® for post-processing. All graphs reported here, with the exception of surface plots, which are taken straight from COMSOL's graphical interface, are produced using the Graphics Layout Engine (GLE®) scripting language.

3.3 Results and discussion

3.3.1 Hydrodynamic equilibrium

We first investigate the system's charging and geometry effects on the fluid motion. This corresponds to a situation where fluid transport stems solely from an externally applied

[1]Note that the Poisson equation often results in a stiff problem.

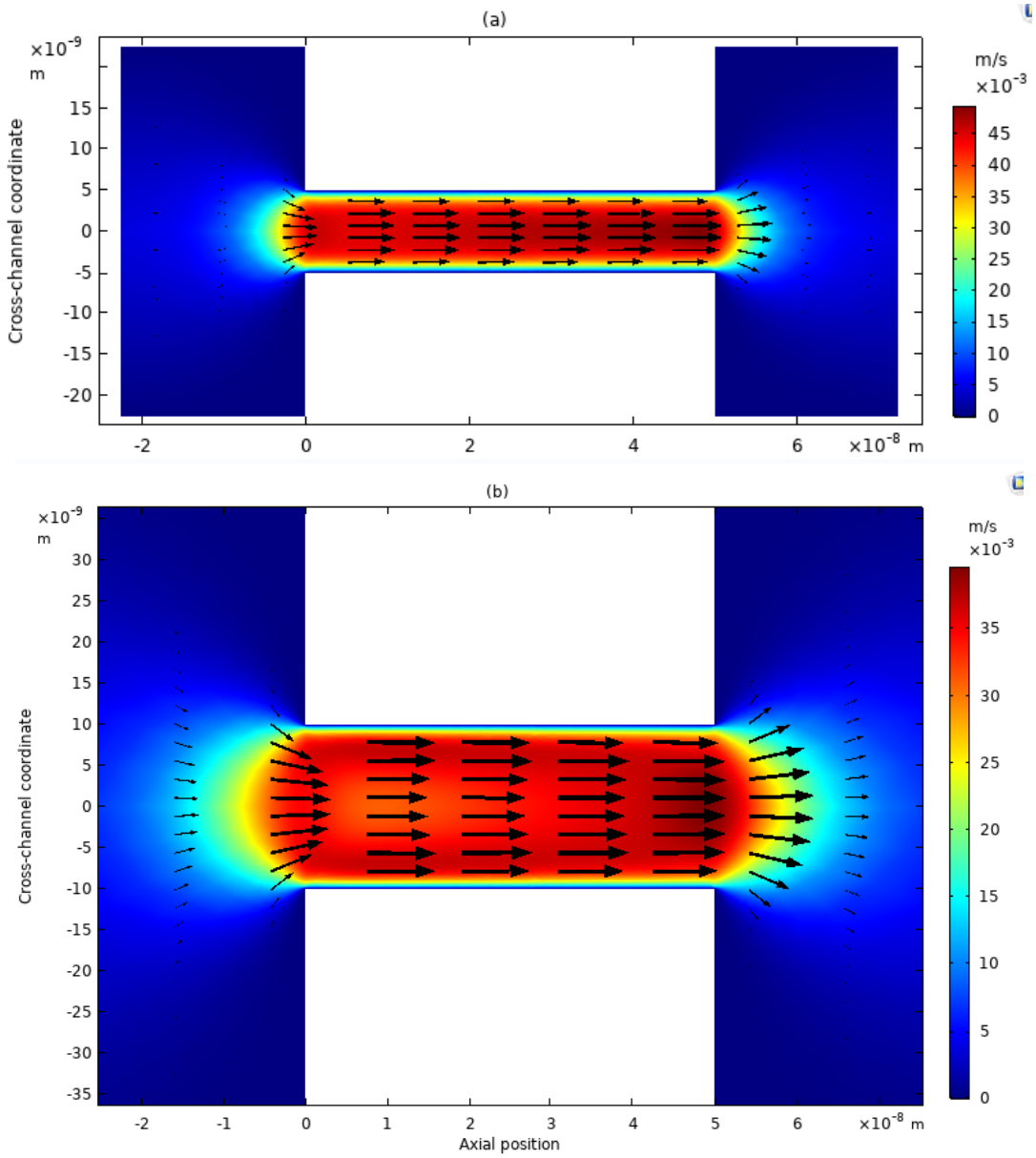

Figure 3.3: Typical surface plot of the computed fluid axial velocity u_z in the system's r–z plane for $R_p = 5$ nm (top figure) and $R_p = 10$ nm (bottom figure). Arrows indicate the velocity vector field.

electric field and surface charges on the channel walls. The pressure at the reservoirs is maintained the same (i.e., $P_\ell = 0$). In a sense, the surface charges break the symmetry of the system by introducing the EDL, resulting in fluid flow.

The computed fluid velocity plots in a two-dimensional slice that includes the channel axis are shown in Figure 3.3 for channel radii (a) $R_p = 5$ nm (top) and (b) $R_p = 10$ nm (bottom). The surface plot represents the axial velocity component only, and the arrows

symbolize the velocity vector field. We remark that the cross-channel coordinate for all plots is shown, for convention, to run from negative values to show positions from one wall of the channel to the other on the r–z plane. As expected, the flow within the channel is along the axial direction only. The radial component of the fluid velocity is only seen near the channel's inlet and outlet regions. These regions extend a few multiples of R_p away from the channel ends. At reservoir regions far away from the channel, fluid flow is much slower than inside the channel. For the larger channel radius, the EDL region accounts for a small fraction of the total cross-sectional area, and, thus, the flow is fully plug-like (the velocity profile converges quickly towards a constant, non-zero value as one moves from the channel wall towards the pore center). At some regions along the channel, we observe the formation of a local minimum in the axial velocity profile around the center of the channel for large R_p. For the smaller radius, however, the flow profile is not fully plug-like but nearly parabolic.

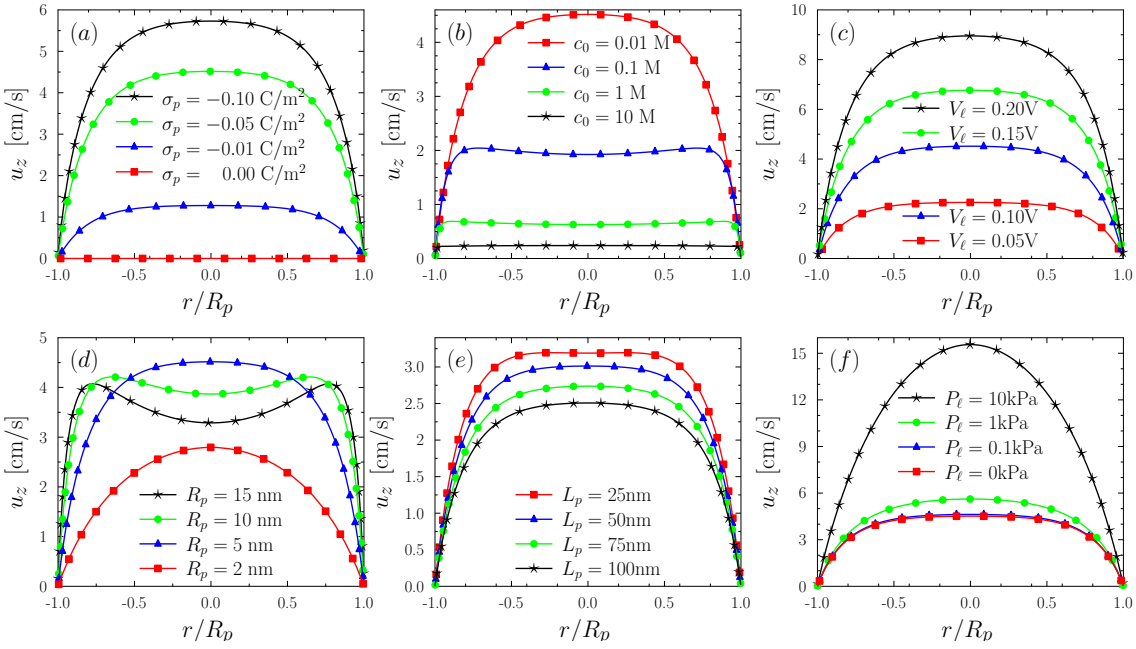

Figure 3.4: Fluid axial velocity profile in r direction at the center of the channel for varying (a) σ_p, (b) c_0, (c) V_ℓ, (d) R_p, (e) L_p and (f) P_ℓ. Reference case: $R_p = 5$ nm, $L_p = 50$ nm, $\sigma_p = -0.05$ C/m^2, $V_\ell = 0.1$ V, $c_0 = 0.1$ M, $P_\ell = 0$ Pa.

A detailed depiction of the full parametric effects on the cross-sectional flow velocity (axial) profiles is shown in Figure 3.4. Profiles are computed in the r direction[2] at the center of the channel ($z = L_p/2$). In Figure 3.4(a), we note the role played by the surface charges in speeding up the flow everywhere across the channel's interior. Figure 3.4(b)

[2]The coordinate r/R_p represents a straight line from one point on the channel wall ($r/R_p = -1$) to the opposite side ($r/R_p = 1$), passing through the center of the pore ($r/R_p = 0$).

depicts that high bulk ion concentrations (1) lower the fluid flow speed, (2) enforce plug-like profiles and (3) introduce a central local minimum in the velocity profile. This stems from a reduced Debye length at high c_0, forcing substantial electroosmotic-induced flow only very close to the walls. At high c_0, this near-wall flow can be faster than at the channel's central region, hence the local minimum. Increasing V_ℓ increases the velocity equally across the channel (Figure 3.4(c)). This is attributed to the change in the externally applied electric field $E_z = V_\ell/L_p$, which increases with V_ℓ and decreases with L_p. In addition to the emergence of the central local minimum at large channel radii, the velocity in the central region diminishes while it still increases near the wall (Figure 3.4(d)). This is because the Debye length becomes much smaller than the channel radius, forcing most of the flow to regions close to the channel walls. Increasing the channel length reduces the velocity equally across the channel (Figure 3.4(e)). Finally, the effect of the pressure difference P_ℓ is shown in Figure 3.4(f). At very high P_ℓ, the flow profile becomes parabolic, a characteristic of Poiseuille flow [137] – the quadratic laminar flow profile across a long cylindrical channel.

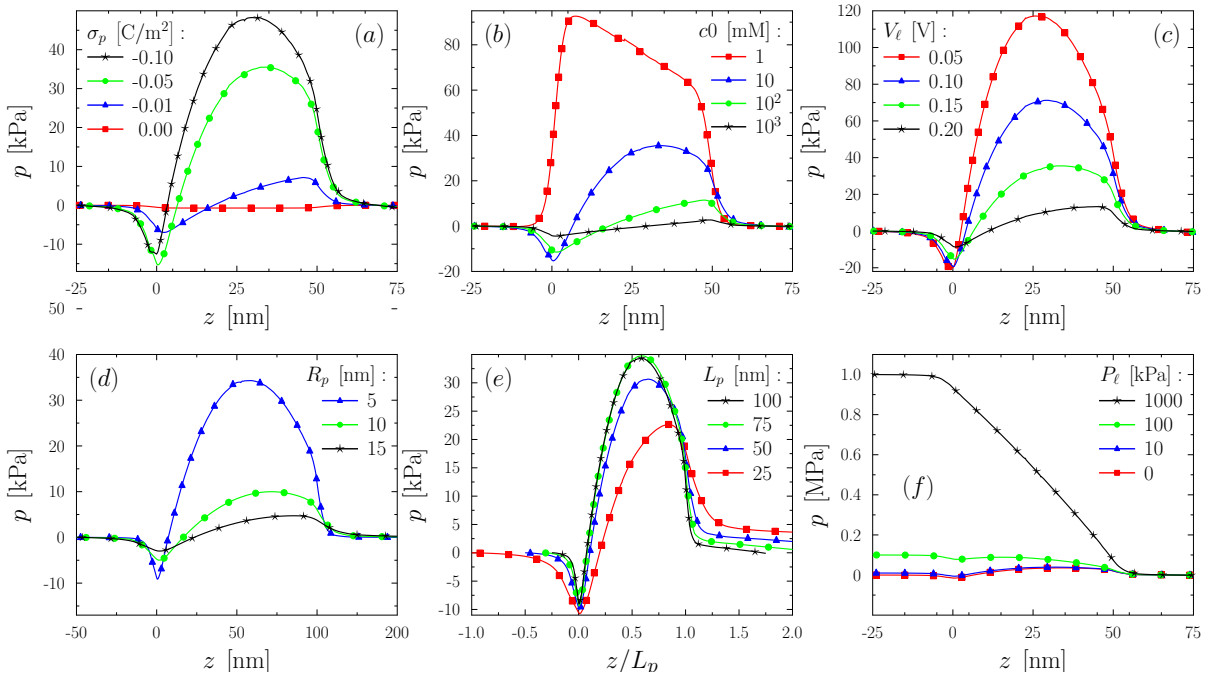

Figure 3.5: Fluid pressure profile in z direction along the channel's centerline ($r = 0$) as a function of (a) σ_p, (b) c_0, (c) V_ℓ, (d) R_p, (e) L_p and (f) P_ℓ. Reference case: $R_p = 5$ nm, $L_p = 50$ nm, $\sigma_p = -0.05$ C/m^2, $V_\ell = 0.1$ V, $c_0 = 0.1$ M, $P_\ell = 0$ Pa.

Pressure profiles along the channel's centerline ($r = 0$), extending to the reservoirs, are shown in Figure 3.5. The asymmetric patterns of the plots, with respect to rotation/reflection across $z = L_p/2$, arise from the surface charges on the channel walls and the applied external voltage differential. One noteworthy feature observed in each profile is

the development of a fluid pressure gradient inside the channel even in the absence of an external pressure drop. We call this pressure gradient 'electrochemically induced pressure', and it arises from the arrangement of ions due to an electrochemical potential gradient (Donnan potential) inside the channel. This allows for an insightful formulation of the total fluid pressure,

$$p(r,z) = p_{\text{electrochemical}}(r,z) + p_{\text{applied}}(z)\ , \tag{3.2}$$

accounting for the electrochemically induced pressure $p_{\text{electrochemical}}$ and externally applied pressure drop p_{applied}. Note that at channel walls $p_{\text{electrochemical}}$ becomes the so-called 'electroosmotic pressure' [138]. From Figure 3.5(a), we observe that $p_{\text{electrochemical}}$ near the center of the channel increases with $|\sigma_p|$. Evidently, at large σ_p most of the counter-ions flow near the walls leaving the wide fraction of the channel cross-section ion-depleted (with relatively few co-ions, depending on c_0) and fluid-saturated. Hence a high fluid pressure develops in that central region. A similar effect is seen in Figures 3.5(b) and (c), where ion-depletion (reduced co-ions) in the central region is prominent at low c_0 and low V_ℓ (co-ions are drawn towards electrified reservoirs); resulting in high fluid pressure. Narrower and longer channels generally exhibit high fluid pressure (Figure 3.5(d) and (e)). In Figure 3.5(f), we see the superimposed external pressure drop p_{applied} on $p_{\text{electrochemical}}$. The 1 MPa curve corresponds to the case when $p_{\text{electrochemical}}(r,z) \ll p_{\text{applied}}(z)$, where a constant pressure gradient develops along the entire channel. This pressure gradient is given by $\mathcal{P} = P_\ell/L_p$ and, hence, $p_{\text{applied}}(z) \sim \mathcal{P}z$ inside the channel.

3.3.2 Ionic fluxes

Hereafter, we explore ion transport in the nanochannel. Figure 3.6 shows the electric potential on a two-dimensional slice that includes the channel axis for $\sigma_p = -0.05$ C/m^2 (top figure) and $\sigma_p = -0.3$ C/m^2 (bottom figure). Arrows represent vector field of the cation flux density, $\boldsymbol{J}_+$. The channel is under the reservoir potential bias $V_\ell = 0.1$ V. Within the channel, the direction of the ion flow is along the channel's axis. The channel's surface charges force more ions to flow in the EDLs near the walls. In principle, the narrower EDLs at high σ_p strengthens near-wall ion transport quite significantly.

If we let $\mathcal{S}$ be the surface of the cross-section located at the center of the channel ($z = L_p/2$), the ionic current I can be evaluated in terms of the flux by

$$I = \int_{\mathcal{S}} q\Big(\sum_{j=1}^{2} z_j \boldsymbol{J}_j\Big) \cdot \hat{\boldsymbol{n}}\, d\mathcal{S}\ . \tag{3.3}$$

Recall that the total current J has contributions from advection, diffusion and migration. Our first course of action is to closely investigate the radial profile of each contribution

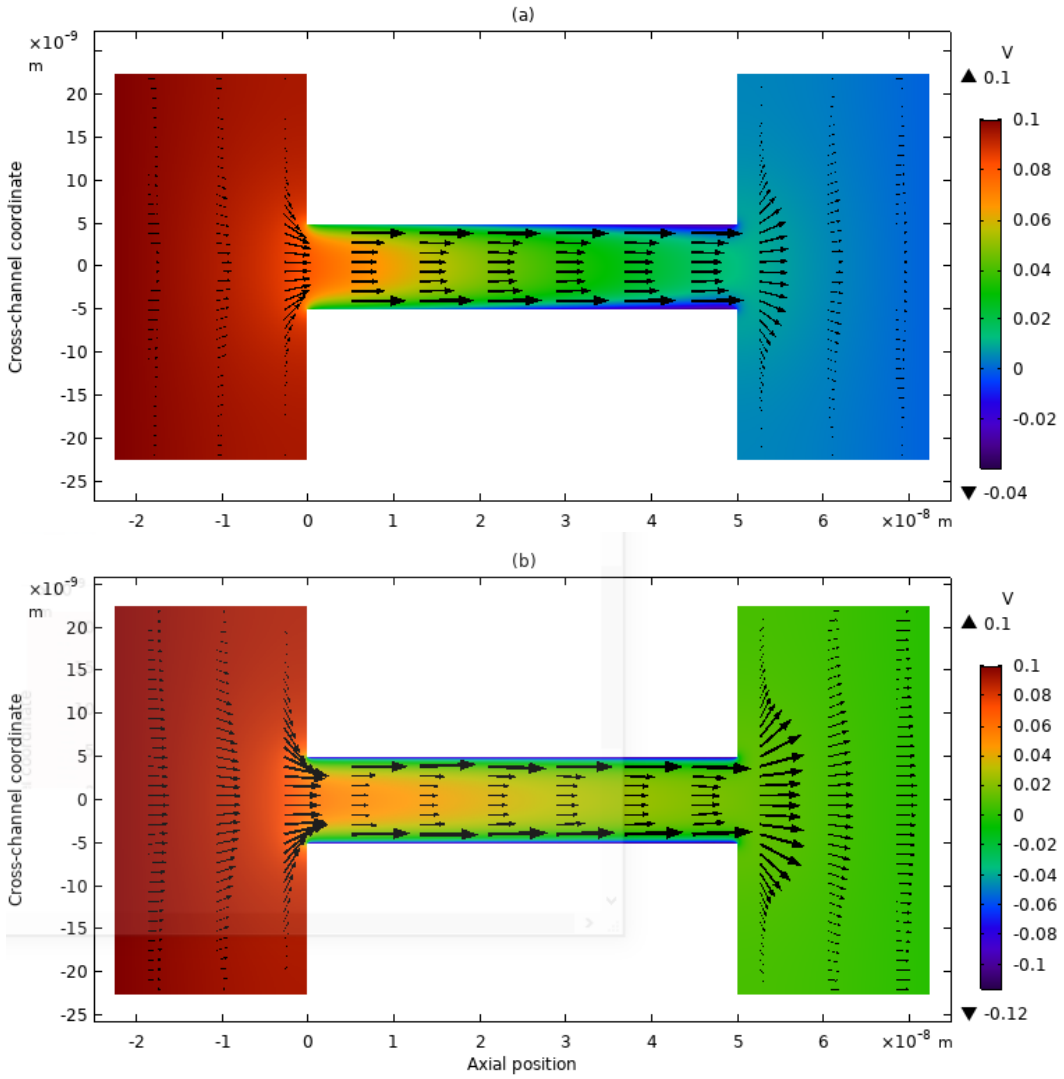

Figure 3.6: Surface plot of the computed electric potential in the system's r–z plane for $\sigma_p = -0.05$ C/m^2 (top figure) and $\sigma_p = -0.3$ C/m^2 nm (bottom figure). Arrows represent the cation flux density vector field. Reference case: $R_p = 5$ nm, $L_p = 100$ nm, $V_\ell = 0.1$ V, $c_0 = 0.1$ M, $P_\ell = 10$ kPa.

across $\mathcal{S}$. We define the following coefficients:

$$\eta_{\text{adv}} = \frac{I^{\text{adv}}}{I}, \quad \eta_{\text{diff}} = \frac{I^{\text{diff}}}{I}, \quad \eta_{\text{migr}} = \frac{I^{\text{migr}}}{I},$$

measuring the ratio of current contributions due to advection, diffusion and migration, respectively, to the total current.

Figure 3.7 shows radial profiles of η_{adv}, η_{diff} and η_{migr} across $\mathcal{S}$ at different parameters, each varied in each row. An immediate observation is that η_{diff} is generally much smaller (about 10 times) than the other ionic current contributions. Instead of focusing on these

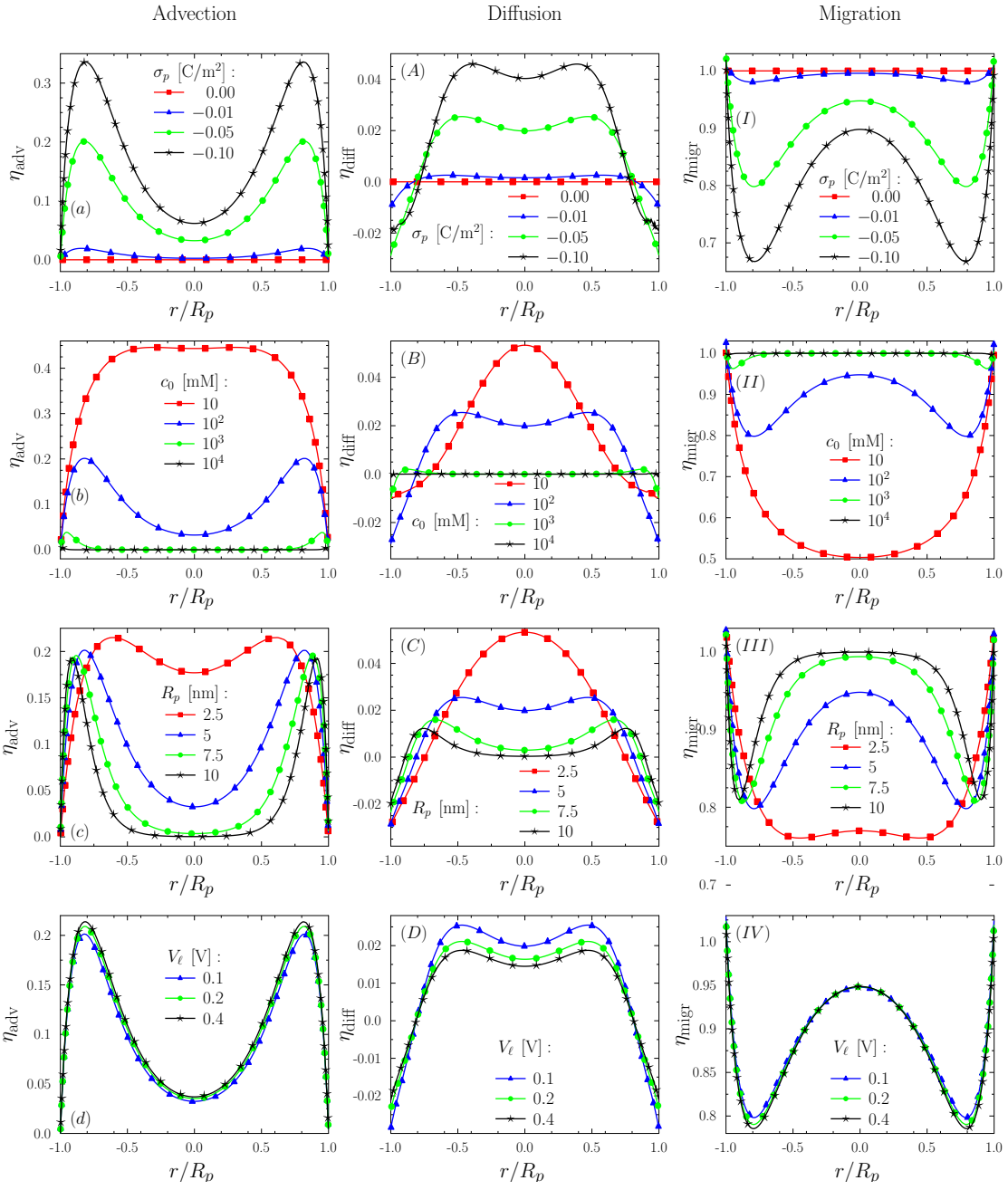

Figure 3.7: Contributions of advection (first column), diffusion (second column) and migration (third column) to the total ionic current as functions of σ_p (first row), c_0 (second row), R_p (third low) and V_ℓ (fourth row). Fluxes are calculated at the cross section located at the channel center ($z = L_p/2$). Reference case: $R_p = 5$ nm, $L_p = 100$ nm, $\sigma_p = -0.05$ C/m^2, $V_\ell = 0.1$ V, $c_0 = 0.1$ M, $P_\ell = 10$ kPa.

stark differences, which can easily be eliminated by changing parameters like V_ℓ, we try to understand the shapes of the profiles. Additionally, the diffusive contribution is negative in the proximity of the walls due to the streaming potential in the EDL, and increases to positive values towards the center of the channel.

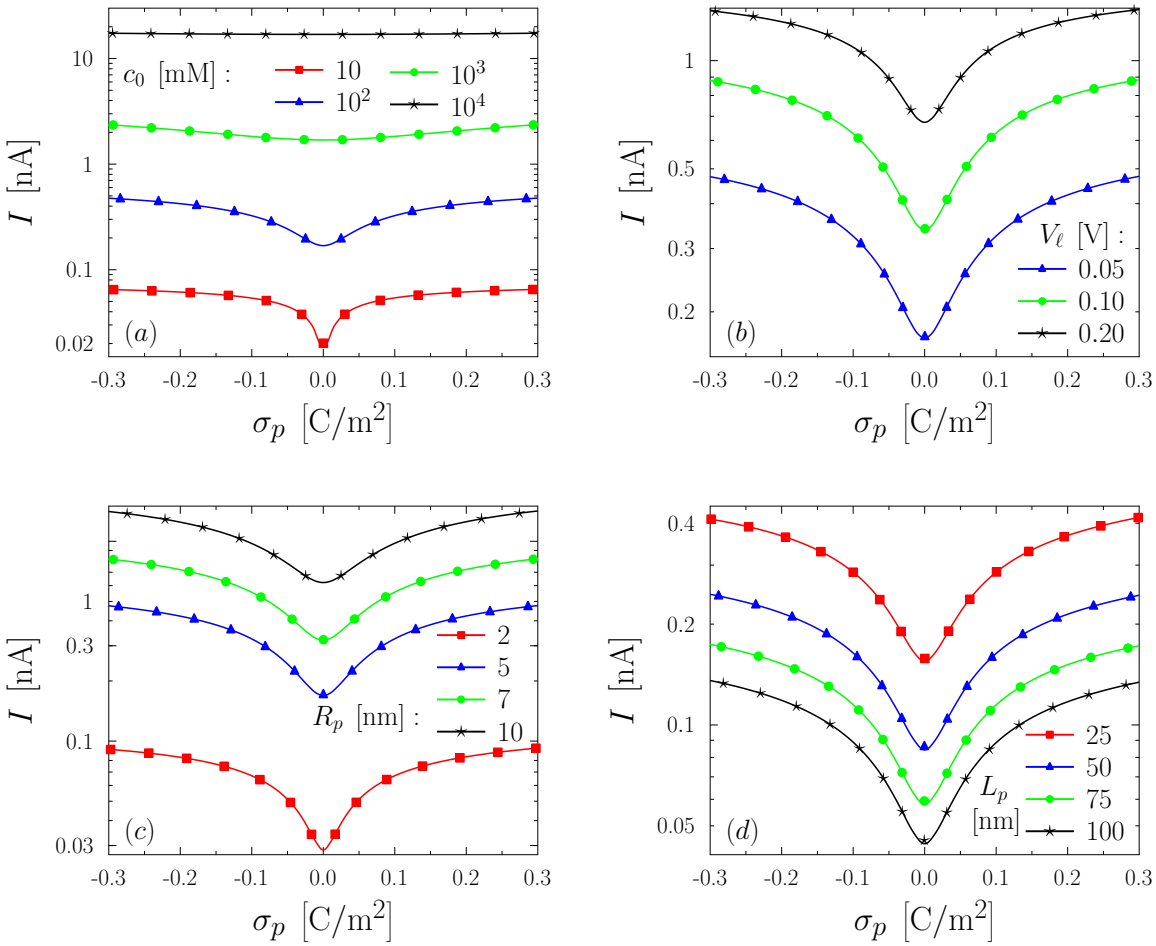

Figure 3.8: Sectionally averaged current plotted as a function of σ_p for different values of (a) c_0, (b) V_ℓ, (c) R_p and (d) L_p. Reference case: $R_p = 5$ nm, $L_p = 50$ nm, $\sigma_p = -0.05$ C/m^2, $V_\ell = 0.1$ V, $c_0 = 0.1$ M, $P_\ell = 10$ kPa.

Generally, η_{adv} profiles are concave-shaped and assume maximal values in the EDLs near the channel's walls, where a majority of counter-ions reside and trigger strong surface-induced electroosmotic flow of the fluid. For each concave profile, we define Δ_{central} as the radial region over which the local central minimum of the profile extends. This relates to the position of the local maximum located near the walls, which, in turn, depends on the Debye length parameter, $\ell_D = \lambda_D/R_p$. Accordingly, c_0 and R_p are the only parameters explored in Figure 3.7 that affect Δ_{central} since they control ℓ_D. This is in accord with the respective

results in Figure 3.7(b) and (c). Individual profiles and all parameters have opposite effects on η_{adv} and η_{migr} profiles, since the diffusion contribution is relatively small.

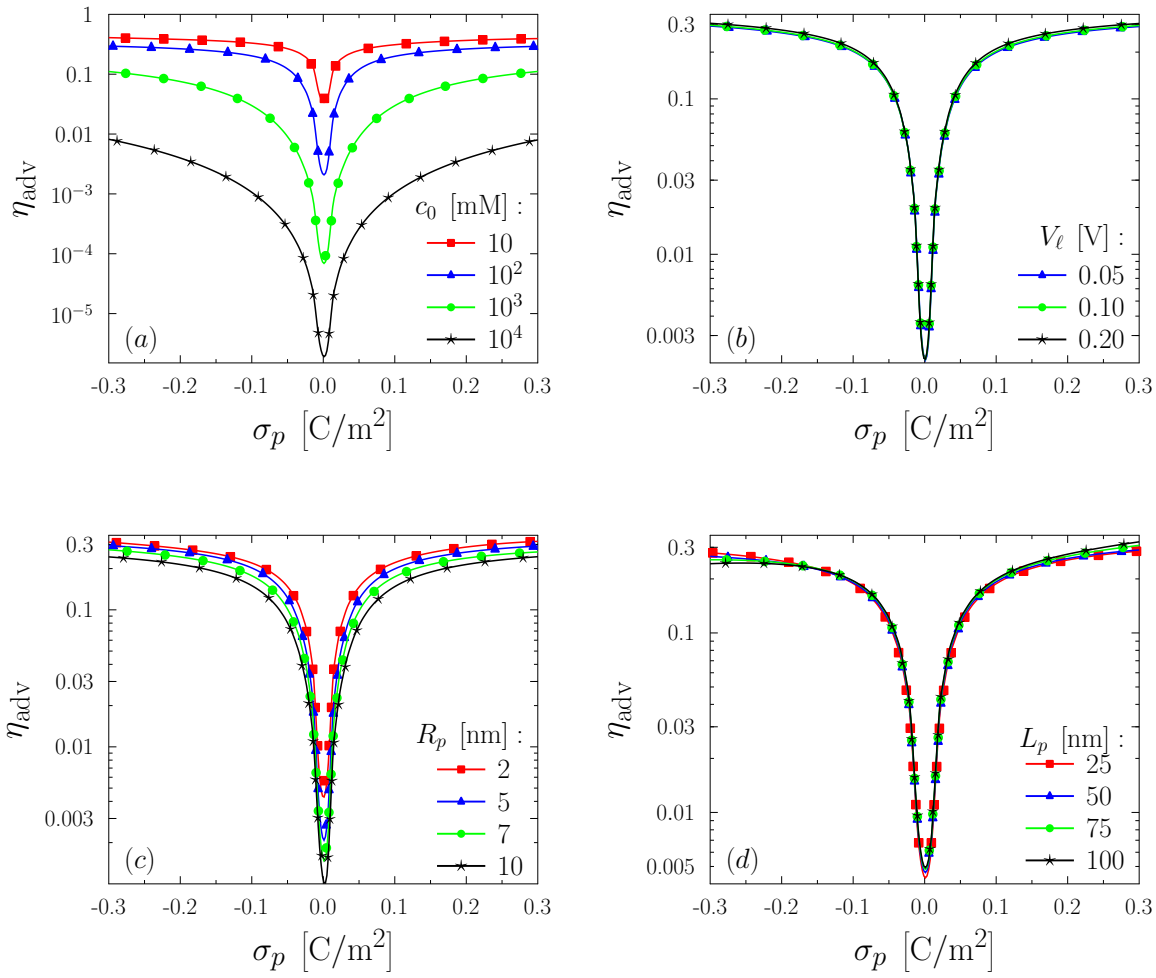

Figure 3.9: Sectionally averaged fluid-induced ionic current coefficient η_{coef} plotted as a function of σ_p for different values of (a) c_0, (b) V_ℓ, (c) R_p and (d) L_p. Reference case: $R_p = 5$ nm, $L_p = 50$ nm, $\sigma_p = -0.05$ C/m^2, $V_\ell = 0.1$ V, $c_0 = 0.1$ M, $P_\ell = 10$ kPa.

Based on the results above, the cross-sectional domain of the channel can be divided into three regions depending on which of η_{adv}, η_{diff}, and η_{migr} peaks. The EDL region is where η_{adv} peaks, while η_{migr} peaks in the central region (and at the edges of the channel walls), and η_{diff} peaks in the region in between the two.

Figure 3.8 shows the total current I across $\mathcal{S}$, plotted against σ_p for different parametric values. A universal feature of the plots is that I increases with $|\sigma_p|$, and the current adopts a local minimum at $\sigma_p = 0$. As anticipated, ionic current increases with c_0, R_p and V_ℓ due to both cation and anion enrichment in the channel. The channel's length, however, has the opposite effect owing to a reduced electric field at large L_p.

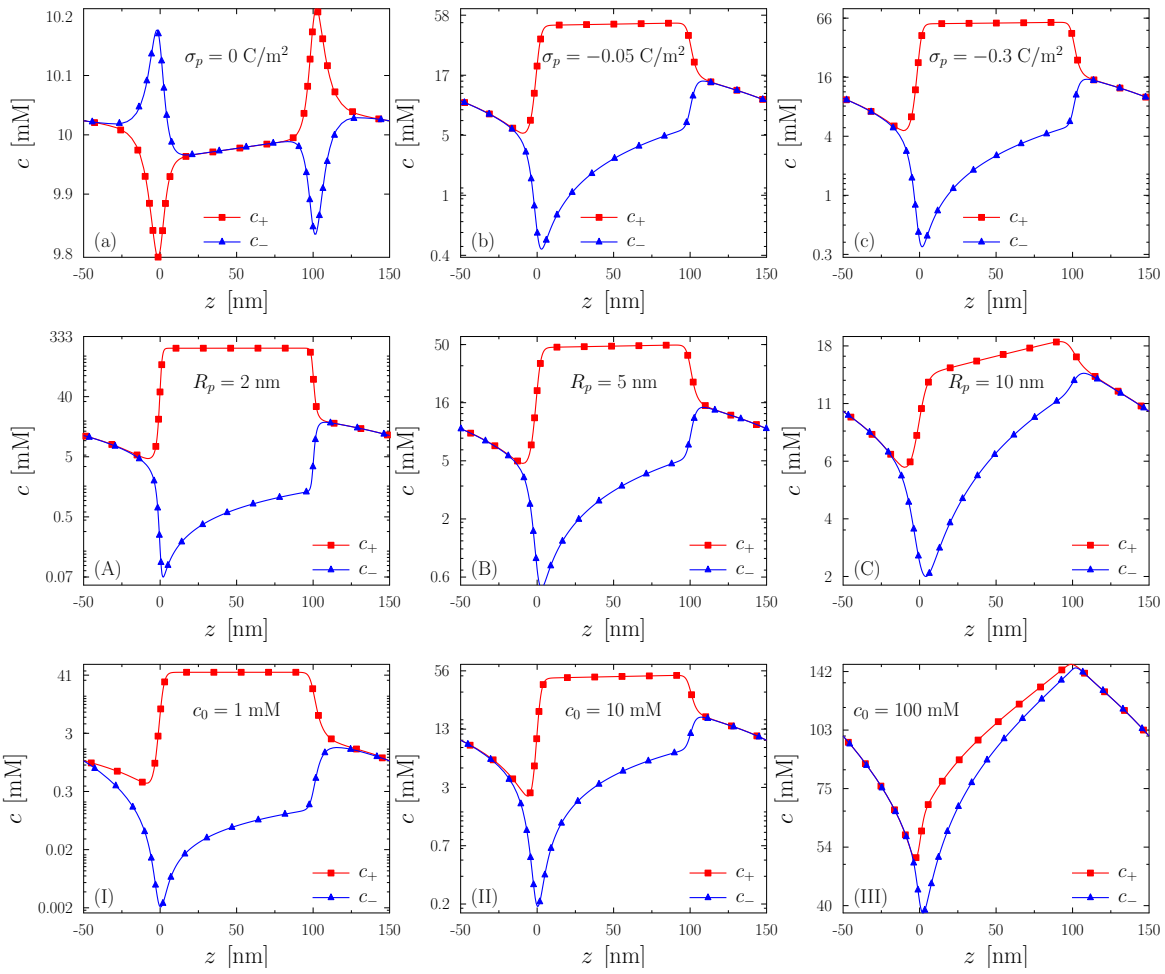

Figure 3.10: The concentration of cations and anions along the center of the channel at different values of σ_p (row 1), R_p (row 2) and c_0 (row 3) (All plots are in the semi-log scale). Reference case: $R_p = 5$ nm, $L_p = 100$ nm, $\sigma_p = -0.05$ C/m^2, $V_\ell = 0.1$ V, $c_0 = 10$ mM, $P_\ell = 10$ kPa.

Neglecting fluid flow in modelling electrokinetic transport phenomena is common in the literature [139–143]. The standard assumption is that the time scale for fluid flow is much larger than that of ion flow. In Figure 3.9, we explore the validity of this assumption by plotting η_{adv} against σ_p for different parameters. Results demonstrate that η_{adv} goes to zero sharply as $|\sigma_p|$ approaches 0. This implies that the channel's surface charges speed up ionic transport faster than fluid transport at low $|\sigma_p|$, and the opposite is true for high $|\sigma_p|$. The other parameter that has strong influence on η_{adv} is c_0: high c_0 lowers η_{adv} to the point where advective transport can be ignored altogether. The potential bias V_ℓ and the channel length L_p do not have much influence on η_{adv}. Increasing R_p, however, lowers η_{adv}. For all plots, the opposite trends in co- and counter-ions at the two ends of the channel

come from the externally applied electric field.

3.3.3 Ionic selectivity

As discussed in Chapter 2, charged nanochannels tend to allow counter-ions to pass through and repel co-ions. In what follows, we analyse the perm-selective properties of the channel as functions of σ_p, R_p, and c_0. Figure 3.10 shows the concentrations of cations and anions along the channel's centerline. Results reveal that the channel is more selective at large σ_p, small R_p and small c_0, which is somewhat intuitive. These conditions are realized when the Debye length parameter ℓ_D is larger than 1, corresponding to the strong EDL overlap regime. For a highly selective nanochannel, we notice that the concentration of counter-ions stays virtually constant along the channel.

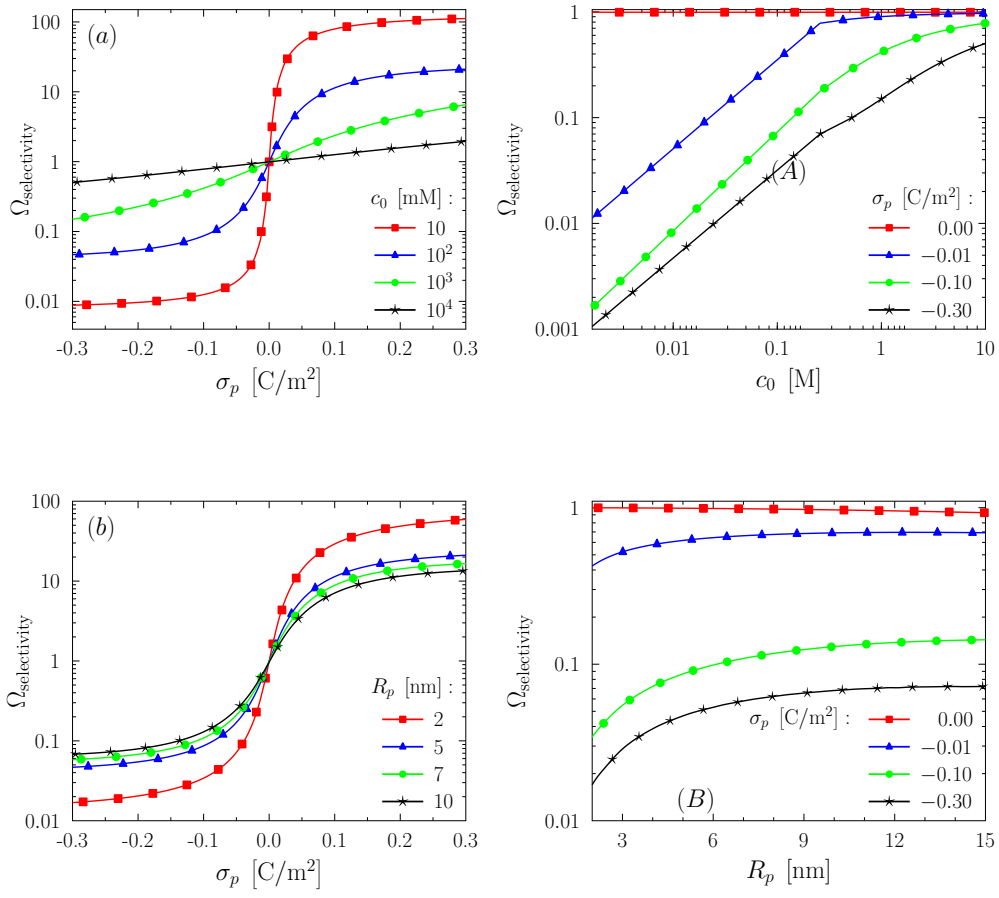

Figure 3.11: Ionic selectivity of the channel at different values of σ_p , R_p and c_0. Reference case: $R_p = 5$ nm, $L_p = 100$ nm, $\sigma_p = -0.05$ C/m^2, $V_\ell = 0.1$ V, $c_0 = 10$ mM, $P_\ell = 10$ kPa.

To quantify the channel's perm-selective properties, we define the ion selectivity

$$\Omega_{\text{selectivity}} = \frac{\displaystyle\int_{\mathcal{S}} |\boldsymbol{J}_-(\boldsymbol{r})| d^2\boldsymbol{r}}{\displaystyle\int_{\mathcal{S}} |\boldsymbol{J}_+(\boldsymbol{r})| d^3\boldsymbol{r}} \,, \tag{3.4}$$

which is the ratio of the total sectionally-averaged flux of cations to anions on the channel's cross section $\mathcal{S}$. With this definition, $\Omega_{\text{selectivity}}$ directly measure the passage of particular ions so that $\Omega_{\text{selectivity}} = 1$ corresponds to a non-selective channel, $0 < \Omega_{\text{selectivity}} \ll 1$ corresponds to a cation-selective channel, and $\Omega_{\text{selectivity}} \gg 1$ corresponds to an anion-selective channel.

Figure 3.11 shows $\Omega_{\text{seclectivity}}$. The results agree with what we expect from Figure 3.10. These results will be useful in Chapter 4, where we make an assumption that the channel only allows counter-ions to pass through due to its small radius. As seen in Figure 3.11(B), $\Omega_{\text{seclectivity}}$ can approach 1% when $R_p < 3$ nm for a negatively charged channel.

3.3.4 Experimental validation

The validity of the continuum model and numerical method used is verified by the experimental data of Smeets *et al.* [144] on the conductance of a solid-state nanochannel filled with a KCl solution. Parameters used are in accordance with those from Ref. [144]. The diffusivities of K^+ and Cl^- ions are 1.96×10^{-9} m^2/s and 2.03×10^{-9} m^2/s, respectively. Note that we now have $D_+ \neq D_-$. Other parameters adopted are $\nu = 1\times10^{-3}$ Pa·s, $L_p = 34$ nm, $\sigma_p = -60$ mC/m^2, $R_p = 5$ nm, $V_\ell = 200$ mV, and a background solution pH of 7.5. The conductance is calculated via

$$G = \frac{I}{V_\ell} = \frac{1}{V_\ell} \int_{\mathcal{S}} q\Big(\sum_{j=1}^{2} z_j \boldsymbol{J}_i\Big) \cdot \hat{\boldsymbol{n}}\, d\mathcal{S} \,. \tag{3.5}$$

Results are shown in Figure 3.12. We notice a good agreement with experimental data at concentrations larger than about 1 mM. Below this threshold concentration, the model overestimates the conductance. These results confirm the validity of the numerical model in capturing the essential physics of the ionic conductance in a silica nanochannel at concentrations greater that 1 mM. The failure at lower concentrations comes from the invalidity of the continuum approximation when very few ions are in the system.

3.4 Summary

In this chapter, we conducted numerical simulations of ionic and fluid transport in a charged nanochannel connected to reservoirs. The coupled Poisson-Nernst-Planck and Stokes system of equations was used to model a system with cylindrical geometry. The fluid velocity profiles

were found to be plug-like and concave-shaped at high charging of the system and at large channel size. We observed a pressure build-up in the center of the channel, which comes from the electrochemical potential gradients in the system. The ionic current was evaluated at different parameters. We found that the advective contribution to the overall current dominates at regions near the channel walls, while migration dominates at the center of the channel. The overall current was found to increase with the channel's surface charge density, the bulk concentration and the channel size. The perm-selective properties of the channel were investigated. Results indicate that the channels become highly selective to counter-ions at high surface charge densities, low bulk concentrations and small channel sizes. Predictions of the model about the nanochannel conductance agrees well with the experimental data available from the literature, only above a certain concentration of ions.

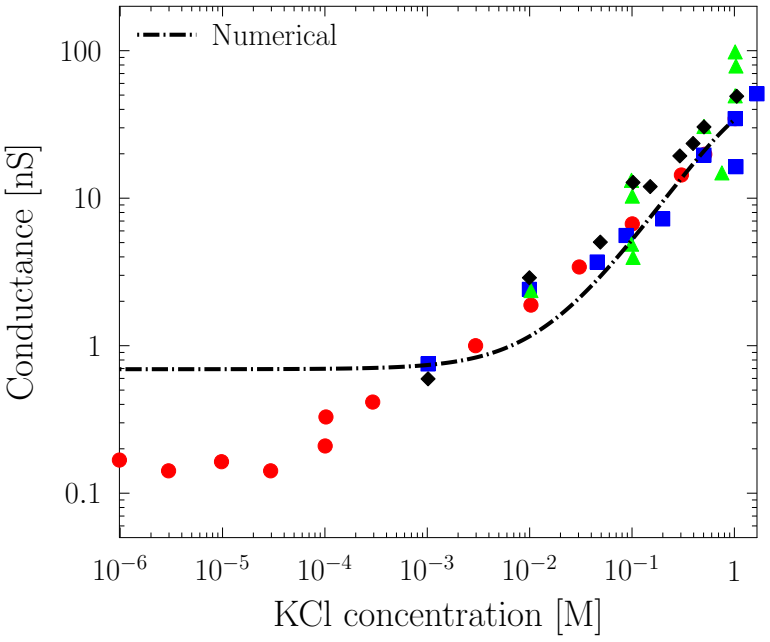

Figure 3.12: Comparison of numerical results with experimental data for the dependence of the electric conductance on the bulk KCl concentration. Dashed line represents numerical results. Symbols represent experimental data from Smeets *at al.* [144]. Different symbols are for different samples prepared. Simulation input parameters used were chosen to match those of the experiments: $R_p = 5$ nm, $L_p = 34$ nm, $\sigma_p = -0.06$ C/m^2, $V_\ell = 0.2$ V, $P_\ell = 0$ kPa.

Chapter 4

Theory of Proton Transport Through a Soft Nanochannel

In the last chapter, we evaluated the flow of ions and fluids in a rigid and cylindrical nanochannel that is connected to reservoirs. In general, simulating the reservoirs is crucial for accurate modelling in finite channels, while intrinsic complexities arise near the channel's inlet and outlet. In many cases, this renders analytical tractability of the problem an enormous challenge, so that a nontrivial numerical treatment may be necessary to address even a simple problem in the system. If the channel is very long, however, reservoirs can be neglected and the problem can be simplified significantly without sacrificing any essential physics. This enables us to theoretically investigate additional aspects of the system, such as the impact of the deformational properties of channel walls. In essence, we focus on the channel interior and roll any effects due to reservoirs and inlets and outlets into the boundary conditions.

In this chapter, we explore theoretically electrokinetic flow in a long, soft cylindrical channel. The goal here is to establish a baseline scenario and analytical relationships that reveal the role of core processes and parameters governing charged fluid flow in viscoelastic channels. The chapter is divided into two parts. The first part, Sections 4.1 and 4.2, examines a rigid, negatively charged channel that is long enough that reservoirs can be ignored, and the flow of water and protons in the highly-selective channel is studied. Analytical solutions of the problem are presented, and the electroneutrality property of the channel is evaluated.

In the second part, Sections 4.3 and 4.4, a theoretical model of water and protons is constructed that couples channel wall deformations and flows. This nonlinear coupling considers a charged, deformable nanochannel whose viscoelasticity is governed by the linear Kelvin-Voigt model. Using continuum mean-field theories for mass and momentum conservation of the solid-liquid coupled system, a set of one-dimensional nonlinear partial differential equations is derived to capture the dynamics of wall deformations. Section 4.4 concludes the chapter with a summary of results.

4.1 Analytical solutions for a long and rigid nanochannel

4.1.1 Assumptions

Consider a channel of radius R_p and length L_p connected to reservoirs filled with a symmetric (valency of cations is the same as that of anions) and binary aqueous electrolyte solution, identical to the problem studied numerically in the previous chapter. The size of the channel can be defined using the aspect ratio,

$$r_{\text{aspect}} = \frac{L_p}{R_p} \, . \tag{4.1}$$

In the numerical work discussed in Chapter 3, r_{aspect} can be easily controlled by changing R_p and fixing L_p to maintain the strengths of external fields applied. Typical numerical results are shown in Figure 4.1, where R_p is varied from 1 to 4 nm and the axial electric field, fluid pressure, fluid velocity, and ionic concentrations are plotted as functions of the distance along the channel's centerline (note that qualitatively similar results are obtained when $r \neq 0$). The highest r_{aspect} is attained when $R_p = 1$ nm (red curves). Away from reservoirs ($z \approx L_p/2$), the following conclusions can be drawn about the nature of the transport at high r_{aspect}:

- The electric field is constant along z (see Figure 4.1(a)). Given this, the total electric potential (ψ) can be written as a superposition of the radially-varying potential (ϕ) due to the charged channel walls and the axially-varying potential due to the constant electric field (E_z), i.e.,
$$\psi(r, z) \approx \phi(r) - E_z z \, . \tag{4.2}$$

- The pressure gradient remains constant along z (see Figure 4.1(b)). The overall pressure gradient is approximately equal to the pressure drop between the channel ends. Hence, the fluid pressure can be expressed as
$$p \approx \mathcal{P} z \, , \tag{4.3}$$
where $\mathcal{P}$ is the constant pressure gradient. Recall, from Chapter 3, that we can still obtain this same effect when a very high pressure drop is applied at the reservoirs. In this case, the constant pressure gradient extends to the reservoirs.

- The fluid velocity remains constant along z (see Figure 4.1(c)).

- The channel becomes strongly ion-selective (see Figure 4.1(d)). Co-ions are repelled and only counter-ions pass through. Hence, it is reasonable to assume only counter-ions are present in such channels.

- The concentration of counter-ions remains constant along z (see Figure 4.1(d)).

To leading order, these findings describe a perturbation of the system about its equilibrium, driven by an applied axial electric field and pressure gradient. With these observations, the transport equations can be simplified to remove the z-dependence in some field quantities so that only the surface-induced radial dependence is taken into account. The often drastic departures from the qualitative findings near the entry/exit mouths of the channel come from weakened electrostatic interactions between the channel center and the reservoirs. Here, we are only concerned about the middle of the channel, not the overall channel.

Inspired by proton exchange membranes, whose near-complete dissociation provides conductive protons to the water-filled interior, we assume that the channel walls are negatively charged and only protons ($z = 1$), along with water, are transported through. In principle, the theoretical study in this work is a special case of the more general analysis of co- and counter-ion flow inside charged nanochannels, conducted by Peters *et al.* [145]. The difference is that the presence of co-ions considered in that work does not allow for the derivation of closed-form expressions and flow solutions but instead requires numerical calculations. The limiting case of counter-ions-only, on the other hand, neglects the crucial coupling of the channel to surrounding reservoirs via electric double layers at the channel ends which, among other things, determines the boundary conditions for the fluid flow and electric potential in the channel interior.

4.1.2 Analytical solutions

If only protons (with concentration $c = c_+$) are considered in a negatively charged channel, the PNP and Stokes equations (Equations (3.1a)–(3.1d)) can be written in 2-D axisymmetric cylindrical coordinates as (exploiting the symmetry of a cylindrical channel of circular cross-section)

$$\frac{1}{r}\frac{\partial}{\partial r}\left(r\frac{\partial \psi}{\partial r}\right) + \frac{\partial^2 \psi}{\partial z^2} = -\frac{qc}{\varepsilon \varepsilon_0} \,, \tag{4.4a}$$

$$\nabla \cdot \boldsymbol{J} \;=\; 0 \,, \begin{cases} J_r \;=\; -D\dfrac{\partial c}{\partial r} - \omega c \,\dfrac{\partial \psi}{\partial r} \,, \\[2ex] J_z \;=\; -D\dfrac{\partial c}{\partial z} - \omega c \,\dfrac{\partial \psi}{\partial z} + c u_z \,, \end{cases} \tag{4.4b}$$

$$\nu\left[\frac{1}{r}\frac{\partial}{\partial r}\left(r\frac{\partial u_z}{\partial r}\right) + \frac{\partial^2 u_z}{\partial z^2}\right] - \frac{\partial p}{\partial z} - qc\,\frac{\partial \psi}{\partial z} = 0 \,. \tag{4.4c}$$

In the above, $\omega = D/k_B T$ is the proton mobility, and the subscripts in u and J indicate

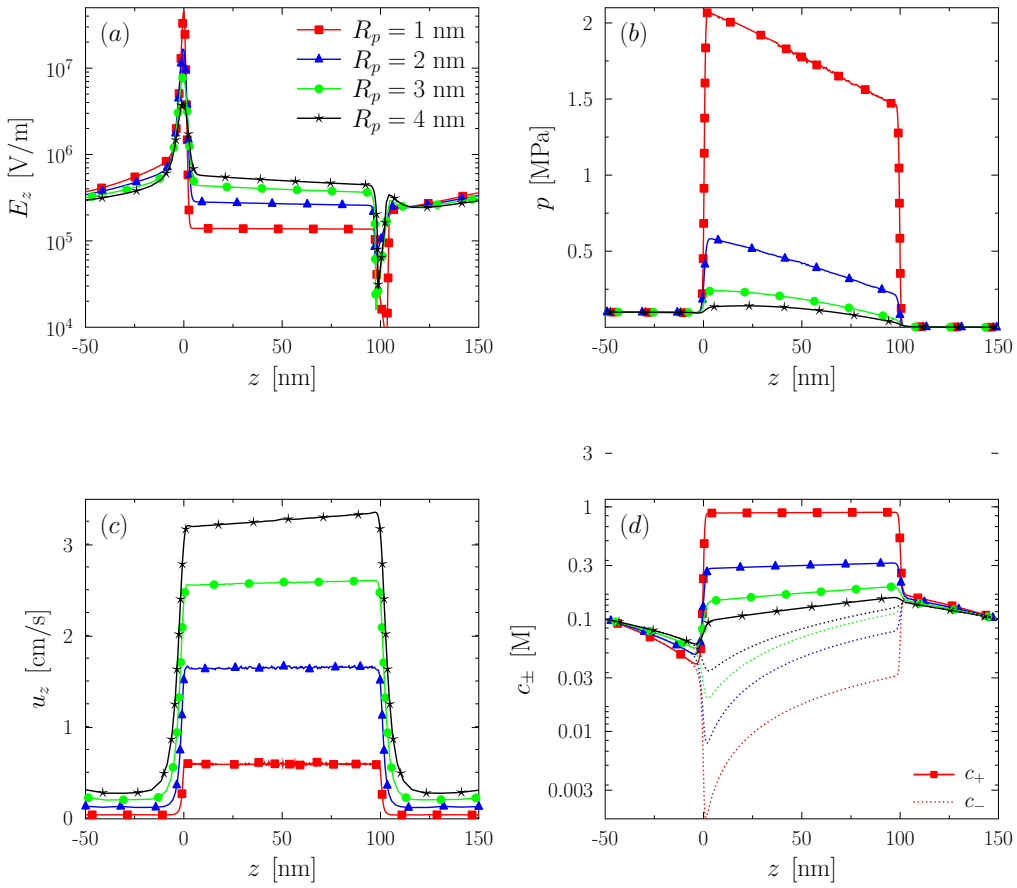

Figure 4.1: Numerical results illustrating the effect of the channel's aspect ratio on the (a) axial electric field, (b) fluid pressure, (c) axial fluid velocity, and (d) ionic concentrations along the central axis of the channel. The plot legend in graph (a) applies to all other graphs. Reference case: $L_p = 100$ nm, $\sigma_p = -0.1$ C/m^2, $V_\ell = 0.1$ V, $c_0 = 0.01$ M, $P_\ell = 10$ kPa.

vector components (along r and z) of the fluid velocity $\boldsymbol{u}$ and proton flux density $\boldsymbol{J}$. The radial component of $\boldsymbol{u}$ is ignored, i.e., $u_r = 0$.

Due to the radial symmetry and the vanishing proton flux at the channel walls, radial components of the proton flux must be zero,

$$J_r = 0 \quad \Longleftrightarrow \quad -D\frac{\partial c}{\partial r} - \omega c\,\frac{\partial \psi}{\partial r} = 0 \quad \Longleftrightarrow \quad c(r) = c_0 \exp\left(-\frac{q\phi(r)}{k_B T}\right), \tag{4.5}$$

giving the Boltzmann distribution of protons along r. Here, we used Equation (4.2) for $\psi(r, z)$ in terms of $\phi(r)$, and c_0 is taken to be the concentration at the center of the channel ($r = 0$) where we set $\phi = 0$. Noting that $\psi_{zz} = 0$ (since $\psi_z = 0$) and substituting Equation (4.5) for c into Equation (4.4a), we obtain the 1D Poisson-Boltzmann (PB) equation,

$$\frac{1}{r}\frac{d}{dr}\left(r\frac{d\phi}{dr}\right) = -\frac{q}{\varepsilon\varepsilon_0}\, c_0 \exp\left(-\frac{q\phi}{k_B T}\right) . \tag{4.6}$$

The following boundary conditions hold,

$$\frac{d\phi}{dr} = 0, \quad \text{at } r = 0 , \tag{4.7}$$

$$\frac{d\phi}{dr} = \frac{\sigma_p}{\varepsilon\varepsilon_0}, \quad \text{at } r = R_p , \tag{4.8}$$

where a uniform surface charge density σ_p is assumed. Equation (4.7) is due to radial symmetry: the radial component of the electric field must be zero in the pore centre). An analytical solution of Equation (4.6) was derived by Berg and Ladipo [48]:

$$\phi(\hat{r}) = \frac{k_B T}{q} \ln\left[\left(1 - \Lambda\hat{r}^2\right)^2\right] , \tag{4.9}$$

where $\hat{r} = r/R_p$ and Λ is a dimensionless parameter given as

$$\Lambda = \frac{R_p^2 q^2 c_0}{8\varepsilon\varepsilon_0 k_B T} , \tag{4.10}$$

and Equation (4.8) enables us to to determine the concentration at the channel's center:

$$c_0 = \frac{8\sigma_p}{q^2 R_p^2 \sigma_p / 8\varepsilon\varepsilon_0 k_B T - 4qR_p} . \tag{4.11}$$

The proton concentration can be determined via Equation (4.5) as

$$c(\hat{r}) = \frac{c_0}{(1 - \Lambda\hat{r}^2)^2} . \tag{4.12}$$

A comparison of the analytical solutions from Equation (4.9) with numerical results from Chapter 3 is shown in Figure 4.2. Here, plots of ϕ vs. $\hat{r}$ at the central cross-section of the channel are shown for $R_p = 1, 2, 3$ nm. Results establish that numerical results match analytical results very well when $R_p = 1$ nm, and a slight deviation is noticed as the channel radius increases. This highlights the effect of changing the channel's aspect ratio on the validity of the results presented above.

Taking $\partial^2 u_z/\partial z^2 = 0$, $\partial p/\partial z = \mathcal{P}$, and $\partial\psi/\partial z = -E_z$, the Stokes equation (Equation 4.4c) yields

$$\nu\frac{d}{dr}\left(r\frac{du_z(r)}{dr}\right) - \mathcal{P} + qc(r)E_z = 0 , \tag{4.13}$$

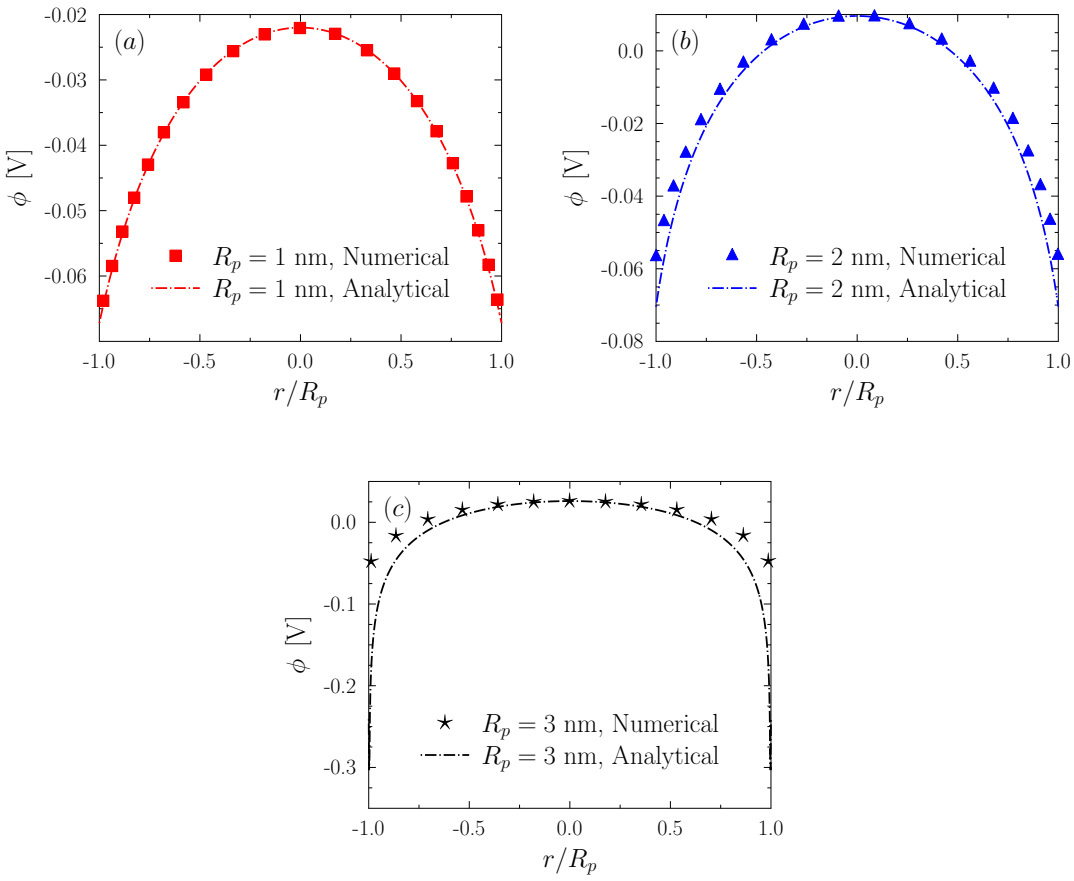

Figure 4.2: Comparison of numerical results with analytical results for the electric potential across the centre of the channel computed for (a) $R_p = 1$ nm, (b) $R_p = 2$ nm, and (c) $R_p = 3$ nm. Reference case: $L_p = 100$ nm, $\sigma_p = -0.1$ C/m^2, $V_\ell = 0.1$ V, $c_0 = 0.01$ M, $P_\ell = 10$ kPa.

where $c(r)$ is given by Equation (4.12). Symmetry and no-slip boundary conditions should be fulfilled:

$$\frac{du_z}{dr} = 0, \quad \text{at} \quad r = 0\,, \tag{4.14}$$

$$u_z = 0, \quad \text{at} \quad r = R\,. \tag{4.15}$$

Solving Equation (4.13), subject to these boundary conditions, results in the velocity profile [49],

$$u_z(\hat{r}) = \frac{qc_0E_zR_p^2}{4\Lambda\nu}\ln\left(\frac{1-\Lambda\hat{r}^2}{1-\Lambda}\right) - \frac{\mathcal{P}R_p^2}{4\nu}(1-\hat{r}^2)\,. \tag{4.16}$$

The first term gives rise to the plug-like nature of the flow and comes from electroosmotic flow, and the second term reflects pressure-driven Poiseuille flow.

4.2 Breakdown of electroneutrality

Electroneutrality is usually assumed to hold away from the channel-reservoir interfaces where Donnan equilibria are established. For a sufficiently long channel, it seems intuitive that electroneutrality certainly holds at the center of the channel. In fact, for symmetry reasons the center of the channel must be the point where electroneutrality is violated the least and the maximum violation occurs near the channel-reservoir interface, where axial (between reservoir and pore interior) and radial double layers overlap. Such electroneutrality breakdown in nanochannels has been reported in Refs. [146–150]. Therefore, we will focus on the center of the channel so as to determine a lower bound for the violation of electroneutrality. At $z = L_p/2$, we have $E_z = -\psi_{zz} = 0$ for symmetry reasons, which turns the analysis for the electric field into a one-dimensional problem, similar in spirit to the electroneutral case considered in Section 4.1.2.

4.2.1 Non-insulating channel walls

As argued in Chapter 2, one situation that leads to electroneutrality breakdown is when the channel walls (assumed thick) are non-insulating. A consistent treatment of the problem demands us to solve the Laplace equation outside the electrolyte, in addition to the PB equation inside:

$$\frac{1}{r}\frac{d}{dr}\left(r\frac{d\psi_{\text{ext}}}{dr}\right) = 0, \qquad \text{outside channel}, \tag{4.17}$$

$$\frac{1}{r}\frac{d}{dr}\left(r\frac{d\psi_{\text{in}}}{dr}\right) = -\frac{q}{\varepsilon_{\text{in}}\varepsilon_0}\, c_0 \exp\left(-\frac{q\psi_{\text{in}}}{k_B T}\right), \qquad \text{inside channel}. \tag{4.18}$$

Here, ψ_{in} and ψ_{ext} denote the electric potentials inside and outside the channel, respectively. Similarly, ε_{in} and ε_{out} are the dielectric constants inside and outside the channel.

Four boundary conditions are now required to solve this problem, three of which are easy to determine: a symmetry condition at the channel centre ($r = 0$), a vanishing electric potential at infinity and a continuous electric potential at the channel walls where the channel interior and exterior meet. These translate successively into

$$\frac{d\psi_{\text{in}}}{dr} = 0, \qquad \text{at} \quad r = 0\,, \tag{4.19}$$

$$\psi_{\text{ext}} = 0, \qquad \text{as} \quad r \to \infty\,, \tag{4.20}$$

$$\psi_{\text{in}} = \psi_{\text{ext}}, \qquad \text{at} \quad r = R_p\,. \tag{4.21}$$

The fourth condition is obtained from the jump condition of the electric field at the channel surface where fixed charges are present,

$$\frac{d\psi_{\text{ext}}}{dr} - \frac{d\psi_{\text{in}}}{dr} = 4\pi\sigma_p, \qquad \text{at} \quad r = R_p\,. \tag{4.22}$$

Levy and Bazant [150] have shown that in the limit of high-aspect-ratio channels, the problem of solving Equations (4.17) and (4.18), subject to the conditions (4.19)–(4.22), is equivalent to solving Equation (4.18), subject to the boundary conditions (4.19) and

$$\frac{d\psi_{\text{in}}}{dr} = \frac{\sigma}{\varepsilon_{\text{in}}} + \frac{\varepsilon_{\text{ext}}}{\varepsilon_{\text{in}}}\frac{\psi_{\text{in}}}{R_p M}, \qquad \text{at } r = R_p \, . \tag{4.23}$$

Here, M is a geometric parameter that represents the aspect ratio of the channel,

$$M = \ln\left(\frac{2L}{\pi R_p}\right) - \gamma_p \, , \tag{4.24}$$

with the Euler-Mascheroni constant $\gamma_p \approx 0.577$. Define

$$\varepsilon_{\text{ratio}} = \frac{\varepsilon_{\text{ext}}}{\varepsilon_{\text{in}}} \, , \tag{4.25}$$

the ratio of the dielectric constants. The electroneutral case is found in the limit $\varepsilon_{\text{ratio}} \to 0$. For real systems, this ratio may be of the order $O\left(10^{-1}\right)$ but this alone does not speak to the magnitude of the violation of electroneutrality. Therefore, we need to pursue the analysis further. First, we non-dimensionalize the equations by introducing

$$\hat{r} = \frac{r}{R_p}, \;\; \hat{\psi}_{\text{in}} = \frac{q\psi_{\text{in}}}{k_B T}, \;\; \hat{\sigma} = \frac{R_p q \sigma_p}{\varepsilon_{\text{in}} k_B T}, \;\; \hat{c} = \frac{R_p^2 q^2 c}{8\varepsilon_{\text{in}} k_B T} \, , \tag{4.26}$$

transforming Equation (4.18) into

$$\frac{1}{\hat{r}}\frac{d}{d\hat{r}}\left(\hat{r}\frac{d\hat{\psi}_{\text{in}}}{d\hat{r}}\right) = -\hat{c} = -\Lambda e^{-\hat{\psi}_{\text{in}}} \, , \tag{4.27}$$

subject to the boundary conditions

$$\frac{d\hat{\psi}_{\text{in}}}{d\hat{r}} = 0, \qquad \text{at } \hat{r} = 0 \, , \tag{4.28}$$

$$\frac{d\hat{\psi}_{\text{in}}}{d\hat{r}} = \hat{\sigma} + \frac{\varepsilon_{\text{ratio}}}{M}\hat{\psi}_{\text{in}}, \qquad \text{at } \hat{r} = 1 \, . \tag{4.29}$$

A solution can be found step-by-step with a slight generalization of the solution for the electroneutral case, presented in Equation (4.9), namely, with the one-parameter family of functions

$$\hat{\psi}_{\text{in}}(\hat{r}) = \ln\left[\theta\left(1 - \frac{\Lambda}{\theta}\hat{r}^2\right)^2\right] \, , \tag{4.30}$$

where the parameter θ is chosen so that ψ_{in} satisfies Equation (4.29) for an arbitrary $\varepsilon_{\text{ratio}}$. Note that the electroneutral scenario for the counter-ions-only case is recovered by setting $\theta = 1$, but Λ in Equation (4.27) is then a function of R_p and σ_p only, since c_0 becomes a

function of R_p and σ_p (see [48, 49]). In other words, only one particular choice of c_0 yields perfect electroneutrality. In what follows, we consider the general case of independent R_p, σ_p and bulk concentration c_0.

As can be seen by inspection, Equation (4.30) is a solution to (4.27). Due to the symmetry of Equation (4.30) in $\hat{r}$, the boundary condition in Equation (4.28) is also naturally met. This only leaves Equation (4.29). Substitution of Equation (4.30) into Equation (4.29) results in

$$\frac{4\Lambda}{\Lambda - \theta} = \hat{\sigma} + \frac{\varepsilon_{\text{ratio}}}{M} \ln\left[\theta\left(1 - \frac{\Lambda}{\theta}\right)^2\right]. \tag{4.31}$$

This is a nonlinear algebraic equation for θ, given Λ (see Equation (4.10)).

With θ determined, we can finally compute the total dimensionless charge (density) inside the cross section of the channel at $z = L_p/2$ via

$$\hat{c}_T^p = 2\pi \int_0^1 \hat{c}(\hat{r})\, \hat{r}\, d\hat{r}, \tag{4.32}$$

and compare that to the total density of fixed charges along the wall,

$$\hat{c}_T^w = 2\pi\hat{\sigma}, \tag{4.33}$$

so as to assess the degree to which electroneutrality is violated.

Using Equations (4.30), (4.26) and (4.5), the integral in Equation (4.32) can be computed in closed form, yielding

$$\hat{c}_T^p = \frac{\pi\Lambda}{\theta - \Lambda}\,. \tag{4.34}$$

Hence, the degree of violation of electroneutrality, as expressed by the ratio of total counter-ion charge density within a cross section and the corresponding wall charge density, becomes

$$\chi \equiv \frac{\hat{c}_T^p}{\hat{c}_T^w} = \frac{1}{2\hat{\sigma}} \frac{\Lambda}{\theta - \Lambda}. \tag{4.35}$$

For self-consistency, however, it is important to ensure that

$$\hat{\psi}_{\text{in}}(\hat{r} = 0, z = 0) \ll -1 \tag{4.36}$$

holds so that it is justified to neglect co-ions and approximate the local charge density by

$$\hat{c}(\hat{r}) = -\sinh(\hat{\psi}) \quad \rightarrow \quad \hat{c}(\hat{r}) = \Lambda e^{-\hat{\psi}_{\text{in}}}, \tag{4.37}$$

as done above for the PB equation (Equation (4.18)).

4.2.2 Impact on water and proton transport

The solution for the electric potential, Equation (4.30), which also determines the counter-ion concentration via Equation (4.5), depends on θ. However, the structure of $\hat{\psi}_{\text{in}}$ is such that it still allows for the derivation of closed-form expressions for fluxes of water and counter-ions (protons) along the channel.

The fluid (water) velocity u_z in the axial direction, driven by a constant axial electric field E_z and a constant axial pressure gradient $\mathcal{P}$, is given by the Stokes equation (Equation (4.16)). Introducing the dimensionless variable $\hat{u} = \mu q u_z/\varepsilon_{\text{in}} k_B T E_z$ and the dimensionless pressure parameter $\mu_p = q\mathcal{P}R_p^2/\varepsilon_{\text{in}} k_B T E_z$, Equation (4.16) can be cast into the dimensionless form,

$$\frac{1}{\hat{r}}\frac{d}{d\hat{r}}\left(\hat{r}\frac{d\hat{u}(\hat{r})}{d\hat{r}}\right) = -\hat{c}(\hat{r}) + \mu_p \ , \tag{4.38}$$

with the boundary conditions

$$\hat{u} = 0, \qquad \text{at} \quad \hat{r} = 1 \ , \tag{4.39}$$

$$\frac{d\hat{u}}{d\hat{r}} = 0, \qquad \text{at} \quad \hat{r} = 0 \ . \tag{4.40}$$

Integrating Equation (4.38) and using $\hat{c}(\hat{r}) = \Lambda e^{-\psi_{\text{in}}(\hat{r})}$ with the boundary conditions above gives the velocity profile [49]

$$\hat{u}(\hat{r}) = 2\ln\left(\frac{\theta - \Lambda\hat{r}^2}{\theta - \Lambda}\right) + \frac{\mu_p}{4}\left(\hat{r}^2 - 1\right) \ . \tag{4.41}$$

The advective and total proton flux densities ($\hat{j}_{\text{adv}}$ and $\hat{j}_{\text{tot}}$, respectively) at $z = L_p/2$ can be expressed, in dimensionless form, as

$$\hat{j}_{\text{adv}}(\hat{r}) = \hat{u}(\hat{r})c(\hat{r}) \ , \tag{4.42}$$

$$\hat{j}_{\text{tot}}(\hat{r}) = \hat{u}(\hat{r})c(\hat{r}) + \mu_{_D}\hat{c}(\hat{r}) \ . \tag{4.43}$$

Here, $\mu_{_D} = \frac{\mu q^2 D}{\varepsilon_{\text{in}}(k_B T)^2}$ is a dimensionless proton mobility parameter, where D is the proton diffusion coefficient. The fluxes have been normalized by $\frac{\pi(\varepsilon_{\text{in}} k_B T)^2 E_z}{\mu q^3 R_p^2}$. Note that the diffusive contribution to the total flux vanishes since $\partial c/\partial z = 0$. We compute the average flux densities across the circular section of the channel as follows,

$$\begin{aligned}\langle\hat{j}_{\text{adv}}\rangle &= 2\int_0^1 \hat{u}(\hat{r})\hat{c}(\hat{r})\hat{r}d\hat{r} \\ &= 16(a\mu_p - 1)\ln\left(\frac{\theta - \Lambda}{\theta}\right) + \frac{\Lambda + 2\mu_p(\theta - \Lambda)}{\theta - \Lambda} \ ,\end{aligned} \tag{4.44}$$

and

$$\langle \hat{j}_{\text{tot}} \rangle = 2 \int_0^1 \left[\hat{u}(\hat{r})\hat{c}(\hat{r}) + \mu_{_D} \hat{c}(\hat{r}) \right] \hat{r} d\hat{r}$$
$$= 16(\mu_p \theta - 1) \ln \left(\frac{\theta - \Lambda}{\theta} \right) + \frac{\Lambda(1 + 8\mu_{_D}) + 2\mu_p(\theta - \Lambda)}{\theta - \Lambda} \, . \tag{4.45}$$

This result is fortuitous and allows for a fairly straightforward calculation of transport parameters for fluid flow along the channel, albeit restricted to regions in the interior of the channel which are far away from the channel-reservoir interfaces. Figure 4.3 shows the impact of $\varepsilon_{\text{ratio}}$ on χ, $\langle \hat{j}_{\text{adv}} \rangle$ and $\langle \hat{j}_{\text{tot}} \rangle$. For the set of parameters used, we notice that χ starts deviating from unity noticeably at around $\varepsilon_{\text{ratio}} = 0.02$. The dielectric leakage effects also reduce the proton flux density. This effect is noticeable from around $\varepsilon_{\text{ratio}} = 0.1$ and, therefore, one may consider 0.1 as the ratio of external and internal dielectric constants above which the violation of electroneutrality plays a role in nanochannels as considered in this thesis.

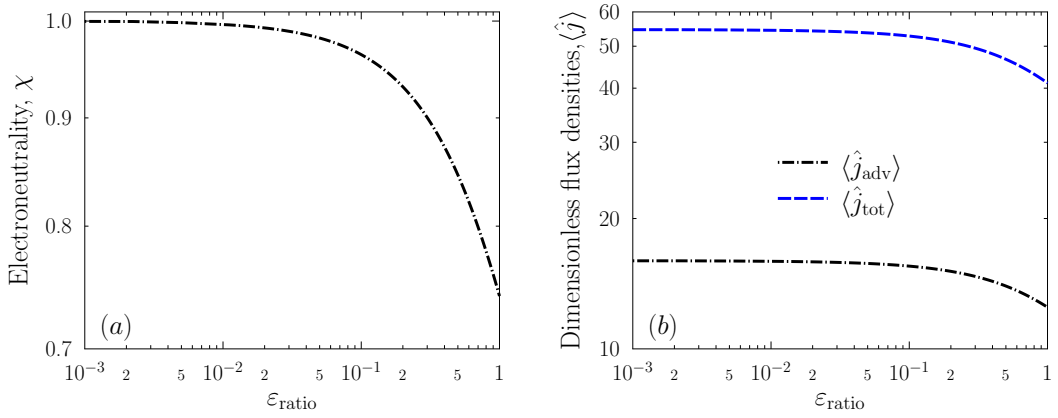

Figure 4.3: Effect of $\varepsilon_{\text{ratio}}$ on (a) the electroneutrality parameter χ and (b) proton fluxes (advective flux density $\langle \hat{j}_{\text{adv}} \rangle$ and total flux density $\langle \hat{j}_{\text{tot}} \rangle$). Used parameters: $L_p = 100$ nm, $\sigma_p = -0.1$ C/m^2, $R_p = 1$ nm, $c_0 = 0.01$ M, $\mathcal{P} = 10^{10}$ Pa/m, $E_z = 10^6$ V/m.

4.3 Model of deformable nanochannels

This section considers the long-channel limit, but with wall deformations accounted for. For soft polymeric channels, such as Nafion® channels in PEM, deformations are known to be an important consideration. Consider a deformable cylindrical nanochannel initially at equilibrium with uniform radius and high aspect ratio ($L_p \gg R_p$), connected to two reservoirs, as shown in Figure 4.4(a). Inner walls of the cylindrical section are lined by negative

charges with uniform surface charge density σ_0, balanced by a proton distribution with concentration c inside the channel to establish electroneutrality. Reservoirs are filled with an aqueous solution with controlled pH and liquid pressure. Cylindrical coordinates, with the origin fixed at the center of the nanochannel entrance, are adopted. This is effectively identical to the system considered in Chapter 3, and its theoretical considerations follow the previous sections of this chapter. Electroosmotic (EO) flow in the z-direction arises from an externally applied electric field (and from the pressure drop) between the reservoirs.

Now let us introduce deformations to the channel. An axial section of the channel far away from reservoirs is considered. This channel interior is, in terms of the corresponding Donnan equilibrium, at least a Debye length away from the channel-reservoir interfaces. It has uniform radius R_0 and length L_0, and it is the actual channel we will focus on from now on. Nevertheless, the boundary conditions at the channel ends will effectively reflect the coupling to the reservoirs. A constant pressure and voltage drop exists between the ends of this channel, denoted ΔV_0 and Δp, respectively. A key assumption undertaken here is that the pressure and the axial electric field are constant over the entire cross-sections at the channel ends. It should be stressed that the effect of axial double layers that form at the channel-reservoir interface is not modelled explicitly with this assumption. This is not always justifiable in real systems but, at high aspect ratios, the effect is negligible when considering the physics only at the middle cross-section of the channel. From Section 4.1, it is understood that field quantities like the axial electric field, axial water velocity, axial liquid pressure gradient and proton concentration are all constant along the channel, but may vary with r.

Consider the following scenario: At $t = 0$, a jump in pressure or electric potential of the left channel end (via reservoirs in the complete system) is applied, resulting in dynamic displacement of water and protons, and prompting the deformation of channel walls, as illustrated in Figure 4.4(b). In this configuration the channel's radius is denoted R. The deformation propagates along the channel, creating gradients in the axial electric field component, proton concentration, and liquid pressure in the axial direction. We want to build a model that couples this deformation to the transport within the channel and understand the nature of this deformation. A theoretical approach is taken, since it can be computationally expensive to simulate the whole system with moving boundary conditions. The methodology proposed here allows us to reduce the dimensional complexity of the problem and explore the effect of channel deformations on the transport of protons.

4.4 Effective 1-D viscoelastic model

To model the dynamic behaviour of the deformations coupled with EO flow within the channel, we use the general system of governing equations to obtain a reduced 1-D model.

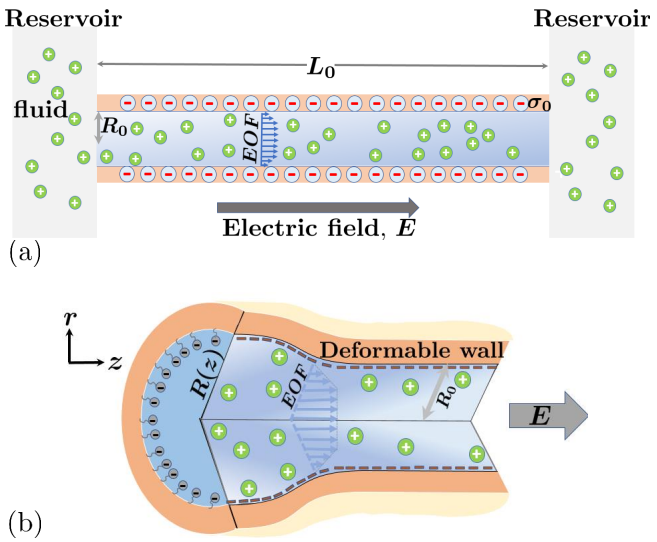

Figure 4.4: Schematic illustration of the examined configuration: (a) equilibrium nanochannel in 2-D cross-section and (b) 3-D deformed nanochannel.

The reduction in dimensionality from 2-D to 1-D is based on the assumption, reasonable for high-aspect-ratio channels ($R_0 \ll L_0$), that the rate of change of variables is much slower in the axial direction than in the radial direction. Under this so-called lubrication approximation, flow is nearly one-dimensional, i.e., $\mathbf{u} = [0, u_z(r,z,t)]^{\mathrm{T}}$ and $\mathbf{J} = [0, j_z(r,z,t)]^{\mathrm{T}}$. In this perspective, it is important to point out that the channel radius in the deformed configuration is non-uniform, i.e., $R = R(z,t)$.

The 1-D reduction approach that we will use is based on the work of Marconi *et al.* [151]. To exclude the dependence on the radial coordinate r, we use cross-sectional averaging of variables viz. c, u_z, p and E_z. The sectional average of a general field $f(r,z)$ is defined as

$$\langle f(r,z)\rangle \equiv \bar{f}(z) = \frac{2}{R^2(z)} \int_0^{R(z)} r dr f(r,z) \ , \tag{4.46}$$

and its axial gradient is determined as [151]

$$\left\langle \frac{\partial f(r,z)}{\partial z} \right\rangle = \frac{\partial \bar{f}(z)}{\partial z} + \frac{2\left[\bar{f}(z) - f(R,z)\right]}{R} \frac{\partial R}{\partial z} \ . \tag{4.47}$$

4.4.1 Water continuity equation in 1-D

Accounting for a change in cross sectional area, $A(z,t) = \pi R^2(z,t)$, conservation of mass for the fluid requires redefining the continuity equation so that it takes a form that conserves the volumetric flow rate along the non-uniform radius channel:

$$\frac{\partial\left(\rho_f A\right)}{\partial t} + \nabla\cdot\left(\rho_f A\boldsymbol{u}\right) = 0\ , \tag{4.48}$$

where ρ_f is the mass density of the fluid. With $u_r = 0$ and ρ_f taken to be a constant (fluid is incompressible), and applying the sectional averaging operator (Equation 4.46), the fluid's volumetric flow rate is conserved via the 1-D equation,

$$\frac{\partial\left(R^2\right)}{\partial t} + \frac{\partial\left(R^2\bar{u}_z\right)}{\partial z} = 0\ . \tag{4.49}$$

4.4.2 Stokes equation in 1-D

With the help of the lubrication approximation ($\partial_{zz}(u_z) = 0$), Equation (4.4c) gives the axial Stokes equation,

$$\nu\left[\frac{\partial^2 u_z}{\partial r^2} + \frac{1}{r}\frac{\partial u_z}{\partial r}\right] - \frac{\partial p}{\partial z} + qcE_z = 0\ . \tag{4.50}$$

We apply sectional averaging on Equation (4.50) term by term using Equations (4.46) and (4.47):

$$\left\langle\frac{\partial^2 u_z}{\partial r^2}\right\rangle = \frac{2}{R^2}\int_0^R rdr\ \frac{\partial^2 u_z}{\partial r^2} = \frac{2}{R}\left.\frac{\partial u_z}{\partial r}\right|_R + \frac{2u_z(0)}{R^2}\ , \tag{4.51}$$

$$\left\langle\frac{1}{r}\frac{\partial u_z}{\partial r}\right\rangle = \frac{2}{R^2}\int_0^R dr\ \frac{\partial u_z}{\partial r} = -\frac{2u_z(0)}{R^2}\ , \tag{4.52}$$

$$\left\langle\frac{\partial p}{\partial z}\right\rangle = \frac{\partial\bar{p}}{\partial z} + \frac{2\left[\bar{p} - p(R,z)\right]}{R}\frac{\partial R}{\partial z}\ , \tag{4.53}$$

$$\langle qcE_z\rangle \approx q\bar{c}\bar{E}_z. \tag{4.54}$$

The last approximation assumes E_z is weakly dependent on r. Collecting the above results, Equation (4.50) becomes

$$\frac{2\tau_w}{R} - \frac{\partial\bar{p}}{\partial z} - \frac{2\left[\bar{p} - p_w\right]}{R}\frac{\partial R}{\partial z} + q\bar{c}\bar{E}_z = 0\ , \tag{4.55}$$

where $\tau_w = \nu\partial u_z(R,z)/\partial r$ is the shear wall stress and $p_w = p(R,z)$ is the pressure at the wall. The radial dependence of the flow velocity has two contributions; namely, pressure-driven (Poiseuille) velocity U_{PO} and electroosmotic velocity U_{EO}, i.e., $u_z = U_{\mathrm{PO}} + U_{\mathrm{EO}}$. Assuming a quadratic form of the Poiseuille component, i.e.,

$$U_{\mathrm{PO}} = a_0 + a_1 r + a_2 r^2\ , \tag{4.56}$$

and approximating the electroosmotic component with results from Section 4.1.2,

$$U_{\mathrm{EO}}(r) = \frac{q\bar{E}_z}{4\boldsymbol{\lambda}_B\nu}\ \ln\left[\frac{1-\Lambda\left(\frac{r}{R}\right)^2}{1-\Lambda}\right]\ , \tag{4.57}$$

we can express τ_w as a function of the averaged quantities – $\bar{u}_z$, $\bar{c}$ and $\bar{E}_z$. Here, $\boldsymbol{\lambda}_B = q^2/4\varepsilon\varepsilon_0 k_B T$ is the Bjerrum length (discussed in Chapter 2). The coefficients a_0, a_1 and a_2 can be found by imposing the conditions,

$$U_{\mathrm{PO}}\Big|_R = 0,\ \ \frac{\partial U_{\mathrm{PO}}}{\partial r}\Big|_0 = 0,\ \ \nu\frac{\partial U_{\mathrm{PO}}}{\partial r}\Big|_R = \tau_w\ . \tag{4.58}$$

This gives

$$u_z = \left(\frac{Rq\bar{c}\bar{E}_z + 2\tau_w}{4\nu R}\right)\left(r^2 - R^2\right) + \frac{q\bar{E}_z}{4\boldsymbol{\lambda}_B\nu}\ \ln\left[\frac{1-\Lambda\left(\frac{r}{R}\right)^2}{1-\Lambda}\right]\ , \tag{4.59}$$

and

$$\bar{u}_z = \frac{2}{R^2}\int_0^R ru_z\,dr \ \ \Leftrightarrow\ \ \tau_w = -\frac{4\nu}{R}\,\bar{u}_z - \left\{\frac{\Lambda(2-\Lambda)+2(1-\Lambda)\ln(1-\Lambda)}{2\Lambda^2}\right\}Rq\bar{c}\bar{E}_z\ . \tag{4.60}$$

If we assume $\bar{p} \approx p_w$ (externally-induced pressure variation along z is much stronger than that along r), substituting Equation (4.60) into Equation (4.55) gives

$$\frac{8\nu}{R^2}\,\bar{u}_z + \frac{\partial\bar{p}}{\partial z} - q\bar{c}\bar{E}_z\left[1-\xi_u(\Lambda)\right] = 0\ , \tag{4.61}$$

where

$$\xi_u(\Lambda) = \frac{\Lambda^2 + 2\Lambda(1-\Lambda) + 2(1-\Lambda)\ln(1-\Lambda)}{\Lambda^2} = \sum_{i=1}^{\infty}\frac{2}{(i+1)(i+2)}\Lambda^i$$

$$= \frac{1}{3}\Lambda + \frac{1}{6}\Lambda^2 + \frac{1}{10}\Lambda^3 + \mathcal{O}(\Lambda^4)\ . \tag{4.62}$$

Recall that Λ is a dimensionless parameter measuring how strongly protons interact electrostatically (see Equation (4.10)),

$$\Lambda = \frac{1}{8}\left(\frac{R}{\boldsymbol{\lambda}_D}\right)^2\ . \tag{4.63}$$

In the above, $\boldsymbol{\lambda}_D$ is the characteristic decay length (Debye length) of the electric potential away from the charged channel walls. To test the validity of the 1-D Stokes model in approximating the fluid velocity (Equation (4.61)) against the full 2-D model, we run simulations (from Chapter 3) of the transport in a long channel with uniform radius R_0.

The sectionally-averaged fluid velocity is calculated from the 2-D numerical data obtained, and this is compared with $\bar{u}_z$ found via Equation (4.61) for some values of $|\sigma_0|$ (note that $\sigma_0 \leq 0$). Results are shown in Figure 4.5, obtained at the cross-section in the middle of the channel ($z = L_0/2$). We obtain a perfect match for low values of $|\sigma_0|$ (<0.05 C/m^2). A small deviation, however, is seen when the channel is strongly charged. The qualitative behaviour of the curves, however, is the same.

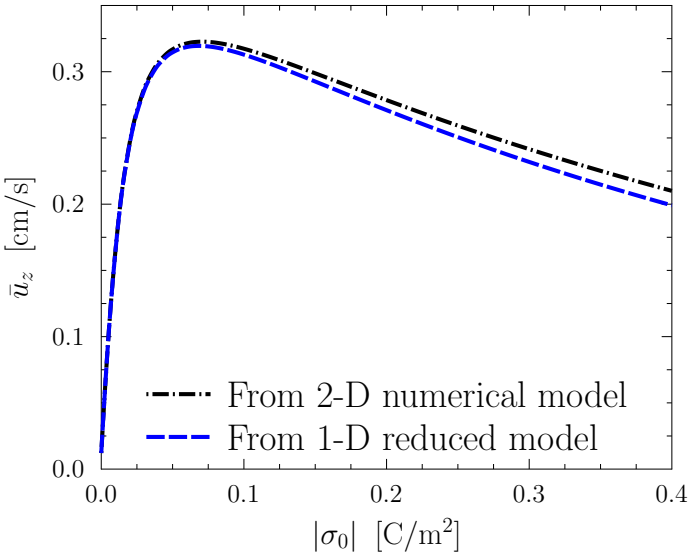

Figure 4.5: Comparison of $\bar{u}_z$ from 2-D numerical model with results of the 1-D model given in Equation (4.61) as a function of σ_0 for a rigid channel. Used parameters: $R_0 = 1$ nm, $L_0 = 200$ nm, $\Delta V_0 = 0.1$ V, $c_0 = 0.01$ M, $\Delta P = 10$ kPa.

4.4.3 Nernst-Planck equation in 1-D

The continuity equation for protons, taking into account the variable cross-sectional area, takes the form

$$\frac{\partial (Ac)}{\partial t} + \nabla \cdot (A\boldsymbol{J}) = 0 \,, \tag{4.64}$$

and the 2-D formulation of the axial proton flux density is given by the axial Nernst-Planck equation (note that $J_r = 0$),

$$J_z = cu_z - D\frac{\partial c}{\partial z} + \omega qcE_z = J_z^{\text{adv}} + J_z^{\text{diff}} + J_z^{\text{migr}} \,, \tag{4.65}$$

where we distinguish contributions due to advection of the fluid, J_z^{adv}, diffusion, J_z^{diff}, and migration, J_z^{migr}. Before sectional averaging of Equation (4.65), we present the following equations which are found from algebraic manipulations of Equation (4.12) for $c(r)$:

$$c(r) \;=\; c_0\left[1-\Lambda\left(\frac{r}{R}\right)^2\right]^{-2} \;=\; c_0\sum_{i=1}^{\infty} i\,\left[\Lambda\cdot\left(\frac{r}{R}\right)^2\right]^{i-1}\;, \tag{4.66}$$

$$\bar{c} \;=\; \frac{2}{R^2}\int_0^R c(r)rdr = \frac{c_0}{1-\Lambda}\;, \tag{4.67}$$

$$c_w = c(R) = \frac{c_0}{(1-\Lambda)^2}\;, \tag{4.68}$$

$$\Lambda = \tfrac{1}{2}\lambda_B R^2 c_0 = \tfrac{1}{2}\lambda_B R^2\bar{c}(1-\Lambda) \;\;\Rightarrow\;\; \Lambda = \frac{\lambda_B R^2\bar{c}}{2+\lambda_B R^2\bar{c}}\;. \tag{4.69}$$

In accordance with Equation (4.59), we rewrite u_z as follows,

$$u_z(r) = A + Br^2 + C\ln\left[1-\Lambda\left(\frac{r}{R}\right)^2\right] = A + Br^2 - C\sum_{i=1}^{\infty}\frac{1}{i}\,\left[\Lambda\left(\frac{r}{R}\right)^2\right]^i\;, \tag{4.70}$$

where the coefficients A and B are found by demanding that $u_z(R)=0$ and $\partial u_z(0)/\partial r = 0$, and $C = \frac{q\bar{E}_z}{4\lambda_B\nu}$. Accordingly, we obtain

$$A = 2\bar{u}_z + \frac{R^2 q\bar{c}\bar{E}_z}{4\nu}\underbrace{\left[\xi_u - \frac{1-\Lambda}{\Lambda}\ln(1-\Lambda) - 1\right]}_{\xi_A}, \tag{4.71}$$

$$B = -\frac{1}{R^2}\times\left\{2\bar{u}_z + \frac{R^2 q\bar{c}\bar{E}_z}{4\nu}\underbrace{[\xi_u - 1]}_{\xi_B}\right\}, \tag{4.72}$$

$$C = \frac{q\bar{E}_z}{4\ell_B\nu} = \underbrace{\frac{R^2 q\bar{c}\bar{E}_z}{4\nu}}_{U^*}\underbrace{\left(\frac{1-\Lambda}{\Lambda}\right)}_{\xi_C}\;. \tag{4.73}$$

We derive the expression for the cross-sectionally averaged advective term $\bar{j}_z^{\text{adv}}$ using the

results above:

$$\bar{J}_z^{\text{adv}} = \langle u_z c \rangle = \frac{2}{R^2}\int_0^R u_z c\, r dr$$

$$= \frac{2}{R^2}\Bigg\{ Ac_0 \int_0^R r \sum_{i=1}^{\infty} i \left[\Lambda \cdot \left(\frac{r}{R}\right)^2\right]^{i-1} dr + Bc_0 \int_0^R r^3 \sum_{i=1}^{\infty} i \left[\Lambda \cdot \left(\frac{r}{R}\right)^2\right]^{i-1} dr$$

$$- Cc_0 \int_0^R \sum_{i=1}^{\infty} i \left[\Lambda \cdot \left(\frac{r}{R}\right)^2\right]^{i-1} \sum_{i=1}^{\infty} \frac{1}{i}\left[\Lambda \left(\frac{r}{R}\right)^2\right]^{i} dr \Bigg\} \tag{4.74}$$

$$= c_0 \left\{ A \sum_{i=0}^{\infty} \Lambda^i + BR^2 \sum_{i=0}^{\infty} \left(\frac{i+1}{i+2}\right)\Lambda^i - C \sum_{i=1}^{\infty} \frac{1}{i+1}\left(\sum_{k=1}^{i} \frac{k}{1+i-k}\right)\Lambda^i \right\}. \tag{4.75}$$

Using $c_0 = \bar{c}(1-\Lambda)$ (from Equation (4.67)) in Equation (4.75), we obtain

$$\bar{J}_z^{\text{adv}} = \bar{u}_z \bar{c} \Bigg\{ 1 - \underbrace{\sum_{i=1}^{\infty} \frac{2\Lambda^i}{(i+1)(i+2)}}_{\xi_u} \Bigg\} + U^* \bar{c} \underbrace{\left\{ \frac{1-\Lambda}{\Lambda} \sum_{i=1}^{\infty} \left[\xi_A - \frac{i\xi_B + \sum_{k=1}^{i} \frac{k(\Lambda-1)}{1+i-k}}{i+1} \right] \Lambda^i \right\}}_{1-\xi_E}$$

$$= \bar{u}_z \bar{c}(1-\xi_u) + \frac{R^2 q \bar{c}^2 \bar{E}_z}{4\nu}(1-\xi_E)\,, \tag{4.76}$$

where ξ_u is given in Equation (4.62) and the other Λ-dependent function ξ_E is given by

$$\xi_E = 1 - \frac{1-\Lambda}{\Lambda} \sum_{i=1}^{\infty} \left[\frac{(1-\Lambda)\sum_{k=1}^{i} \frac{k}{1+i-k} - i(1-\xi_u)}{i+1} + \xi_u - \sum_{k=1}^{\infty} \frac{\Lambda^k}{(k+1)(k+2)} \right] \Lambda^i$$

$$= \frac{1}{3}\Lambda + \frac{5}{36}\Lambda^2 + \frac{4}{45}\Lambda^3 + \mathcal{O}(\Lambda^4)\,. \tag{4.77}$$

On the basis of Equation (4.69), we notice that $\Lambda \in [0,1]$. For a weakly charged channel with small radius, one finds $\Lambda \approx \lambda_B R^2 \bar{c} \to 0$ and, hence, $\xi_u \,\&\, \xi_E \to 0$. For a strongly charged channel with large radius, $\Lambda \to 1$ and, hence, $\xi_u \,\&\, \xi_E \to 1$. According to Equations (4.61) and (4.76), the effects of charge strength on the sectionally averaged electroosmotic

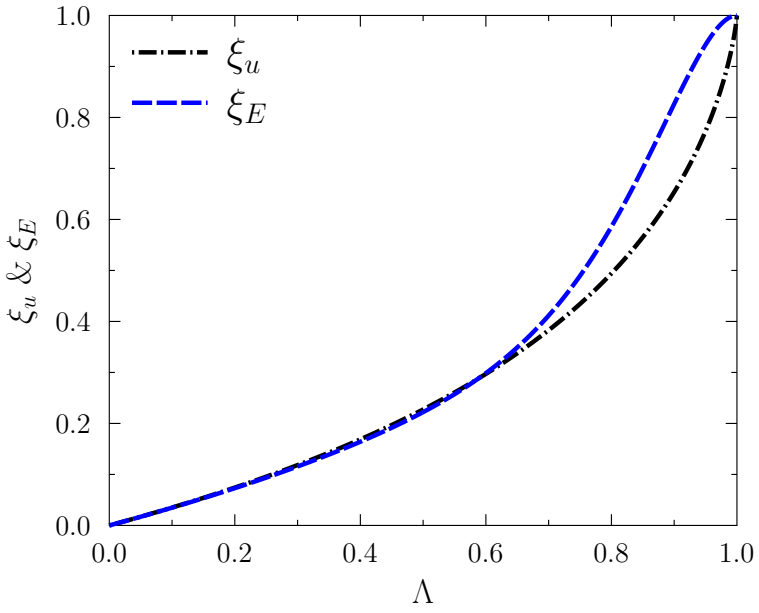

Figure 4.6: Dependence of ξ_u and ξ_E on Λ.

flow diminish at very high proton concentration. The functions ξ_u and ξ_E are plotted in Figure 4.6 as functions of Λ.

Sectional diffusion and migration flux densities follow directly from Equations (4.46) & (4.47). Expressing the proton concentration at the wall as $c_w = c(R,z) \approx \frac{1}{2}\bar{c}(2+\lambda_B R^2 \bar{c})$ (derived in Equation (4.68)), which holds exactly in the limit of an infinite aspect ratio, leads to the fluxes

$$\bar{J}_z^{\mathrm{adv}} = \bar{c}\bar{u}_z(1-\xi_u) + \frac{R^2 q \bar{c}^2 \bar{E}_z}{4\nu}(1-\xi_E)\ , \tag{4.78a}$$

$$\bar{J}_z^{\mathrm{diff}} = -D\left(\frac{\partial \bar{c}}{\partial z} - \lambda_B R \bar{c}^2 \frac{\partial R}{\partial z}\right)\ , \tag{4.78b}$$

$$\bar{J}_z^{\mathrm{migr}} = \omega q \bar{c} \bar{E}_z\ . \tag{4.78c}$$

In a manner similar to Figure 4.5, Figure 4.7 compares $\bar{J}_z$ computed from numerical results obtained for the full 2-D channel with $\bar{J}_z$ found from the equations above for the reduced 1-D model, for the case of uniform R. Again, we notice a small deviation only at high values of $|\sigma_0|$. This highlights the reliability of using ξ_u and ξ_E in the 1-D model to approximate the 2-D model.

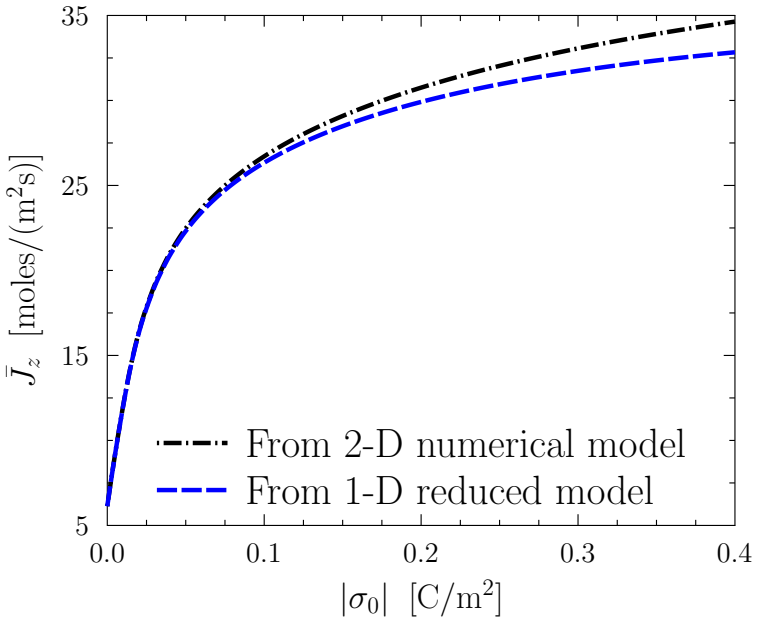

Figure 4.7: Comparison of $\bar{J}_z$ from 2-D numerical model with results of the 1-D model given in Equation (4.61) as a function of σ_0 for a rigid channel. Used parameters: $R-0=1$ nm, $L_0=100$ nm, $\Delta V_0=0.1$ V, $c_0=0.01$ M, $\Delta P=10$ kPa.

4.4.4 Poisson equation in 1-D

In terms of the electric field $\boldsymbol{E}$, the Poisson equation reads

$$\nabla\cdot\boldsymbol{E}=\frac{qc}{\varepsilon\varepsilon_0}\,, \tag{4.79}$$

along with the boundary condition at the wall,

$$\boldsymbol{E}\cdot\hat{\boldsymbol{n}}\Big|_{r=R}=-\frac{\sigma_p}{\varepsilon\varepsilon_0}\,. \tag{4.80}$$

Here, σ_p is the surface charge density at the wall and $\hat{\boldsymbol{n}}$ is a unit normal vector to the wall. Accounting for the deformed state of the channel, $\hat{\boldsymbol{n}}$ can be expressed as

$$\hat{\boldsymbol{n}}\;=\;\frac{dz\hat{\boldsymbol{e}}_r-dR\hat{\boldsymbol{e}}_z}{\sqrt{(dR)^2+(dz)^2}}\,, \tag{4.81}$$

for some small element dz. Equation (4.79) takes the 2-D form

$$\frac{1}{r}\frac{\partial(rE_r)}{\partial r}+\frac{\partial E_z}{dz}-\frac{qc}{\varepsilon\varepsilon_0}=0\,. \tag{4.82}$$

We apply cross-sectional averaging to Equation (4.79) term by term:

$$\left\langle \frac{1}{r}\frac{\partial(rE_r)}{\partial r} \right\rangle \;=\; \frac{2}{R^2}\int_0^R \frac{1}{r}\frac{\partial(rE_r)}{\partial r}\, rdr \;=\; \frac{2E_r\big|_R}{R}\,, \tag{4.83}$$

$$\left\langle \frac{\partial E_z}{\partial z} \right\rangle \;=\; \frac{\partial \bar{E}_z}{\partial z} \;+\; \frac{2\left(\bar{E}_z - E_z\big|_R\right)}{R}\,\frac{\partial R}{\partial z}\,, \tag{4.84}$$

$$\left\langle \frac{qc}{\varepsilon\varepsilon_0} \right\rangle \;=\; \frac{q\bar{c}}{\varepsilon\varepsilon_0}\,. \tag{4.85}$$

Hence, Equation (4.82) becomes

$$\frac{2E_r\big|_R}{R} + \frac{\partial \bar{E}_z}{\partial z} + \frac{2\left(\bar{E}_z - E_z\big|_R\right)}{R}\,\frac{\partial R}{\partial z} - \frac{q\bar{c}}{\varepsilon\varepsilon_0} \;=\; 0\,, \tag{4.86}$$

and the electroneutrality boundary condition (Equation (4.80)) becomes

$$-\left(\boldsymbol{E}\cdot\boldsymbol{n}\right)\Big|_R \;=\; \frac{\left[(dR/dz)\;E_z\big|_R \;-\; E_r\big|_R\right]}{\sqrt{1\;+\;(dR/dz)^2}} \;=\; \frac{\sigma_p}{\varepsilon\varepsilon_0} \tag{4.87}$$

$$\Rightarrow \quad E_r\Big|_R \;=\; E_z\Big|_R\,\frac{\partial R}{\partial z} \;-\; \frac{\sigma_p\,\sqrt{1+(dR/dz)^2}}{\varepsilon\varepsilon_0}\,. \tag{4.88}$$

Substituting Equation (4.88) into Equation (4.86), and using the assumption $\bar{E}_z = E_z\big|_R$, we get the 1-D Poisson equation,

$$\frac{1}{R^2}\frac{\partial\left(R^2\bar{E}_z\right)}{\partial z} - \frac{2\sigma_p\sqrt{1+(dR/dz)^2}}{\varepsilon\varepsilon_0 R} - \frac{q\bar{c}}{\varepsilon\varepsilon_0} = 0\,. \tag{4.89}$$

For weak deformations, we assume $(dR/dz)^2 \ll 1$ so that the $(dR/dz)^2$ term in Equation (4.89) vanishes. We model the surface charge density as [47]

$$\sigma_p = \sigma_0 \times \left(\frac{R_0}{R}\right)^{\alpha}\,, \tag{4.90}$$

where the channel geometry parameter α measures the extent of surface group reorganization upon deformation. Weak surface charge reorganization corresponds to $\alpha \to 0$ and $\alpha \to 1$ indicates strong reorganization of surface charges. Note that the total surface charge within the channel, equal to $\int_0^L 2\pi R(z)\sigma_p(z)dz$, remains constant under deformation, implying a dynamic change in channel length under deformation, except when $\alpha = 1$. In each cross-section, located at some z, the charge density is proportional to $2\pi R(z)\sigma_p(z) \sim R^{1-\alpha}$. This means that the amount of protons changes when a cross-sectional element grows or shrinks in size, again except for $\alpha = 1$ when the number of protons remains constant. Any

dramatic changes in the channel lengths are ignored.

4.4.5 Wall pressure balance

In an effort to couple the fluid transport with the deformation of the walls, we assume that the walls' viscoelasticity leads to a time-dependent deformation given by the linear Kelvin-Voigt model [152],

$$\boldsymbol{\sigma} = Y\boldsymbol{\varepsilon} + \eta\frac{\partial\boldsymbol{\varepsilon}}{\partial t} \,, \tag{4.91}$$

describing a balance between the stress, $\boldsymbol{\sigma}$, and the strain, $\boldsymbol{\varepsilon}$ at the channel wall. Y is the modulus of elasticity and η is the viscosity constant for the walls. The Kelvin-Voigt model captures effects of creep, stress relaxation and storage of strain energy at equilibrium in the simplest manner possible by being linear in strain and its rate of change.

For symetry reasons, Equation (4.91) can be treated in 1-D along the circumferential direction only. Assuming thin channel walls with constant thickness h_0, the balance of pressure forces normal to the wall gives the coupling between the 1-D flow equations and wall deformations. We consider (1) the fluid pressure at the wall $p_w = \bar{p}$, (2) the electroosmotic pressure $p_{\text{osm}} = k_B T c_w$, and (3) the tangential stress σ_θ, also referred to as circumferential or hoop stress, and Equation (4.91) as

$$\sigma_\theta = Y\varepsilon_\theta + \eta\frac{\partial\varepsilon_\theta}{\partial t} \,. \tag{4.92}$$

Here, the tangential strain is determined by $\varepsilon_\theta = (R - R_0)/R_0$, whereas the axial strain is neglected as is justified for $R_0 \ll L_0$. Moreover, maintaining the pressure balance at the wall requires

$$(\bar{p} + p_{\text{osm}})R_0 - h_0\sigma_\theta = 0 \,. \tag{4.93}$$

4.4.6 Dimensionless viscoelastic model formulation

Collecting Equations (4.49), (4.61), (4.78), (4.93), we present a summary of the 1-D model equations to solve for the cross-sectional variables R, $\bar{u}_z$, $\bar{p}$, $\bar{E}_z$ and $\bar{c}$:

$$\frac{\partial\left(R^2\right)}{\partial t} + \frac{\partial\left(R^2\bar{u}_z\right)}{\partial z} = 0 \,, \tag{4.94a}$$

$$\frac{8\nu}{R^2}\,\bar{u}_z + \frac{\partial\bar{p}}{\partial z} - q\bar{c}\bar{E}_z(1-\xi_u) = 0 \,, \tag{4.94b}$$

$$\frac{1}{R^2}\frac{\partial\left(R^2\bar{E}_z\right)}{\partial z} - \frac{2\sigma_0}{\varepsilon\varepsilon_0 R}\left(\frac{R_0}{R}\right)^\alpha - \frac{q\bar{c}}{\varepsilon\varepsilon_0} = 0 \,, \tag{4.94c}$$

$$\bar{p}R + k_B T R\bar{c}(1+\tfrac{\lambda_B}{2}R^2\bar{c}) - \frac{Yh_0}{R_0}(R-R_0) - \frac{\eta h_0}{R_0}\frac{\partial R}{\partial t} = 0\ , \tag{4.94d}$$

$$\bar{J}_z = \bar{c}\bar{u}_z(1-\xi_u) + \frac{R^2 q\bar{c}^2\bar{E}_z}{4\nu}(1-\xi_E) - D\left(\frac{\partial \bar{c}}{\partial z} - \boldsymbol{\lambda}_B R\bar{c}^2\frac{\partial R}{\partial z}\right) + \omega q\bar{c}\bar{E}_z\ . \tag{4.94e}$$

For further analysis, Equations (4.94) are non-dimensionalized using properties of the initially equilibrated channel in Figure 4.4(a). We thus use the following non-dimensionalization scheme,

$$x = \frac{z}{L_0},\ \tau = \frac{t}{\left(\frac{8\nu L_0^2}{|\sigma_0|R_0\Delta V_0}\right)},\ \tilde{R} = \frac{R}{R_0},\ \tilde{u} = \frac{\bar{u}_z}{\left(\frac{|\sigma_0|R_0\Delta V_0}{8\nu L_0}\right)},$$

$$\tilde{p} = \frac{\bar{p}}{\left(\frac{|\sigma_0|\Delta V_0}{R_0}\right)},\ \tilde{c} = \frac{\bar{c}}{\left(\frac{|\sigma_0|}{qR_0}\right)},\ \tilde{E} = \frac{\bar{E}_z}{\left(\frac{\Delta V_0}{L_0}\right)}\ . \tag{4.95}$$

Note that the above non-dimensionalization scheme is different from that used in Equations (4.26). The tilde ('$\sim$') on top of symbols indicates dimensionless and sectionally-averaged field quantities, and the bar ('–') only indicates sectionally-averaged field quantities in proper dimensions. The scheme transforms Equations (4.94) into dimensionless form,

$$\frac{\partial\left(\tilde{R}^2\right)}{\partial\tau} + \frac{\partial\left(\tilde{R}^2\tilde{u}\right)}{\partial x} = 0\ , \tag{4.96a}$$

$$\tilde{u} = -\tilde{R}^2\left(\frac{\partial\bar{p}}{\partial x} - \tilde{c}\tilde{E}(1-\xi_u)\right)\ , \tag{4.96b}$$

$$\frac{1}{\tilde{R}^2}\frac{\partial\left(\tilde{R}^2\tilde{E}\right)}{\partial x} - \mathcal{K}_\sigma\left(\tilde{c} - \frac{2}{\tilde{R}^{\alpha+1}}\right) = 0\ , \tag{4.96c}$$

$$\tilde{p} = \frac{\mathcal{K}_Y(\tilde{R}-1)}{\tilde{R}} - \mathcal{K}_{\text{osm}}\tilde{c}(1+\kappa\tilde{R}^2\tilde{c}) + \mathcal{K}_\eta\frac{\partial\tilde{R}}{\partial\tau}\ , \tag{4.96d}$$

$$\tilde{j}_z = \tilde{c}\tilde{u}(1-\xi_u) + 2(\tilde{R}\tilde{c})^2\tilde{E}(1-\xi_E) - \mathcal{K}_{\text{diff}}\left(\frac{\partial\tilde{c}}{\partial x} - 2\kappa\tilde{R}\tilde{c}^2\frac{\partial\tilde{R}}{\partial x}\right) + \mathcal{K}_{\text{migr}}\tilde{c}\tilde{E}\ . \tag{4.96e}$$

In the above, the dimensionless parameter $\mathcal{K}_\sigma = \frac{|\sigma_0|L_0^2}{\varepsilon\varepsilon_0 R_0\Delta V_0}$ measures the strength of the electric field in the radial direction relative to the axial direction; $\mathcal{K}_Y = \frac{Yh_0}{|\sigma_0|\Delta V_0}$, $\mathcal{K}_{\text{osm}} = \frac{k_B T}{q\Delta V_0}$ and $\mathcal{K}_\eta = \frac{\eta h_0 R_0}{8\nu L_0^2}$ measure the strength of elastic, osmotic and viscous forces, respectively, relative to electroosmotic forces; $\mathcal{K}_{\text{diff}} = \frac{8\nu D}{|\sigma_0|R_0\Delta V_0}$ and $\mathcal{K}_{\text{migr}} = \frac{8\nu qD}{|\sigma_0|R_0 k_B T}$

measure the strengths of the diffusion and migration fluxes, respectively, relative to the convection flux from electroosmotic forces. Finally, $\kappa = \lambda_B|\sigma_0|R_0/2q$ is a new dimensionless parameter introduced so that $\Lambda = \frac{\kappa\tilde{R}^2\tilde{c}}{1+\kappa\tilde{R}^2\tilde{c}}$.

4.4.7 Non-viscous and elastic nanochannel

Equations (4.96) provide the generic 1-D model for the flow-deformation system at high aspect ratio. One approach to simplifying these equations is to scrutinize the dimensionless parameters and eliminate terms that are negligible for a particular case of interest. An example is transport through a PEM Nafion membrane. Typical viscoelastic variables are $Y = 0.5$ GPa and $\eta = 0.1$ MPa·s [153, 154]. Other typical variables governing the flow are $R_0 = 1$ nm, $L_0 = 50$ nm, $T = 353$ K, $\nu = 0.335$ mPa·s, $\sigma_0 = -0.16$ C/m^2, $\Delta V_0 = 0.1$ V, $D = 7 \cdot 10^{-6}$ cm^2/s, and $\varepsilon = 45$. These give the following parameters: $\mathcal{K}_Y = 1.6$, $\mathcal{K}_\eta = 0.007$, $\mathcal{K}_{\text{osm}} = 0.3$, $\mathcal{K}_{\text{diff}} = 0.2$, $\mathcal{K}_{\text{migr}} = 0.4$, and $\mathcal{K}_\sigma = 1 \cdot 10^{10}$. These channels exhibit high aspect ratio and they feature strongly charged surfaces ($1 \ll \mathcal{K}_\sigma$) and very small wall viscosity ($\mathcal{K}_\eta \ll 1$). Hence, we can neglect the viscous term in Equation (4.96d).

4.4.8 Advection-diffusion model

As mentioned in the model description above, this contribution focuses on the nanochannel interior which is at least a Debye length away from the nanochannel-reservoir interface. Hence, we can assume that local electroneutrality holds at leading order ($\frac{\varepsilon_{\text{out}}}{\varepsilon_{\text{in}}} < 0.1$) and, consequently, that the electric flux is conserved at leading order. In mathematical form, these assumptions follow from Equation (4.96c) as

$$\tilde{c} \approx \frac{2}{\tilde{R}^{\alpha+1}} \quad \& \quad \tilde{E} \approx \frac{\text{Const.}}{\tilde{R}^2} \, . \tag{4.97}$$

Here, we set Const. = 1 without loss of generality. The problem can be simplified further by substituting Equations (4.97) back into Equations (4.96a)–(4.96d) and setting $\mathcal{K}_\eta = 0$. Substituting Equations (4.97) into Equations (4.96), from Equation (4.96d) backwards to Equation (4.96a), the wall dynamics model is reduced to a nonlinear 1-D equation of the 'advection-diffusion' type,

$$\frac{\partial \tilde{a}}{\partial \tau} = \frac{\partial}{\partial x}\left[\mathcal{D}(\tilde{a}) \cdot \frac{\partial \tilde{a}}{\partial x}\right] - \frac{\partial}{\partial x}\left[\mathcal{G}(\tilde{a})\right] , \tag{4.98}$$

where $\tilde{a} = \tilde{R}^2$, and the diffusion and drift functions are

$$\mathcal{D}(\tilde{a}) = \frac{\mathcal{K}_Y \tilde{a}^{\frac{1}{2}}}{2} + \mathcal{K}_{\text{osm}} \left[(1+\alpha)\tilde{a}^{\frac{1-\alpha}{2}} + 4\alpha\kappa\tilde{a}^{1-\alpha} \right] , \tag{4.99}$$

$$\mathcal{G}(\tilde{a}) = 2(1-\xi_u)\tilde{a}^{\frac{1-\alpha}{2}} . \tag{4.100}$$

Equation (4.98) is solved in the finite domain $x \in [0,1]$ by imposing an initial profile corresponding to uniform radius and thus mechanical equilibrium of the channel with $\Delta p = 0$. Assuming the pressure at the inlet is perturbed by $\Delta\tilde{p}_i$, resulting in a deformation of radius $\Delta\tilde{R}_i$, the inlet steady-state (mechanical equilibrium) deformation gives,

$$\Delta\tilde{R}_i = \frac{\Delta\tilde{p}_i}{\mathcal{K}_Y} , \tag{4.101}$$

found from Equation (4.96d) by substituting $\tilde{p} = \Delta\tilde{p}_i - p_0 = \Delta\tilde{p}_i - p(\tilde{R}=1)$, $\tilde{R} - 1 = \Delta\tilde{R}_i$ and $\tilde{R} \approx 1$. Assuming that Equation (4.101) is valid at $\tau = 0$ (immediately after applying the perturbation) is based on a simplifying assumption that the response of the inlet radius to a pressure perturbation at the inlet is instantaneous. There is a time scale associated with the change of R at the inlet after applying the perturbation. However, we assume that this time is very short in comparison to the time for the deformation front to penetrate the channel. For sufficiently high aspect ratios, this condition will be fulfilled. The boundary conditions at the channel ends are $\tilde{R}(0,t) = 1 + \Delta\tilde{R}_i$, $\tilde{R}(1,t) = 1$.

4.5 Summary

In this chapter, we presented analytical solutions for water-proton flow in a long, cylindrical and negatively charged channel, starting from the continuum-based Poisson-Nernst-Planck and Stokes model. This enabled us to assess the electroneutrality of the channels when the walls are non-insulating. A theoretical model was developed that describes nonlinear coupling between wall deformation and water and proton flows in a charged, deformable nanochannel whose viscoelasticity is governed by the Kelvin-Voigt model. Using continuum mean-field theories for mass and momentum conservation of the solid-liquid coupled system, a set of one-dimensional nonlinear partial differential equations was derived to capture the dynamics of wall deformations. Our theory suggests that for elastic but non-viscous walls undergoing small deformation, the problem simplifies to one of advection-diffusion type.

Chapter 5

Impact of Channel Elasticity on Proton and Water Transport

In the previous chapter, we derived a 1-D model for the nonlinear coupling between wall deformations and water-proton transport in a nanochannel with negatively charged walls. Assuming that transport occurs in a channel of very high aspect ratio, we demonstrated that the equations can be reduced to a 1-D system which simplifies to an equation of the 'advection-diffusion' type when the channel walls are elastic but nonviscous.

The present chapter extends from the preceding one. Results from Chapter 4 are used to investigate the effect of the system's charging on the wall deformational and proton-water transport properties. Within the framework of nonequilibrium thermodynamics, compact formulae are derived for the electrokinetic transport parameters in terms of Onsager phenomenological coefficients and, subsequently, for the energy conversion efficiency. The chapter is structured as follows: In Section 5.1, an approximate analytical solution for weak deformations is presented. Section 5.2 discusses the interplay between the wall charges and elasticity in driving the deformations within the channel. Section 5.3 explores the coupling between the channel's elasticity and the water-ion fluxes within. Section 5.4 contains derivations and a discussion of the Onsager transport coefficients. In Section 5.5, we discuss the energy conversion efficiency of the electrokinetic system explored herein. Finally, Section 5.6 gives a summary of results.

5.1 Linear perturbative solution

We recall the channel's advection-diffusion model for deformations derived in Chapter 4:

$$\frac{\partial \tilde{a}}{\partial \tau} = \frac{\partial}{\partial x}\left[\mathcal{D}(\tilde{a}) \cdot \frac{\partial \tilde{a}}{\partial x}\right] - \frac{\partial}{\partial x}\left[\mathcal{G}(\tilde{a})\right], \tag{5.1}$$

where $\tilde{a} = \tilde{R}^2$ (where $\tilde{R}(z) = R(z)/R_0$), and the diffusion and drift functions are

$$\mathcal{D}(\tilde{a}) = \frac{\mathcal{K}_Y \tilde{a}^{\frac{1}{2}}}{2} + \mathcal{K}_{\text{osm}} \left[(1+\alpha)\tilde{a}^{\frac{1-\alpha}{2}} + 4\alpha\kappa\tilde{a}^{1-\alpha} \right] , \tag{5.2}$$

$$\mathcal{G}(\tilde{a}) = 2(1-\xi_u)\tilde{a}^{\frac{1-\alpha}{2}} . \tag{5.3}$$

For deformations which are small compared to the channel radius, i.e., $\Delta\tilde{R} \ll 1$, Equation (5.1) can be solved using a linear perturbation approach via expansion about $\tilde{a} = 1$,

$$\tilde{a} = 1 + \tilde{\varepsilon}\Delta\tilde{a} + \mathcal{O}\left(\tilde{\varepsilon}^2\right) , \tag{5.4}$$

and

$$\mathcal{D}(\tilde{a}) = \mathcal{D}(1) + \tilde{\varepsilon}\mathcal{D}'(1)\Delta\tilde{a} + \mathcal{O}\left(\tilde{\varepsilon}^2\right) , \tag{5.5}$$

$$\mathcal{G}(\tilde{a}) = \mathcal{G}(1) + \tilde{\varepsilon}\mathcal{G}'(1)\Delta\tilde{a} + \mathcal{O}\left(\tilde{\varepsilon}^2\right) , \tag{5.6}$$

where the prime ($'$) indicates derivatives with respect to $\tilde{a}$. The first-order problem governing $\Delta\tilde{a}$ can later be recovered by setting $\tilde{\varepsilon} = 1$ in the original equation. Substituting Equations (5.4)–(5.6) into Equation (5.1) gives the 1-D linear advection-diffusion equation,

$$\frac{\partial \Delta\tilde{a}}{\partial \tau} = \mathcal{D}_0 \frac{\partial^2 \Delta\tilde{a}}{\partial x^2} - \mathcal{V}_0 \frac{\partial \Delta\tilde{a}}{\partial x} , \tag{5.7}$$

where $\mathcal{D}_0 = \mathcal{D}(1)$ and $\mathcal{V}_0 = \mathcal{G}'(1)$, and the accompanying initial and boundary conditions are

$$\begin{aligned} \Delta\tilde{a}(0,\tau) &= \Delta\tilde{a}_i, \ \tau \geq 0 , \\ \Delta\tilde{a}(x,0) &= 0, \ x \geq 0 , \\ \Delta\tilde{a}(1,\tau) &= 0, \ \tau \geq 0 . \end{aligned} \tag{5.8}$$

The solution to the above problem was found by Davis [155] employing the Laplace Transform technique,

$$\Delta\tilde{a}(x,\tau) = \Delta\tilde{a}_i \exp(\boldsymbol{\lambda} x)\left\{ \frac{\sinh[\boldsymbol{\lambda}(1-x)]}{\sinh(\boldsymbol{\lambda})} - 2\pi \sum_{n=1}^{\infty} \frac{n \sin(n\pi x)}{(\boldsymbol{\lambda}^2 + n^2\pi^2)} \, e^{-\left(\boldsymbol{\lambda}^2 + n^2\pi^2\right)\mathcal{D}_0\tau} \right\} , \tag{5.9}$$

where $\boldsymbol{\lambda} = \mathcal{V}_0/2\mathcal{D}_0$ and

$$\Delta\tilde{a}_i = \Delta\tilde{R}_i(2 + \Delta\tilde{R}_i) = \frac{\Delta\tilde{p}_i}{\mathcal{K}_Y}\left(2 + \frac{\Delta\tilde{p}_i}{\mathcal{K}_Y}\right) . \tag{5.10}$$

5.2 Wall deformation dynamics

Using the formalism and the solution presented in the previous section, we model the dynamics of the walls as a dispersive transport process, characterized by Equation (5.1) and having solutions at small deformations approximated by Equation (5.9). In this section, we study the relaxation characteristics of the deformable channel corresponding to different regimes of interest. Following PEM operating conditions, we use the following parameters: $T = 353$ K, $\nu = 3.3 \cdot 10^{-4}$ kg/m·s, $L_0 = 50$ nm, $D = 7 \cdot 10^{-6}$ cm^2/s and $h_0 = 0.5$ nm. (Parameters and reference values are listed in Table 5.1. Table 5.2 lists the variables that depend on the axial coordinate z.)

Parameter	Description	Reference value
D	proton diffusivity	$7 \cdot 10^{-6}$ cm^2/s
h_0	channel wall thickness	0.5 nm
k_B	Boltzmann constant	$1.38 \cdot 10^{-23}$ J/K
L_0	channel equilibrium length	50 nm
q	elementary charge	$1.602 \cdot 10^{-19}$ C
R_0	channel equilibrium radius	2 nm
T	Temperature	353 K
Y	wall elasticity constant	0.1 GPa
α	surface charge scaling parameter	0.5
ΔV_0	voltage across channel length	0.1 V
ε	permittivity	45
ε_0	vacuum permittivity	$8.85 \cdot 10^{-12}$ F/m
η	channel wall viscosity	0.1 MPa s
μ	proton mobility	$1.43 \cdot 10^{15}$ m^2/J s
ν	fluid kinematic viscosity	$3.35 \cdot 10^{-4}$ Pa s
σ_0	equilibrium surface charge density	-0.2 C/m^2

Table 5.1: Parameters of the deformable channel system, based on common properties of PEMs.

Variable	Description	Units
c	proton concentration (number density)	1/m^3
E_z	axial electric field	V/m
p	fluid pressure	Pa
R	channel radius	m
u_z	axial fluid velocity	m/s
σ_p	surface charge density	C/m^2

Table 5.2: Axial-dependent variables of the system.

We begin by numerically solving for the deformation dynamics and comparing them with analytical results for small deformations. Equation (5.1) is solved, using the finite difference method considering the central difference approximation for the spatial derivative terms and the forward difference approximation for the temporal derivative terms. Figure 5.1

shows the variation in the channel deformation variable $\tilde{a}$ expressed along the dimensionless length of the channel at various values of non-dimensional time, while keeping $\Delta\tilde{a}_i = 0.1$, $\mathcal{K}_Y = 0.5$, $\mathcal{K}_{\text{osm}} = 0.3$, $\kappa = 2$ and $\alpha = 0.5$ constant. Symbols display the numerical solution of Equation (5.1) and solid lines correspond to analytical results from Equation (5.9). Simulation results are only shown at times ($\tau \geq 0.01$) not very far from equilibrium (from $\tau \to \infty$), since the inviscid assumption for the channel walls is invalid at very small time scales. We observe excellent agreement between numerical and analytical solutions, suggesting that we can confidently use the linearized problem (solved as Equation (5.9)) as a basis for analysing the dynamics of the system in the discussion that follows.

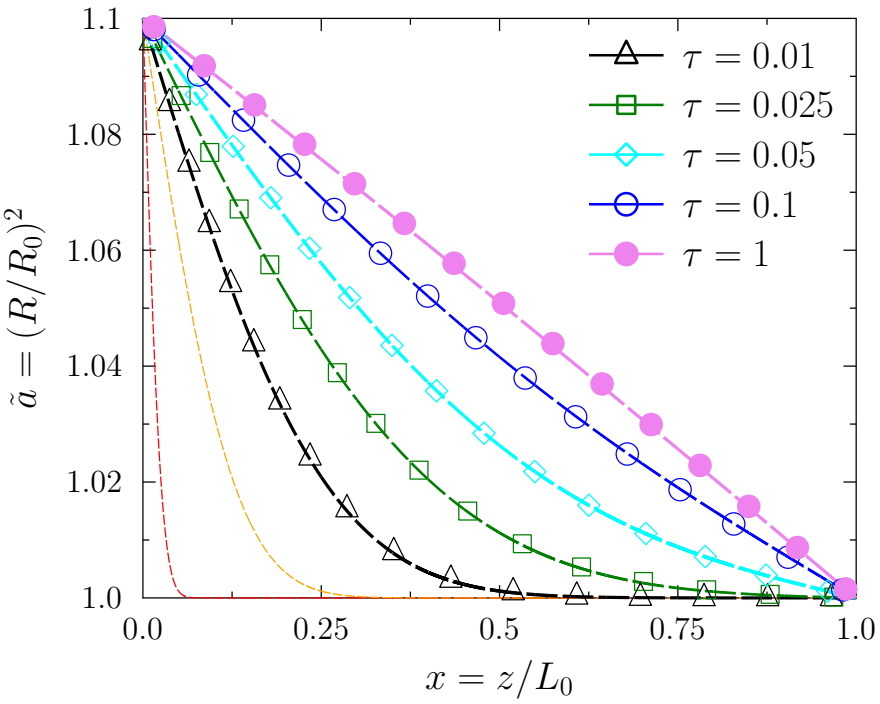

Figure 5.1: Deformation profile for a nanochannel after application of a pressure step for a small deformation ($\Delta\tilde{a}_i = 0.1$). Solid lines represent analytical solutions in the limiting case of non-viscous flow, given by Equation (5.9); symbols correspond to the numerical solutions of the fully coupled model. The reference case corresponds to $\tilde{a} = 1$. Reference parameters used are: $\mathcal{K}_Y = 0.5$, $\mathcal{K}_{\text{osm}} = 0.3$, $\kappa = 2$ and $\alpha = 0.5$.

The channel will change its length under deformation unless $\alpha = 1$ holds. This dynamic change in length calls, in principle, for an advanced modelling approach, resulting in complex governing equations that are not conducive to intuitive interpretation or the derivation of approximate solutions. However, for $\alpha = 0.5$ a 10% variation in radius along the channel (see Figure 5.1) corresponds to a change in length of less than 5%. Hence, the error made

by neglecting the change in channel length has a negligible bearing on the overall results presented herein.

We investigate the driving mechanism behind deformation and relaxation dynamics of the channel walls. The diffusion and advection time scales reveal essential information about the different mechanisms driving the deformations. We consider the Peclet number $\mathrm{Pe} = \mathcal{V}_0/\mathcal{D}_0$, which is a dimensionless measure of the relative importance of advection and diffusion ($\mathrm{Pe} \gg 1$ when advection dominates). For this consideration, it can be shown that

$$\mathrm{Pe} = \frac{(1-\alpha)(2\,\kappa - \ln(2\,\kappa+1))}{(8\,\mathcal{K}_{\mathrm{osm}}\alpha\kappa + 2\,\mathcal{K}_{\mathrm{osm}}\alpha + \mathcal{K}_Y + 2\,\mathcal{K}_{\mathrm{osm}})\kappa^2}\ . \tag{5.11}$$

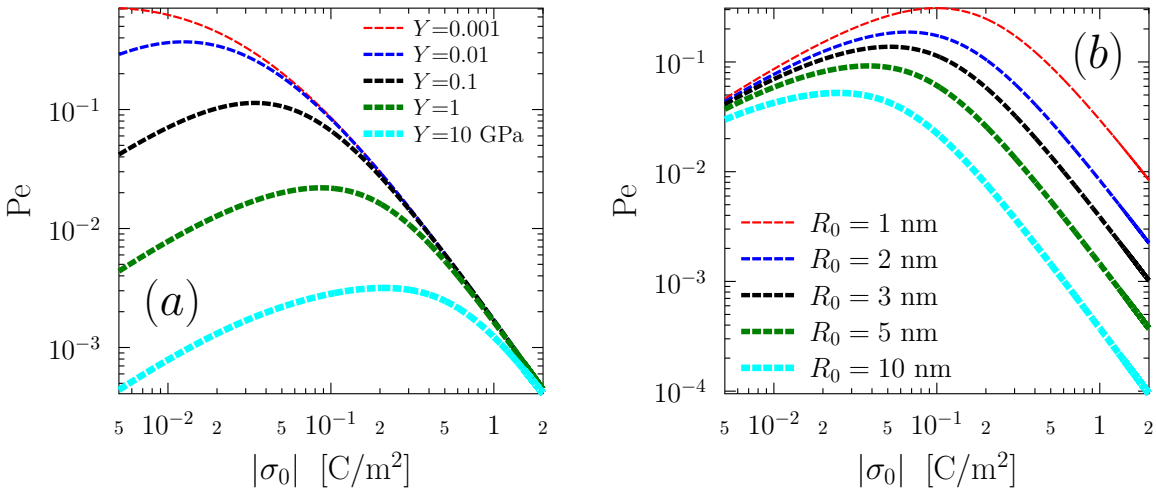

Figure 5.2: Variation of the Peclet number with the channel surface charge density for different values of (a) the elasticity constant Y and (b) initial channel radius R_0. Other parameters used are: $L_0 = 50$ μm, $\Delta V_0 = 0.1$ V, $R_0 = 2$ nm, $Y = 0.05$ GPa, and $\alpha = 0.5$.

Figure 5.2 shows the variation of the Peclet number with the surface charge density at the channel walls. In Figure 5.2(a), this variation is explored at different elasticity constants. For the reference set of parameters which represents the case of a soft membrane, the wall dynamics are mostly controlled by diffusion (Pe<1). Advection becomes more prominent as the surface charge density increases owing to the internally generated force by electrosmotic drag. However, for very high $|\sigma_0|$, the dynamics are dominated by diffusion again. For this condition, electroosmotic drag (and, hence, advection) is reduced owing to friction introduced by the abundance of protons in the double layer, close to the walls, where fluid motion is diminished significantly. This effect is accounted for in Equation (4.61): at large $|\sigma_0|$, one has $\xi_u \to 1$, diminishing the electrosmotic drag term. Consequently,

the Peclet number is greatly reduced with increasing $|\sigma_0|$ beyond the peak, and diffusive transport dominates. The coupling between wall deformation, surface charge density, and elasticity is demonstrated by the various graphs in Figure 5.2(a). It can be seen that a large elastic modulus reduces the Peclet number and, hence, favors diffusion. This is because high elasticity enforces strong ion concentration gradients along the channel. One key feature of the graphs is the vanishing dependence on the elastic modulus at very large $|\sigma_0|$. The physics behind this observation is explained in the next section. Hence, the coupling between channel deformations $|\sigma_0|$ vanishes for strongly charged nanochannels. Figure 5.2(b) reveals an opposite coupling behaviour between deformations and charge density and channel size: the coupling between deformations and R_0 and σ_0 vanishes for weakly charged nanochannels.

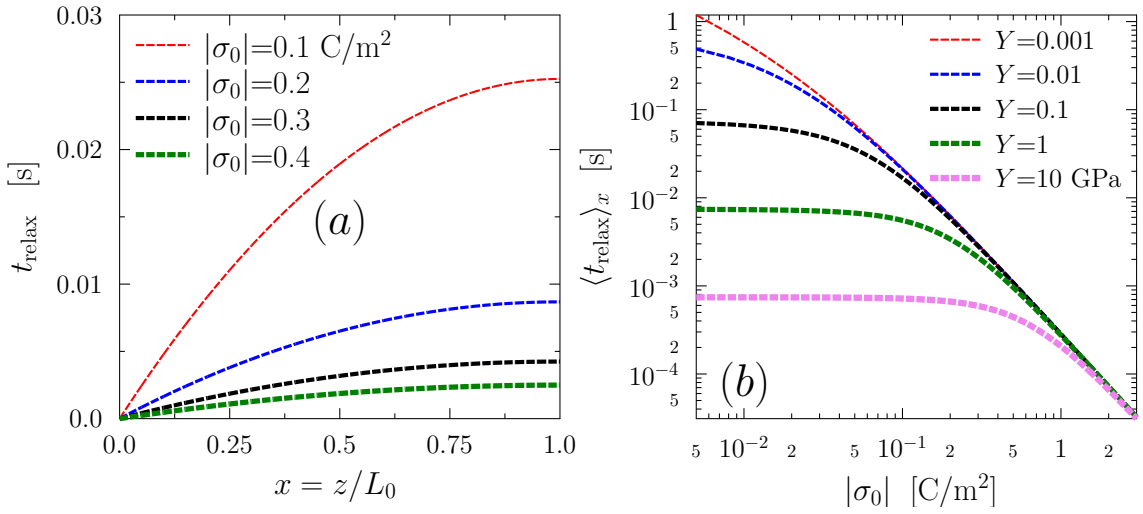

Figure 5.3: (a) Variation of the relaxation time of the walls with the position along the channel. (b) Variation of the averaged relaxation time with the charge density at different elasticity constants. Among the fixed parameters are: $L_0 = 50$ μm, $\Delta V_0 = 0.1$ V, $R_0 = 2$ nm, $Y = 0.1$ GPa, and $\alpha = 0.5$.

One critical time scale is the time it takes for the channel walls to relax to equilibrium after the inlet is perturbed. This dimensionless relaxation time can be estimated by the mean value theorem [156],

$$\tau_{\text{relax}}(x) = \int_0^\infty \frac{\Delta\tilde{a}_\infty(x) - \Delta\tilde{a}(x,\tau)}{\Delta\tilde{a}_\infty(x) - \Delta\tilde{a}_0(x)} d\tau \ , \tag{5.12}$$

where $\Delta\tilde{a}_0(x)$ is the initial deformation profile and $\Delta\tilde{a}_\infty(x) = \lim_{\tau\to\infty} \Delta\tilde{a}(x,\tau)$ is the steady-state profile.

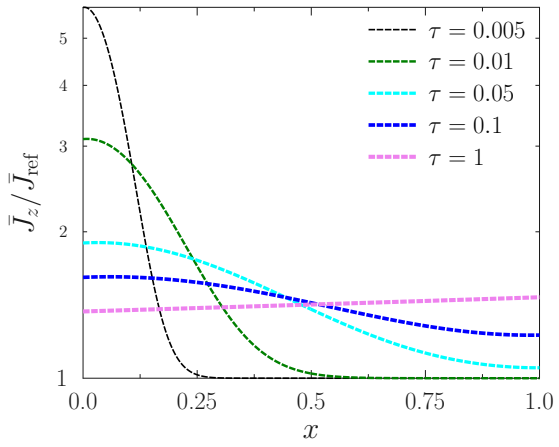

Figure 5.4: Profiles of total proton flux along the nanochannel at different times. The reference case corresponds to $\bar{J}_z/\bar{J}_{\text{ref}} = 1$. Reference parameters are: $L_0 = 50$ μm, $\Delta V_{\text{ref}} = 0.1$ V, $R_{\text{ref}} = 2$ nm, $Y_{\text{ref}} = 0.1$ GPa, $\sigma_{\text{ref}} = -0.5$ C/m^2, $\Delta\tilde{p}_i = 0.05$ and $\alpha_{\text{ref}} = 0.5$.

Equation (5.9) applies in the linear regime and we find

$$\tau_{\text{relax}}(x) = \frac{2\pi \sinh(\lambda)}{\sinh[\lambda(1-x)]} \sum_{n=1}^{\infty} \frac{n \sin(n\pi x)}{(\lambda^2 + n^2\pi^2)^2 \mathcal{D}_0}, \tag{5.13}$$

which is independent of the initial inlet deformation $\Delta\tilde{a}_i$. We multiply Equation (5.13) by $t_0 = 8\nu L_0^2/|\sigma_0|R_0\Delta V_0$ to obtain the physical relaxation time t_{relax} as a function of position along the channel. The results are shown in Figure 5.3, for different surface charge densities. The surface charges drive the overall deformation. The average relaxation time over the channel length was calculated according to $\langle t_{\text{relax}} \rangle_x = \int_0^1 t_{\text{relax}} dx$, and the results are shown in Figure 5.3(b) for different elasticity constants. We notice that both σ_0 and Y enhance the axial speed of the deformation. However, for strongly charged channels the elasticity has no influence on the relaxation time owing to the weak coupling discussed before.

5.3 Deformation-flux coupling

Next, we explore the proton flux within the channel given by $\tilde{J}_z = \tilde{R}^2\tilde{j}_z$, where $\tilde{j}_z$ is determined in Equation (4.96e). To gain deeper insight into the underlying proton transport dynamics, we consider the dimensionless flux normalized by the reference flux $\tilde{J}_{\text{ref}}$ corresponding to the initial uniform flux before the pressure perturbation is applied at the inlet. In dimensionless form, this reference flux can be shown to be

$$\tilde{J}_{\text{ref}} = 4(1-\xi_u(1))^2 + 8(1-\xi_E(1)) + 2\mathcal{K}_{\text{migr}} \ , \tag{5.14}$$

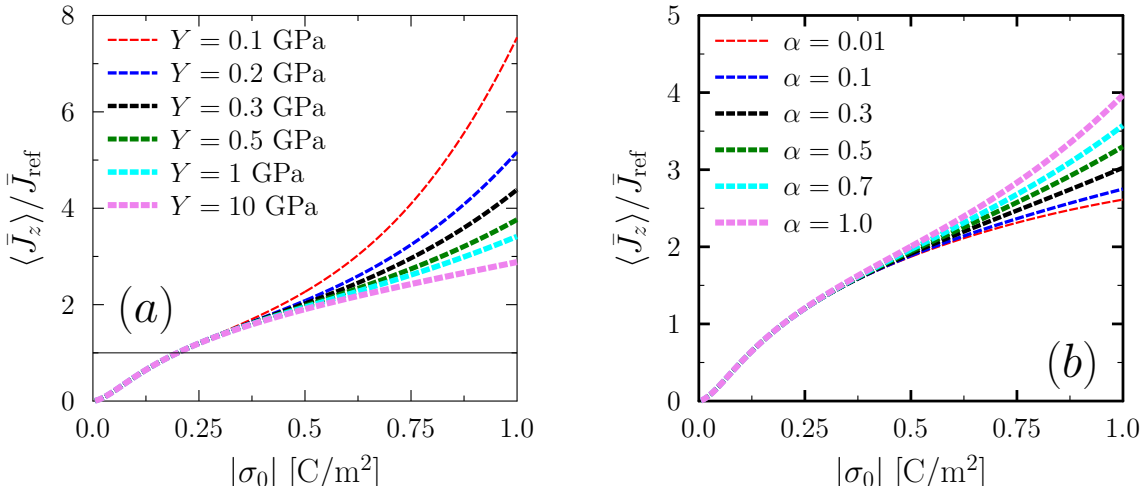

Figure 5.5: Variation of the average proton flux at steady state with surface charge for different (a) elasticity constants Y and (b) channel charge parameters α. Reference parameters are: $L_0 = 50$ μm, $\Delta V_{\rm ref} = 0.1$ V, $R_{\rm ref} = 2$ nm, $Y_{\rm ref} = 0.1$ GPa, $\sigma_{\rm ref} = -0.2$ C/m^2, $\Delta \tilde{p}_i = 0.05$ and $\alpha_{\rm ref} = 0.5$.

and it is kept constant for all calculations. With this normalization, the computed flux can be interpreted relative to the fixed initial transport without channel deformation. Profiles of the normalized total flux at different time scales (expressed in dimensionless units) are shown in Figure 5.4. Close to the steady state, attained at $\tau = 1$, the total flux exceeds that of the initial state (which is $\tilde{J}_z = 1$). The accuracy of the model is reflected in the steady-state flux, which should be constant in light of Equation (4.64). Our results give non-constant flux (violated by a few percent). This could be due to the imposed local electro-neutrality condition. Note again that, for $\alpha = 0.5$, an increasing cross-section gains mobile charges (protons) to maintain local electro-neutrality (while the channel, strictly speaking, shortens). This is reflected by the profile of the proton flux in Figure 5.4 with its non-zero axial divergence ($\partial_x J \neq 0$) until steady state is reached.

Figure 5.5 shows the dependence of the average flux $\langle \tilde{J}_z \rangle$ on surface charge density, for different Y and α, representing the impact of channel elasticity and deformation on the flux response. There are two charging regimes revealed: at low $|\sigma_0|$ (< 0.3 C/m^2), all curves lie on top of each other and the curvature is convex; at high $|\sigma_0|$ (> 0.3 C/m^2), curves fan out and the curvature changes. Hence, proton transport characteristics strongly depend on elasticity and channel geometry for strongly charged channels. From Figure 5.5(a), the channel elasticity inhibits the proton flow at very high $|\sigma_0|$; whereas flow is independent of Y at weakly charged channels. The same effect is observed for the charge parameter α, shown in Figure 5.5(b): the proton flux is independent of α for weakly charged channels,

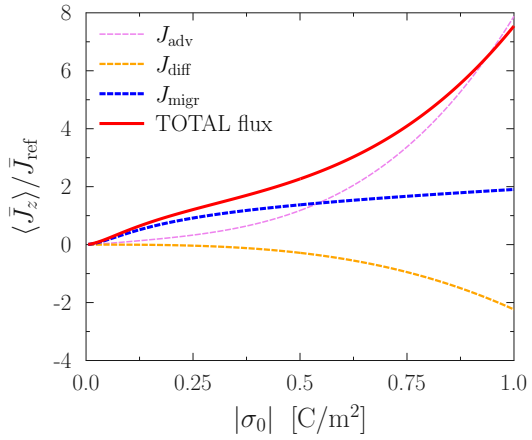

Figure 5.6: Variation of the average convective, diffusive and migration proton fluxes against surface charge density. Reference parameters are: $L_0 = 50$ μm, $\Delta V_{ref} = 0.1$ V, $R_{ref} = 2$ nm, $Y_{ref} = 0.1$ GPa, $\sigma_{ref} = -0.2$ C/m^2, $\Delta\tilde{p}_i = 0.05$ and $\alpha_{ref} = 0.5$.

whereas a small dependence is seen for strongly charged channels; large values of α enhance transport of protons.

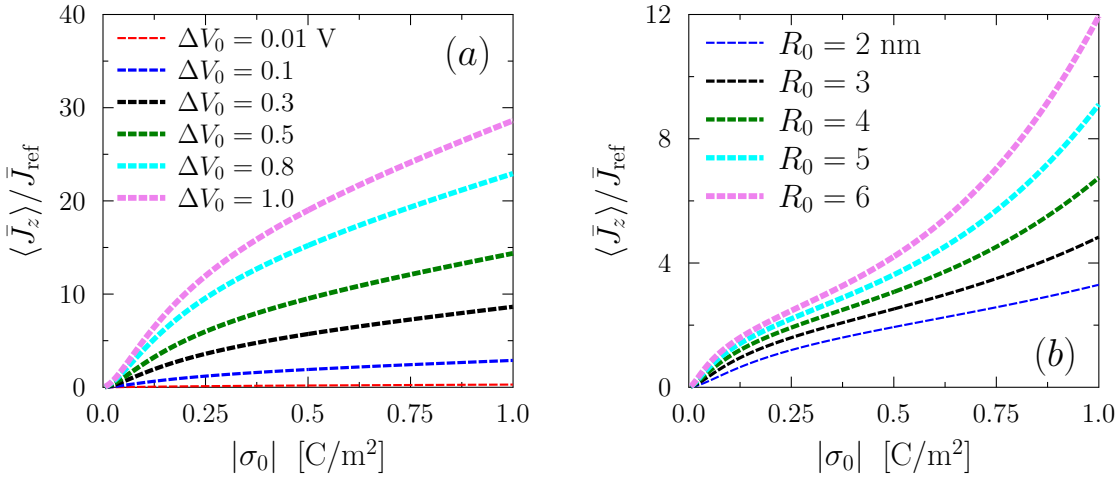

Figure 5.7: Variation of the average proton flux at steady state with surface charge for different (a) voltage drops and (b) channel radii. Reference parameters are: $L_0 = 50$ μm, $\Delta V_{ref} = 0.1$ V, $R_{ref} = 2$ nm, $Y_{ref} = 0.1$ GPa, $\sigma_{ref} = -0.2$ C/m^2, $\Delta\tilde{p}_i = 0.05$ and $\alpha_{ref} = 0.5$.

These results can be explained by examining separate contributions of convection, diffusion, and migration to the total steady-state proton flux within the channel. Results are shown in Figure 5.6. We show results for parameters in which convection, diffusion and migration fluxes of comparative importance. Diffusion opposes the other two fluxes due to

the deformation of the channel. Since, for $\alpha < 1$, an increase in cross-sectional area of the channel results in a smaller total charge of protons in that cross section. Hence, diffusion points in the direction of increasing channel radius. We find a different curve shape for the convective flux and the migration component. At low $|\sigma_0|$, the diffusion and migration fluxes increase with $|\sigma_0|$ faster than the convective flux, and transport is independent of Y and α. This is a consequence of the small osmotic pressure within the channel. This weakens the elastic response so that the overall transport is independent of Y. In the high charge regime, convective flux grows exponentially with $|\sigma_0|$ and migration increases linearly with $|\sigma_0|$. This arises because a majority of protons resides within the EDL, close to the wall, where advection plays a minor role and migration is the dominant transport process. Meanwhile, the flow of water near the center of the channel is enhanced by an increased concentration of protons as $|\sigma_0|$ grows, resulting in a large fluid velocity and an even larger convective flux since it is the product of proton concentration and fluid velocity. Here, the elasticity response is not only strongly correlated with the elasticity constant, Y, but also with the charge reorganization factor, α, which determines the proton distribution within a cross-section. Both factors have a substantial impact at large charge densities, meaning small ℓ_D, because the electroosmotic pressure at the channel wall is large and the impact on channel deformation significant. In contrast, at low wall-charge densities the dependencies of the flow on these two parameters diminishes since the electroosmotic pressure at the channel wall is now small and it no longer affects the channel shape in significant ways, leaving the flow unchanged.

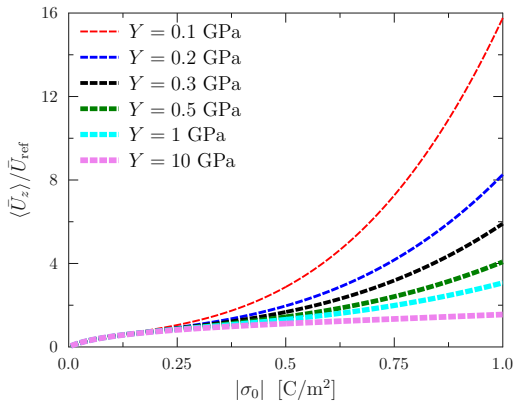

Figure 5.8: Variation of the average water flux at steady state with surface charge for different elasticity constants. Reference parameters are: $L_0 = 50$ μm, $\Delta V_{\text{ref}} = 0.1$ V, $R_{\text{ref}} = 2$ nm, $Y_{\text{ref}} = 0.1$ GPa, $\sigma_{\text{ref}} = -0.2$ C/m^2, $\Delta\tilde{p}_i = 0.05$ and $\alpha_{\text{ref}} = 0.5$.

Figure 5.7 shows the average steady-state flux as a function of surface charge density, for different ΔV_0 and R_0. We see that the channel behaves essentially like a simple linear proton resistor, where flow is proportional to the applied voltage difference. The conductance is a

nonlinear function of $|\sigma_0|$, with the conductance slowing down at very high $|\sigma_0|$, which is an effect of electrostatic correlations, i.e., stronger pinning of protons to walls and, hence, gradual immobilization of protons (reduced mobility) at higher $|\sigma_0|$. Finally, Figure 5.8 shows the steady-state water flux ($\bar{U}_z = R^2\bar{u}_z$, normalized by $\bar{U}_{\mathrm{ref}} = |\sigma_{\mathrm{ref}}|R_{\mathrm{ref}}^3\Delta V_{\mathrm{ref}}/8\nu L_0$) against $|\sigma_0|$ for different values of Y. We observe the same behaviour found in Figure 5.5(a) in terms of the two charging regimes: water flux is independent of Y only at low $|\sigma_0|$ (< 0.25 C/m^2).

5.4 Onsager transport coefficients

The axial fluid velocity, proton flux density, and fluid pressure can be reformulated (in dimensionless form) as

$$\tilde{u}_z = -\tilde{R}^2\left(\frac{\partial\tilde{p}}{\partial x} - \tilde{c}\tilde{E}_z[1-\xi_u]\right)\,, \tag{5.15}$$

$$\tilde{j}_z = \tilde{c}\tilde{u}_z[1-\xi_u(\tilde{R})] - \mathcal{K}_{\mathrm{diff}}\left(\frac{\partial\tilde{c}}{\partial x} - 2\kappa\tilde{R}\tilde{c}^2\frac{\partial\tilde{R}}{\partial x}\right) + \left(\mathcal{K}_{\mathrm{migr}} + 2(\tilde{R}\tilde{c})^2(1-\xi_E)\right)\tilde{E}_z\,, \tag{5.16}$$

$$\tilde{p} = \mathcal{K}_Y\left(\frac{\tilde{R}-1}{\tilde{R}}\right) - \mathcal{K}_{\mathrm{osm}}\tilde{c}(1+\kappa\tilde{R}^2\tilde{c})\,. \tag{5.17}$$

In the linear response regime, the Onsager coefficient matrix $[\boldsymbol{\mu}]$ relates the volumetric water flux $Q = R^2\bar{u}_z$ and the axial proton current $I = qR^2\bar{j}_z$ to the pressure gradient $\nabla\bar{p} = \partial_z\bar{p}$ and the axial electric field $\bar{E}_z$ via

$$\begin{pmatrix} Q \\ \\ I \end{pmatrix} = \begin{pmatrix} \mu_{\mathrm{hyd}} & \mu_{\mathrm{osm}} \\ \\ \mu_{\mathrm{str}} & \mu_{\mathrm{ele}} \end{pmatrix}\begin{pmatrix} -\nabla\bar{p} \\ \\ \bar{E}_z \end{pmatrix}\,. \tag{5.18}$$

The μ_{ij} denote Onsager phenomenological transport coefficients: μ_{hyd} characterizes the hydraulic conductance (and permeability) in accordance with Darcy's law, $\tilde{\mu}_{\mathrm{ele}}$ the electric conductance in accordance with Ohm's law, μ_{osm} the electroosmotic effect, and μ_{str} the streaming potential effect.

We assume that in the system under consideration the fixed charges located on the walls are balanced by a proton concentration $\bar{c}$ inside the channel and in each cross-section so that global and local electroneutrality are both preserved. This condition is met for long-aspect-ratio channels, for which i) the rate of change of the electric field in the axial direction is much slower than that in the radial direction, and ii) the radius varies gradually along the channel. From Equation (4.90), this condition yields

$$\tilde{c} = \frac{1}{\tilde{R}^{1+\alpha}}\,. \tag{5.19}$$

Essentially, these assumptions eliminate any free choice in concentration gradients, leaving only two driving forces (due to gradients in pressure and electric potential) for two fluxes, those of water and ions[1]. This consistent description would need to be extended to three driving forces, including concentration gradients, and three fluxes, including co-ions, if local electroneutrality is not guaranteed [145]. Using Equations (5.15), (5.16), (5.17) and (5.19), and setting $\tilde{a} = \tilde{R}^2$, one finds the transport coefficients

$$\mu_{\mathrm{hyd}} = \left(\frac{R_0^4}{8\nu}\right)\tilde{a}^2 \,, \tag{5.20}$$

$$\mu_{\mathrm{ele}} = \frac{(R_0\sigma_0)^2}{2\nu}\left\{\tilde{a}^{(1-\alpha)/2}\Big[\mathcal{K}_{\mathrm{migr}} + 2\tilde{\tilde{a}}^{(1-\alpha)/2}[1-\xi_E(a)]\Big] + \tilde{a}^{1-\alpha}[1-\xi_u(\tilde{a})]^2\right\}, \tag{5.21}$$

$$\mu_{\mathrm{osm}} = \frac{R_0^3\sigma_0}{4\nu}\left\{\tilde{a}^{(3-\alpha)/2}\left[1-\xi_u(\tilde{a})\right]\right\}. \tag{5.22}$$

$$\mu_{\mathrm{str}} = \begin{cases} \mu_{\mathrm{osm}} \,, \quad \text{for a rigid channel } (\mathcal{K}_Y \to \infty) \,, \\ \\ \mu_{\mathrm{osm}} + \dfrac{R_0^3\sigma_0}{4\nu}\left\{\dfrac{\mathcal{K}_{\mathrm{diff}}\left[2\kappa\sqrt{\tilde{a}} + \tilde{a}^{\alpha/2}(1+\alpha)\right]\tilde{a}^{1-\alpha}}{\mathcal{K}_Y + \mathcal{K}_{\mathrm{osm}}\left[2\sqrt{\tilde{a}} + \tilde{a}^{\alpha/2}(1+\alpha)\right]}\right\}, \text{ for a deformed channel.} \end{cases} \tag{5.23}$$

From Equations (5.23), Onsager's reciprocal relation is upheld with $\mu_{\mathrm{osm}} = \mu_{\mathrm{str}}$ when the channel has a uniform radius and is rigid ($\mathcal{K}_Y \to \infty$). However, when the channel is deformable and has non-uniform radius, the symmetry of $[\boldsymbol{\mu}]$ is broken. A channel curvature, or more precisely a gradient in the channel radius, $\partial_z R$, introduces a diffusive proton-driving force. This results in a violation of Onsager's reciprocal relation. Since p is related to R according to Equation (5.17), we do not classify $\partial_z R$ or $\partial_z A$, where A is the cross-sectional area of the channel ($\partial_z A = \partial_z[\pi R^2]$), as a thermodynamic force. After all, they can be expressed in terms of $\partial_z p$ which is a true driving force. Instead, we refer to $\partial_z A$ as a pseudo-force and it is associated with the curvature coefficient,

$$\mu_{\mathrm{curv}} = \frac{\sigma_0^2\Delta V_0}{2\nu}\left\{\frac{\mathcal{K}_{\mathrm{diff}}\left[2(\tilde{a}^{(1-\alpha)/2}\kappa + 1) - (1-\alpha)\right]\tilde{a}^{(1-\alpha)/2}}{2\tilde{a}}\right\}. \tag{5.24}$$

It stems from the reduction of a three-dimensional system to a one-dimensional problem, coupled with local electroneutrality. In contrast, in the original three-dimensional formulation of the problem, Onsager's reciprocal relations are not violated at any point in the fluid.

[1]Here, we assume isothermal conditions so that a temperature gradient ∇T is absent

In the deformed state, the system's linear response can be formulated as

$$\bar{\mathbf{J}} = [\boldsymbol{\mu}]\bar{\mathbf{X}} + \bar{\boldsymbol{\xi}} \,, \tag{5.25}$$

where $\bar{\mathbf{J}} = [Q,\ I]^T$, $\bar{\mathbf{X}} = [-\nabla p,\ E_z]^T$ and $\bar{\boldsymbol{\xi}} = [0,\ \mu_{\text{curv}}\partial_z A]^T$ give the thermodynamic fluxes, thermodynamic forces and the diffusional pseudo-force, respectively.

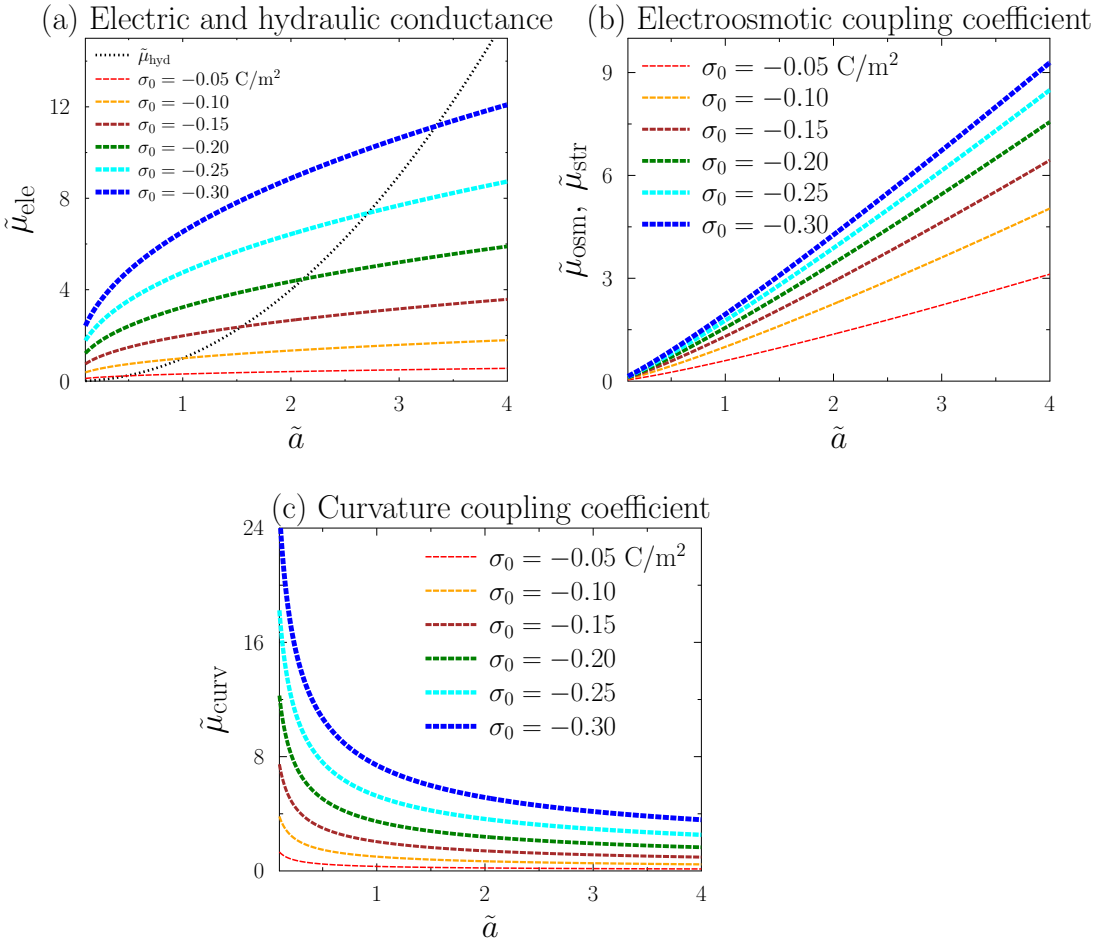

Figure 5.9: Transport coefficients vs. channel cross-sectional area $\tilde{a}$. Coefficients are normalized with reference parameters, i.e., $\tilde{\mu}_{\text{ele}} = \mu_{\text{ele}}/\left(\mu_{\text{ele}}\right)_{\text{ref}}$, etc. The fixed parameters used as reference are: $L_0 = 50$ μm, $D = 7 \times 10^{-6}$ cm^2/s, $\Delta V_0 = 0.1$ V, $R_0 = 2$ nm, $Y = 0.05$ GPa, $T = 300$ K, $h_0 = 1$ nm, $\varepsilon = 45$, $\nu = 3.35 \times 10^{-4}$ Pa s, and $\alpha = 0.5$.

Figure 5.9 shows plots of the transport coefficients as a function of the channel cross-sectional area relative to its equilibrium area (note that $\tilde{a} = A/A_{\text{eq}}$), for different values of σ_0. Coefficients are normalized with reference parameters, i.e., $\tilde{\mu}_{\text{ele}} = \mu_{\text{ele}}/\left(\mu_{\text{ele}}\right)_{\text{ref}}$, etc. Figure 5.9(a) illustrates the relative strength of electric and hydraulic conductance at different values of $\tilde{a}$. The model predicts that electric conductance increases with σ_0 in

a concave fashion. On the other hand, the hydraulic conductance, which is independent of σ_0, increases in a convex manner and eventually dominates electric conductance as the radius grows much larger than the relaxed state. Very large $\tilde{a}$ ramps up the fluid pressure within the channel, owing to the enhanced elastic response of the channel walls. This directly leads to large hydraulic conductance, and hence high pressure-induced water flux. Figure 5.9(b) shows the expected linear increase of electroosmotic and streaming coupling coefficients with $\tilde{a}$. The curvature coefficient that measures the extent to which the system's Onsager symmetry is broken as a result of curvature-induced proton diffusion is plotted in Figure 5.9(c). The symmetry breaking is more pronounced at small $\tilde{a}$ and large σ_0, equivalent to highly charged channels.

5.5 Electrokinetic energy conversion

In this part, we investigate the thermodynamic efficiency of (1) electrokinetic power harvesting devices and (2) electrokinetic pumping devices. Energy conversion is realized in an individual nanochannel by means of streaming currents and electroosmotic flow. The resistance of the reservoirs is neglected in our calculations. In order to calculate the conversion efficiency, transport properties explored in Section 5.4 have to be determined.

The thermodynamic efficiency χ of energy conversion is defined as the ratio of power output, P_{out}, to power consumption, P_{in}:

$$\chi = \begin{cases} \dfrac{I\bar{E}_z}{Q\nabla\bar{p}}\,, & \text{electrical power generation mode.} \\ \\ \dfrac{Q\nabla\bar{p}}{I\bar{E}_z}\,, & \text{pumping mode.} \end{cases} \tag{5.26}$$

Substituting Q and I by the expressions in Equation (5.18), P_{out} and χ for each energy conversion mode in Equation (5.26) are established as functions of the output thermodynamic force only, provided the input thermodynamic forces and all Onsager transport coefficients are known (we assume a linear response). Therefore, the output thermodynamic force and the conversion efficiency under maximization of either the power output P_{out} or the efficiency χ can be obtained separately.

5.5.1 Maximizing power output

We start by working out the output thermodynamic forces ($\bar{E}_{\max}$ for power generation mode and $\nabla\bar{p}_{\max}$ for pumping mode) and efficiency $\chi_{\max}$ at maximum power output ($I\bar{E}_z$ for power generation mode and $Q\nabla\bar{p}$ for pumping mode). This is done by differentiating P_{out} with respect to the corresponding output thermodynamic force. For the two conversion modes, one obtains the maximum output force for each case,

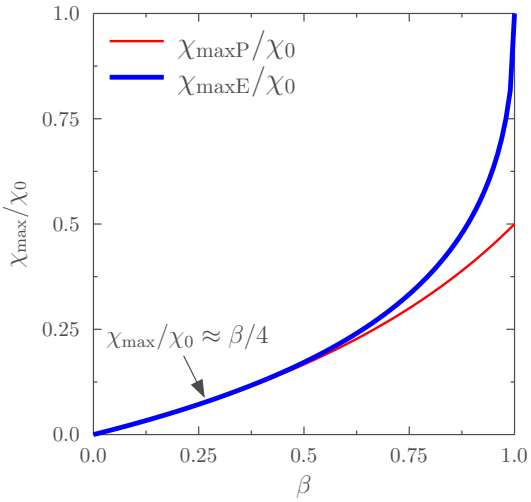

Figure 5.10: Dependence of electrokinetic conversion efficiency on the cross-correlation coefficient at maximum output power and maximum efficiency.

$$\bar{E}_{\max} = \frac{\mu_{\mathrm{str}}}{2\mu_{\mathrm{ele}}} \nabla \bar{p} \,, \tag{5.27}$$

$$\nabla \bar{p}_{\max} = \frac{\mu_{\mathrm{osm}}}{2\mu_{\mathrm{hyd}}} \bar{E}_z \,. \tag{5.28}$$

The efficiency at maximum power output, which is the same for both power generation and pumping modes, can be shown to be

$$\chi_{\mathrm{maxP}} = \frac{\chi_0}{2} \, \frac{\beta}{2-\beta} \,, \tag{5.29}$$

where $\beta = (\mu_{\mathrm{osm}}/\mu_{\mathrm{ele}}) \times (\mu_{\mathrm{str}}/\mu_{\mathrm{hyd}})$ and $\chi_0 = \mu_{\mathrm{str}}/\mu_{\mathrm{osm}}$. The dimensionless parameter β is a cross-correlation coefficient, usually called the 'figure of merit' [157, 158], and can be described as the product of the streaming current effect and the electro-osmotic effect. The coefficient χ_0 measures the symmetry of the Onsager coefficient matrix $[\boldsymbol{\mu}]$, and it assumes a value of 1 for rigid channels.

5.5.2 Maximizing efficiency

Using a similar approach, we determine the output forces that maximize the conversion efficiency. This is done by differentiating χ with respect to the corresponding output thermodynamic force. The resulting optimum output forces obtained for pumping and power generation modes, respectively, are

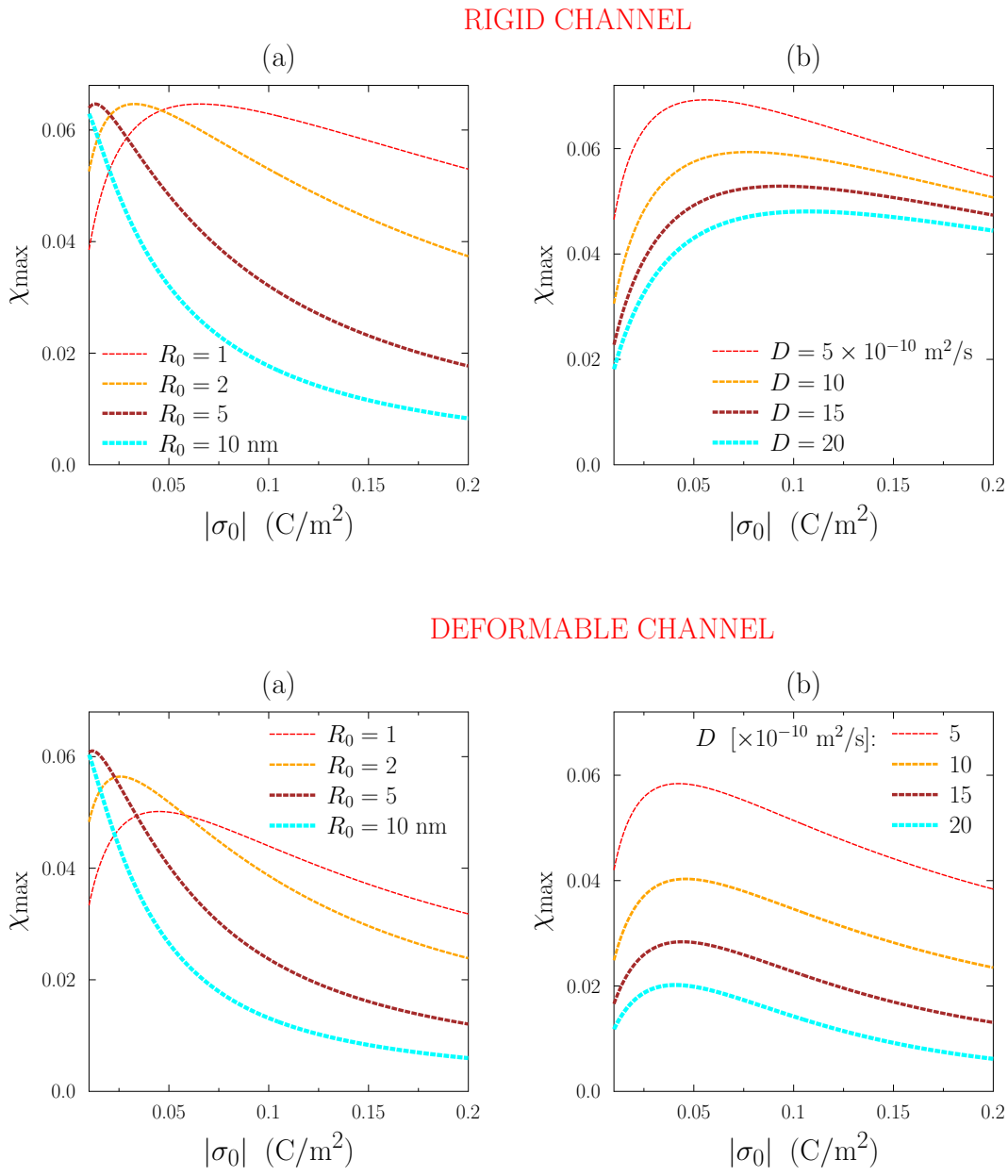

Figure 5.11: Electrokinetic energy conversion efficiency at maximum efficiency against surface charge density at different (a) channel radii and (b) cation diffusion constants. The first row corresponds to the case of a rigid channel and the second row is for a deformable channel. Results are obtained via Equation (5.32). Among the fixed parameters used as references are: $D = 7 \times 10^{-6}$ cm^2/s, $R_0 = R = 2$ nm, $Y = 0.05$ GPa, $T = 300$ K, $h_0 = 1$ nm, $\varepsilon = 45$, $\nu = 3.35 \times 10^{-4}$ Pa s, and $\alpha = 0.5$.

$$\bar{E}_{\max} = \frac{\mu_{\text{hyd}}}{\mu_{\text{osm}}} \left(1 - \sqrt{1-\beta}\right) \nabla \bar{p}\,, \tag{5.30}$$

$$\nabla \bar{p}_{\max} = \frac{\mu_{\text{ele}}}{\mu_{\text{str}}} \left(1 - \sqrt{1-\beta}\right) \bar{E}_z \ . \tag{5.31}$$

The corresponding efficiency, which is also the same for both power generation and pumping modes, can be shown to be

$$\chi_{\text{maxE}} = \chi_0 \left(\frac{1 - \sqrt{1-\beta}}{1 + \sqrt{1-\beta}}\right) \ , \tag{5.32}$$

and all equations are valid under the constraint $0 \leq \beta < 1$ to maintain non-negative intrinsic entropy generation in electrokinetic flows. Variation of $\chi_{\text{maxP}}/\chi_0$ and $\chi_{\text{maxE}}/\chi_0$ with β is shown in Figure 5.10. In the low β limit (i.e., $\beta \to 0$), both $\chi_{\text{maxP}}/\chi_0$ and $\chi_{\text{maxE}}/\chi_0$ vary linearly with β ($\chi_{\max}/\chi_0 \approx \beta/4$). In the high β limit (i.e., $\beta \to 1$), $\chi_{\text{maxP}}/\chi_0$ and $\chi_{\text{maxE}}/\chi_0$ are monotonically increasing hyperlinear functions of β, with χ_{maxP} assuming half the value of χ_{maxE}.

Plots of maximum efficiency determined via Equation (5.32) against σ_0, which are almost the same as those obtained from Equation (5.29) for the case of $\beta \ll 1$ (i.e., $\chi_{\max} = \chi_{\text{maxP}} = \chi_{\text{maxE}}$), are shown in Figure 5.11. For a typical set of parameters, $\chi_{\max}$ is on the order of 5%, and β is on the order of 0.2. The behaviour is similar to what has been reported from experiments [159–163]: $\chi_{\max}$ increases with σ_0 for sufficiently small σ_0 but reaches a maximum at an absolute value of around 0.05 C/m^2; a further increase in σ_0 results in a decrease in $\chi_{\max}$. At very large σ_0, corresponding to regions past the peak, the coupled fluid-ion transport is reduced since a large fraction of protons occupy the EDL where fluid flow is significantly hampered. This affects both electroosmotic flow and the streaming current.

Furthermore, we explored the dependence of $\chi_{\max}$ on R_0 and D for the case of a rigid channel, and then for a deformable channel using results from Equation (5.32). For a rigid channel, increasing R_0 only shifts the peak of $\chi_{\max}$ towards smaller σ_0; whereas for a deformable channel, this effect further changes the value of $\chi_{\max}$ at the peak. For large σ_0, $\chi_{\max}$ achieves larger values when R_0 is small. The opposite effect is observed for small σ_0. Conditions for which a smaller fraction of protons reside in the EDL yield a higher $\chi_{\max}$. In other words, $\chi_{\max}$ is optimized when the double layers from opposite walls of the channel overlap. From Figure 5.11, we see that higher proton diffusivity tends to lower the efficiency. This effect is even more significant for the case of a deformable channel where the channel curvature induces a diffusional force that opposes the migration of protons, thereby reducing the overall transport.

Finally, the dependence of $\chi_{\max}$ on elastic and geometric properties of the channel is shown in Figure 5.12. In each plot, the black solid curve represents a rigid channel. $\chi_{\max}$ increases with the elastic coefficient, Y. Optimal $\chi_{\max}$ is realized when the channel is rigid. Hence, the model predicts that softness of the channel walls is not beneficial for energy harvesting. For soft channels, energy is lost due to elastic deformations taking place along

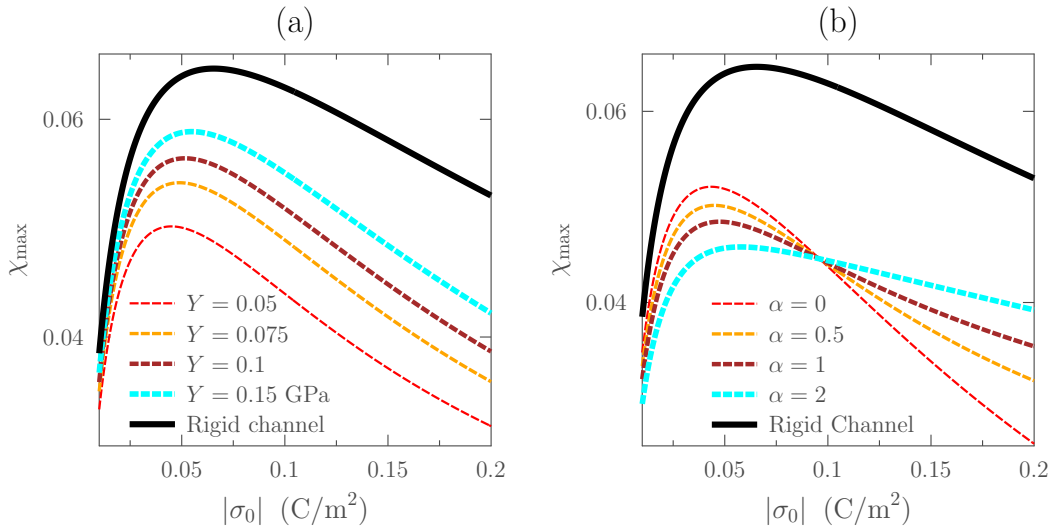

Figure 5.12: Electrokinetic energy conversion efficiency at maximum efficiency against surface charge density at different (a) elasticity constants and (b) values of surface geometry parameter α. Results are obtained via Equation (5.32). Among the fixed parameters used as references are: $D = 7 \times 10^{-6}$ cm^2/s, $R_0 = R = 2$ nm, $Y = 0.05$ GPa, $T = 300$ K, $h_0 = 1$ nm, $\varepsilon = 45$, $\nu = 3.35 \times 10^{-4}$ Pa s, and $\alpha = 0.5$.

the walls, thereby changing the flow dynamics and reducing $\chi_{\max}$ as a consequence. Figure 5.12(b) shows that $\chi_{\max}$ is also influenced by the channel geometry parameter α. All curves converge at one specific value of σ_0, which is ~ 0.1 C/m^2 for the case shown in Figure 5.12(b). Below this value, smaller values of α optimize $\chi_{\max}$. The opposite is seen for values of σ_0 above this convergence point. The convergence can be well understood from a mathematical point of view. Dependence on α, for the case of $\tilde{a} = 1$ and a deformable channel, is only seen through μ_{osm} given in Equation (5.23). This dependence vanishes when $2\kappa = \mathcal{K}_Y/\mathcal{K}_{\text{osm}} + 2$, and this gives the value of σ_0 at which all curves converge.

One universal feature of the results reported here is that the efficiency gets amplified and peaks over a narrow regime at low σ_0. The peak region is not much affected by the channel's elasticity. Figure 5.13 compares results with data obtained from experiments and MD simulations. In Figure 5.13(a), we compare with experimental results reported by Xie *et al.* [160], where the efficicieny χ is plotted against the sectionally-averaged counterion concentration ($\bar{c} = 2|\sigma_0|/qR_0$). Xi *et al.* studied single track-etched nanochannels by measuring the streaming currents and conductance. Data reported is from two of their samples, corresponding to nanochannels with inner radii 32 nm and 31 nm. We use $R_0 = 32$ nm and $D = 20 \times 10^{-6}$ cm^2/s to calculate $\chi_{\max}$ from the 1-D model and compare with the data. The peak region obtained in our 1-D model matches that from the experimental data. However, the model gives a larger decay of χ towards lower concentrations. This could arise from the failure of the continuum model at low ion concentrations. In Figure 5.13(b),

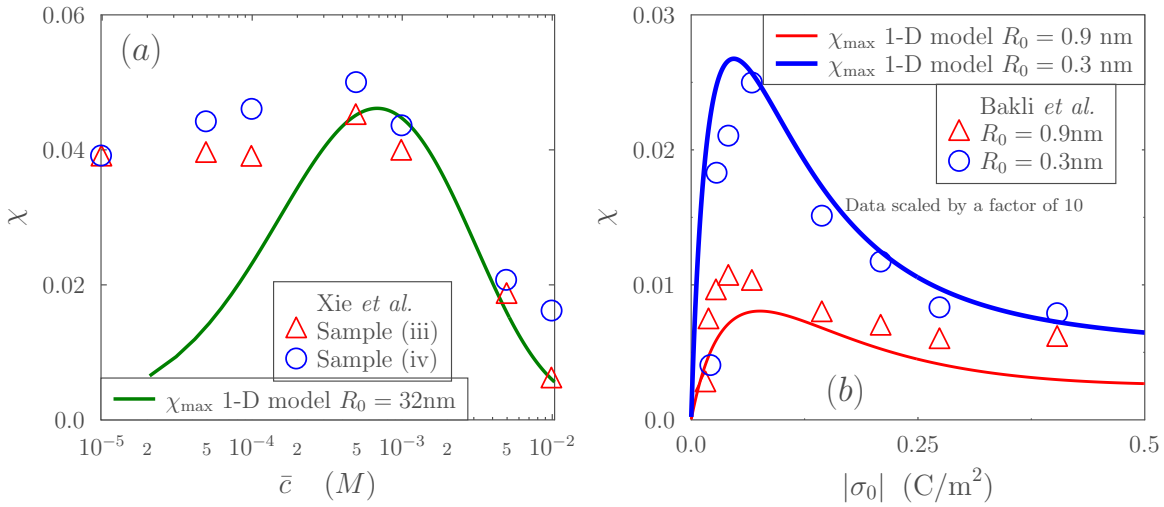

Figure 5.13: Comparison of the 1-D model with (a) experimental results from Xie *et al.* [160] and (b) MD simulations results from Bakli *et al.* [163]. For experimental results shown in (a), single track-etched nanochannels with outer radius of 120nm. Two samples are reported, with inner channel radii of 32 nm (sample (iii)) and 31 nm (sample (iv)), and values of χ were scaled by a factor of 1/10 to make qualitative comparison.. For MD simulations results shown in (b), channel radii of 0.3 nm and 0.9 nm were used $D = 20 \times 10^{-6}$ cm^2/s was used for the model results in (a), and $D = 15 \times 10^{-6}$ cm^2/s was used in (b). Among the fixed parameters used are $Y = 0.5$ GPa, $T = 300$ K, $h_0 = 1$ nm, $\varepsilon = 45$, $\nu = 3.35 \times 10^{-4}$ Pa s, and $\alpha = 0.5$.

we compare our 1-D model results with MD simulation results reported by Bakli and Chakraborty [163]. The numerical values they obtained for the efficiency are much higher than obtained in our model. Hence, we scaled their efficiency values by a factor of 1/10 to match our results. With this modification, we obtain the same qualitative behaviour as theirs. Data is from channels of radii 0.3 nm and 0.9 nm, and $D = 15 \times 10^{-6}$ cm^2/s was used for the model results. Our model gives an efficiency peak at a region that matches that from their data. Note that a deformable nanochannel ($Y = 0.5$ GPa and $\alpha = 0.5$) was assumed to obtain the 1-D model results in Figure 5.13.

5.6 Summary

In this chapter, we used the formalism from Chapter 4 to investigate the coupling between deformations of the channel walls and the transport of water and protons within the channel. Relaxation time scales of wall deformation and transport properties of the channel upon application of a pressure perturbation at the channel inlet were investigated. Results reveal a strong coupling of the wall deformations and transport within the channel with the

channel elasticity and surface charge density. In the limit of high charging, deformation and proton flux exhibit a strong dependence on surface charge density and channel geometry. For strongly charged channels, the dynamics are inhibited by the channel's elasticity. These results unravel the role played by the elasticity of a nanoporous host medium in controlling electrokinetic transport processes, more significant for strongly charged nanochannels. The Debye parameter ℓ_D is the main control parameter that steers transition between transport regimes. Closed-form formulae for Onsager transport coefficients were derived first for the case of rigid and subsequently for deformable channels. For the general case of co- and counter-ions, the coefficients are only attainable numerically. For the limiting case of low co-ion concentration inside the channel, closed-form solutions may still be attainable via a perturbative analysis of the counter-ions-only case. Results reveal that the Onsager reciprocity principle holds for rigid channels but is not fulfilled when the channel is deformed. As demonstrated in this article, the symmetry violation is caused by a 'fictitious' contribution to diffusion introduced by the reduction of the model to 1D. Furthermore, this work explored the energy conversion mechanism of electrokinetic systems. The maximum efficiency was calculated as a function of the phenomenological transport coefficients. We found that the efficiency of an electrokinetic system is maximized when there is a strong double-layer overlap within the channel. Moreover, the proposed model predicts that the softness of channel walls diminishes the efficiency compared to their rigid counterparts.

Chapter 6

Cylindrical and Finite Nanochannel Under Closed Confinement

While the previous chapters focused on transport, this chapter explores the formation and structure of equilibrium electric double layers (EDLs) within the channel. In our study, the EDLs under consideration are established between the electrolyte solution filling the channel and flat electrode surfaces at the channel ends. A large body of research activity has been aimed at understanding the formation of EDLs in an electrolyte where interaction forces and potentials exist between charged surfaces. The structure and properties of the electric double layer (EDL) determines the electrostatic and electrokinetic properties of electrified interfaces, playing an important role in diverse technological and bio-physiochemical applications involving, among others, capacitive energy storage and conversion [164, 165], stabilization of colloidal systems [166–169], biomolecular recovery in oil/water interfaces [170], control of ion transport through charged channels of biological membranes [171–173], plasma treatment of surfaces [174], scanning electrometer for electric double-layer operation [175], and dielectrophoresis [176, 177].

When studying electrokinetic phenomena near interfaces, it is crucial to include steric (finite size) effects since ion sizes dictate the structure of the EDL. From a computational point of view, the Bikerman model remains popular due to its ease of implementation and qualitatively good agreement with experiments and molecular dynamics simulations [178, 179]. Owing to recent numerical studies [180–186] grounded in Bikerman modelling, many interesting phenomena such as capacitance-voltage curves, confinement effects, lattice saturation, improvement of cross-stream diffusion, over-screening effects and layering of ions near electrode surfaces are now reasonably well understood.

A majority of these studies consider systems under open boundaries, in which the electrolyte is presumed to be in thermodynamic equilibrium with an electrolyte reservoir, the so-called 'semi-grand canonical ensemble'. The most studied system is an electrolyte solu-

tion in contact with a planar electrode surface or between two parallel-plates with a voltage applied between them. The apparent scarcity of studies concerning closed systems could be due to two main reasons: (1) The difficulty of numerically solving the system of integro-differential-equations, complicated by the inclusion of conservation constraints. (2) In practice, electrokinetic devices are usually connected to reservoirs. However, closed confinement of electrolytes between charged walls can present additional effects potentially resulting in rich phenomena that are particularly important in nanoscale devices. Particularly, electric double-layer capacitors for electrical energy storage and electroactive polymer actuators for artificial muscles are closed systems whose performance is dictated by the underlying EDL structure.

This chapter presents a physical-mathematical treatment and numerical simulations of electric double layer charging in a closed, finite and cylindrical nanochannel of circular cross section, embedded in a polymeric host with charged walls and sealed at both ends by metal electrodes under external voltage bias. This means we are dealing with a closed system with a fixed number of ions and water molecules. Modified Poisson-Nernst-Planck equations are used to account for finite ion sizes, subject to the electroneutrality condition. A binary electrolyte solution is enclosed inside the channel to maintain electro-neutrality. While we focus on rigid nanochannels in this chapter, an extension to flexible channels [187, 188] will be considered in Chapter 7. We study the EDL formation and relaxation near the electrodes. Differential capacitance data is presented and analysed, with a focus on its dependence on the channel surface charge density, electrolyte concentration, ion size and channel size. The numerical model is modified to also account for asymmetry in the charge valencies and ion sizes of each individual ionic species, as well as a non-uniform distribution of charges along the channel surface.

This chapter is organised as follows. The physical-mathematical methodology will be presented in Section 6.1, including a brief outline of the governing equations, a presentation of the electroneutrality condition imposed onto the system for self-consistency, and the description of the numerical method employed. Section 6.2 presents numerical results. Here, the time evolution of the formation and relaxation of the double layers is explored. Moreover, equilibrium ion distributions and differential capacitance curves are investigated as functions of the channel surface charge density, electrolyte concentration, ion sizes and channel size. Finally, Section 6.3 concludes this chapter with a summary of the results.

6.1 Methodology

6.1.1 Schematics and assumptions

In what follows, we are concerned with a binary symmetric $z : z$ electrolyte solution. The case of asymmetric ion charges will be considered in Section 6.2.4. The electrolyte is confined

inside a charged cylindrical polymeric channel of radius R and length L with electrodes attached at both ends; see Figure 6.1 for a schematic illustration. The walls of the channel carry charged head groups which we will model as a uniform distribution with surface charge density σ_p. The problem is two-dimensional, with coordinates in radial (r) and axial (z) directions. Cylindrical coordinates are adopted, with the origin fixed at the center of the inner surface of the left electrode. An externally applied potential bias ΔV is introduced between the electrodes, with the right electrode sitting at a higher potential and located at $z = L$.

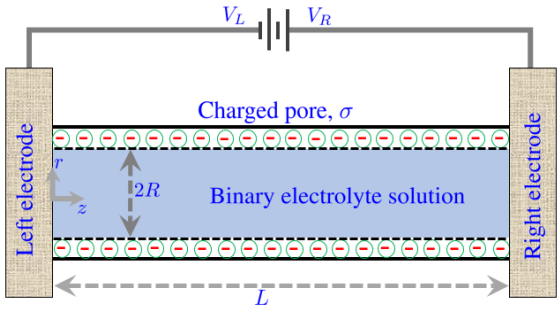

Figure 6.1: Schematic illustration of the examined configuration: electrolyte in a closed, cylindrical channel of circular section and channel wall surface charges of density σ_p.

In the basic simplified variant, both cations and anions are assumed to be equi-sized hard spheres of constant diameter a. Steric ion-ion interactions, included in the free energy, are taken into account within a continuous dielectric medium approach with constant permittivity, while advection of the electrolyte is assumed negligible – a reasonable assumption for pores with small radius (1-2 nm). Isothermal conditions are assumed to prevail in the system. Ions can accumulate at the electrode surfaces but without ion insertion into the electrode. We denote the net accumulated ion charges on the left and right electrode as Q_L and Q_R, respectively.

From a physical point of view, the model system presented above mimics closely confined and nearly cylindrical energy storage (e.g., capacitors, batteries) and generation devices, or electroactuation devices [104–106]. We would like to emphasize that the highly confined ionic system studied in this work is expected to exhibit properties that are not accounted for in the Bikerman model. Because of this limitation, model results are expected to deviate from experimental findings. However, the goal here is to explore essential trends revealing the impact of core parameters on the double-layer capacitance. Other effects such as overscreening and the transition to crowding [189] are expected to play a role in regimes with high ion concentration. In addition, ion-wall interactions [190,191], correlations between water molecules, and image effects are expected to play a role. Such effects can be accounted for by employing molecular dynamics simulations of the system, which will be a subject of future work.

6.1.2 Governing equations

Following the Bikerman model, the free energy functional of the ionic system is modified, based on a mean-field approximation, by adding an ideal-gas-like solvent entropy term to account for over-crowding of ions and solvent molecules:

$$\begin{aligned} F = \int d^3\boldsymbol{r} \Big\{ & -\frac{\varepsilon\varepsilon_0}{2}|\nabla\psi|^2 + zq\psi\,(c_+ - c_-) \\ & + k_BT\left[c_+\log\left(c_+a^3\right) + c_-\log\left(c_-a^3\right)\right] \\ & + k_BT\left[\frac{1-a^3(c_+ + c_-)}{a^3}\log\left[1-a^3(c_+ + c_-)]\right)\right]\Big\}, \end{aligned} \tag{6.1}$$

where ψ is the electrostatic potential; $c_\pm$ denotes the local concentration of positive and negative ionic species; k_B is the Boltzmann constant; ε_0 the permittivity of free space; ε the dielectric constant of the electrolyte; T the absolute temperature. The first two terms of the integral in Equation (6.1) can be interpreted as the total electrostatic free energy. The first term is the dielectric self-energy of the electric field $\boldsymbol{E} = -\nabla\psi$, and the second term gives the electrostatic energy of mobile ions. The remaining two terms represent entropic contributions of ions and solvent molecules, respectively. These terms impose a cut-off on the value of ionic concentration, $c_\pm^{\max} = 2^{1/2}/a^3$, which is the maximum density of close-packed (face-centered cubic or hexagonal close-packed) spheres of diameter a.

Demanding the variation of F with respect to $c_\pm$ to be equal to the electrochemical potential $\mu_\pm$ of ionic species and the variation of F with respect to ψ to be zero, one obtains

$$\mu_\pm = \pm zq\psi + k_BT\log\left[\frac{c_\pm a^3}{1-a^3(c_+ + c_-)}\right], \tag{6.2}$$

and the Poisson equation

$$-\nabla\cdot(\varepsilon\varepsilon_0\nabla\psi) = zq(c_+ - c_-)\,, \tag{6.3}$$

respectively. Assuming that the diffusivities D for each ionic species are the same and constant, the modified Nernst-Planck equations for ionic fluxes are

$$\begin{aligned} \boldsymbol{J}_\pm &= -\frac{D}{k_BT}\,c_\pm\nabla\mu_\pm \\ &= -D\nabla c_\pm \mp \frac{Dzq}{k_BT}\,c_\pm\nabla\psi + a^3D\,\frac{c_\pm\nabla(c_+ + c_-)}{1-a^3(c_+ + c_-)}\,, \end{aligned} \tag{6.4}$$

and the conservation equations for the ionic species take the form

$$\frac{\partial c_\pm}{\partial t} + \nabla\cdot\boldsymbol{J}_\pm = 0\,. \tag{6.5}$$

At equilibrium, no ionic and fluid flows are present, i.e., $\boldsymbol{J}_{\pm} = 0$. Using Equation (6.4) and integrating $\boldsymbol{J}_{\pm} = 0$ from some reference concentration c_0 gives the ionic concentrations (number density) in terms of the electric potential

$$c_{\pm} = \frac{c_0 \exp\left(\frac{\mp zq\psi}{k_B T}\right)}{1 + 2(z+1)c_0 a^3 \sinh^2\left(\frac{zq\psi}{2k_B T}\right)} \,. \tag{6.6}$$

In this context, $c_0 = c_{\pm}(\psi = 0)$ is the reference concentration of both cations and anions at which the electric potential is set to be zero. Note that the region where $c_{\pm} = c_0$ does not need to be defined within the system. Substituting Equation (6.6) into Equation (6.3) gives the modified PB (mPB) equation for the local steady-state electric potential in the electrolyte solution,

$$\nabla \cdot (\varepsilon\varepsilon_0 \nabla\psi) \;=\; \frac{2zqc_0 \sinh\left(\frac{zq\psi}{k_B T}\right)}{1 + 2(z+1)c_0 a^3 \sinh^2\left(\frac{zq\psi}{2k_B T}\right)} \,. \tag{6.7}$$

6.1.3 Boundary conditions and electroneutrality

Having established the equations that model the dynamics and steady-state equilibrium for electrochemical properties of the system, we turn to the task of identifying all boundary conditions. All equations in Sec. 6.1.2 are valid in the cylinder's inner volumetric domain Ω ($r \in [0, R], \theta \in [0, 2\pi], z \in [0, L]$), which is bounded by the cylindrical channel ∂_p ($r = R, \theta \in [0, 2\pi], z \in [0, L]$), left electrode ∂_L ($r \in [0, R], \theta \in [0, 2\pi], z = 0$) and right electrode ∂_R ($r \in [0, R], \theta \in [0, 2\pi], z = L$).

The boundary condition at the channel's inner walls are determined by the surface charge density and a vanishing electric field outside the channel,

$$(\varepsilon\varepsilon_0 \nabla\psi \cdot \hat{\boldsymbol{n}})\Big|_{\partial_p} = \sigma_p \,. \tag{6.8}$$

Here, $\hat{\boldsymbol{n}}$ is a unit vector normal to the respective boundaries. At the channel surface, we do not consider any chemical reaction involving ions or functional groups.

As a side note, the smaller the ratio is between the dielectric constants of channel walls and electrolyte, the lesser is the degree to which the field will extend into the surrounding wall region. Strictly speaking, Equation (6.8) is only valid in the limit of that ratio tending to zero but it is an on-going debate as to how to assess the violation of Equation (6.8) for small but non-zero ratios [150].

A central aspect of the model is the boundary condition for the electrostatic potential bias between the metal electrodes, which is introduced externally. It can be expressed by

$$\psi\Big|_{\partial_R} = V_R \quad \text{and} \quad \psi\Big|_{\partial_L} = V_L \ . \tag{6.9}$$

Each electrode surface, free of adsorbed species and charge transfer reactions, is taken to be ideally polarizable (no Faradaic current exists between the electrode surface and the electrolyte) and its apparently nonuniform surface charge density is an unknown quantity, which can be controlled by adjusting the potential bias $\Delta V = V_R - V_L$ or the concentration of the electrolyte solution.

Conditions (6.8) and (6.9) are sufficient to numerically solve Equation (6.7) for the potential and ion density distribution at equilibrium. If the boundary conditions for the mPB problem are not chosen carefully, however, global electroneutrality will generally be violated, which is unphysical for a closed system that must retain the electroneutrality of its initial (reference) state. We define a reference state with uncharged electrodes, $Q_L = Q_R = 0$, for which $\Delta V = 0$, corresponding to the potential (or, better in this case, voltage) of zero charge of the capacitor configuration. In this state, an exact charge balance is fulfilled between the net ionic charge in the electrolyte solution and the fixed surface charge on the polymeric channel walls, given by

$$zq \int_\Omega d^3\boldsymbol{r}(c_+ - c_-) + \int_{\partial_p} d^2\boldsymbol{r}\,(\varepsilon\varepsilon_0 \nabla\psi \cdot \hat{\boldsymbol{n}}) = 0 \ , \tag{6.10}$$

and this is referred to as global electroneutrality (GEN) in the context of our study. In the case with charged electrodes, we control the metal-phase potential at one of the electrode interfaces, tacitly assumed to be uniform, relative to the potential of zero charge. Then the metal-phase potential of the second electrode cannot be known a priori but needs to be chosen self-consistently so as to uphold the condition of global electroneutrality. In addition to (6.9), the following balance condition must be fulfilled in the charged state,

$$Q_L + Q_R = -\int_{\partial_L} d^2\boldsymbol{r}\,(\varepsilon\varepsilon_0 \nabla\psi \cdot \hat{\boldsymbol{n}}) - \int_{\partial_R} d^2\boldsymbol{r}\,(\varepsilon\varepsilon_0 \nabla\psi \cdot \hat{\boldsymbol{n}}) = 0 \ , \tag{6.11}$$

where the total charges on left and right electrodes, Q_L and Q_R, are defined through the respective integrals. In essence, the metal phase potential at one electrode is treated as a free parameter. For numerical calculations reported herein, V_R is provided and a potential range must be scanned until the unique value of V_L is found so that condition (6.11) holds for a given value of c_0. These conditions are sufficient to find a unique and physically-consistent solution of the problem. Thus, the output of numerical calculations includes the total voltage difference and amount of charge that is being shifted between the electrodes.

6.1.4 Constitutive relations and numerical methods

The present study focuses on aqueous binary and monovalent (symmetric) electrolyte solutions at room temperature, with the basic set of parameters listed in Table 6.1. Equations (6.5) and (6.7), along with the boundary conditions given by Equations (6.8)–(6.11), are solved using the commercial finite element solver COMSOL 5.4. To reduce computational cost, only a single 2D domain of the rotationally symmetric model is considered. This is realized in COMSOL by choosing the '2D Axisymmetric' component. The 'general form PDE' mode and electrostatics module are used to solve for the time-dependent PNP and the stationary PB problem, respectively.

The computational domain ($R \times L = 2$ nm $\times$ 10 nm) is discretized into quadratic triangular elements. Nonuniform elements are employed with a finer mesh generated near boundaries to capture the EDLs. Typically, the applied triangular mesh comprises mesh elements with dimensions ranging from about 0.03 Å in the vicinity of the electrodes and channel interfaces to about 0.1 Å at the center of the domain. The numerical model includes about $10,000$ mesh elements and $20,000$ degrees of freedom. COMSOL's numerical scheme has been validated to be adequately accurate for solving comparable electrokinetic problems, and a comprehensive description of its numerical implementation is accessible in the literature [192]. Convergence and mesh-independence of all results are verified first.

Parameter	Description	Reference value
q	elementary charge	$1.602 \cdot 10^{-19}$ C
k_B	Boltzmann constant	$1.38 \cdot 10^{-23}$ J/K
ϵ_0	vacuum permittivity	$8.85 \cdot 10^{-12}$ F/m
ϵ	dielectric constant	80
T	temperature	300 K
σ_p	surface charge density	-0.1 C/m^2
D	ion diffusivity	$7 \cdot 10^{-6}$ cm^2/s
R	channel radius	2 nm
L	channel length	10 nm

Table 6.1: Parameters of the system.

6.2 Results and discussion

6.2.1 Time evolution of double layers

Steady-state solutions are the main focus in the literature for comparable problems, chiefly for EDL structure and capacitance studies. In this work, the preliminary step is to investigate the non-equilibrium dynamical aspects. In particular, we examine the temporal evolution of the electric potential and ion density distribution across the entire domain. Our own interest in exploring the system's nonequilibrium dynamics stems from two key motivations: (1) Understanding the formation and relaxation of EDLs is critically important

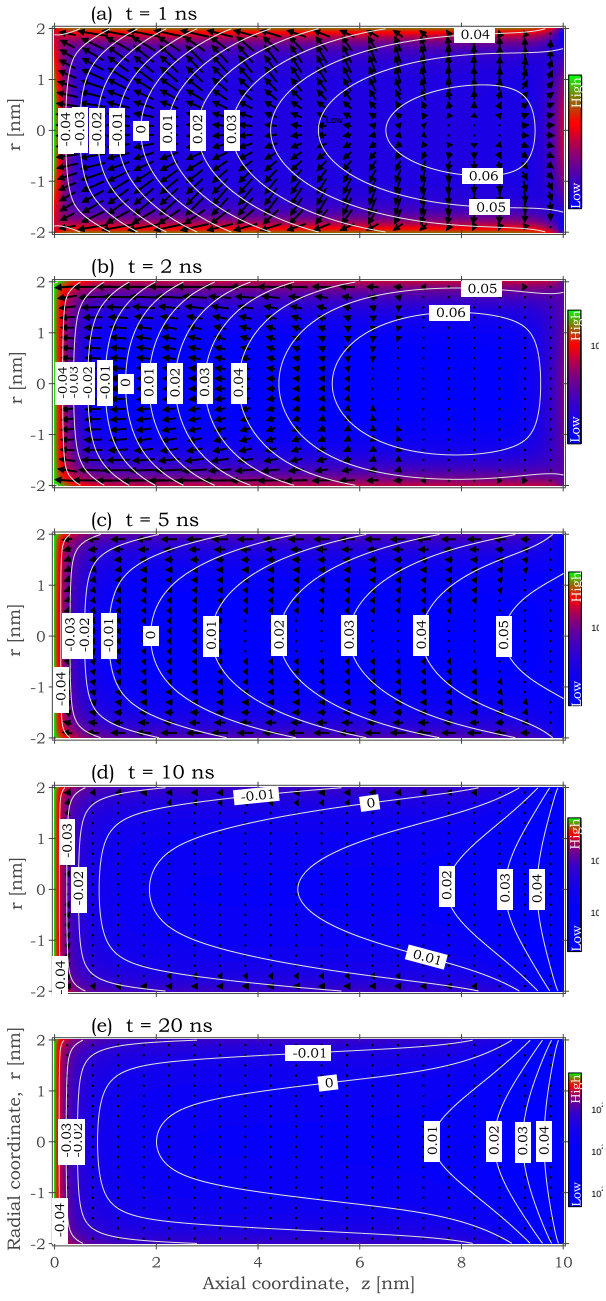

Figure 6.2: Two-dimensional view of the time evolution and relaxation of the EDL. Surface plot gives the concentration of cations c_+, contour plots represent the electric potential ψ and the arrows give the flux density vector for positive ions $\boldsymbol{J}_+$. Parameter values: $\sigma_p = -0.1$ C/m^2, $\Delta V = 1.21$ V, $c_0 = 1 \cdot 10^{25}$ /m^3.

for practical applications like controlling the performance of electrochemical devices such as supercapacitors. (2) The second motivation, detailed below, is that numerical simulations of the dynamics will provide useful insight into the connection between the dynamical model

described by the modified PNP (mPNP) equations and the equilibrium model. The latter is characterized by the mPB equation that satisfies the electroneutrality condition (6.11).

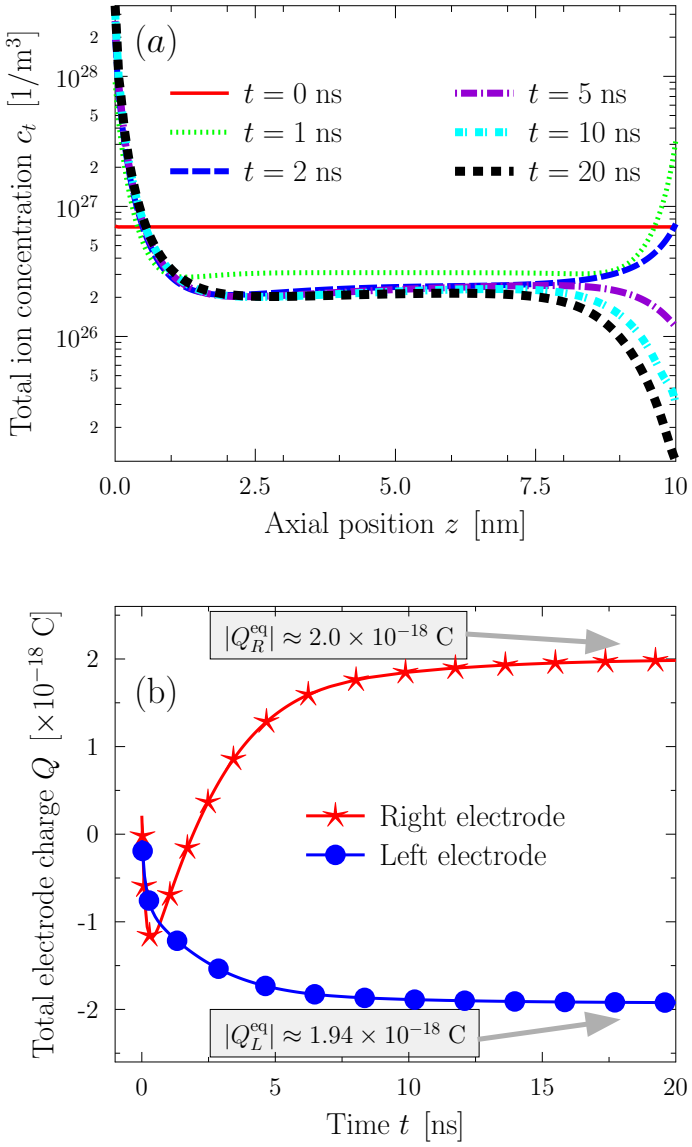

Figure 6.3: (a) Variation of the total ion concentration, $c_t = c_+ + c_-$, along the center of the channel. (b) Variation of total charge on left and right electrode, viz. Q_L and Q_R, as a function of time. Parameters are $\sigma_p = -0.1$ C/m^2, $\Delta V = 1.21$ V, $c_0 = 1 \cdot 10^{25}$ /m^3.

In Sec. 6.1.3, we highlighted that for a given set of conditions, there is a unique potential difference between the electrodes that ensures electroneutrality. For numerical solutions at equilibrium via the mPB equation, this ΔV is essentially the output of the model. For solving the dynamics via the mPNP-based numerical solver, however, it is necessary that ΔV is predetermined initially. Our general strategy to ensure that the dynamics is driven

to a globally electroneutral equilibrium state involves an initial equilibration of the system, before studying its dynamics. In this approach, we begin with the task of solving for the equilibrium problem by appealing to the mPB equation, given a set of conditions such as σ_p and the total magnitude of charges enclosed in the volume, dictated by c_0. From the results of the mPB solver, ΔV is extracted to be used as the Dirichlet boundary condition for the dynamical model. The second step is to solve the full mPNP equations assuming no fluxes at all boundaries, along with boundary conditions (6.8)–(6.9). Convection is neglected. The dynamics start off with a globally electroneutral state. For simplicity, a uniform density of cations and anions $c_\pm^{\text{initial}}$ is prescribed as the initial condition at $t = 0$. The value of c_0 used in the equilibration step places a powerful constraint on the choice of $c_\pm^{\text{initial}}$. Although this choice of $c_\pm^{\text{initial}}$ seems unphysical, it helps us understand a typical nonequilibrium response of ions in the channel to both the surface charges and the electrode potential bias. To understand this idea more concretely, the link between c_0 and $c_\pm^{\text{initial}}$ needs to be addressed.

Within the mPB solver, the channel wall surface charge density σ_p determines the net charge, Q_{net}, due to electrolyte ions in the volumetric domain, and c_0 determines the total positive and negative ionic charges (Q_+ and Q_-) enclosed:

$$Q_{\text{net}} = -\int_{\partial_p} d^2\boldsymbol{r}\ \sigma_p, \tag{6.12}$$

and

$$Q_\pm = \pm\int_\Omega d^3\boldsymbol{r}\ \frac{qc_0 \exp\left(\frac{\mp zq\psi}{k_BT}\right)}{1 + 2(z+1)c_0a^3\sinh^2\left(\frac{zq\psi}{2k_BT}\right)}\ , \tag{6.13}$$

where $Q_{\text{net}} = Q_+ + Q_-$ must be fulfilled – the condition of global electroneutrality. In light of this, it is a straightforward matter that the initial condition $c_\pm^{\text{initial}} = Q_\pm/q\pi R^2L$ will lead to a consistent solution for the dynamics when charge conservation is enforced in the mPNP solver. The system is then driven accordingly from this non-equilibrium state to an equilibrium state, whose solutions converge to those of the mPB solver.

In COMSOL, the mPB solver is executed by solving Equation (6.7) using the 'Charge Conservation' model builder under the 'AC/DC - Electrostatics' module. Constraint (6.11) is implemented via the 'Floating Potential' function. The mPNP-based solver, however, introduces time dependence by additionally solving Equation (6.5) and using the 'General Form PDE' solver under the 'Mathematics - PDE interfaces' module.

Figure 6.2 shows a 2-D representation of the time evolution of the EDL in a channel, whose polymer walls are negatively charged ($\sigma_p = -0.1$ C/m^2) and to which a potential bias $\Delta V = 1.21$ V, obtained from the mPB solver, is applied at $t = 0$. The underlying color shows the local cation concentration, white contours represent the electric potential and arrows give the cation flux density vector field. In a more compact way of illustrating the ion dynamics in the channel, Figure 6.3(a) presents the total ion concentration, $c_t = c_+ + c_-$,

along the center of the channel ($r = 0$) at different times, and Figure 6.3(b) shows the charge on each electrode, $Q_{\mathrm{L}}$and Q_{R}, as a function of time in the range 1–20 ns.

By virtue of these results, we distinguish four regimes in the relaxation dynamics: at very short times, Figure 6.2 shows a sudden displacement of counter-ions (cations) towards all boundaries. This corresponds to a time regime far out of equilibrium. The system is forced to balance strong local electric fields that develop from it being initially set to be extremely out of equilibrium. Here, all boundaries become negatively charged. This effect manifests itself as the rapid dip in the blue curve in Figure 6.3(b). In the next time regime, anions accumulate at the right electrode (sitting at higher potential) and counter-ions (cations) are translated towards the negative electrode. This is observed in Figure 6.2 at $t = 5$ ns. The lateral diffusion of counter-ions in the first layer near the channel walls is actually faster than that in the bulk. The next time regime, which occurs on a much longer time scale, is the 'EDL relaxation' phase. In this regime, seen at $t = 10$ ns in Figure 6.2, there is no diffusion of counter-ions in the bulk. However, we observe a small-scale translation of counter-ions in the EDL largely due to the slow ion diffusion involved during EDL reorganization. The final time regime corresponds to a steady-state equilibrium. This is characterized by the plateaus of both curves in Figure 6.3(b), approached at around $t = 20$ ns. It is imperative that the results in this regime agree with those from the mPB solver, i.e., electroneutrality must be fulfilled. According to Figure 6.3(b), the values of Q_{R}^{eq} and Q_{L}^{eq} are 2×10^{-18} C and -1.94×10^{-18} C, respectively, exhibiting a deviation of no more than 3%. Hence, we can confidently say that, through using the mPNP model and a careful choice of initial conditions, we are able to drive the system from some non-equilibrium state to an equilibrium state that satisfies both the electroneutrality condition (6.11) and the mPB equation.

6.2.2 Differential capacitance

The voltage-dependent capacitance of the EDL is a parameter that plays a significant role in the characterization of the EDL structure in electrochemical systems. Of key interest in experimental studies is the differential capacitance, C_{diff}, defined as

$$C_{\mathrm{diff}} = \frac{1}{\pi R^2} \frac{\partial Q_{\mathrm{R}}^{\mathrm{eq}}}{\partial \Delta V} , \tag{6.14}$$

where the total charge at the right electrode

$$Q_{\mathrm{R}}^{\mathrm{eq}} = \int_{\partial_R} \mathrm{d}^2 \boldsymbol{r} \left(\varepsilon \varepsilon_0 \frac{\partial \psi}{\partial z} \right) , \tag{6.15}$$

is evaluated at equilibrium. In essence, C_{diff} represents the ability of an electrochemical cell to store charge at its electrodes in response to a perturbation potential applied between them. Capacitance data provide an important indirect means to assess the EDL structure since the local charge imbalance occurs only in the EDL region.

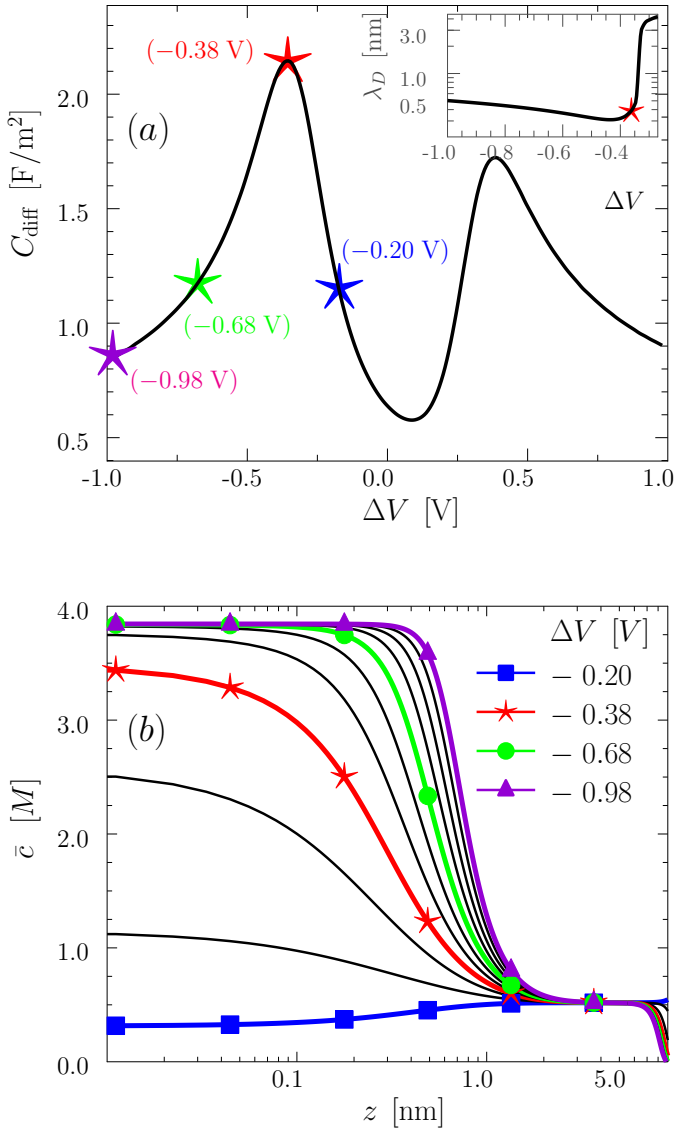

Figure 6.4: (a) Variation of C_{diff} with ΔV. (b) Cross-sectionally averaged total ion concentration, $\bar{c}_{\text{t}}(z)$, as a function of distance from the left electrode. Parameter values: $\sigma_p = -0.1$ C/m^2, $a = 3$ Å, $c_0 = 1 \cdot 10^{25}$ /m^3, $Q_{\text{T}} = 1.63 \cdot 10^{-17}$ C.

When calculating the differential capacitance, the total amount of combined positive and negative charges enclosed in the volumetric domain,

$$\begin{aligned} Q_{\text{T}} &= |Q_+| + |Q_-| \\ &= \int_{\partial V} \frac{zqc_0 \left[\exp\left(-\frac{zq\psi}{k_B T}\right) + \exp\left(\frac{zq\psi}{k_B T}\right)\right]}{1 + 2(z+1)c_0 a^3 \sinh^2\left(\frac{zq\psi}{2k_B T}\right)} \, d^3\boldsymbol{r} \,, \end{aligned} \tag{6.16}$$

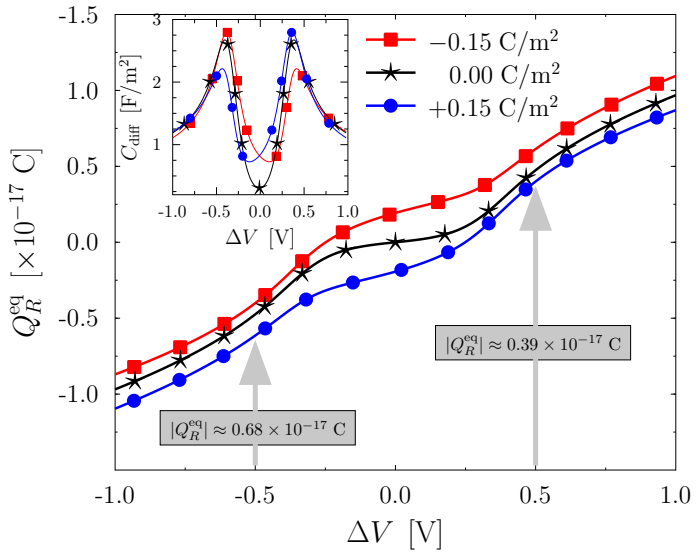

Figure 6.5: Variation of the total net charge on the right electrode against the electrode potential bias ΔV to illustrate the lack of symmetry in differential capacitance curves (insert shows the corresponding differential capacitance curves). Parameter values: $c_0 = 1 \cdot 10^{25}$ /m^3, $a = 3$Å, $Q_{\rm T} = 1.63 \cdot 10^{-17}$ C.

is conserved. This is achieved by setting the constraint (6.16) for some constant Q_T while ΔV is adjusted, via changing V_R, so that condition (6.11) is fulfilled. The 'Global Constraints' function in COMSOL enforces this condition. In this work, $C_{\rm diff}$ curves are computed as follows: The total charge at each voltage is calculated via Eq. (6.15). The derivative in Eq. (6.14) is then computed numerically, for ascending values of ΔV. About 100 data points (voltages) are used for each curve.

Figure 6.4(a) shows a typical plot of $C_{\rm diff}$ as a function of ΔV. Two noteworthy features of the $C_{\rm diff}$ curve are apparent: (1) the presence of a double peak and (2) the lack of symmetry with respect to ΔV. The former is attributed to excluded-volume-interaction effects. We present and discuss Figure 6.4(b) to support this view. Foremost, we formalize the discussion by defining the cross-sectionally averaged total ion density with respect to the axial distance from the left electrode,

$$\bar{c}_{\rm t}(z) = \frac{2}{R^2} \int_0^R c_{\rm t}(r, z)\, r dr\ . \tag{6.17}$$

This quantity, compared to taking $c_{\rm t}$ along the center of the channel, provides a more rigorous measure of the axial ion density profile in 1-D due to the strong radial variations of c when the channel is strongly charged.

Figure 6.4(b) shows plots of $\bar{c}_{\rm t}(z)$ for a few values of ΔV around, and inclusive of, the left peak in Figure 6.4(a). Four coloured markers in Figure 6.4(a) correspond to the coloured

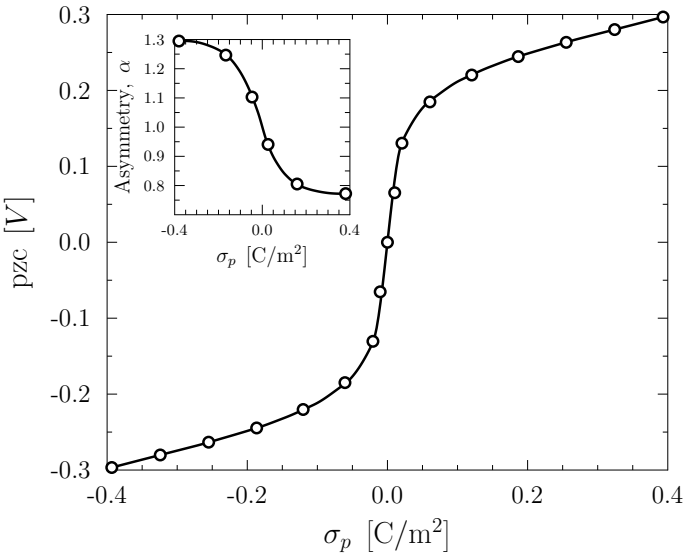

Figure 6.6: The influence of surface charge density on the point of zero charge on the right electrode (insert shows the ratio of the voltage peak on the left to that on the right in the DC curve). Parameter values: $c_0 = 1 \cdot 10^{25}$ /m^3, $a = 3$Å, $Q_{\mathrm{T}} = 1.63 \cdot 10^{-17}$ C.

distributions shown in Figure 6.4(b). On account of these results, we understand that the decline of C_{diff} at high positive or negative ΔV appears to be a consequence of overcrowding of counter-ions near the electrodes: at higher $|\Delta V|$, $\bar{c}_{\mathrm{t}}$ increases at a faster rate near the electrode surface and the decay length (λ_D) of $\bar{c}_{\mathrm{t}}(z)$ decreases sharply. (Here, the decay length is defined as the distance from the left electrode at which $\bar{c}_{\mathrm{t}}(z)$ is reduced to $1/e$ of its peak value attained directly at the electrode surface.) This behaviour is observed up to the peak voltage, indicated by the red curve in Figure 6.4(b). Beyond the peak, counter-ions saturate near the electrode and can only further accumulate by growing the thickness of the saturation layer to distances further away from the surface. This leads to a sudden change in λ_D as a function of ΔV, shown in the insert of Figure 6.4(a), caused by ion screening.

The lack of symmetry in C_{diff} in Figure 6.4(a) is attributed to the presence of fixed charges on the channel wall. This effect is demonstrated in Figure 6.5, where $Q_{\mathrm{R}}^{\mathrm{eq}}$ is plotted against ΔV at different values of σ_p. We recognize the existence of symmetry only when the channel is uncharged, i.e., at $\sigma_{\mathrm{p}} = 0$. When the channel is charged, reversing the sign of ΔV leads to a different magnitude of net charge on each electrode. This can be ascribed to the global electroneutrality condition enforced in the system: consider the channel with $\sigma_p < 0$ and the right electrode at negative potential with respect to the left electrode; by electroneutrality, there are more cations (majority charge carriers) than anions (minority charge carriers) in Ω; in this case, C_{diff} arises primarily from the large amount of cations in the channel, giving a high $Q_{\mathrm{R}}^{\mathrm{eq}}$. If the right electrode is at a positive potential, the low

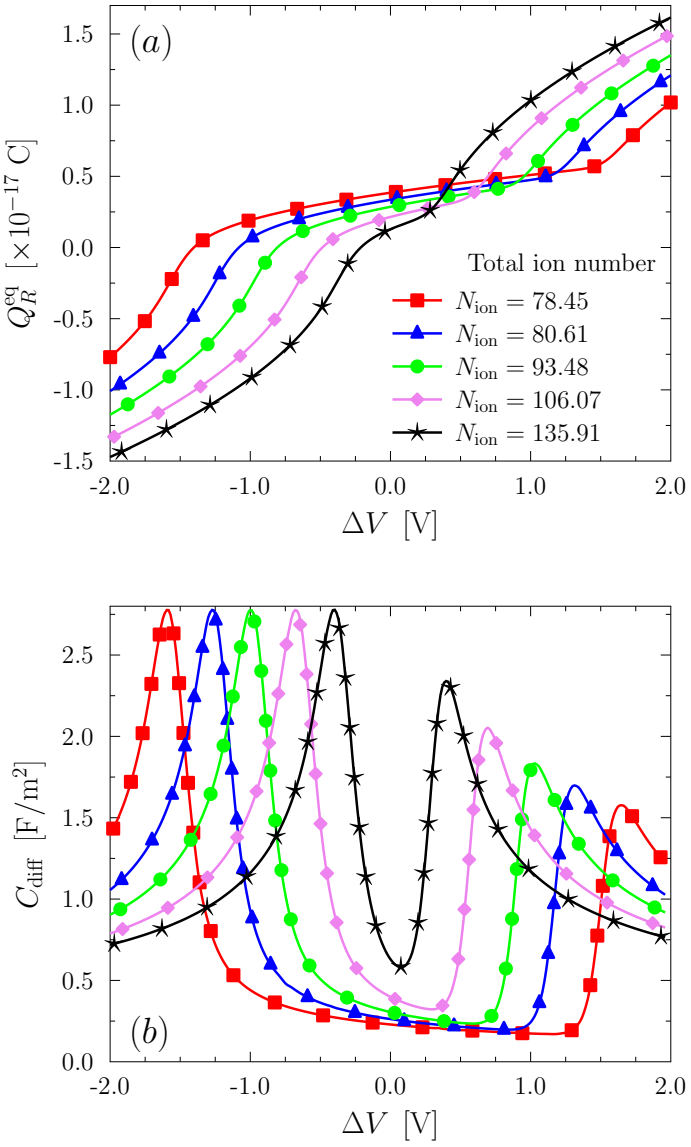

Figure 6.7: The influence of $Q_{\rm T}$ on (a) the total charge on the right electrode and (b) the differential capacitance as a function of the voltage bias. Parameter values: $\sigma_p = -0.1$ C/m^2, $a = 3$Å.

amounts of negative charged co-ions (minority charge carrier in the channel) are drawn towards this electrode; resulting in a relatively diminished $|Q_{\rm R}^{\rm eq}|$.

Figure 6.6 shows the effect of σ_p on the potential (or voltage) of zero charge (pzc), i.e., the point at which $|Q_{\rm R}^{\rm eq}| = 0$. As a consequence of the previously explained asymmetry, the pzc is shifted relative to ΔV, with the sign and magnitude of this shift exhibiting a dependence on σ_p: the more negative σ_p is, the more negative is the value of ΔV at which $|Q_{\rm R}^{\rm eq}| = 0$. This figure thus embodies in a highly condensed form the consequence of using a charged

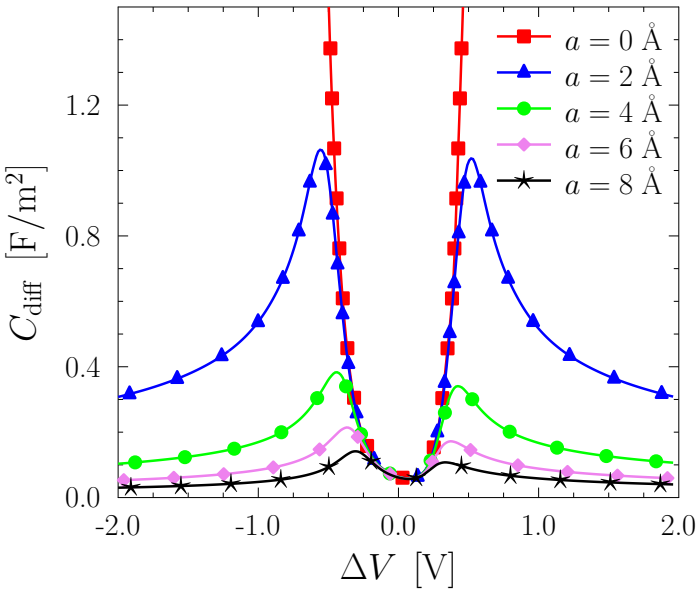

Figure 6.8: Variation of the differential capacitance with the electrode potential bias at different values of a. Reference parameter values: $\sigma_p = -0.1$ C/m^2, $a = 4$Å, $c_0 = 1 \cdot 10^{23}$ 1/m^3, $R = 2$ nm., $Q_{\text{T}} = 1.03 \cdot 10^{-17}$ C.

porous host matrix, such as provided by a polymer electrolyte membrane, for energy storage in double-layer capacitive devices. The insert of Figure 6.6 shows the symmetry parameter $\alpha = C_{\text{diff}}^{\text{peak, left}}/C_{\text{diff}}^{\text{peak, right}}$, which is the ratio of the left peak in the differential capacitance to the right one.

The effect of Q_{T} on the electrode charging is illustrated in Figure 6.7. At low Q_{T}, the electrode charging is insensitive to changes in low ΔV and only high ΔV can lead to EDL overcrowding, forcing the peaks in C_{diff} to be farther apart and thus widening the low-capacitive plateau. At high Q_{T}, however, the peaks move closer together, owing to ion saturation, and the local central minimum of C_{diff} increases. This agrees with similar studies in the literature [193], albeit for different geometries, where it is observed that, at even higher Q_{T}, the C_{diff} curve transitions to just a single peak. For the case of a closed cylinder, simulations do not allow for such high concentrations required to see a single peak.

Figure 6.8 shows the effects of a on C_{diff}. Here, a shifts the voltage bias at peak C_{diff} (ΔV_{peak}) without affecting the results at small $|\Delta V|$. This underlines the excluded-volume-interaction effects seen only at high $|\Delta V|$, and the reduction to the Gouy-Chapman regime at low $|\Delta V|$. Predictably, a large a enhances the overcrowding effect of counter-ions as the competition for volume becomes fiercer. Hence, peaks in C_{diff} occur at lower $|\Delta V|$.

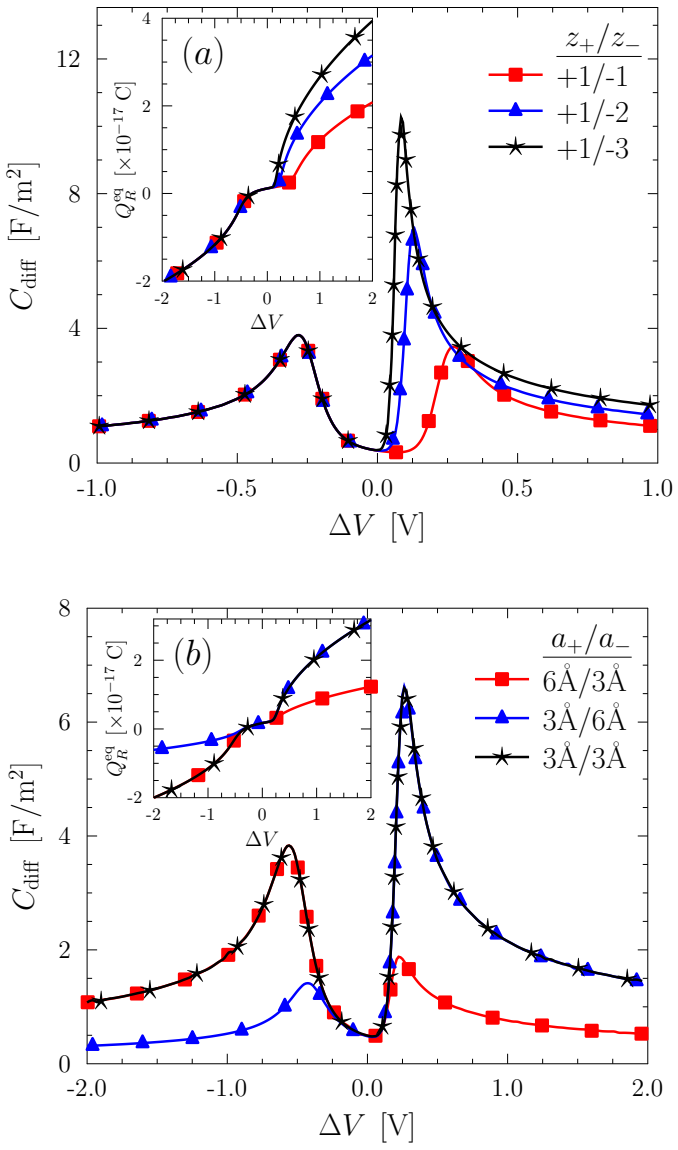

Figure 6.9: Differential capacitance against the electrode potential bias at various values of (a) z_+/z_- and (b) a_+/a_-. The inserts show the net charge on the right electrode. Graph (b) uses asymmetric valences $z_+/z_- = +1/-2$. Parameter values: $\sigma_p = -0.05$ C/m^2, $c_0 = 1 \cdot 10^{23}$ /m^3, $a = 4$ Å, $Q_{\rm T} = 1.03 \cdot 10^{-17}$ C.

6.2.3 Effect of asymmetry in ion properties

So far, we have considered electrolytes having two ionic species with identical valence and size. However, experimental data reported on capacitors in the literature [194–196] utilize electrolytes with asymmetric valence. Also, asymmetric electrolytes have practical implications in capacitive deionization [197] and biosensors [198].

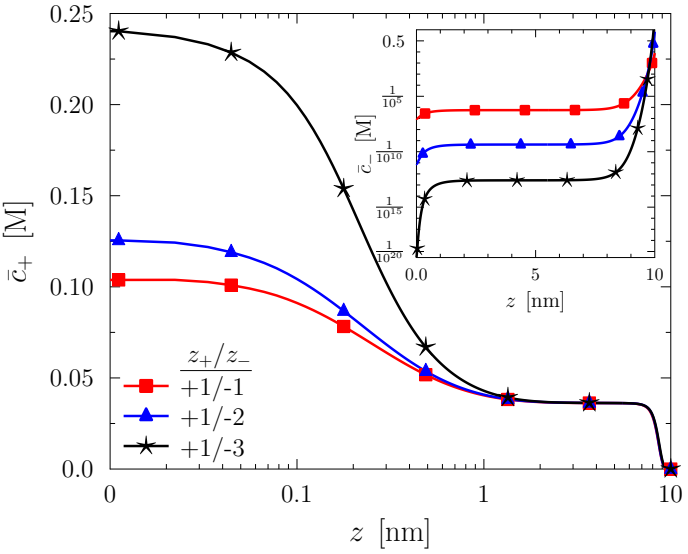

Figure 6.10: Cross-sectional concentration of cations along the length of the channel at different anion valencies. The insert shows the cross-sectional concentration of anions (y-axis on log scale). Parameter values: $\sigma_p = -0.05$ C/m^2, $c_0 = 1 \cdot 10^{25}$ /m^3, $a = 4$ Å, $Q_{\mathrm{T}} = 1.63 \cdot 10^{-17}$ C.

We now investigate the impacts of asymmetry in the electrolyte valence within the mPB description. For nonidentical valency and ionic sizes, a complete rederivation based on the formalism presented in Section 6.1.2 gives the modified Boltzmann distributions of cations and anions [199],

$$c_\pm = \frac{c_0 e^{\mp \frac{z_\pm q\psi}{k_B T}}}{1 + c_0 a_+^3 \left(e^{-\frac{z_+ q\psi}{k_B T}} - 1\right) + c_0 a_-^3 \left(e^{-\frac{z_- q\psi}{k_B T}} - 1\right)}, \tag{6.18}$$

where $z_\pm$ and $a_\pm$ denote the valency and ion size, respectively, for cations and anions.

Differential capacitance results are shown in Figure 6.9. In Figure 6.9(a), the valency of anions is varied. We see a pronounced asymmetry in C_{diff} curves as a manifestation of the asymmetry in ionic valency. Asymmetry in the double layer structure originates from an imbalance between the magnitude of forces experienced by cations and anions, dictated by the ionic valence. The effect of z_+/z_- is only seen at positive ΔV since the valency of positive ions, which controls the DC curve when $\Delta V < 0$, is fixed here. Another key observation is that the position of a local maximum shifts towards lower ΔV when the ionic asymmetry increases. This observation is consistent with the prediction that high valency leads to a stronger electric force and, hence, a stronger ion saturation effect. Figure 6.9(b) shows a similar effect when ion sizes are asymmetric. Changing a_+ only affects the left hump of the

C_{diff} curve, and a_- affects the right hump. These results highlight feasible exploitations of valence asymmetry as a way to tune the energy and power density of capacitors.

The sectional ion density profiles along the channel at different values of z_+/z_- are shown in Figure 6.10. Both cation and anion profiles are affected. The more pronounced saturation of cations near the left electrode is observed at larger z_-, while their distribution away from the left electrode is unaffected. The anion distribution, however, is affected throughout the length of the channel. We see a stronger pull of anions towards the left electrode at higher z_-.

6.2.4 Effect of surface charge density modulation

We saw in Section 6.2.2 that the presence of a uniform charge density on the channel surface introduces asymmetry in C_{diff} curves and offers a way of modifying the double-layer structure near each electrode. In this section, we investigate the effect of a non-uniform distribution of σ_p, similar in spirit to nanofluidic diodes [200].

First, we consider a $\sigma_p(z)$ profile that follows a cyclic square-wave like modulation defined in the following manner: let n_σ be the (even) number of equal segments along the length of the channel with a constant surface charge density that switches between $-\sigma_0$ and σ_0. Mathematically, this can be expressed by

$$\sigma_p(z) = \begin{cases} -\sigma_0, & \text{for } \dfrac{2kL}{n_\sigma} \leq z < \dfrac{(2k+1)L}{n_\sigma} \\ +\sigma_0, & \text{for } \dfrac{(2k+1)L}{n_\sigma} \leq z < \dfrac{2kL}{n_\sigma} \end{cases}, \tag{6.19}$$

where $k = 0, 1, 2, \cdots, n_\sigma/2$ and n_σ being even. With this profile, the net amount of charge on the channel surface is zero. We use $\sigma_0 > 0$, so that the negatively-charged left electrode is closer to a negative section of the channel.

The case $n_\sigma = 2$ is of particular relevance, as it corresponds to the case of nanofluidic diodes [201]. Moreover, this channel configuration mimics the interfacial conditions encountered in electrochemical devices with bipolar membranes [202–204], where a contact region between a proton exchange membrane (PEM) and an anion exchange membrane (AEM) exists. In the latter context, it is of foremost interest to determine the potential distribution and corresponding electric field strength in the contact or space charge region where the two ion-conducting media with different majority carriers meet. Figure 6.11 shows results for a 2-D slice of the channel along the axial direction for $n_\sigma = 2$ for different values of σ_0. Coloured images show the net ion concentration $c_{\text{net}} = c_+ - c_-$, and labelled contours illustrate the electric potential in volts. As expected, counter-ions are drawn towards oppositely charged sections of the channel. Figure 6.12 shows the variation of the axial electric field and net ion concentration (see insert) with σ_0 along the center of the channel ($r = 0$). The strength of the local electric field in the space charge region reaches

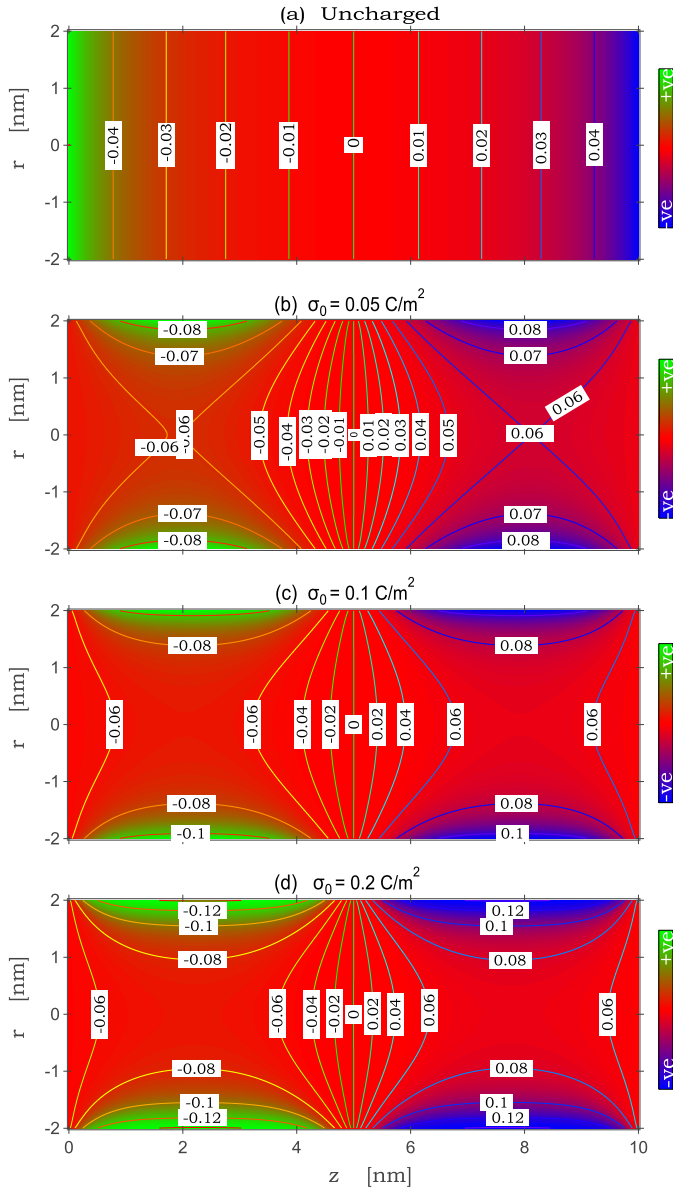

Figure 6.11: Effect of σ_0 on charge distribution within the channel for the case $n_\sigma = 2$. Distribution of net ion concentration (colour plot) and the electric potential (contour plots with labels in volts) on a 2-D slice along the channel. Parameter values: $c_0 = 1 \cdot 10^{25}$ /m^3, $a = 6$ Å, $Q_\mathrm{T} = 0.71 \cdot 10^{-17}$ C.

values of 10^8 V m^{-1}; the region is about 5 nm wide. These results imply water splitting in the channel, the same as observed in [204].

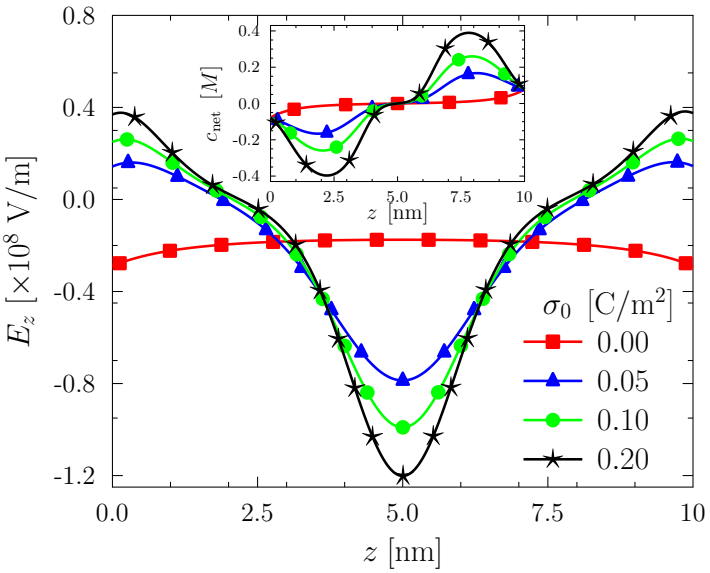

Figure 6.12: Net ion concentration along the center of the channel for different values of σ_0. Insert shows the corresponding axial electric field ($E_z = -\psi_z$). Parameter values: $c_0 = 1 \cdot 10^{25}$ /m^3, $a = 6$ Å, $Q_{\rm T} = 0.71 \cdot 10^{-17}$ C.

6.3 Summary

This chapter presented numerical simulations of electric double layers formed by a binary electrolyte in a closed, cylindrical and charged nanochannel whose ends are met by metal electrodes, subject to an externally applied potential bias. The applied model consists of the modified Poisson-Nernst-Planck/Poisson-Boltzmann equations, accounting for finite ion sizes similar to the Bikerman model. A self-consistent electroneutrality condition at equilibrium was enforced that requires equal magnitudes of net charges on the electrodes. Application of this condition establishes the correct correspondence between the modified Poisson-Nernst-Planck and Poisson-Boltzmann equations at equilibrium. Numerical results were presented that illustrate the formation and relaxation of double-layer charging near the electrodes and the internal channel surface. Differential capacitance data were analysed and discussed, with a focus on their dependence on the channel surface charge density, electrolyte concentration, ion sizes and channel size. Results indicate that the structure of the double layer near the electrode can be controlled, or is affected by, the charge distribution along the channel, the asymmetry in the total charges for each ion species in the electrolyte, and the ion sizes.

Chapter 7

Closed and Deformable Nanochannel: Model for an Ionic Polymer Actuator

Closed, charged nanochannels exhibit interesting properties when the walls are flexible. In addition to demonstrating double-layer charging behaviour near electrodes, as seen in Chapter 6, such channels undergo wall deformations under an applied voltage. Voltage-induced drifting and diffusion of mobile ions cause accumulation or depletion of excess ions at different regions within the channel, resulting in a bending actuation due to volume expansion or contraction in these regions. An example of a device that uses such a mechanism is the ionic metal-polymer composite (IMPC) actuator [61, 104–106]. It is composed of an ionic ionomeric membrane material like Nafion®, Teflon® or Flemion® whose surfaces are chemically plated or physically coated with highly conductive metal electrodes such as platinum or gold.

IPMC actuators have unique advantageous characteristics such as softness, light weight, biocompatibility, relatively high degree of deformation, quick response to low driving voltages, and facile processability at low costs. This makes them ideal candidates for many electromechanical transduction applications such as sensing [74], soft biorobotics [66–68], artificial muscles [65], bio-medicine [70–72], polymer-based microelectromechanical systems (MEMS) [69], and energy harvesting [73]. Considerable efforts have been made to develop models [205–207] for the electromechanical transduction of IMPC, primarily to enable advanced IMPC device design.

In this chapter, we study electromechanical transduction induced by counter-ions in a closed channel of circular cross section. This is a continuation of Chapter 6. Contrary to the preceding work, the channel is allowed to deform elastically in response to fluid and osmotic pressure variations along the channel walls. The steady state distribution of ions is described by the equilibrium PB equation, and the neo-Hookean model is employed for the elastic polymer walls. The chapter is organized as follows: Section 7.1 describes the

physical system and contains a comparison to IMPC devices. A 1-D model for the system is derived in Section 7.2. Section 7.3 presents the numerical method used to solve the model. Subsequently, Section 7.4 contains results and discussion. The chapter is concluded with a summary of results in Section 7.5.

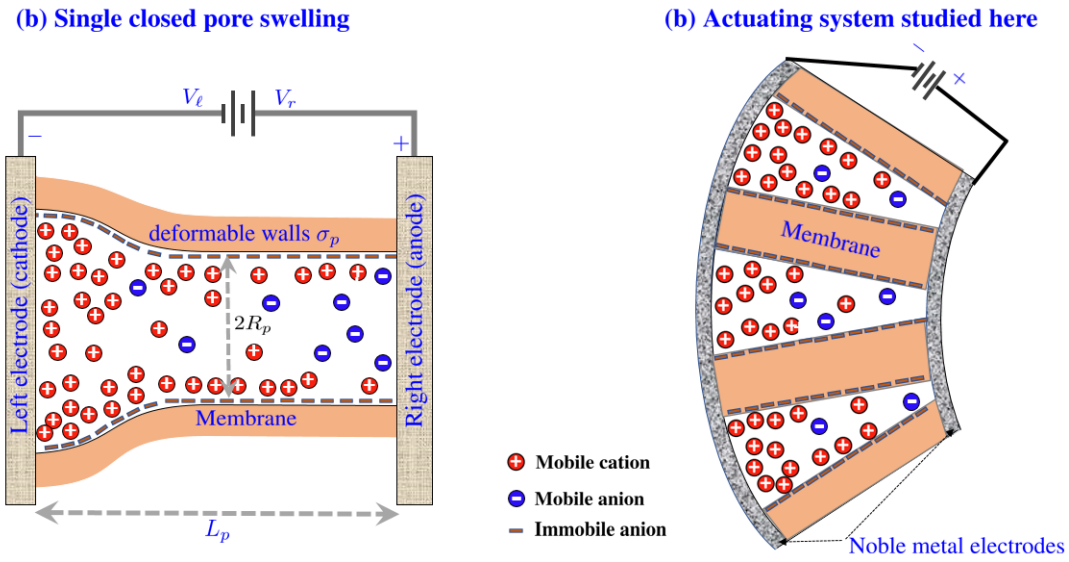

Figure 7.1: Schematic illustration of (a) the swelling of a single closed pore and (b) the electroactuating system studied here.

7.1 Model system

Consider a closed, negatively charged and deformable nanochannel of radius R_p and length L_p containing a binary 1:1 electrolyte solution sandwiched between two metal electrodes. A majority of counter-ions occupy regions close to the channel walls. When a voltage bias is applied at the electrodes, the electric field drives cations towards the cathode. Migrating cations drag the water molecules along, causing osmotic pressure changes along the channel. More osmotic pressure exerted on the walls near the cathode leads to swelling in that region, and contraction of the polymer walls near the anode results from ion (only relatively few co-ions are present) and water depletion (see Figure 7.1(a)).

In this study, it is essential to distinguish our model actuating system from the IMPC actuator. In the IMPC system, the metal electrodes are coated on the membrane surface and anions are immobile fixed charges attached to the polymer backbone, leading to more mobile cations than mobile anions in the solution. Cations, which are abundant, drag fluid molecules along with them towards the cathode side when an electric field is applied at the electrodes. Immense electroosmotic and fluid pressure at the cathode side lead to

bending of the polymer toward the anode. The model system considered herein consists of a soft membrane (e.g., Nafion), clamped between two mesh electrodes. The membrane is assumed, for simplicity, to consist of straight parallel pores, running perpendicular to the electrode interfaces. We assume further that all pores are equal and organized in an ordered 2-D lattice in the electrode planes. When a voltage is applied at the electrodes, each pore, seen as a unit cell in the whole system, follows the same mechanoelectrical transduction mechanism illustrated in Figure 7.1(a). Ion-induced electromechanical bending takes place at the channel walls and at the electrodes. Using this unit cell model, the deformation of each pore scales up to the whole system, resulting in a configuration similar to Figure 7.1(b).

7.2 Model in 1-D

As hinted in Chapter 4, numerically solving the full 2-D continuum-based problem can pose an enormous challenge if the radius of the channel is not uniform. Seeking solutions of the system at the single pore level, we reduce the 2-D problem to a 1-D problem which can be readily solved numerically, and even analytically (this is beyond the scope of this work). The methodology hinges on the assumption that the channel is weakly charged. We are only concerned about equilibrium solutions. The 2-D system is framed in the domain $r \in [0, R_p(z)]$ and $z \in [-L_p/2, +L_p/2]$, i.e., we let the origin be located at the center of the channel. Hence, the channel can change its shape only in the radial direction. In deriving the model equations, the channel is assumed to be long enough that each electrode surface can be taken to be flat.

7.2.1 Theory for the electric potential in 1-D

At equilibrium, the charge distribution in the closed system is described by the Poisson-Boltzmann equation,

$$\nabla \cdot (\varepsilon\varepsilon_0 \nabla\psi) = 2zqc_0 \sinh\left(\frac{zq\psi}{k_B T}\right) , \tag{7.1}$$

because ionic and fluid fluxes all vanish. In 2-D and for constant permittivity, we have

$$\frac{1}{r}\frac{\partial}{\partial r}\left(r\frac{\partial\psi}{\partial r}\right) + \frac{\partial^2\psi}{\partial z^2} - \frac{2zqc_0}{\varepsilon\varepsilon_0}\sinh\left(\frac{zq\psi}{k_B T}\right) = 0 , \tag{7.2}$$

with the electroneutrality boundary condition at the channel walls

$$\left.\frac{\partial\psi}{\partial r}\right|_{r=R_p} = \frac{\sigma_p}{\varepsilon\varepsilon_0} . \tag{7.3}$$

The channel considered here is weakly charged, and we expect small radius perturbations. Hence, the axial contribution to $(\nabla\psi\cdot\hat{\boldsymbol{n}})\big|_{R_p} = \frac{\sigma_p}{\varepsilon\varepsilon_0}$ is neglected, and Equation (7.3) is presumed to be sufficient to enforce vanishing electric fields outside the channel.

The left and right electrodes sit at potentials $\psi = V_L$ and $\psi = V_R$, respectively, and the potential difference between the electrodes is $\Delta V = V_R - V_L$. Charge balance between the inner surfaces of each electrode is demanded for self-consistency and electroneutrality,

$$\int_{z=-L_p/2} \frac{\partial\psi}{\partial z} r dr = \int_{z=L_p/2} \frac{\partial\psi}{\partial z} r dr \; . \tag{7.4}$$

As discussed previously, c_0 in Equation (7.2) is the reference concentration when $c_+ = c_- = c_0$ and the electric potential is set to zero there. Apart from ψ and $c_\pm$, two further functions must be solved for, viz, the channel radius $R_p(z)$ and fluid pressure on the wall. Hence, it is helpful to define the reference radius and reference pressure at the wall. Define the reference R_0 as the radius when the wall is in the undeformed state. At $R_p = R_0$, the surface charge density is σ_0. The surface charge density at $R_p(z)$ is modelled by

$$\sigma_p(z) = \sigma_0 \left(\frac{R_0}{R_p}\right)^{\alpha} \; , \tag{7.5}$$

where α is the surface charge reorganization parameter, the details of which are contained in Chapter 4. The reference for pressure will be discussed in Section 7.2.2.

We use these reference parameters to make Equation (7.2) dimensionless by introducing the scheme,

$$\tilde{R} = \frac{R_p}{R_0}, \quad \tilde{z} = \frac{z}{R_0}, \quad \tilde{r} = \frac{r}{R_0}, \quad \tilde{\psi} = \frac{zq\psi}{k_BT}, \quad \tilde{c}_0 = \frac{2(zR_0q)^2 c_0}{\varepsilon\varepsilon_0 k_BT}, \quad \tilde{\sigma} = \frac{zR_0q\sigma_0}{\varepsilon\varepsilon_0 k_BT} \; , \tag{7.6}$$

and by using the linear approximation $\sinh(\tilde{\psi}) \approx \tilde{\psi}$, valid when $\psi \ll k_BT/zq$. Equation (7.2) then takes the dimensionless form,

$$\frac{\partial}{\partial\tilde{r}}\left(\tilde{r}\frac{\partial\tilde{\psi}}{\partial\tilde{r}}\right) + \frac{\partial^2\tilde{\psi}}{\partial\tilde{z}^2} - \tilde{c}_0\tilde{\psi} = 0 \; . \tag{7.7}$$

Note that the linear approximation $\sinh(\tilde{\psi}) \approx \tilde{\psi}$ requires that the channel is weakly charged and the applied voltage bias should be less than k_BT/zq. In contrast, high values of σ_p can result in high potentials developing inside the channel. Equation (7.7) is solved, along with

$$\left.\frac{\partial\tilde{\psi}}{\partial\tilde{r}}\right|_{\tilde{r}=\tilde{R}} = \tilde{\sigma}\tilde{R}^{-\alpha} \; , \tag{7.8}$$

in the domain $\tilde{r} \in [0, \tilde{R}(\tilde{z})]$ and $\tilde{z} \in [-\ell, +\ell]$, where $\ell = L_p/R_0$.

From the previous chapters, we noted that the electric potential profile along $\tilde{r}$ follows a smooth function that ranges from nearly quadratic to highly concave-shaped as the surface

charge density is varied. It is therefore reasonable to approximate $\tilde{\psi}$ as a polynomial function of $\tilde{r}$ whose coefficients are functions of $\tilde{z}$,

$$\tilde{\psi}(\tilde{r},\tilde{z}) = \sum_{i=0}^{\infty} \tilde{\psi}_{2i}(\tilde{z})\tilde{r}^{2i} = \tilde{\psi}_0(\tilde{z}) + \tilde{\psi}_2(\tilde{z})\tilde{r}^2 + \tilde{\psi}_4(\tilde{z})\tilde{r}^4 + \tilde{\psi}_6(\tilde{z})\tilde{r}^6 + \cdots \ . \tag{7.9}$$

Odd-power terms are assumed to vanish based on the analytical form of $\psi(r)$ encountered in Chapter 3. We will consider terms up to 6th order, based on the assumption that the functions $\tilde{\psi}_i$ converge fast to zero as i is increased

$$\tilde{\psi} = \tilde{\psi}_0 + \tilde{\psi}_2\tilde{r}^2 + \tilde{\psi}_4\tilde{r}^4 + \tilde{\psi}_6\tilde{r}^6 \ . \tag{7.10}$$

Equation (7.8) enables us to eliminate $\tilde{\psi}_6$ and write it in terms of $\tilde{R}$, $\tilde{\psi}_2$ and $\tilde{\psi}_4$:

$$\tilde{\psi}_6(\tilde{R}) = -\frac{2\tilde{\psi}_2\tilde{R} + 4\tilde{\psi}_4\tilde{R}^3 - \tilde{\sigma}\tilde{R}^{-\alpha}}{6\tilde{R}^5} \ . \tag{7.11}$$

Substituting Equation (7.10) into Equation (7.7) and equating powers of $\tilde{r}$ yields the following system of second order ODEs in $\tilde{\psi}_0$, $\tilde{\psi}_2$ and $\tilde{\psi}_4$:

$$\tilde{r}^0: \quad \frac{d^2\tilde{\psi}_0}{d\tilde{z}^2} = \tilde{c}_0\tilde{\psi}_0 - 4\tilde{\psi}_2 \ , \tag{7.12}$$

$$\tilde{r}^2: \quad \frac{d^2\tilde{\psi}_2}{d\tilde{z}^2} = \tilde{c}_0\tilde{\psi}_2 - 16\tilde{\psi}_4 \ , \tag{7.13}$$

$$\tilde{r}^4: \quad \frac{d^2\tilde{\psi}_4}{d\tilde{z}^2} = \left(\frac{12}{\tilde{R}^4}\right)\tilde{\psi}_2 + \left(\frac{24 + \tilde{c}_0\tilde{R}^2}{\tilde{R}^2}\right)\tilde{\psi}_4 - \frac{6\tilde{\sigma}}{R^{5+\alpha}} \ . \tag{7.14}$$

To satisfy $\tilde{\psi} = \tilde{V}_L$ and $\tilde{\psi} = \tilde{V}_R$ at $\tilde{z} = \ell/2$ and $\tilde{z} = -\ell/2$, respectively, the functions $\tilde{\psi}_2$, $\tilde{\psi}_4$ and $\tilde{\psi}_6$ should vanish at the channel ends. The boundary conditions are thus

$$\tilde{\psi}_2 = \tilde{\psi}_4 = 0 \quad \text{at} \ \ \tilde{z} = \pm\frac{\ell}{2} \ , \tag{7.15}$$

$$\tilde{\psi}_0 = \tilde{V}_R \quad \text{at} \ \ \tilde{z} = +\frac{\ell}{2} \ , \tag{7.16}$$

$$\tilde{\psi}_0 = \tilde{V}_L \quad \text{at} \ \ \tilde{z} = -\frac{\ell}{2} \ , \tag{7.17}$$

with $\Delta\tilde{V} = \tilde{V}_R - \tilde{V}_L$. The condition given in Equation (7.4) leads to

$$\left[24\tilde{R}^{\alpha}\,\frac{\partial\tilde{\psi}_0}{\partial\tilde{z}} + 10\tilde{R}^{\alpha+2}\,\frac{\partial\tilde{\psi}_2}{\partial\tilde{z}} + 4\tilde{R}^{\alpha+4}\,\frac{\partial\tilde{\psi}_4}{\partial\tilde{z}} + \left[8\tilde{R}^{\alpha+1}(\tilde{\psi}_2 + \tilde{\psi}_4\tilde{R}^2) - (5+\alpha)\tilde{\sigma}\right]\,\frac{\partial\tilde{R}}{\partial\tilde{z}}\right]\Bigg|_{\tilde{z}=-\ell/2}$$

$$= \left[24\tilde{R}^{\alpha}\,\frac{\partial\tilde{\psi}_0}{\partial\tilde{z}} + 10\tilde{R}^{\alpha+2}\,\frac{\partial\tilde{\psi}_2}{\partial\tilde{z}} + 4\tilde{R}^{\alpha+4}\,\frac{\partial\tilde{\psi}_4}{\partial\tilde{z}} + \left[8\tilde{R}^{\alpha+1}(\tilde{\psi}_2 + \tilde{\psi}_4\tilde{R}^2) - (5+\alpha)\tilde{\sigma}\right]\,\frac{\partial\tilde{R}}{\partial\tilde{z}}\right]\Bigg|_{\tilde{z}=+\ell/2} \ . \tag{7.18}$$

The 2-D problem has been reduced to a 1-D problem given by Equations (7.12)–(7.14), along with the boundary condition given by Equations (7.15)–(7.18). An additional constraint is required to ensure that the total volume inside the closed channel does not change from the undeformed configuration as the channel swells at one side and shrinks at the other side. This volume conservation constraint takes the dimensionless form,

$$\int_{-\ell/2}^{\ell/2} \tilde{R}^2(\tilde{z})\, d\tilde{z} \;-\; \ell \;=\; 0\,. \tag{7.19}$$

We have six conditions for three 2$^{\text{nd}}$-order ODEs and are now, in principle, in a position to solve the problem. Note that conditions (7.18) and (7.19) are non-local. However, a swelling model remains to be defined.

7.2.2 Swelling model

Mathematical modelling of the mechanical behaviour of the channel wall's polymer material focuses, to a large extent, on the development of an appropriate function that couples the pressure on the channel walls to the the channel radius. The undeformed configuration has the radial coordinate defined as r_0, radius R_0 and channel wall thickness H_0, i.e., $R_0 \leq r_0 \leq R_0 + H_0$. The deformed configuration has radius R_p and wall thickness H, i.e., $R_p \leq r \leq R_p + H$. This is illustrated in Figure 7.2, where a cross-section of the channel is shown. To conduct the stress analysis of the channel walls, we assume the channels are thick and undergo elastic deformation.

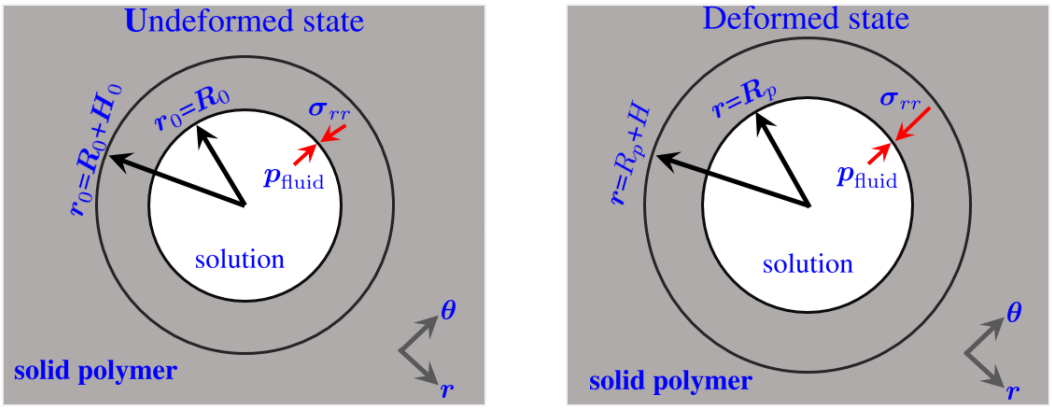

Figure 7.2: Stress analysis in a cross-section of the cylindrical channel.

For an element of the membrane, we formulate the Biot stress tensor and Green's deforma-

tion tensor, respectively, describing the forces in action,

$$\boldsymbol{\sigma} = \begin{bmatrix} \sigma_{rr} & 0 & 0 \\ 0 & \sigma_{\theta\theta} & 0 \\ 0 & 0 & \sigma_{zz} \end{bmatrix}, \qquad \boldsymbol{\lambda} = \begin{bmatrix} \lambda_r^2 & 0 & 0 \\ 0 & \lambda_\theta^2 & 0 \\ 0 & 0 & \lambda_z^2 \end{bmatrix}, \tag{7.20}$$

where the σ_{ii}'s are the principal stresses and λ_i's are the principal stretches in radial, azimuthal and axial directions.

According to the assumption that the channel material is incompressible, we have the constraint $\lambda_r\lambda_\theta\lambda_z = 1$. From geometry, $\lambda_\theta = r/r_0$ must hold. Assuming that the channel is long enough so that λ_z remains almost constant after deformation, i.e., $\lambda_z = 1$, and using the incompressibility constraint, we have

$$\lambda_\theta = \frac{r}{r_0}, \;\; \lambda_r = \frac{r_0}{r}, \qquad \lambda_z = 1 \; . \tag{7.21}$$

The standard relation between the stress and deformation tensors is given by

$$\sigma_{ii} = \frac{\partial W}{\partial \lambda_i} - p/\lambda_i \qquad (i = r, \theta, z) \; , \tag{7.22}$$

where p is the undetermined Lagrange multiplier, taken as the arbitrary hydrostatic pressure which arises due to the condition of incompressibility, and W is the strain-energy function. The membrane is assumed to be a neo-Hookean material, whose strain-energy function takes the simple form,

$$W(\lambda_r, \lambda_\theta, \lambda_z) = \frac{Y}{2}\left(\lambda_r^2 + \lambda_\theta^2 + \lambda_z^2 - 3\right) \; , \tag{7.23}$$

where Y is the linear elastic shear modulus.

At equilibrium, the membrane configuration is described by the Cauchy momentum equation,

$$\nabla \cdot \boldsymbol{\sigma} = 0 \; . \tag{7.24}$$

Due to symmetry, Equation (7.24) gives only one nontrivial equation,

$$\frac{\mathrm{d}\sigma_{rr}}{dr} + \frac{1}{r}\left(\sigma_{rr} - \sigma_{\theta\theta}\right) = 0 \; , \tag{7.25}$$

for any point in the element located at radial coordination r. Inner walls of the channel experience stress due to the fluid pressure p_{fluid} at the wall, while the outer walls are traction-free (assume no applied pressure from outside the channel):

$$\sigma_{rr}\Big|_{r=R_p} = p_{\text{fluid}}\Big|_{r=R_p}, \;\; \sigma_{rr}\Big|_{r=R_p+H} = 0 \; . \tag{7.26}$$

Using Equations (7.21), (7.22) and (7.23), along with the boundary conditions (7.26), and integrating Equation (7.25) over $r/r_0 \in [R_p/R_0, (R_p+H)/(R_0+H_0)]$, one obtains

$$p_{\text{fluid}}\Big|_{r=R_p} = \frac{Y}{2}\left[\left(\frac{R_p + R_0H_0/R_p}{R_0+H_0}\right)^2 - \left(\frac{R_p}{R_0}\right)^2\right] - Y\ln\left[\frac{R_0(R_p+R_0H_0/R_p)}{R_p(R_0+H_0)}\right] , \quad (7.27)$$

where we used $R_0H_0 = R_pH$ for the incompressible wall so as to eliminate H. Using the dimensionless scheme,

$$\tilde{Y} = \frac{Y}{c_0k_BT}, \quad \tilde{p}_{\text{fluid}} = \frac{p_{\text{fluid}}}{c_0k_BT}, \quad \tilde{h} = \frac{H_0}{R_0} , \quad (7.28)$$

Equation (7.27) takes the dimensionless form ,

$$\tilde{p}_{\text{fluid}}\Big|_{\tilde{r}=\tilde{R}} = \tilde{Y}\left\{\frac{1}{2}\left[\left(\frac{\tilde{R}+\tilde{h}/\tilde{R}}{1+\tilde{h}}\right)^2 - \tilde{R}^2\right] - \ln\left[\frac{\tilde{R}+\tilde{h}/\tilde{R}}{\tilde{R}+\tilde{h}\tilde{R}}\right]\right\} . \quad (7.29)$$

The right-hand side of Equation (7.29) is the elastic pressure, p_{elastic}, giving the elastic response to the fluid pressure so that the balance $\tilde{p}_{\text{fluid}} = \tilde{p}_{\text{elastic}}$ is achieved at the channel walls. A plot of $\tilde{p}_{\text{elastic}}$ as a function of $\tilde{R}$ is shown in Figure 7.3, for $\tilde{h} = 0.1,\ 0.5$ and 1. The elastic pressure is such that it becomes zero at $\tilde{R} = 1$, corresponding to the undeformed configuration.

The fluid pressure at the wall can also be described as resulting from local electrokinetics and can be expressed in terms of the electric potential at the channel's inner surface by appealing to the Stokes equation at equilibrium, where $\boldsymbol{u} = 0$:

$$\nabla p_{\text{fluid}} = -qc\nabla\psi . \quad (7.30)$$

Integrating Equation (7.30) along r from the potential reference point $\psi = 0$ to the channel wall, one obtains the dimensionless equation,

$$\tilde{p}_{\text{fluid}}\Big|_{\tilde{r}=\tilde{R}} = \tilde{p}_0 - \tilde{\psi}^2\Big|_{\tilde{r}=\tilde{R}} . \quad (7.31)$$

Note that the linear approximation $\tilde{c} = \tilde{c}_0\tilde{\psi}$ was used (see Equation (7.7)). In Equation (7.31), $\tilde{p}_0$ is the fluid pressure (in dimensionless form) at the reference $\tilde{\psi} = 0$, and it can be found by using the condition $\tilde{p}_{\text{fluid}}|_{\tilde{r}=1} = 0$. This gives $\tilde{p}_0 = \tilde{\psi}^2|_{\tilde{r}=1}$.

7.3 Numerical methods

We summmarize the 1-D system of differential-algebraic equations for $\tilde{\psi}_0$, $\tilde{\psi}_2$, $\tilde{\psi}_4$ and $\tilde{R}$ that need to be solved:

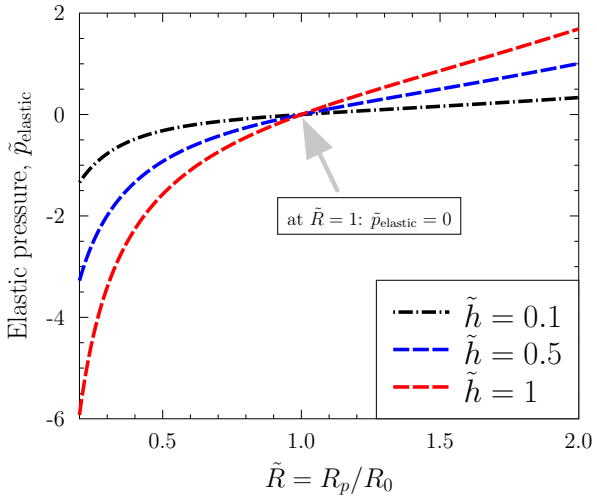

Figure 7.3: The elastic response of the channel vs. the radius.

$$\frac{d^2\tilde{\psi}_0}{d\tilde{z}^2} = \tilde{c}_0\tilde{\psi}_0 - 4\tilde{\psi}_2 \,, \tag{7.32a}$$

$$\frac{d^2\tilde{\psi}_2}{d\tilde{z}^2} = \tilde{c}_0\tilde{\psi}_2 - 16\tilde{\psi}_4 \,, \tag{7.32b}$$

$$\frac{d^2\tilde{\psi}_4}{d\tilde{z}^2} = \left(\frac{12}{\tilde{R}^4}\right)\tilde{\psi}_2 + \left(\frac{24 + \tilde{c}_0\tilde{R}^2}{\tilde{R}^2}\right)\tilde{\psi}_4 - \frac{6\tilde{\sigma}}{R^{5+\alpha}} \,, \tag{7.32c}$$

$$\tilde{\psi}^2|_{\tilde{r}=1} - \tilde{\psi}^2|_{\tilde{r}=\tilde{R}} = \tilde{Y}\left\{\frac{1}{2}\left[\left(\frac{\tilde{R} + \tilde{h}/\tilde{R}}{1+\tilde{h}}\right)^2 - \tilde{R}^2\right] - \ln\left[\frac{\tilde{R} + \tilde{h}/\tilde{R}}{\tilde{R} + \tilde{h}\tilde{R}}\right]\right\} \,, \tag{7.32d}$$

where $\tilde{\psi}(\tilde{\boldsymbol{r}}) = \tilde{\psi}(\tilde{\psi}_0(z), \tilde{\psi}_2(z), \tilde{\psi}_4(z), \tilde{r})$ according to Equation (7.10). Equations (7.32) go along with the boundary conditions

$$\tilde{\psi}_2 = \tilde{\psi}_4 = 0 \quad \text{at} \quad \tilde{z} = \pm\frac{\ell}{2} \,, \tag{7.33a}$$

$$\tilde{\psi}_0 = \tilde{V}_R \quad \text{at} \quad \tilde{z} = +\frac{\ell}{2} \,, \tag{7.33b}$$

$$\tilde{\psi}_0 = \tilde{V}_L \quad \text{at} \quad \tilde{z} = -\frac{\ell}{2} \,, \tag{7.33c}$$

$$\left[24\tilde{R}^{\alpha}\,\frac{\partial\tilde{\psi}_0}{\partial\tilde{z}}+10\tilde{R}^{\alpha+2}\,\frac{\partial\tilde{\psi}_2}{\partial\tilde{z}}+4\tilde{R}^{\alpha+4}\,\frac{\partial\tilde{\psi}_4}{\partial\tilde{z}}+\left[8\tilde{R}^{\alpha+1}(\tilde{\psi}_2+\tilde{\psi}_4\tilde{R}^2)-(5+\alpha)\tilde{\sigma}\right]\,\frac{\partial\tilde{R}}{\partial\tilde{z}}\right]\Bigg|_{\tilde{z}=-\ell/2}$$

$$=\left[24\tilde{R}^{\alpha}\,\frac{\partial\tilde{\psi}_0}{\partial\tilde{z}}+10\tilde{R}^{\alpha+2}\,\frac{\partial\tilde{\psi}_2}{\partial\tilde{z}}+4\tilde{R}^{\alpha+4}\,\frac{\partial\tilde{\psi}_4}{\partial\tilde{z}}+\left[8\tilde{R}^{\alpha+1}(\tilde{\psi}_2+\tilde{\psi}_4\tilde{R}^2)-(5+\alpha)\tilde{\sigma}\right]\,\frac{\partial\tilde{R}}{\partial\tilde{z}}\right]\Bigg|_{\tilde{z}=+\ell/2}, \tag{7.33d}$$

and constraint (7.19). The swelling model and the scaling of the surface charge density $\sim 1/R^{5+\alpha}$ make the model nonlinear, even in the linear regime for ψ. The equations are solved using the finite element method implemented in Comsol Multiphysics. The 'General Form PDE' interface is used to implement Equations (7.32a)–(7.32c), and the 'Domain ODEs and DAEs' interface is used to implement Equation (7.32d). The 'Global Constraint' function is used to implement all constraints. Boundary conditions are enforced using the standard 'Dirichlet and flux' functions under the 'General Form PDE' interface.

7.4 Results and discussion

We first consider a rigid channel characterized by $\tilde{R}=1$. This conforms to the 2-D problem investigated in Chapter 6. Figure 7.4 shows the functions $\tilde{\psi}_0$, $\tilde{\psi}_2$, $\tilde{\psi}_4$ and $\tilde{\psi}_6$ along the channel for different values of $\tilde{\sigma}$. We observe that high $|\tilde{\sigma}|$ values lead to high potentials along the channel. Equation (7.10) relies on the assumption that $\psi_0 \geq \psi_2 \geq \psi_4 \geq \psi_6$. However, when $|\tilde{\sigma}|$ is high, this assumption is not valid near the channel ends, where $\tilde{\psi}_6 > \tilde{\psi}_4$. Hence, it is essential that the channel is weakly charged for the 1-D model to hold.

We now analyse the validity of the 1-D model in detail. Figure 7.5 shows the electric potential profiles across the center of the channel ($\tilde{z}=0$). Results are compared with those from the 2-D model from Chapter 6. We notice an agreement between the two results for all three values of $\tilde{\sigma}$ explored. Hence, the sensitivity of our model to $\tilde{\sigma}$ is only noticeable near the channel ends but not at the center of the channel.

Upon deformation, the total number of ions N_T in the channel should be conserved. This is also required when one does parametric studies of the problem. This constraint is enforced via

$$N_T=\int_{\Omega}c(\boldsymbol{r})d^3\boldsymbol{r}\;\approx\;\frac{qz^2c_0}{k_BT}\int_{-L_p/2}^{L_p/2}\int_0^{R_p}\psi(r,z)rdrdz\;, \tag{7.34}$$

which can be expressed in dimensionless form as

$$\tilde{N}_T=\int_{-\ell/2}^{\ell/2}\left[\frac{4[(6\tilde{\psi}_0+3\tilde{\psi}_2+2\tilde{\psi}_4)\tilde{R}^5-2\tilde{\psi}_4\tilde{R}^3-\psi_2\tilde{R}]\tilde{R}^{\alpha}+\sigma}{48\tilde{R}^{5+\alpha}}\right]d\tilde{z}\;, \tag{7.35}$$

where $\tilde{N}_T=N_T/c_0R_0^3$.

Figure 7.6 shows the variation of the channel radius $\tilde{R}$ along the channel's length after deformation. We see deformations up to the order of 10%. The parameters used correspond

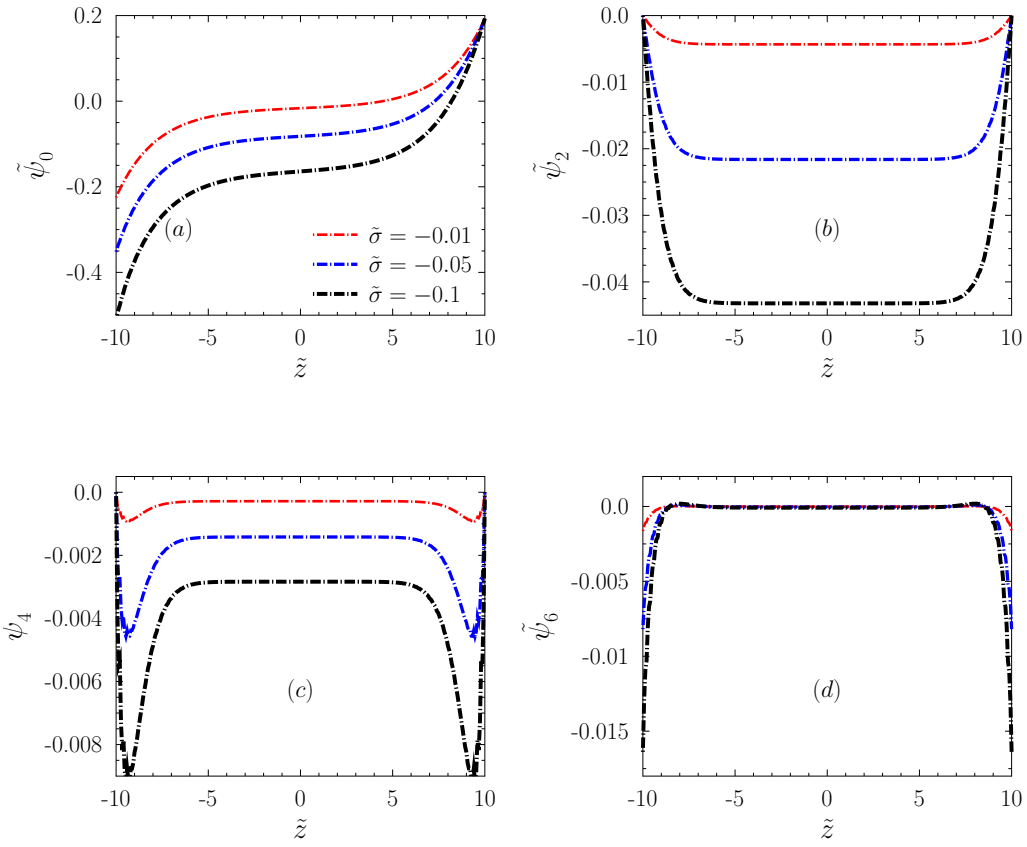

Figure 7.4: Typical axial profiles of the functions $\tilde{\psi}_0$, $\tilde{\psi}_2$, $\tilde{\psi}_4$ and $\tilde{\psi}_6$. Different curves represent different values of $\tilde{\sigma}$ shown in the legend of (a). Parameters used: $\tilde{c}_0 = 1$, $\tilde{R} = 1$, $\tilde{V}_R = 0.2$, $\ell = 20$.

to surface charge densities ~ 1 mC/m^2, voltage bias ~ 1 mV, ionic concentration ~ 10 mM. One noteworthy observation is that a weakly charged channel deforms more, with deformation more pronounced near electrodes. This can be argued from the fact that at low $|\tilde{\sigma}|$ more counterions are drawn towards the cathode than towards the channel walls. Also, the anode is ion-deficient. This leads to more pronounced swelling and shrinkage near the cathode and anode, respectively. For high $|\tilde{\sigma}|$, however, the channel walls draw more ions and swelling near the channel center is also realized. We notice this with the black curve in Figure 7.6, which floats above 1 at the channel center. Near the channel ends, deformations are not as predominant as for the case when $|\tilde{\sigma}|$ is low. Higher $\Delta\tilde{V}$ leads to high deformations near the electrodes, as anticipated. Apparently, deformations are more sensitive to $\Delta\tilde{V}$ than the other parameters explored. Note that in all calculations we used $\alpha = 1$ to conserve the total amount of charge on the channel walls, since L_p is assumed constant.

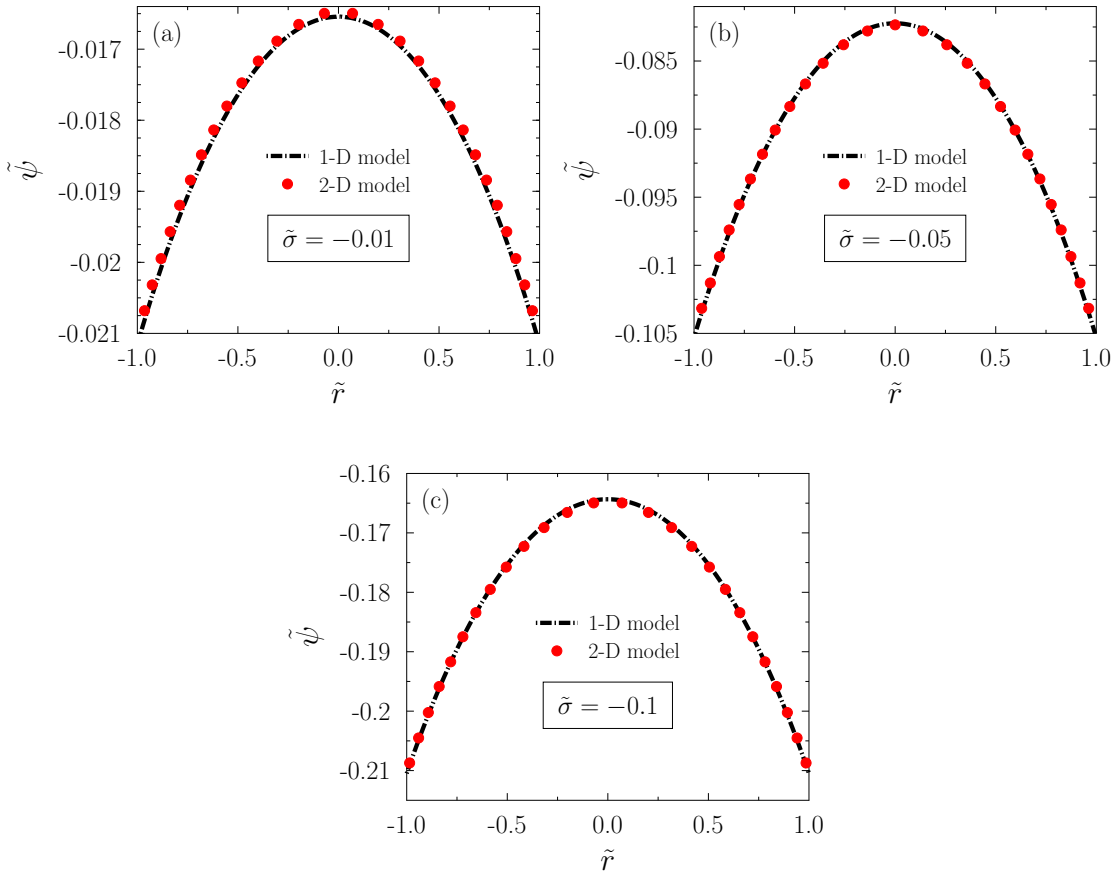

Figure 7.5: Typical radial profiles of the electric potential $\tilde{\psi}(\tilde{r})$ at $\tilde{z} = 0$ for (a) $\tilde{\sigma} = -0.01$, (b) $\tilde{\sigma} = -0.05$ and (c) $\tilde{\sigma} = -0.1$. Red dots show numerical results from the full 2-D model. Parameters used: $\tilde{c}_0 = 1,\ \tilde{R} = 1,\ \tilde{h} = 0.5,\ \ell = 20$.

From Figure 7.6(c), we see that c_0 only affects the decay length of the curvature in $\tilde{R}(z)$, as measured from the electrodes. At low c_0, the axial decay length of ψ near the electrodes becomes larger, implying a slower decay of ionic distributions near the channel ends. Consequently, the decay length of $\tilde{R}(z)$ will be increased. Finally, Figure 7.6(d) shows that at very low aspect ratio, the channel deforms linearly along z, assuming a conical shape. It is essential to underline that all results, with the exception of Figure 7.6(b), are found while enforcing $\Delta\tilde{V} = 0.2$, and the constraint in Equation (7.35) is relaxed for results in Figure 7.6(c). Also, the analysis is restricted to the linear regime which includes any small pertubations around the equlibrium channel configuration $\Delta\tilde{V} = 0,\ \tilde{r}(\tilde{z}) = 1$.

One means of understanding the nature of the deformation is by looking at the channel displacement $|\Delta\tilde{R}| = |\tilde{R} - 1|$ at the ends ($\tilde{z} = \pm\ell/2$). This gives the extent of opening and closing of the channel at the cathode and anode ends, respectively. Plots of $|\Delta\tilde{R}|$ are shown in Figure 7.7 as continuous functions of $\tilde{\sigma}$, $\Delta\tilde{V}$, $\tilde{c}_0$ and ℓ. With the exception of Figure

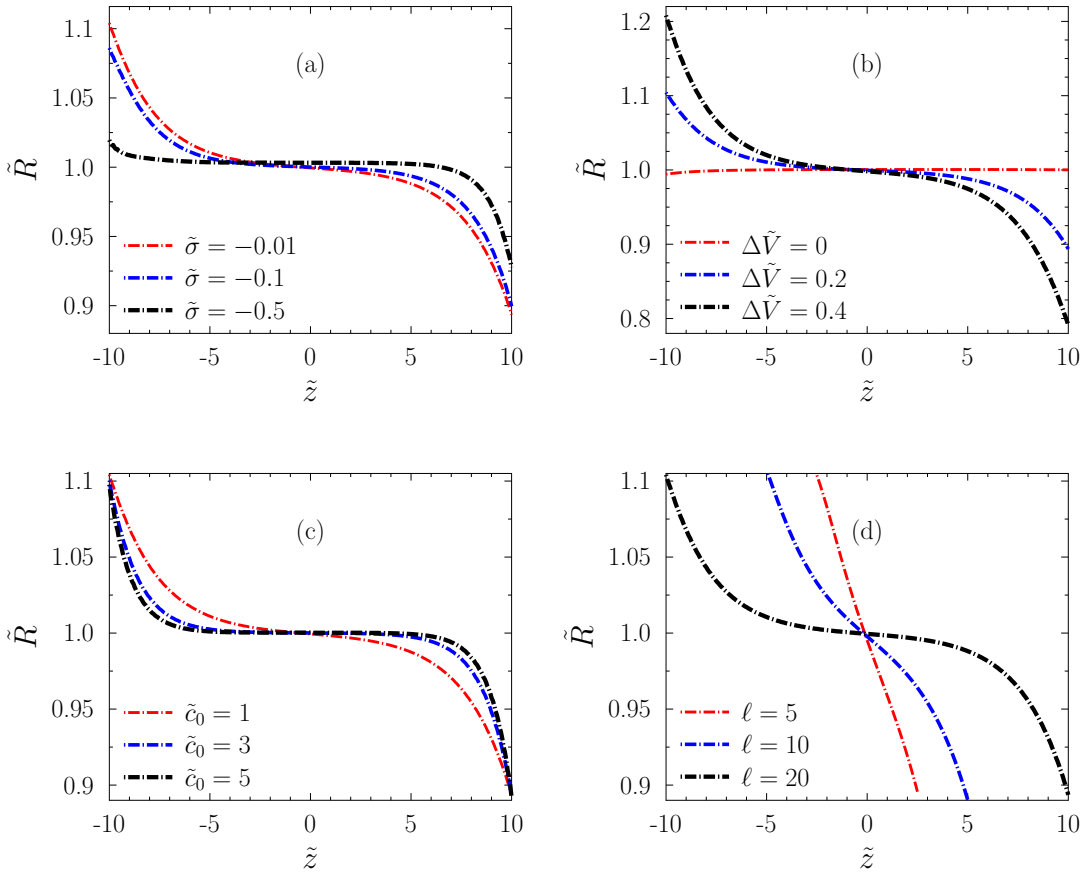

Figure 7.6: Radial deformation of the channel as a function of $\tilde{z}$ for different values of (a) $\tilde{\sigma}$, (b) $\Delta\tilde{V}$, (c) $\tilde{c}_0$ and (d) ℓ. Parameters used: $\tilde{\sigma} = -0.01,\ \tilde{c}_0 = 1,\ \Delta\tilde{V} = 0.2,\ \tilde{h} = 0.5,\ \ell = 20,\ \alpha = 1$.

7.7(b), displacement changes along each parameter sweep are very small, of the order of 1%. However, one can learn a lot from the qualitative behaviour of each plot. The opening of the cathode end is more sensitive to $\tilde{\sigma}$, compared to the closing of the anode end (see Figure 7.7(a)). Both ends have linear sensitivity to $\tilde{\sigma}$. From Figure 7.7(b), we observe that $|\Delta\tilde{R}|$ is strongly and equally sensitive to ΔV for both ends of the channel. Increasing $\tilde{c}_0$ forces the cathode end to start shrinking and the anode end to start opening (see Figure 7.7(c)). This drives the channel to the state in which the highly abundant ions occupy all regions in the channel. As the channel's aspect ratio increases, the channel ends open and close less due to reduced overall concentration of ions within the channel (see Figure 7.7(d)).

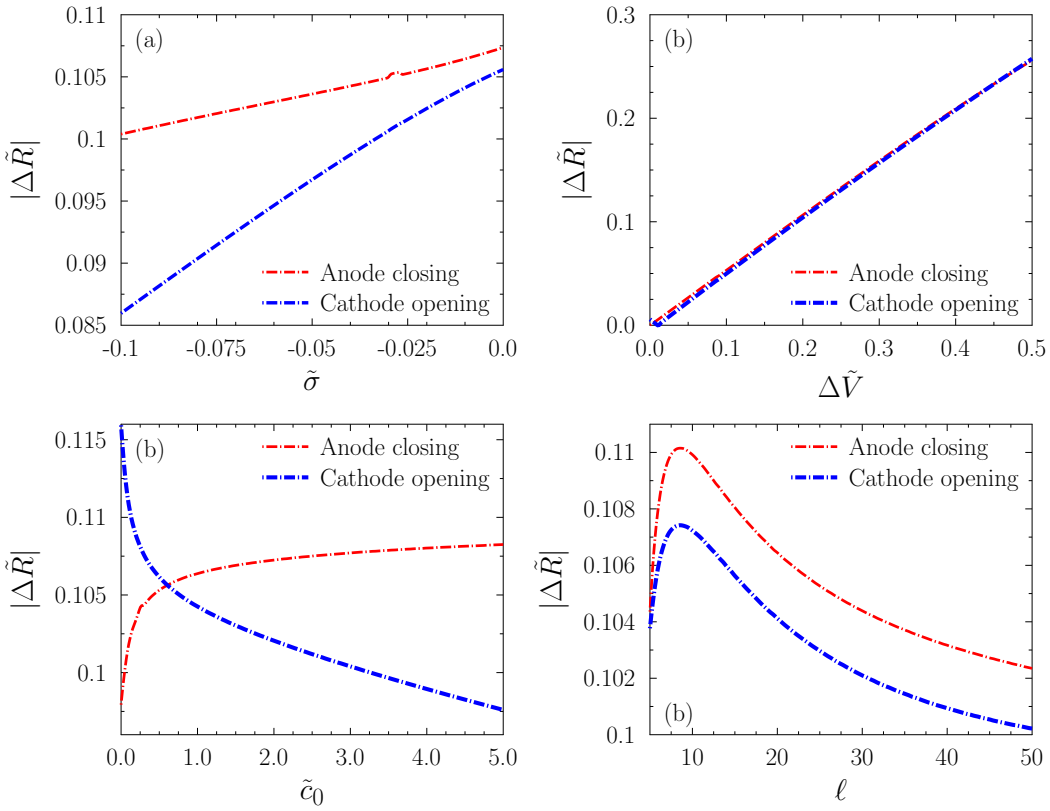

Figure 7.7: The influence of (a) $\tilde{\sigma}$, (b) $\Delta\tilde{V}$, (c) $\tilde{c}_0$ and (d) ℓ on the opening of the cathode end and shrinkage of the anode side of the channel. The hiccup in the data seen in (a) comes from an unidentified numerical error. Parameters used: $\tilde{\sigma} = -0.01,\ \tilde{c}_0 = 1,\ \Delta\tilde{V} = 0.2,\ \tilde{h} = 0.5,\ \ell = 20,\ \alpha = 1$.

7.5 Summary

As an extension to the previous chapter, this chapter provided a preliminary exploration of the behaviour of a deformable nanochannel of circular cross section, sealed at both ends by metal electrodes under external voltage bias. Based on a polynomial expansion of the electric potential in the radial coordinate, a 1-D model was derived that couples the equilibrium distribution of ions and the elastic deformations of the neo-Hookean channel walls in response to fluid pressure on the surface. Numerical results show agreement between the 1-D model and the full 2-D model studied in Chapter 6 for the case of a rigid channel with uniform radius. Channel deformations are sensitive to the surface charge density on the channel walls, the voltage bias between electrodes, the number of ions in the channel, and the channel geometry. We explored how sensitive the extent of channel opening and closing are to these parameters. Somewhat surprisingly, weakly charged channel walls deform more

than strongly charged ones. Compared to all other explored parameters, we found that the deformations are most sensitive to the voltage bias.

Chapter 8

Conclusions and Outlook

In this final chapter, the main findings of the work are summarised and discussed, and suggestions are presented for future studies.

8.1 Conclusions

In this thesis, theoretical and numerical investigations of electrokinetic effects in soft cylindrical nanochannels were carried out. The aim was to provide a theoretical framework through which one can obtain a comprehensive understanding of the coupling between electrokinetic transport, double-layer charging and wall deformations in nanochannels embedded in soft polymeric membranes. To reach this goal, the work provided in this thesis is divided into four parts.

In the first part (Chapter 3), numerical calculations using the coupled Poisson-Nernst-Planck and Stokes equations were conducted to quantify ion and fluid transport in a finite, cylindrical and rigid nanochannel connected to cylindrical electrolytic reservoirs. Results from this part of the thesis served as a guideline for theoretical investigations in later components of the thesis. We presented numerical results from COMSOL for the fluid pressure, velocity profiles and ionic current within the channel. The study substantiates that high surface charging and large channel widths give rise to plug-like and concave-shaped fluid velocity profiles across the channel. We observed the emergence of the Donnan potential gradient along the channel, which manifests as a fluid pressure build-up in the channel's interior. Calculations of the ionic current reveal that advective current flow dominates at the EDL regions in the vicinity of the channel walls, while eloctromigration current dominates at the center of the channel. Results manifest a pronounced influence on the overall current of the channel's surface charge density, the bulk concentration and the channel size. The channel was found to exhibit a high degree of perm-selectivity at high surface charge densities, low bulk concentrations and small channel sizes. Numerical results match conductance experimental data available from the literature.

In the second part of the thesis (Chapters 4 and 5), the transport of protons and water in a long, negatively charged channel was studied from a theoretical point of view. At the outset, we presented simplifications of the otherwise complex continuum equations for a uniform radius and long channel, enabling us to access analytical solutions and explore electroneutrality properties and their impact on the transport. Next, a theoretical model was developed that describes nonlinear coupling between wall deformation and water and proton flows in a charged, deformable nanochannel whose viscoelasticity is governed by the Kelvin-Voigt model. Using continuum mean-field theories for mass and momentum conservation of the solid-liquid coupled system, a set of one-dimensional nonlinear partial differential equations was derived to capture the dynamics of wall deformations. For elastic but non-viscous walls undergoing small deformation, the problem simplifies to one of advection-diffusion type which is analytically solvable at first-order perturbation.

Perhaps the most striking finding of this work is the evidence for a rich coupling between the elasticity and charge distribution of the channel walls, which vanishes in the limit of weakly charged channels. This coupling significantly alters the quantitative response of the walls' relaxation dynamics and the channel's electrokinetic transport, thereby having important consequences for the description and understanding of electrokinetic flow through charged, elastic media. Within the framework of nonequilibrium thermodynamics, compact formulae are derived for the electrokinetic transport parameters in terms of Onsager phenomenological coefficients and, subsequently, for the energy conversion efficiency. Results confirm that Onsager's reciprocity principle holds for rigid channels. However, the methodology used to derive a 1D formulation of the problem does not maintain the symmetry of Onsager's matrix when the channel is deformed, owing to the introduction of a 'fictitious' diffusion term of counter-ions. Furthermore, the model predicts a reduced efficiency of electrokinetic energy harvesting for channels with soft deformable walls.

The third part (Chapter 6) of the thesis took a different direction from the previous chapters. Instead of focusing on transport phenomena in an open nanochannel, we directed our attention to the equilibrium structure of the electric double layers. This was achieved by considering a physical situation where the charged channel is finite and sealed at both ends by metal electrodes under external voltage bias. Size-modified mean-field equations were used to account for finite ion sizes, subject to a self-consistent electroneutrality condition which demands that the net charge on both electrode surfaces balances. The time evolution of the formation and relaxation of the double layers was explored. Moreover, equilibrium ion distributions and differential capacitance curves were investigated as functions of the pore surface charge density, electrolyte concentration, ion sizes and pore size. Asymmetric properties of the differential capacitance curves reveal that the structure of the double layer near each electrode is controlled by the charge concentration along the pore surface and by charge asymmetry in the electrolyte. These results carry implications for accurately simulating cylindrical capacitors.

The last part (Chapter 7) of the thesis added deformations on the channel walls to the system of a charged channel that is sealed at both ends by metal electrodes under external voltage bias. Motivated by ionic metal polymer composite actuators, the goal was to transform the sealed channel into a surface-charge-mediated actuating system that has the capability to swell and shrink in response to counter-ion flooding at different regions of the channel. To simplify the 2-D equations for the model system, the electric potential was approximated as a polynomial expansion in the radial coordinate, whose coefficients are functions of the axial coordinate. Assuming a weakly charged channel whose walls are neo-Hookean, this enabled us to reduce the 2-D model to a 1-D system of differential-algebraic equations. Numerical solutions of the 1-D model agree with the full 2-D model. Results demonstrate that channel deformations are sensitive to the surface charge density on the channel walls, the voltage bias between electrodes, the number of charged species in the channel, and the channel geometry. We further explored the opening and closing at the channel ends. We found that weakly charged channels deform more than the strongly charged ones, and deformations are more sensitive to the voltage bias than the surface charge density on the channel walls.

8.2 Outlook

There are a number of possible directions for further study. Much attention could be directed to running more numerical simulations for deformational properties of the channel. In this work, numerical work that involves the full channel deformations was avoided. Instead, we opted to reduce the dimensionality of the model first. Simulating the 2-D model equations can be time-consuming and computationally costly since one has to take care of moving boundaries. In the future, with available time and computational resources, numerical simulations of the full model can be conducted. This will enable us to relax some of the assumptions proposed in this work and compare new findings to the results we have obtained so far.

In Chapter 4, we carefully derived a 1-D model for deformations of the channel and found an 'advection-diffusion' type equation. Further work could involve finding travelling wave solutions for the channel deformations. Intuition tells us that such solutions could be obtainable, albeit restricted to a certain domain of parameters or initial conditions. Likewise, we can attempt to find out if shock waves are characteristic of the deformations. If travelling waves are obtained, one can find their properties, such as the wave speed, as functions of the charging properties of the channel.

Collaborations with experimentalists can be helpful in assessing the validity of our results pertaining to channel deformations. So far, experimental work in the literature does not focus on the coupling between transport and deformations in nanochannels. The last chapter, for instance, introduced a model system that can use a sealed cylindrical channel

as an electroactuator. This system can be studied experimentally and can potentially find applications in designing new nano-sensitive actuating devices.

Bibliography

[1] F. F. Reuss, Mem. Soc. Imp. Nat. Moscou **2**, 327 (1809).

[2] F. F. Reuss, Comment. Soc. Phys. Med. Univ. Lit. Caesaream Mosquensem **2**, 307 (1821).

[3] H. L. F. Helmholtz, Wied. Ann. **7**, 337 (1879).

[4] M. Smoluchowski, Phys. Z. **6**, 529 (1905).

[5] A. J. Bard and L. R. Faulkner, *Electrochemical methods: fundamentals and applications*, 2nd ed. (Wiley New York, 1980).

[6] M. Gouy, J. Phys. Theor. Appl. **9**, 457 (1910).

[7] D. L. Chapman, Phil. Mag. S. **25**, 475 (1913).

[8] M. Z. Bazant, M. S. Kilic, B. D. Storey, and A. Ajdari, Adv. Colloid Interface Sci. **152**, 48 (2009).

[9] O. Stern, Z. Elektrochem. **30**, 508 (1924).

[10] I. Borukhov, D. Andelman, and H. Orland Phys. Rev. Lett. **79**, 435 (1997).

[11] I. Borukhov, D. Andelman, and H. Orland, Electrochim. Acta. **46**, 221 (2000).

[12] R. D. Coalson and A. Duncan, J. Chem. Phys. **97**, 5653 (1992).

[13] J. J. Bikerman, Philos. Mag. **33**, 384 (1942).

[14] V. Freise, J. Phys. Chem **58**, 702 (1954).

[15] E. Wicke and M. Eigen, Naturwiss. **38**, 453 (1951).

[16] E. Wicke and M. Eigen, Z. Elektrochem. **56**, 551 (1952).

[17] M. Eigen and E. Wicke, J. Phys. Chem. **58**, 702 (1954).

[18] P. Strating and F. W. Wiegel, J. Phys. A **26**, 3383 (1993).

[19] P. Strating and F. W. Wiegel, Physica A **193**, 413 (1993).

[20] K. Bohinc, V. Kralj-Iglic, and A. Iglic, Electrochim. Acta **46**, 3033 (2001).

[21] K. Bohinc, A. Iglic, T. Slivnik, and V. Kralj-Iglic, Bioelectrochemistry **57**, 73 (2002).

[22] A. A. Kornyshev, J. Phys. Chem. B **111**, 5545 (2007).

[23] M. S. Kilic, M. Z. Bazant, and A. Ajdari, Phys. Rev. E **75**, 021502 (2007).

[24] M. S. Kilic, M. Z. Bazant, and A. Ajdari, Phys. Rev. E **75**, 021503 (2007).

[25] M. Z. Bazant, M. S. Kilic, B. D. Storey, and A. Ajdari, Adv. Colloid Interface Sci. **152**, 48 (2009).

[26] M. Z. Bazant, K. Thornton, and A. Ajdari, Phys. Rev. E **70**, 021506 (2004).

[27] S. Prakash and A. T. Conlisk, Lab on a Chip **16**, 3855 (2016).

[28] T. Tsukahara, K. Mawatari, and T. Kitamori, Chem. Soc. Rev **39**, 1000 (2010).

[29] M. Tagliazucchi and I. Szleifer, Mater. Today **18**, 131 (2015).

[30] S. J. Kim, S. H. Ko, K. H. Kang, H. Kwan, and J. Han, Nature Nanotechn. **5**, 297 (2010).

[31] H. Daiguji, P. Yang, A. J. Szeri, and A. Majumdar, Nano Lett. **4**, 2315 (2004).

[32] F. H. van der Heyden, H. J. Frank, D. J. Bonthuis, D. Stein, C. Meyer, and C. Dekker, Nano letters **7**, 1022 (2007).

[33] S. Chung, O. S. Anderson, S. Olaf, and V. V. Krishnamurthy, *Biological membrane ion channels: dynamics, structure, and applications* (Springer Science & Business Media, 2007).

[34] R. Kwak, S. J. Kim, and J. Han, Anal. Chem. **83**, 7348 (2011).

[35] C. Dekker, Nat. Nanotechnol. **2**, 209 (2007).

[36] K. Jiao and X. Li, Prog. Energy Combust. Sci. **37**, 221 (2011).

[37] M. Eikerling and A. Kulikovsky, *Polymer electrolyte fuel cells: Physical principles of materials and operation*, (CRC Press, 2014).

[38] K. Kreuer, S. J. Paddison, E. Spohr, and M. Schuster, Chem. Rev. **104**, 4637 (2004).

[39] A. Z. Weber and J. Newman, J. Electrochem. Soc. **150**, A1008 (2003).

[40] A. Z. Weber and J. Newman, J. Electrochem. Soc. **151**, A311 (2004).

[41] A. Z. Weber and J. Newman, Chem. Rev. **104**, 4679 (2004).

[42] Z. Peng, A. Morin, P. Huguet, P. Schott, and J. Pauchet, J. Phys. Chem. B **115**, 12835 (2011).

[43] S. G. Rinaldo, C. W. Monroe, T. Romero, W. Mérida, and M. Eikerling, Electrochem. Commun. **33**, 5 (2011).

[44] J. B. Benziger, M. J. Cheah, V. Klika, and M. Pavelka, J. Polym. Sci. Part B Polym. Phys. **53**, 1580 (2015).

[45] M. J. Cheah, I. G. Kevrekidis, G. Ioannis, and J. Benziger, J. Phys. Chem. B **115**, 10239 (2011).

[46] M. H. Eikerling and P. Berg, Soft Matter **7**, 5976 (2011).

[47] M. Safiollah, P. A. Melchy, P. Berg, and M. Eikerling, J. Phys. Chem. B **119**, 8165 (2015).

[48] P. Berg and K. Ladipo, Proc. Royal Soc. A **465**, 2663 (2009).

[49] P. Berg and J. Findlay, Proc. Royal Soc. A **467**, 3157 (2011).

[50] K. O. Ladipo, P. Berg, S. Kimmerle and A. Novruzi, Int. J. Chem. Phys. **134**, 074103 (2011).

[51] Z. Rao, C. Zheng, and F. Geng, Comput. Mater. Sci. **142**, 122 (2017).

[52] W. Hsu, D. J. Harvie, M. R. Davidson, D. E. Dunstan, J. Hwang, and H. Daiguji, J. Phys. Chem. C **121**, 20517 (2017).

[53] Z. Yuan, A. L. Garcia, G. P. Lopez, and D. N. Petsev, Electrophoresis **28**, 595 (2007).

[54] P. Panda, K. P. Yuet, D. Dendukuri, T. A. Hatton, and P. S. Doyle, New J. Phys. **11**, 115001 (2009).

[55] K. A. Mauritz, and R. B. Moore, Chem. Rev **104**, 4535 (2004).

[56] V. Studer, G. Hang, A. Pandolfi, M. Ortiz, A. W. French, and S. R. Quake, J. Appl. Phys. **95**, 393 (2004).

[57] A. Pandol and M. Ortiz, J. Micromech. Microeng. **17**, 1487 (2007).

[58] A. R. Abate and D. A. Weitz, Appl. Phys. Lett. **92**, 243509 (2008).

[59] O. Eytan and D. Elad, Bull. Math. Biol. **61**, 221 (1999).

[60] H. Shen, Y. Zhu, and K. Qin, Med. Eng. Phys. **38**, 1439 (2016).

[61] D. Pugal, K. Jung, A. Aabloo, and K. J. Kim, Polymer International **59**, 279 (2010).

[62] K. Oguro, Y. Kawami, and H. Takenaka, J. Micromachine Soc. **5**, 27 (1992).

[63] M. Shahinpoor, Y. Bar-Cohen, J. O. Simpson, and J. Smith, Smart Mater. Struct. **7**, R15 (1998).

[64] Z. A. Goodwin, M. Eikerling, H. Löwen, and A. A. Kornyshev, Smart Mater. Struct. **27**, 075056 (2018).

[65] Y. Bar-Cohen, *Electroactive polymer (EAP) actuators as artificial muscles: reality, potential, and challenges*, (Bellingham, WA: SPIE press, 2004).

[66] P. Arena, C. Bonomo, L. Fortuna, M. Frasca, and S. Graziani, IEEE Trans. Syst. Man, Cybern., Part B: Cybern. **36**, 1044 (2006).

[67] P. Calvert, Adv. Mater. **21**, 743 (2009).

[68] S. W. Yeom and I. K. Oh, Smart Mater. Struct. **18**, 085002 (2009).

[69] Y. Kato, T. Sekitani, M. Takamiya, M. Doi, K. Asaka, T. Sakurai, and T. Someya, IEEE Trans. Electron Devices **54**, 202 (2007).

[70] B. K Fang, M. S Ju, and C. C. K. Lin, Sens. Actuators A **137**, 321 (2007).

[71] T. T. Nguyen, N. S. Goo, V. K. Nguyen, Y. Yoo, and S. Park, Sens. Actuators A **141**, 640 (2008).

[72] K. K. C. Lee, N. R. Munce, T. Shoa, L. G. Charron, G. A. Wright, J. D. Madden, and V. X. D. Yang, Sens. Actuators A **153**, 230 (2009).

[73] M. Aureli, C. Prince, M. Porfiri and S. D. Peterson, Smart Mater. Struct **19**, 1 (2010).

[74] Y. Bahramzadeh and M. Shahinpoor, Smart Mater. Struct. **20**, 094011 (2011).

[75] P. M. Ajayan, Nature **361**, 333–334 (1993).

[76] L. D. Gelb, K. E. Gubbins, R. Radhakrishnan, and M. Sliwinska–Bartkowiak, Rep. Prog. Phys. **62**, 1573 (1999).

[77] K. Murata, K. Mitsuoka, T. Hirai, T. Walz, P. Agre, J. B. Heymann, A. Engel, and Y. Fujiyoshi, Nature **407**, 599 (2000).

[78] D. A. Doyle, J. M. Cabral, R. A. Pfuetzner, A. L. Kuo, J. M. Gulbis, S. L. Cohen, B. T. Chait, and R. MacKinnon, Science **280**, 69 (1998).

[79] G. Gebel, Polymer **41**, 5829 (2000).

[80] K. Schmidt-Rohr and Q. Chen, Nat. Mater. **7**, 75 (2008).

[81] D. G. Haywood, A. Saha-Shah, L. A. Baker, and S. C. Jacobson, Anal. Chem. **87**, 172 (2014).

[82] J. W. Perram, R. J. Hunter, and H. J. L. Wright, Chem. Phys. Lett. **23**, 265 (1973).

[83] S. H. Behrens and M. Borkovec, Phys. Rev. E **60**, 7040 (1999).

[84] F. Hingston, R. Atkinson, A. Posner, and J. Quirk, Nature **215**, 1459 (1967).

[85] G. Sposito, N. T. Skipper, R. Sutton, S. H. Park, A. K. Soper, and J. A. Greathouse, Proc. Nat. Acad. Sci. **96**, 3358 (1999).

[86] B. Abecassis, C. Cottin-Bizonne, C. Ybert, A. Ajdari, and L. Bocquet, New J. Phys. **11**, 075022 (2009).

[87] L. Bocquet and P. Tabeling, Lab on a Chip **17**, 3143 (2014).

[88] A. J. Appleby and R. L. Foulkes, *Fuel cell handbook*, (Van Nostrand, New York, 1989).

[89] M. Yoshitake and A. Watakabe, A. Adv. Polym. Sci. **215**, 127 (2008).

[90] K. A. Mauritz and R. B. Moore, Chem. Rev. **104**, 4535 (2004).

[91] T. J. Peckham and S. Holdcroft, Adv. Mater. **22**, 4667 (2010).

[92] Y. Lorrain, G. Pourcelly, and C. Gavach, Desalination **109**, 231 (1997).

[93] S. Liu, Q. Zhao, Q. Li, H. Zhang, L. You, J. Zhan, and D. Yu, Nanotechnology **22**, 115302 (2011).

[94] A. J. Storm, J. H. Chen, X. S. Ling, H. W. Zandbergen, and C. Dekker, C. Nat. Mater. **2**, 537 (2003).

[95] R. Karnik, K. Castelino, R. Fan, P. Yang, and A. Majumdar, Nano Lett. **5**, 1638 (2005).

[96] A. Uddin, S. Yemenicioglu, C. H. Chen, E. Corigliano, K. Milaninia, and L. Theogarajan, Nanotechnology **24**, 155501 (2013).

[97] P. Y. Apel, I. V. Blonskaya, O. L. Orelovitch, P. Ramirez, and B. A. Sartowska, Nanotechnology **22**, 175302 (2011).

[98] L. J. Guo, X. Cheng, and C. F. Chou, Nano Lett. **4**, 69 (2004).

[99] M. L. Kovarik and S. C. Jacobson, Anal. Chem. **79**, 1655 (2007).

[100] J. M. Perry, K. Zhou, Z. D. Harms, and S. C. Jacobson, ACS Nano **4**, 3897 (2010).

[101] S. H. Roelofs, A. van den Berg, and M. Odijk, Lab on a Chip **15**, 3428 (2015).

[102] D. Li and H. Wang, J. Mat. Chem. **20**, 4551 (2010).

[103] D. Deng, W. Aouad, W. A. Braff, S. Schlumpberger, M. E. Suss, and M. Z Bazant, Desalination **357**, 77 (2015).

[104] K. Oguro, N. Fujiwara, K. Asaka, K. Onishi, and S. Sewa, Electroactive Polymer Actuators and Devices **3669**, 64 (1999).

[105] N. Fujiwara, K. Asaka, Y. Nishimura, K. Oguro, and E. Torikai, Chem. Mater. **12**, 1750 (1999).

[106] A. J. Duncan, D. J. Leo, and T. E. Long, Macromolecules **41**, 7765 (2008).

[107] J. F. Osterle, J. Appl. Mech. **31**, 161 (1964).

[108] J. Yang, F. Lu, L. W. Kostiuk, and D. Y. Kwok, J. Micromech. Microeng. **13**, 963 (2003).

[109] W. Olthuis, B. Schippers, J. Eijkel, and A. van den Berg, Sens. Actuators **111**, 385 (2005).

[110] M. C. Lu, S. Satyanarayana, R. Karnik, A. Majumdar, and C. C. Wang, Micromech. Microeng. **16**, 667 (2006).

[111] F. H. van der Heyden, D. J. Bonthuis, D. Stein, C. Meyer, and C. Dekker, Nano Lett. **7**, 1022 (2007).

[112] H. Daiguji, Y. Oka, K. Shirono, and Z. S. Siwy, Nano Lett. **5**, 2274 (2005).

[113] M. A. M. Gijs, Nanotechnol. **2**, 268 (2007).

[114] I. Vlassiouk, T. R. Kozel, and Z. S. Siwy, J. Am. Chem. Soc. **131**, 8211 (2009).

[115] L. J. Cheng and L. J. Guo, ACS Nano **3**, 575 (2009).

[116] C. Cao and Y. T. Long, Acc. Chem. Res. **52**, 331 (2018).

[117] B. Hille, *Ion channels of excitable membranes*, Vol. 50, (Sunderland, Massachusetts: Sinauer, 1992).

[118] B. N. Miles, A. P. Ivanov, K. A. Wilson, F. Doğan, D. Japrung, and J. B. Edel, Chem. Soc. Rev. **42**, 15 (2013).

[119] J. J. Kasianowicz, E. Brandin, D. Branton, and D. W. Deamer, Proc. Nat. Acad. Sci. **93**, 13770 (1996).

[120] D. Fologea, M. Gershow, B. Ledden, D. S. McNabb, and J. A. Golovchenko, Nano Lett. **5**, 1905 (2005)

[121] C. Dekker, Nat. Nanotechnol. **2**, 209 (2007).

[122] D. B. Wells, M. Belkin, J. Comer, and A. Aksimentiev, Nano Lett. **12**, 4117 (2012).

[123] I. Borukhov, D. Andelman, and H. Orland, Phys. Rev. Lett. **79**, 435 (1997).

[124] N. Eliaz and E. Gileadi, *Physical electrochemistry: Fundamentals, techniques, and applications*, (John Wiley & Sons, 2019).

[125] D. A. Saville, Annu. Rev. Fluid Mech. **29**, 27 (1997).

[126] T. Alazard, Arch. Ration. Mech. Anal. **180**, 1 (2006).

[127] A. Plecis, R. B. Schoch, and P. Renaud, Nano Lett. **5**, 1147 (2005).

[128] W. Nernst, Z. Phys. Chem. **4**, 129 (1889).

[129] E. J. Dickinson, J. G. Limon-Petersen, and R. G. Compton, J Solid State Electr. **15**, 1335 (2011).

[130] C. L. Gardner, and J. R. Jones, J. Theor. Biol. **291**, 10 (2011).

[131] D. V. Melnikov, K. H. Hulings, and M. E. Gracheva, Phys. Rev. E **95**, 063105 (2017).

[132] J. P. Hsu, S. T. Yang, C. Y. Lin, and S. Tseng, J. Phys. Chem. C **121**, 4576 (2017).

[133] R. W. Clough, *The finite element method in plane stress analysis*, (In Proceedings of 2nd ASCE Conference on Electronic Computation, Pittsburgh Pa., 1960).

[134] H. Grandin, *Fundamentals of the finite element method*, (Macmillan, New York, 1986).

[135] G. Strang and G. L. Fix, *An analysis of the finite element method*, Vol. 212 (Englewood Cliffs, NJ: Prentice-hall, 2012).

[136] I. M. Smith, D. V. Griffiths, and L. Margetts, *Programming the finite element method*, (John Wiley & Sons, 2013).

[137] D. J.Tritton, *Physical fluid dynamics*, (Springer Science & Business Media, 2012).

[138] J. K. Mitchell, Clays Clay Miner. **10**, 162 (1962). Mitchell, J. K. "Components of pore water pressure and their engineering significance." In Clays and clay minerals, pp. 162-184. Pergamon, 1962.

[139] M. Kato and G. W. Wei, J. Theor. Biol. **177**, 299 (1995).

[140] J. Cervera, B. Schiedt, and P. Ramirez, Europhys. Lett. **71**, 35 (2005).

[141] Y. W. Jung, B. Lu, and M. Mascagni, J. Chem. Phys. **131**, 12B601 (2009).

[142] Q. Zheng and G. W. Wei, J. Chem. Phys. **134**, 194101 (2011).

[143] I. Valent, P. Petrovicč, P. Neograády, I. Schreiber, and M. Marek, J. Phys. Chem. B **117**, 14283 (2013).

[144] R. M. M. Smeets, U. F. Keyser, D. Krapf, M. Y. Wu, N. H. Dekker, and C. Dekker, Nano Lett. **6**, 89 (2006).

[145] P. B. Peters, R. van Roij, M. Z. Bazant, and P. M. Biesheuvel, Phys. Rev. E **93**, 053108 (2016).

[146] W. Y. Lo and K. Y. Chan, Mol. Phys. **86**, 745 (1995).

[147] D. Boda, D. D. Busath, B. Eisenberg, D. Henderson, and W. Nonner, Phys. Chem. Chem. Phys. **4**, 5154 (2002).

[148] D. Boda, M. Valiskó, B. Eisenberg, W. Nonner, D. Henderson, and D. Gillespie, J. Chem. Phys. **125**, 034901 (2006).

[149] Z. X. Luo, Y. Z. Xing, Y. C. Ling, A. Kleinhammes, and Y. Wu, Nat. Commun. **6**, 6358 (2015).

[150] A. Levy, J. P. de Souza, and M. Z. Bazant, "Breakdown of electroneutrality in nanopores," arxiv.org/abs/1905.05789.

[151] U. M. Marconi, S. Melchionna, and I. Ignacio, J. Chem. Phys. **138**, 244107 (2013).

[152] J. N. Reddy, *An introduction to continuum mechanics*, (Cambridge University Press, 2013).

[153] N. C. Rosero-Navarro, E. M. Domingues, N. Sousa, P. Ferreira, and F. M. Figueiredo, Int. J. Hydrog. Energy **39**, 5338 (2014).

[154] J. Melchior, T. Bräuniger, A. Wohlfarth, G. Portale, and K.Kreuer, Macromolecules **48**, 8534 (2015).

[155] G. B. Davis, Appl. Math. Model. **9**, 69 (1985).

[156] A. D. Ellery, M. J. Simpson, S. W. McCue, and R. E. Baker, Phys. Rev. E **85**, 041135 (2012).

[157] F. A. Morrison Jr. and J. F. Osterle, J. Chem. Phys. **43**, 2111 (1965).

[158] Y. Zhang, Y. He, M. Tsutsui, X. S. Miao, and M. Taniguchi, Sci. Rep. **7**, 46661 (2017).

[159] J. Yang, F. Lu, L. W. Kostiuk, and D. Y. Kwok, J. Micromechanics Microengineering **13**, 963 (2003).

[160] Y. Xie, X. Wang, J. Jin, K. Chen, and Y. Wang, Appl. Phys. Lett. **93**, 163116 (2008).

[161] C. C. Chang and R. J. Yang, Microfluidics and Nanofluidics **9**, 225 (2010).

[162] Y. Yan, Q. Sheng, C. Wang, J. Xue, and H. C. Chang, J. Phys. Chem. C **117**, 8050 (2013).

[163] C. Bakli and S. Chakraborty, Electrophoresis **36**, 675 (2015).

[164] J. Vatamanu and D. Bedrov, J. Phys. Chem. Lett. **6**, 3594 (2015).

[165] M. Burgess, J. S. Moore and J. Rodríguez-López, Acc. Chem. Res. **49**, 2649 (2016).

[166] J. P. Valleau, R. Ivkov, and G. M. Torrie, J. Chem. Phys **95**, 520 (1991).

[167] D. F. Evans and H. Wennerstrom, *The colloidal domain: Where physics, chemistry, biology, and technology meet*, 2nd ed. (Wiley New York, 1999).

[168] B. Hou, W. Bu, G. Luo, P. Vanysek and M. L Schlossman, J. Electrochem. Soc. **162**, H890 (2015).

[169] N. Huang, J. Tao, J. Liu, S. Wei, L. Li and Z. Wu, Soft Matter **10**, 4236 (2014).

[170] F. Mugele, B. Bera, A. Cavalli, I. Siretanu, A. Maestro, M. Duits, M. Cohen-Stuart, D. Van Den Ende, I. Stocker, and I. Collins, Sci. Rep. **5**, 10519 (2015).

[171] P. Długołkecki, P. Ogonowski, S. J. Metz, M. Saakes, K. Nijmeijer, and M. Wessling, J. Membrane Sci. **349**, 369 (2010).

[172] A. J. Bard and L. R. Faulkner, *Electrochemical methods: fundamentals and applications*, 2nd ed. (Wiley New York, 1980).

[173] M. Z. Bazant, K. Thornton and A. Ajdari, Phys. Rev. E **70**, 021506 (2004).

[174] V. N. Duradji, and D. E. Kaputkin, J. Electrochem. Soc. **163**, E43 (2016).

[175] S. W. Lee, *Scanning electrometer for electrical double-layer (SEED): The direct measurement of ion dynamics for biosensor*, (University of Nebraska – Lincoln, 2013).

[176] H. Park, D. Kim, and K. S. Yun, Sensors and Actuators B: Chemical **150**, 167 (2010).

[177] H. Zhao, Electrophoresis **32**, 2232 (2011).

[178] X. Jiang, J. Huang, J. Zhao, B. G. Sumpter, and R. Qiao, J. Phys.: Condens. Matter **26**, 284109 (2014).

[179] B. Giera, N. Henson, E. M. Kober, M. S. Shell, and T. M. Squires, Langmuir **31**, 3553 (2015).

[180] J. H. Chaudhry, S. D. Bond, and L. N. Olson, J. Sci. Comput. **47**, 347 (2011).

[181] J. L. Liu and B. Eisenberg, Phys. Rev. E **92**, 012711 (2015).

[182] A. A. Yazdi, A. Sadeghi, and M. H. Saidi, J. Colloid Interface Sci. **442**, 8 (2015).

[183] H. Sugioka, J. Phys. Soc. Jpn. **85**, 124006 (2016).

[184] J. Ying and D. Xie, Appl. Math. Model. **58**, 166 (2018).

[185] J. Xing and Y. Jian, Meccanica **53**, 135 (2018).

[186] J. López-García, J. Horno, and C. Grosse, Micromachines **9**, 647 (2018).

[187] M. Matse, P. Berg, and M. Eikerling, Phys. Rev. E **98**, 053101 (2018).

[188] M. Matse, P. Berg, and M. Eikerling, Eur. Phys. Spec. Top. **227**, 2559 (2019).

[189] M. V. Fedorov and A. A. Kornyshev, Chem. Rev. **114**, 2978 (2014).

[190] S. Kondrat, O. A. Vasilyev, and A. A. Kornyshev, J. Phys. Chem. Lett. **10**, 4523 (2019).

[191] R. L. Fulton, J. Chem. Phys. **130**, 204503 (2009).

[192] W. B. Zimmerman, *Multiphysics modeling with finite element methods*, Vol. 18. (World Scientific Publishing Company, 2006).

[193] D. Henderson, S. Lamperski, L. Bari Bhuiyan, and J. Wu, J. Chem. Phys. **138**, 144704 (2013).

[194] C. Xu, H. Du, B. Li, F. Kang, and Y. Zeng, J. Electrochem. Soc. **156**, A435 (2009).

[195] P. Perret, Z. Khani, T. Brousse, D. Bélanger and D. Guay, Electrochim. Acta. **56**, 8122 (2011).

[196] A. L. d'Entremont and L. Pilon, J. Power Sources **273**, 196 (2015).

[197] J. J. Lado, R. E. Pérez-Roa, J. J. Wouters, M. I. Tejedor-Tejedor, C. Federspill, J. M. Ortiz, and M. A. Anderson, Sep. Purif. Technol. **183**, 145 (2017).

[198] M. Kaisti, Biosensors and Bioelectronics **98**, 437 (2017).

[199] T. L. Horng, P. H. Tsai, and T. C. Lin, Computational and Mathematical Biophysics **5**, 142 (2017).

[200] L. J. Cheng and L. Jay Guo, Chem. Soc. Rev. **39**, 923 (2010).

[201] S. Prakash and A. T. Conlisk, Lab on a Chip **16**, 3855 (2016).

[202] M. Ünlü, J. Zhou, and P. A. Kohl, J. Phys. Chem C. **113**, 11416 (2009).

[203] K. N. Grew, J. P McClure, D. Chu, P. A. Kohl, and J. M. Ahlfield, J. Electrochem. Soc. **163**, F1572 (2016).

[204] J. M. Ahlfield, L. Liu, and P. A. Kohl, J. Electrochem. Soc. **164**, F1165 (2017).

[205] D. Pugal, K. J. Kim, and A. Aabloo, J. Appl. Phys. **110**, 084904 (2011).

[206] Z. Zhu, K. Asaka, L. Chang, K. Takagi, and H. Chen, J. Appl. Phys. **114**, 184902 (2013).

[207] T. Stalbaum, D. Pugal, S. E. Nelson, V. Palmre, and K. J. Kim, J. Appl. Phys. **117**, 114903 (2015).